Deformation mechanism of metastable austenitic steel with TRIP effect and associated kinetics of deformation induced martensitic transformation

2021

Wenqi Mao

Table of Contents

Chapter 1 Background and purpose

1.1. Trade-off between strength and ductility in steels

Steel has been widely applied to automotive applications, which is attributed to its good mechanical properties for relatively high strength and good ductility and relatively low cost compared to other metals. **Figure 1.1** shows the strength and ductility of the steels which are used in the automotive industry history [1]. From the mild steel in the early of 1900s to the first generation of advanced high strength steel (AHSS) in the 1990s, many kinds of steels have been developed in the automotive industry [2]. Many researchers have devoted themselves to improve the strength of steel by developing their composition, fabrication processes, microstructure. The strength of steel increased from 200 MPa in the mild steels to over 1500 MPa in the martensitic steels which is one of the 1st generation of AHSS. The increase of the strength of steel signifies that the thickness of steel components can be reduced without the loss of performance, which is very important for reducing the weight of transport machines, like automobiles. The weight reduction of automobiles has a significant effect to improve the fuel efficiency. It is estimated that a 10% reduction in the automobile results in 6 to 8% improvement in the fuel efficiency [2]. On the other hand, higher strength of steel can also increase the absorption of impact energy and provide more safety protection in traffic accidents. Therefore, steel having higher strength is demanded by the future development of automotive industry.

Besides strength, the ductility of steel is also an important factor for its practical application, which determines the formability of steel during mechanical processes, like cold-rolling and stamping. However, as can be observed in **Figure 1.1**, the elongation (ductility) of steel gradually decreases from the mild steel to the 1st generation of AHSS with increasing the strength, which is usually called the trade-off relationship. Although the 2nd generation AHSS, like twinning induced plasticity (TWIP) steel, overcomes the trade-off relationship to the high-strength and high ductility corner, as shown in **Figure 1.1**, the high cost of the 2nd generation AHSS due to the high alloy content limited their application. During the past ten years, more and more interest has been paid to develop a 3rd generation AHSS with better strength-ductility combinations better than the 1st generation AHSS and having a lower cost than the 2nd generation AHSS. The expectation for the mechanical properties of the 3rd generation AHSS is indicated in **Figure 1.1**. There are several promising solutions for the 3rd generation AHSS.

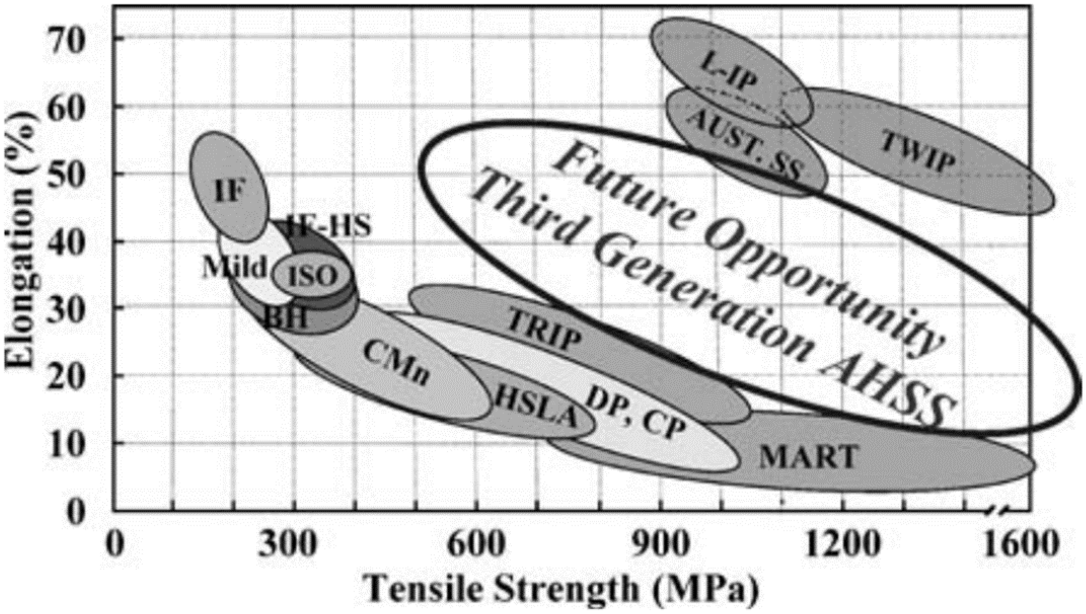

Figure 1.1 Summary of tensile strength and tensile elongation data for various classes of conventional and advanced high strength steels. [1] (IF: interstitial-free steel; IF-HS: interstitial-free high-strength steel; ISO: isotropic steel; BH: bake-hardenable steel; CMn: carbon manganese steel; HSLA: high-strength low alloy steel; DP, CP: dual-phase, complex-phase; TRIP: transformation induced plasticity steel; MART: Martensitic steel; TWIP: twinning induced plasticity steel; AUST.SS: austenitic stainless steel; L-IP: lightweight induced plasticity steel)

(1) Quenching and partitioning (Q&P) steel [3–6]: The Q&P process is a new heat-treatment process to produce high strength steel with significant amounts of retained austenite. **Figure 1.2** shows the schematic illustration of the heat-treatment schedule of the Q&P process and the evolution of the multiphase microstructure [7]. The process involves quenching austenite below the martensitic transformation start

temperature (M_s) to obtained certain amounts of martensite. Then, the steel is reheated and subjected to partitioning treatment, during which the carbon diffuses from the supersaturated martensite to austenite. Due to the increase of carbon content, austenite becomes stable at room temperature. The microstructure of the Q&P steel usually consists of carbon enriched austenite phase and tempered martensite and fresh formed martensite in the final quenching. The austenite could provide TRIP effect to maintain the strain hardening capability of the material, while the martensite could keep the material having a high strength.

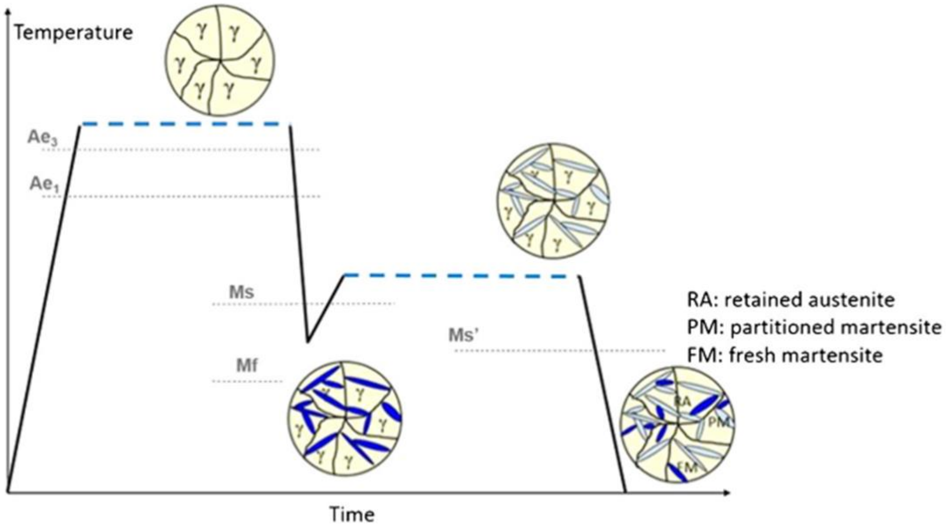

Figure 1.2 Schematic representation of the thermal schedule after cold rolling and typical evolution of the multiphase microstructure in the quench & partitioning (Q&P) thermomechanical process. [7]

(2) Medium Mn steel [8–13]: The medium Mn steel, which contains 5-10wt%Mn, is a promising 3rd generation AHSS for the automotive industry. The medium Mn steel usually has multiphase characteristics consisting of ferrite and retained austenite at room temperature. The tensile properties of the medium Mn steel are similar to the high Mn TWIP steel but at a lower cost. It is mainly contributed to the TRIP effect resulting from the relatively large amount of retained austenite.

(3) Highly deformed microstructure with retained austenite [14,15]: Huang et.al proposed a new process that involves cold-rolling and subsequent low temperature tempering to produce high strength steel with a high dislocation. This thermomechanical process is termed the deformation and partitioning (D&P)

process. The D&P steel, which consists of highly deformed retained austenite and the deformation induced martensite, exhibits over 2 GPa tensile strength and about 20% total elongation. They attributed the good ductility at extremely high tensile stress to the glide of intensive mobile dislocations and the controlled TRIP effect [14].

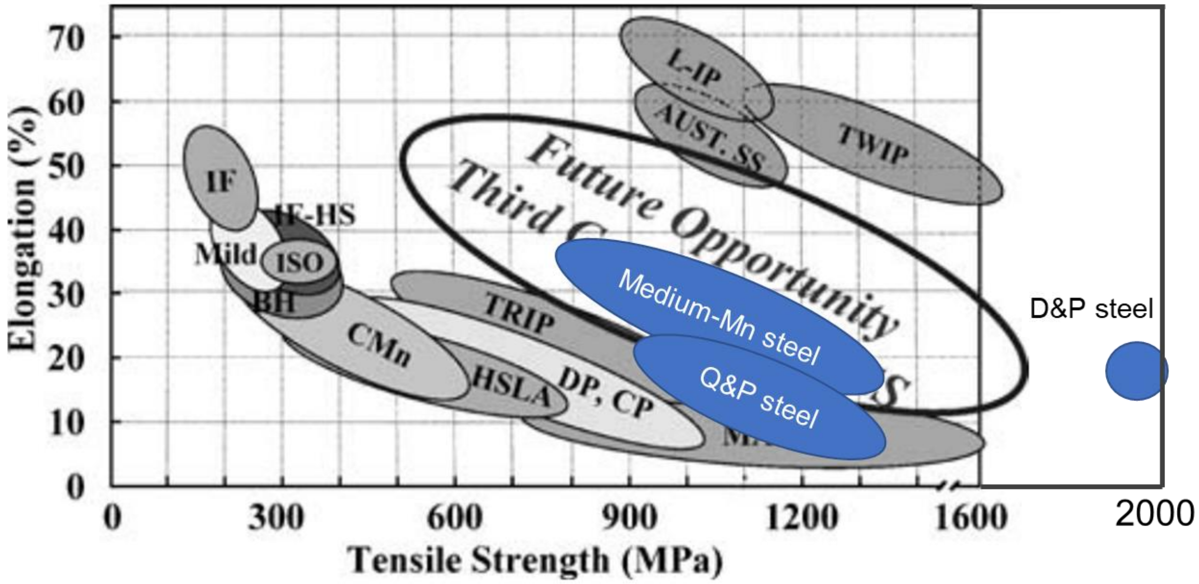

Figure 1.3 Tensile properties of the Q&P steel, the medium-Mn steel and the D&P steel compared with those of other steels. The figure is made based on the results summarized in reference. [14]

Figure 1.3 shows the distribution of the strength and ductility of the Q&P steel, the Medium steel and the D&P steel. They are all located within the region of the expected future 3rd generation AHSS. There are some common characteristics for these promising solutions: (1) multiphase with metastable austenite; (2) fine mean grain size; (3) having TRIP effect during deformation. The high strength of steel can be obtained by the multiphase microstructure consisting of high strength phases such as martensite or ultrafine-grained ferrite and by decreasing the mean grain size. The key point for maintaining relatively large ductility of the high strength steel is the retained austenite which has good deformation compatibility and provides the TRIP effect to increase the strain hardening. Therefore, in the future development of AHSS to overcome the trade-off relationship between strength and ductility, the combination of the TRIP effect and fine-grained or ultrafine-grained microstructure might be one of the promising solutions.

1.2. Ultrafine-grained (UFG) TRIP steel

It has been widely known that grain refinement increases strength of materials due to the Hall-Petch relationship [16]:

$$\sigma_{yield} = \sigma_0 + kd^{-1/2} \qquad (1.1)$$

where σ_{yield} is the yield strength; σ_0 is the friction stress; *k* is a constant depended on material and *d* is the mean grain size. However, it has been found that the tensile ductility significantly decreased when the grain size was refined down to UFG region (d < 1 μm) [17–20]. **Figure 1.4 (a)** and **(b)** shows nominal stress-strain curves of Al and IF steel having various mean grain sizes fabricated by accumulative roll bonding (ARB) and subsequent annealing processes [17]. It is clearly shown that when the grain size decreases in the relatively coarse region the yield strength greatly increases and the uniform elongation does not change so much. However, when the grain size further decreases to smaller than 1 μm the uniform elongation significantly decreases although the yield strength greatly increases.

The limited tensile ductility of UFG materials can be explained by plastic instability criterion [17]. The condition of plastic instability for strain-rate non sensitive materials can be simply expressed by the well-known Considère's criterion shown below:

$$\sigma \geq \frac{d\sigma}{d\varepsilon} \qquad (1.2)$$

where σ is the true stress, ε is the true strain, and $d\sigma/d\varepsilon$ is the strain hardening rate. It is known that the uniform elongation in tensile tests is determined as the elongation at which macroscopic necking starts to develop. When necking occurs, the tensile stress at the necked area becomes higher than that at the un-necked area due to a decrease in the cross section. Meanwhile, the necking area is strain-hardened by the deformation. Whether necking proceeds or not depends on the balance between the tensile stress and strain hardening rate. According to **Equation. 1.2**, when the strain hardening is smaller than the true flow stress, necking will proceed leading to fracture, which is called plastic instability.

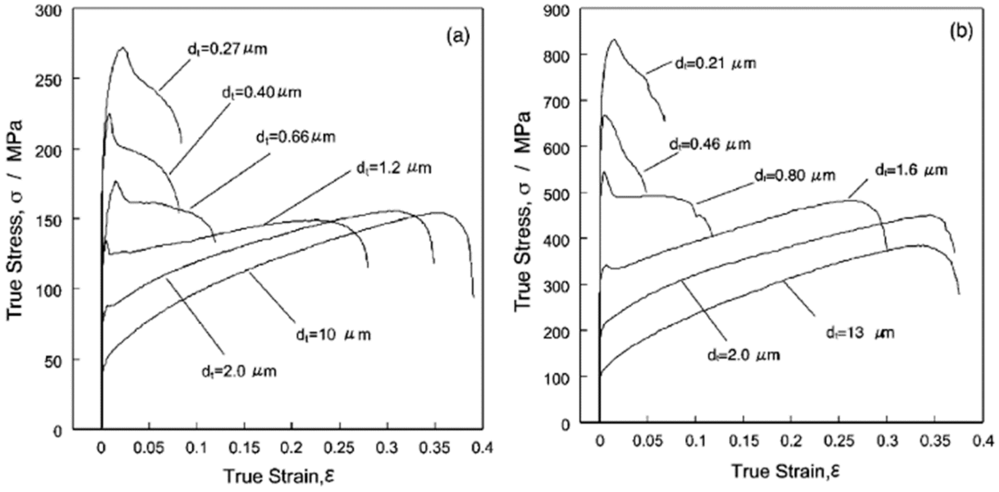

Figure 1.4 True stress-strain curves of the (a) 1100-Al and (b) IF steel with various grain sizes produced by the accumulative roll-bonding (ARB) and subsequent annealing. [17]

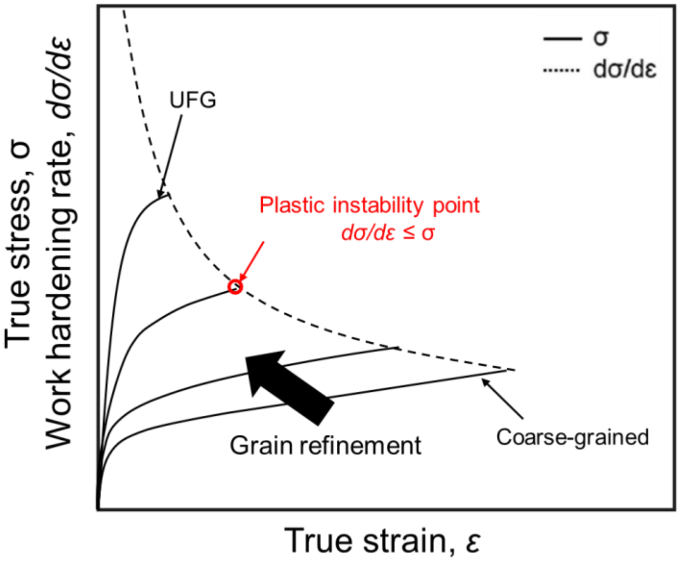

Figure 1.5 Schematic illustration showing change of the plastic instability point that determines the uniform tensile elongation when the yield strength increases by grain refinement under a constant strain hardening capability.

Although the yield strength can be greatly increased by grain refinement, in many cases the strain hardening capability does not change so much. **Figure 1.5** schematically illustrates the limited uniform elongation in UFG materials according to the plastic instability. It is assumed that the strain hardening rate (black broken line) of the material is independent on the grain size, while the yield strength as well as the flow stress of the UFG materials are greatly increased by the grain refinement (black solid lines). It is obviously seen that the tensile strain, at which the plastic instability (necking) occurs, keeps decreasing with decreasing the grain size of the material, resulting in a decrease in the uniform elongation of the material. As the grain size is refined down to UFG regime, plastic instability initiates at very early stage of the tensile test, leading to an immediate necking after macroscopic yielding, as can be seen in **Figure 1.5**. Thus, it is difficult to obtain a good combination of high strength and high tensile ductility in most UFG materials. It is considered that the key factor to manage both high strength and good tensile ductility in UFG materials is to improve the strain hardening capability.

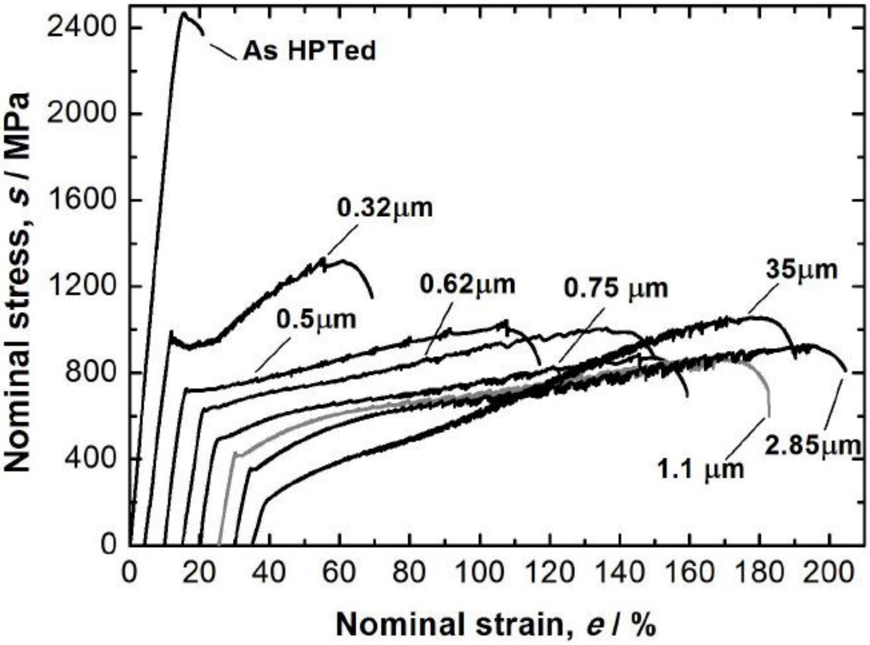

Figure 1.6 Nominal stress-strain curves at room temperature of the Fe-24Ni-0.3C specimens with various grain size and as-HPT processed specimen. [28]

It is well known that martensitic transformation can be initiated in metastable austenite by applying stress and plastic strain above the M_s temperature (and below the T_0 temperature), which is termed as deformation induced martensitic transformation [21,22]. The formation of deformation induced martensite can enhance the strain-hardening rate of the material and lead to high strength and high ductility. The enhancement of ductility is termed as transformation induced plasticity (TRIP) [22]. Therefore, one promising way to improve the strain hardening capability in UFG materials is to introduce the TRIP effect. It has been reported in many researches that UFG TRIP steels show both high strength and large ductility [13,23–27]. Chen Shuai [28], who obtained a doctoral degree in Tsuji lab in 2015, systematically studied the effect of grain size on mechanical properties of the metastable austenitic Fe-24Ni-0.3C (wt.%) ranging from 0.32 μm to 35 μm which were fabricated by HPT process and subsequent annealing. **Figure 1.6** shows the nominal stress-strain curves of Fe-24Ni-0.3C specimens with various mean grain sizes. The yield strength of the specimen significantly increased from 180 MPa to 990 MPa when the mean grain size of austenite reduced from 35 μm to 0.32 μm. Meanwhile, the ultrafine-grained specimen with a mean grain size of 0.32 μm still exhibited a high uniform elongation of about 50 %, which was attributed to the TRIP effect during the deformation. M. Shirdel et.al [26] fabricated UFG 304L austenitic stainless steel by cold rolling and subsequent annealing using the formation and reversion of deformation induced martensite. The UFG specimens of 304L stainless steel with a mean grain size of 0.5 μm also exhibited both high strength and large uniform elongation due to the TRIP effect, as shown in **Figure 1.7**. Not only in the single-phase austenitic steels, but the TRIP effect could also be utilized in the UFG multiphase steel to enhance the ductility, such as UFG medium Mn TRIP steel [13,23,24]. **Figure 1.8** shows the true stress-strain curves and strain hardening rate curve of UFG medium Mn TRIP steel composed of UFG retained austenite and UFG ferrite [13]. The mean grain size of the specimen is about 0.13 μm, in which the sizes were 0.137 μm and 0.125 μm for austenite and ferrite. It can be seen that the UFG medium Mn TRIP steel exhibited both high strength and larger ductility which was also mainly attributed to the formation of martensite in the austenite phase.

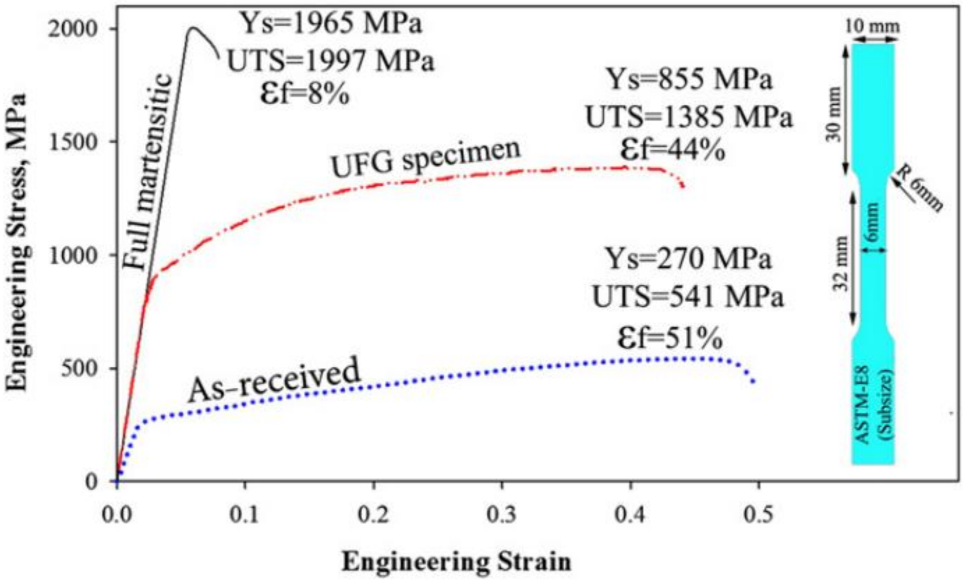

Figure 1.7 The engineering tensile stress-strain curves for the 304L stainless steel with various microstructure at room temperature. [26]

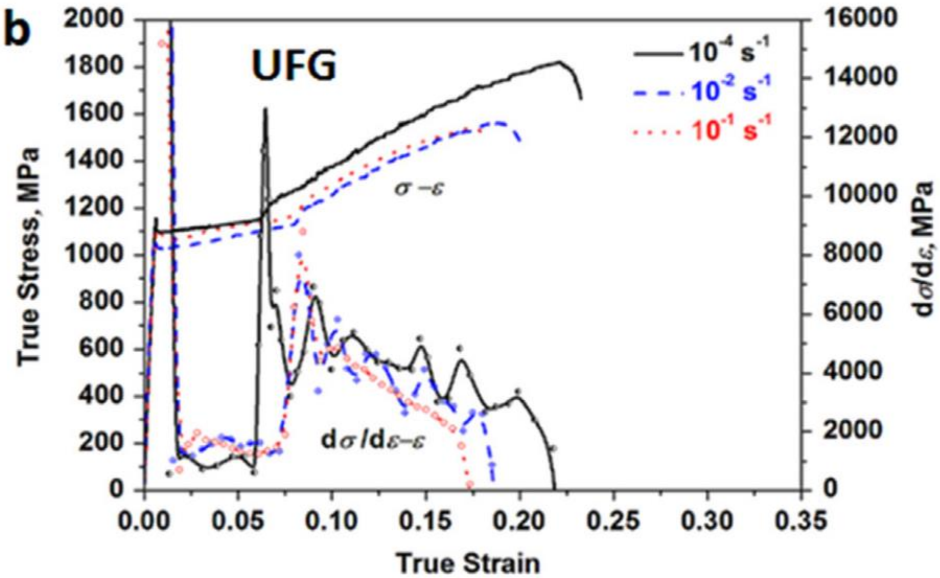

Figure 1.8 Ture stress-strain and strain hardening rate curve of the UFG Mn-based TRIP steel at different strain rate. [13]

The UFG TRIP steels showing both high strength and large ductility have a similar strain hardening behavior, as illustrated in **Figure 1.9**. It clearly demonstrates that to manage both high strength and large ductility in the UFG materials it is necessary to have other deformation mechanisms like martensitic transformation to be activated to regenerate the strain hardening of material when the strain hardening caused by dislocation multiplication becomes not high enough to maintain the uniformed deformation of the material. The increase in the strain hardening rate of the specimen caused by the activation of the martensitic transformation plays a vital role in managing large uniform elongation in the UFG material.

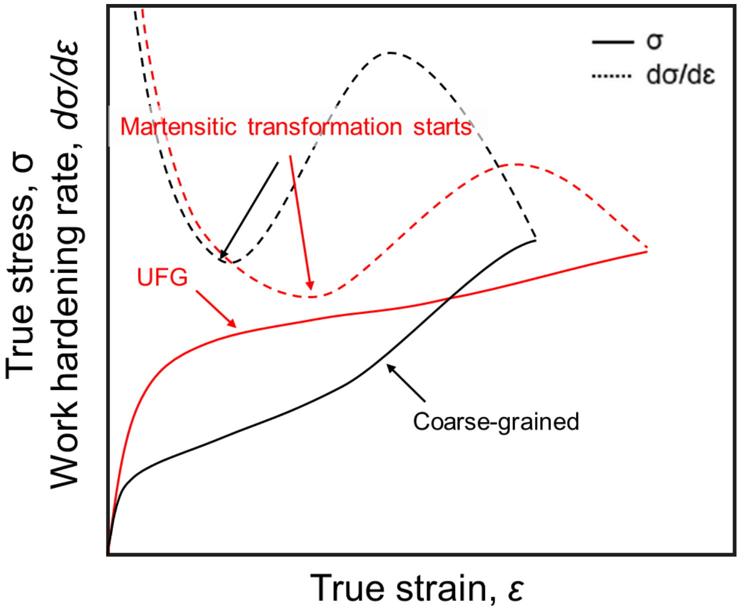

Figure 1.9 Schematic illustration for strain hardening behavior of CG and UFG TRIP steel. During deformation, the strain hardening rate is increased by the initiation of the martensitic transformation, which can increase the uniform elongation of the UFG material.

Many researches have revealed that the increase of the strain hardening rate caused by the formation of martensite greatly depends on its formation rate [29–32]. **Figure 1.10** shows an example in SUS 301L stainless steel [30]. As can be observed in **Figure 1.10**, the deformation of SUS 301L specimens at different temperatures exhibited different strain hardening behaviors accompanying different kinetics of the martensite formation. With decreasing the deformation temperature, the increment of the strain hardening rate of the specimen increased. Meanwhile, the formation rate of the martensite was greatly increased due to the decrease of stability of austenite at a lower temperature. It can be clearly seen that the increment of the strain hardening of the SUS 301L specimen was closely related to the formation rate of the martensite. In the case of metastable austenitic steels, the grain size also greatly influences the stability of austenite [33,34]. In order to maximize the TRIP effect in UFG materials, it is necessary to clarify the effect of the grain size on the DIMT and the strain-hardening behavior.

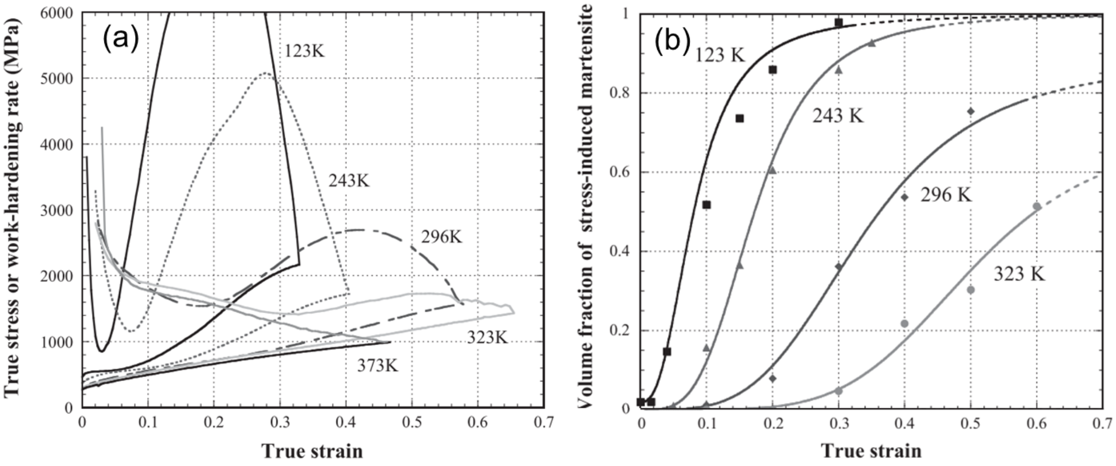

Figure 1.10 (a) True stress-strain curves and strain hardening rate curves of a SUS 301L stainless steel as different deformation temperatures; (b) Changes of volume fraction of the martensite in the SUS 301L stainless steel as a function of temperature at different temperatures. [30]

1.3. Stress partitioning and strain partitioning during the deformation of multiphase material.

Although the tensile behavior of TRIP steels has been extensively studied, researches about the details of the deformation behavior of the austenite and martensite during deformation are still limited. The recent development of in-situ neutron diffraction techniques enables us to investigate the deformation and transformation behaviors of materials during deformation. Phase fraction in the material can be measured from the integrated intensity of diffraction peaks similar to the conventional X-ray diffraction analysis [35].

The stress in a material can be calculated from the lattice strain which is measured according to the peak shift caused by the change of the interplanar spacing due to the stress effect [36].

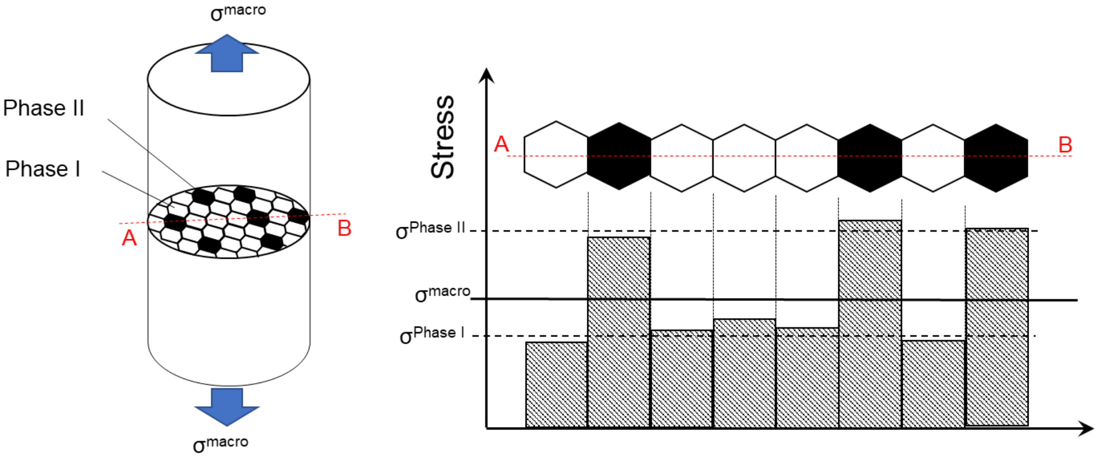

Figure 1.11 Schematic illustration for Type I and Type II stresses in a material, which is composed of soft phase I (white) and hard phase II (black), tensile deformed by applying stress σ_{macro}, as shown in the left side. The distribution of the tensile stress along the red dashed line AB at the intersection is shown in the right side, in which the heights of blocks indicate the average stress in the corresponding grain at the same position in horizontal axis.

Generally, the stress in a material can be classified into three types [36] : (1) Type I stresses are homogeneous over a very large number of crystal domains of the material, which are also termed macro-stress. For instance, in the uniaxial tensile deformation, the macro-stress in the material is the applied tensile stress. (2) Type II stresses are homogeneous within a single grain or phase. The average stress in one phase is termed phase stress. The internal stresses of this type of stress are balanced between different grains or phases. (3) Type III stresses are just homogeneous over a few interatomic distances, such as the stress field around dislocations. **Figure 1.11** shows a schematic illustration for Type I and Type II stresses. Let us assume that a material, which is composed of soft phase I (white) and hard phase II (black), is tensile deformed by applying stress σ^{macro}, as shown in the left side of **Figure 1.11**. The distribution of the tensile stress along the red dashed line AB at the intersection is shown in the right side of **Figure 1.11**, in which the heights of blocks indicate the average stress in the corresponding grain at the same position in the horizontal axis. The average stress of the stress in phase I and phase II is the phase stress $\sigma^{\text{Phase I}}$ and $\sigma^{\text{Phase II}}$, respectively. Meanwhile, the average stress over all grains is equal to the macro-stress. The phase stresses and macro-stress follows the rule of mixture. In the in-situ neutron diffraction experiment, the phase stress in each phase can be measured, respectively, according to their corresponding diffraction profiles. Thus, the stresses directly measured by neutron diffraction are the stress homogenous over many grains having the same orientation or in the same phase, which are the type II stresses.

There have been several reports about deformation behaviors of multi-phased materials studied by the in-situ neutron diffraction [37–39], in which it was found that during the plastic deformation a stress partitioning would occur between different phases due to the phase-to-phase plastic strain incompatibilities. **Figure 1.12** shows an example in a dual-phase steel [37], in which the lattice strain of ferrite of martensite is plotted as a function of applied stress. It can be seen that at the elastic region both the lattice strain of ferrite and martensite had a linear relationship with the applied stress. However, after the plastic yielding of the specimen, the lattice strain of ferrite deviated from the linear relation to the lower side, while the lattice strain of martensite deviated to the upper side. It implies that stress partitioning occurred between ferrite and martensite during the deformation. Such stress partitioning behavior also exits between austenite and martensite during the deformation of TRIP steel [40–42]. We expect that the deformation behavior of the TRIP steels might be determined by the stress partitioning behavior of austenite and martensite and the grain refinement might influence the deformation behavior of TRIP steel by affecting the stress partitioning behavior.

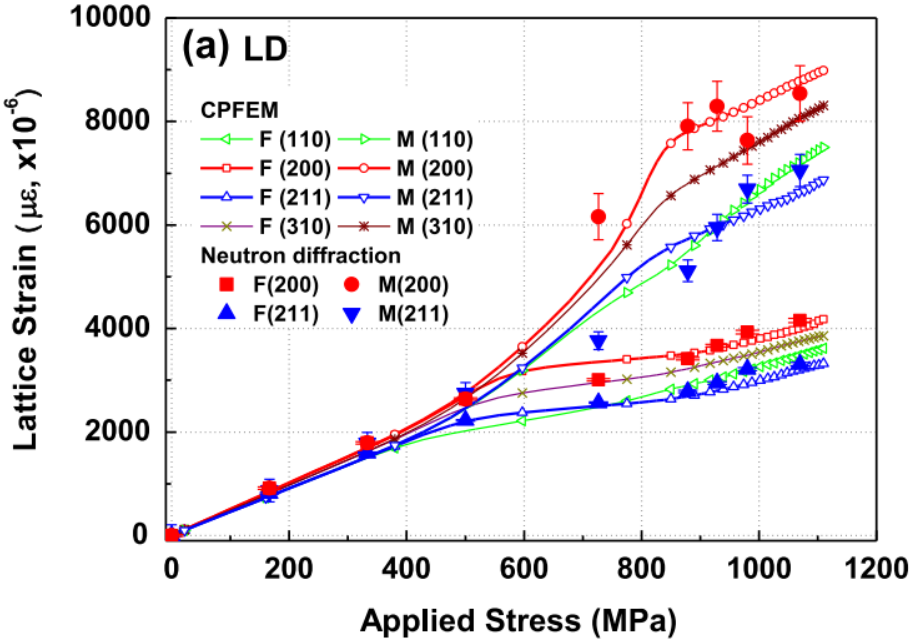

Figure 1.12 In-situ neutron diffraction measured and crystal plasticity finite element method (CPFEM) estimated lattice strain of ferrite (F) and martensite (M) along loading direction (LD) as a function of macroscopically applied stress. [37]

On the other hand, through utilizing the digital image correlation (DIC) method in the deformation of microstructure, the distribution of strain can be mapped on the image of microstructure, which is termed micro-DIC [43–45]. M.H. Park [45] studied the local plastic strain evolution in a dual-phase steel by utilizing the micro-DIC method. The result reveals a very heterogeneous strain distribution in the microstructure in which most of the plastic strain was concentrated on the ferrite with lower hardness, as shown in **Figure 1.13**. In the TRIP steels or metastable austenitic steels, the martensite is much plastically harder than austenite, therefore, the plastic deformation between austenite and martensite must be also heterogeneous. However, there are few researches about the local strain evolution during the deformation of the TRIP steels or austenitic steels. We think clarifying the strain partitioning behavior between austenite and martensite could deepen our understanding of the deformation behavior of the TRIP steels and austenitic steels.

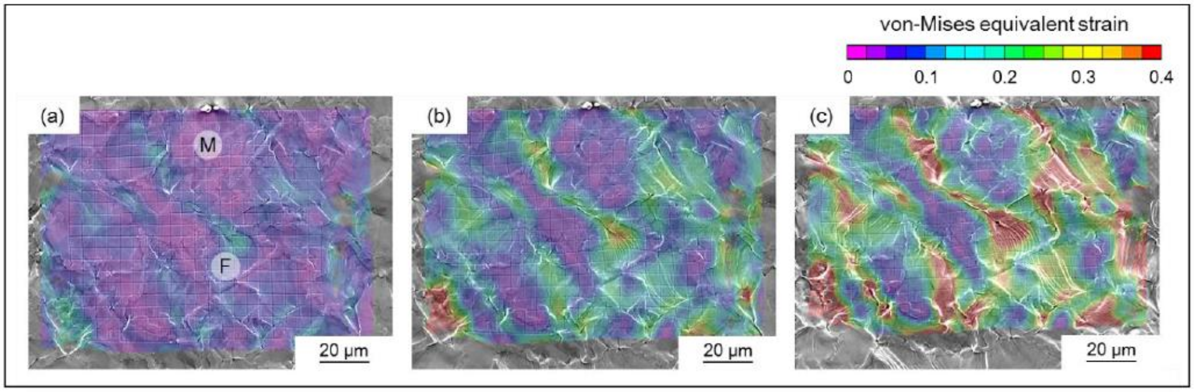

Figure 1.13 Equivalent strain maps of DP structures with grain size of 8.2 μm at the nominal strain of 3.9 % (a), 9.7 % (b) and 15.3 % (c). [45]

1.4. Concept of "PLASTON"

As described above, it is important to have other deformation mechanisms (like martensitic transformation) activated during the deformation to regenerate the strain hardening capability, in order to improve the ductility of UFG materials. Martensitic transformation is a promising deformation model to regenerate the strain hardening capability, as demonstrated in **Section 1.2**. However, it is still unclear why the martensitic transformation can be activated during the deformation of the UFG materials (like UFG Fe-24Ni-0.3C), since the austenite has already been greatly stabilized by the grain refinement at the UFG region. The M_s temperature of Fe-24Ni-0.3C decreased from -26 ^{o}C to -66 ^{o}C when the mean grain size decreased from 35 μm to 0.5 μm [28]. Even so, the UFG Fe-24Ni-0.3C specimen still showed the martensitic transformation during the deformation at room temperature. In order to fully utilizing the TRIP effect in the UFG materials, it is necessary to understand the activation mechanism of the martensitic transformation during the deformation.

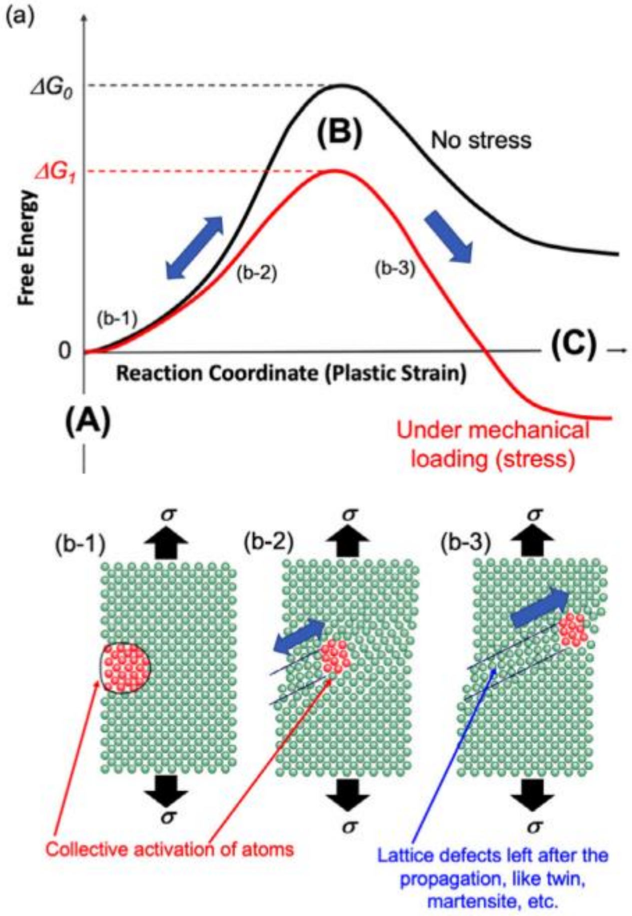

Figure 1.14 (a) Changes in the free energy of the system (material) during the nucleation of a deformation mode according to the reaction coordinate (collective valuable), the plastic strain in this case. Two different free energy curves are drawn, corresponding to a case without stress (black) and a case under a stress (red), respectively. (b) Schematic illustrations showing changes of atomistic structures in a crystal, corresponding to different stages of nucleation shown in (a). Red atoms correspond to the “plaston”, i.e., the local defective region collectively activated mechanically and thermally at a singular region in the material. The propagation of the plaston brings about plastic deformation and may leave a particular lattice defects, such as stacking faults, deformation twins, martensite, etc. [46]

Tsuji et.al [46] proposed a novel concept about the activation of the deformation model from energetics and kinetics. In this novel concept, for the UFG materials which lack dislocation sources, the activation of all deformation model, such as dislocations, stacking faults, deformation twins, martensite, starts from a single region with high local stress and/or high energy in the material, such as grain/phase boundaries, where a certain group of atoms would be activated mechanically and thermally and form a defective zone, as illustrated in **Figure 1.14**. **Figure 1.14 (a)** shows changes in the free energy of the system (material) during the activation of a deformation mode according to the reaction coordinate (collective valuable), i.e., the plastic strain in this case. **Figure 1.14 (b)** illustrates changes of local atomistic structures in a crystal corresponding to different stages in **Figure 1.14 (a)**, in which the red atoms indicate the activated defective zone. **Figure 1.14 (b-1)** and **(b-2)** exhibit the status between the initial point (A) and the peak-energy point (B) in **Figure 1.14 (a)**, and **(b-3)** indicates that between the point (B) and the point (C) in **Figure 1.14 (a)**. In both cases with or without stress, the activation of the deformation model must overcome the energy barrier (activation energy). However, in the case without stress, the energy barrier could only be overcome by thermal activation. But the resultant state (C) should have higher free energy than the initial state (A) because of the lattice defects caused by plastic deformation. Therefore, the activation of the deformation model from (A) to (C) could not spontaneously occur without stress. When a stress is applied to the material, the energy barrier is decreased from ΔG_0 to ΔG_1 by mechanical activation and the final state (C) becomes lower than the initial state (A) because in this the energy would be released by plastic deformation. It means the deformation model can be activated by a stress. After activation, the migration of the defective zone would produce plastic deformation. Depending on the type of deformation model, the migration of the defective zone might leave a particular defect, such as stacking faults, martensite, deformation twins, etc. Such localized defective zone at the front of plastic deformation is defined as “PLASTON”.

Based on the concept of “PLASTON”, we think that the martensitic transformation is activated by deformation might because the applied stress reduces the energy barrier for martensitic nucleation and provide an extra driving force for the transformation. And the kinetics of the deformation induced martensitic transformation which directly determines the TRIP effect depends on the magnitude of the energy barrier (activation energy). Therefore, one of the purposes of this thesis is to investigate the relationship between the stress, plastic strain, grain size and the activation energy of the martensitic transformation.

1.5. Purpose and outline of the thesis

As introduced in the background, although UFG metallic materials have high strength, many of them exhibit early plastic instability due to the lack of strain hardening capability. The TRIP effect is one of the effective ways to increase the tensile ductility of the UFG material by enhancing strain hardening capability. Many researches have demonstrated the combination of the TRIP effect and UFG structure is a promising strategy to manage both high strength and large ductility. However, the exact deformation behavior accompanied by the martensite formation has not been clarified yet. In particular, the detail of deformation behavior of the austenite phase and the martensite phase during deformation of the material and the grain size effect remains unclear. On the other hand, the TRIP effect greatly depends on the kinetics of the martensite formation. However, the mechanism of the kinetics of the deformation induced martensitic transformation is still unclear. And the relationship among stress, plastic strain, and grain size between the kinetics of the deformation induced martensitic transformation also has not been clarified.

In the present study, the deformation behavior of the metastable austenitic Fe-24Ni-0.3C alloy and its grain size dependence is studied from the stress partitioning and strain partitioning behavior between austenite and martensite. In addition, the effect of stress, plastic strain and grain size on the kinetics of the martensitic transformation is investigated in the Fe-23Ni-3.55Mn which exhibits isothermal martensitic transformation at subzero temperature.

The present thesis is composed of five chapters in total. **Chapter 1** introduces the background and purpose of this study. In **Chapter 2**, the deformation behavior of a Fe-24Ni-0.3C specimen with coarse grain size is studied by utilizing in-situ neutron diffraction. The deformation behavior of the specimen is understood from the stress and strain partitioning between austenite and martensite. In **Chapter 3**, the effect of grain size on the deformation behavior of the Fe-24Ni-0.3C is studied. Fe-24Ni-0.3C specimens with fine and ultrafine grain sizes are fabricated by cold-rolling and subsequent annealing, and their tensile behaviors are also investigated by the in-situ neutron diffraction. By comparison of the deformation behavior of the specimens with various grain sizes, the effect of grain size on the deformation behavior of Fe-24Ni-0.3C alloy is discussed. In **Chapter 4**, the effect of tensile stress, prior plastic strain and grain size on the kinetics of isothermal martensitic transformation in Fe-23Ni-3.55Mn is investigated and discussed from the viewpoint of 'PlASTON'. **Chapter 5** is the summary and conclusion of this thesis.

Reference

1. Matlock, D. K. & Speer, J. G. Third Generation of AHSS: Microstructure Design Concepts. in *Proceedings of the international conference on Microstructure and texture in steels* 185–205 (2009).
2. Demeri, M. Y. *Advanced High-Strength Steels*. (2013).
3. Wang, L. & Speer, J. G. Quenching and Partitioning Steel Heat Treatment. *Metallogr. Microstruct. Anal.* **2**, 268–281 (2013).
4. Cho, L., Seo, E. J. & De Cooman, B. C. Near-Ac3 austenitized ultra-fine-grained quenching and partitioning (Q&P) steel. *Scr. Mater.* **123**, 69–72 (2016).
5. Seo, E. J., Cho, L., Estrin, Y. & De Cooman, B. C. Microstructure-mechanical properties relationships for quenching and partitioning (Q&P) processed steel. *Acta Mater.* **113**, 124–139 (2016).
6. Speer, J., Matlock, D. K., De Cooman, B. C. & Schroth, J. G. Carbon partitioning into austenite after martensite transformation. *Acta Mater.* **51**, 2611–2622 (2003).

7. Schmitt, J. H. & Iung, T. New developments of advanced high-strength steels for automotive applications. *Comptes Rendus Phys.* **19**, 641–656 (2018).

8. Suh, D. W. & Kim, S. J. Medium Mn transformation-induced plasticity steels: Recent progress and challenges. *Scr. Mater.* **126**, 63–67 (2017).

9. Cai, Z. H., Ding, H., Misra, R. D. K. & Ying, Z. Y. Austenite stability and deformation behavior in a cold-rolled transformation-induced plasticity steel with medium manganese content. *Acta Mater.* **84**, 229–236 (2015).

10. Hu, B., Luo, H., Yang, F. & Dong, H. Recent progress in medium-Mn steels made with new designing strategies, a review. *J. Mater. Sci. Technol.* **33**, 1457–1464 (2017).

11. Aydin, H., Essadiqi, E., Jung, I. H. & Yue, S. Effect of intercritical heat treatment on the microstructure and mechanical properties of medium Mn steels. *ISIJ Int.* **53**, 1871–1880 (2013).

12. He, B. B., Luo, H. W. & Huang, M. X. Experimental investigation on a novel medium Mn steel combining transformation-induced plasticity and twinning-induced plasticity effects. *Int. J. Plast.* **78**, 173–186 (2016).

13. Cai, M. H. *et al.* Dependence of deformation behavior on grain size and strain rate in an ultrahigh strength-ductile Mn-based TRIP alloy. *Mater. Sci. Eng. A* **653**, 35–42 (2016).

14. He, B. B. *et al.* High dislocation density-induced large ductility in deformed and partitioned steels. *Science (80-.).* **357**, 1029–1032 (2017).

15. Liu, L., He, B. & Huang, M. Processing–microstructure relation of deformed and partitioned (D&P) steels. *Metals (Basel).* **9**, 1–9 (2019).

16. Chokshi, A. H., Rosen, A., Karch, J. & Gleiter, H. On the validity of the Hall-Petch relastionship in nanocrystalline materials. *Scr. Metall.* **23**, 1679 (1989).

17. Tsuji, N., Ito, Y., Saito, Y. & Minamino, Y. Strength and ductility of ultrafine grained aluminum and iron produced by ARB and annealing. *Scr. Mater.* **47**, 893–899 (2002).

18. Valiev, R. Z., Pshenichnyuk, A. I. & Nazarov, A. A. Structural model of ultrafine grained materials produced by severe plastic deformation. *Mech. Corros. Prop. Ser. A, Key Eng. Mater.* **97–98**, 59–64 (1994).

19. Park, K. T., Kim, Y. S., Lee, J. G. & Shin, D. H. Thermal stability and mechanical properties of ultrafine grained low carbon steel. *Mater. Sci. Eng. A* **293**, 165–172 (2000).

20. Zhao, Y. H., Liao, X. Z., Jin, Z., Valiev, R. Z. & Zhu, Y. T. Microstructures and mechanical properties of ultrafine grained 7075 Al alloy processed by ECAP and their evolutions during annealing. *Acta Mater.* **52**, 4589–4599 (2004).

21. Maxwell, P. C., Goldberg, A. & Shyne, J. C. Stress-Assisted and strain-induced martensites in FE-NI-C alloys. *Metall. Trans.* **5**, 1305–1318 (1974).

22. Tamura, I. Deformation-induced martensitic transformation and transformation-induced plasticity in steels. *Met. Sci.* **16**, 245–253 (1982).

23. Zhang, Y. & Ding, H. Ultrafine also can be ductile: On the essence of Lüders band elongation in ultrafine-grained medium manganese steel. *Mater. Sci. Eng. A* **733**, 220–223 (2018).

24. Xie, P. *et al.* A high-performance TRIP steel enhanced by ultrafine grains and hardening precipitates. *Mater. Des.* **127**, 1–7 (2017).

25. Weidner, A., Müller, A., Weiss, A. & Biermann, H. Ultrafine grained high-alloyed austenitic TRIP steel. *Mater. Sci. Eng. A* **571**, 68–76 (2013).

26. Shirdel, M., Mirzadeh, H. & Parsa, M. H. Nano/ultrafine grained austenitic stainless steel through the formation and reversion of deformation-induced martensite: Mechanisms, microstructures, mechanical properties, and TRIP effect. *Mater. Charact.* **103**, 150–161 (2015).

27. Shi, J. *et al.* Enhanced work-hardening behavior and mechanical properties in ultrafine-grained steels with large-fractioned metastable austenite. *Scr. Mater.* **63**, 815–818 (2010).

28. Chen, S. Transformation-Induced Plasticity and Transformation of Ultrafine-Grained Metastable Austenite in Fe-Ni-C Alloy. (2015).

29. Byun, T. S., Hashimoto, N. & Farrell, K. Temperature dependence of strain hardening and plastic instability behaviors in austenitic stainless steels. *Acta Mater.* **52**, 3889–3899 (2004).

30. Tsuchida, N. *et al.* Effects of temperature and strain rate on trip effect in SUS301L metastable austenitic stainless steel. *ISIJ Int.* **53**, 1881–1887 (2013).

31. Järvenpää, A., Jaskari, M., Kisko, A. & Karjalainen, P. Processing and properties of reversion-treated austenitic stainless steels. *Metals (Basel).* **10**, (2020).

32. Gibbs, P. J. *et al.* Austenite stability effects on tensile behavior of manganese-enriched- austenite transformation-induced plasticity steel. *Metall. Mater. Trans. A Phys. Metall. Mater. Sci.* **42**, 3691–3702 (2011).

33. Takaki, S., Fukunaga, K., Syarif, J. & Tsuchiyama, T. Effect of Grain Refinement on Thermal Stability of Metastable Austenitic Steel. *Mater. Trans.* **45**, 2245–2251 (2004).

34. García-Junceda, A., Capdevila, C., Caballero, F. G. & de Andrés, C. G. Dependence of martensite start temperature on fine austenite grain size. *Scr. Mater.* **58**, 134–137 (2008).

35. De, A. K., Murdock, D. C., Mataya, M. C., Speer, J. G. & Matlock, D. K. Quantitative measurement of deformation-induced martensite in 304 stainless steel by X-ray diffraction. *Scr. Mater.* **50**, 1445–1449 (2004).

36. Michael, T. H. & Aaron, D. K. *Measurement of residual and applied stress using neutron diffraction*. *Proceedings of the NATO Advanced Research Workshop* (1991). doi:10.1007/978-94-011-2797-4_46

37. Woo, W. *et al.* Stress-strain relationship between ferrite and martensite in a dual-phase steel studied by in situ neutron diffraction and crystal plasticity theories. *Acta Mater.* **60**, 6972–6981 (2012).

38. Morooka, S., Umezawa, O., Harjo, S., Hasegawa, K. & Toji, Y. Quantitative analysis of tensile deformation behavior by in-situ neutron diffraction for ferrite-martensite type dual-phase steels. *Tetsu-To-Hagane/Journal Iron Steel Inst. Japan* **98**, 311–319 (2012).

39. Cong, Z. H. *et al.* Stress and strain partitioning of ferrite and martensite during deformation. *Metall. Mater. Trans. A Phys. Metall. Mater. Sci.* **40**, 1383–1387 (2009).

40. Tomota, Y. *et al.* Tensile behavior of TRIP-aided multi-phase steels studied by in situ neutron diffraction. *Acta Mater.* **52**, 5737–5745 (2004).

41. Harjo, S. *et al.* In situ neutron diffraction study of alpha-gamma Fe-Cr-Ni alloys under tensile deformation. *Acta Materialia* **49**, 2471–2479 (2001).

42. Harjo, S., Tsuchida, N., Abe, J. & Gong, W. Martensite phase stress and the strengthening mechanism in TRIP steel by neutron diffraction. *Sci. Rep.* **7**, 2–4 (2017).

43. Park, K., Nishiyama, M., Nakada, N., Tsuchiyama, T. & Takaki, S. Effect of the martensite distribution on the strain hardening and ductile fracture behaviors in dual-phase steel. *Mater. Sci. Eng. A* **604**, 135–141 (2014).

44. Ghadbeigi, H., Pinna, C., Celotto, S. & Yates, J. R. Local plastic strain evolution in a high strength dual-phase steel. *Mater. Sci. Eng. A* **527**, 5026–5032 (2010).

45. Park, M. H., Shibata, A. & Tsuji, N. Effect of Grain Size on Mechanical Properties of Dual Phase Steels Composed of Ferrite and Martensite. (2017). doi:10.1557/adv.2016.230

46. Tsuji, N. *et al.* Strategy for managing both high strength and large ductility in structural materials–sequential nucleation of different deformation modes based on a concept of plaston. *Scr. Mater.* **181**, 35–42 (2020).

Chapter 2 Deformation behavior of the metastable austenitic Fe-24Ni-0.3C steel

2.1 Introduction

As introduced in Chapter 1, the TRIP effect is mainly attributed to improvement of strain hardening caused by the formation of deformation induced martensite [1–5]. Numerous researchers have studied the mechanical properties of TRIP steels and its relationship with the evolution of the volume fraction of the deformation induced martensite [6–11]. However, the exact mechanism the enhanced strain hardening and the deformation behavior of TRIP steels is still unclear. In order to fully utilize the TRIP effect in advanced high strength steels, it is necessary to understand the mechanism of the enhanced strain hardening caused by the formation of martensite and the deformation behavior of austenite and martensite during the deformation of TRIP steels.

Generally, it is considered that there are two kinds of mechanisms contributing to the enhancement of strain-hardening by deformation induced martensitic transformation. On one hand, the second phase hardening is considered as the main reason for the enhanced strain-hardening [12–14]. It is believed that deformation induced martensite is plastically much harder than the austenite matrix and bears an important part of the stress applied on the whole material, depending on its volume fraction and strength. Thus, the entire strength of material increases with increasing the volume fraction of martensite, that is, the strain-hardening rate is mainly controlled by the formation rate of the deformation induced martensite. On the other hand, it is considered that the formation of deformation induced martensite can accelerate the accumulation of dislocation around the transformed martensite in austenite and enhance the strain-hardening of the entire material [15–18]. The increase in dislocation density caused by deformation induced martensitic transformation is mainly attributed to (1) the generation of extra dislocation required to accommodate the relatively large transformation strain in the transformed region [16,18] and (2) the production of dislocations from ledge sources in martensite/austenite interfaces [15,17]. Although the mechanism of enhanced strain-hardening caused by deformation induced martensitic transformation has been extensively studied, very limited quantitative analysis on the contribution of deformation induced martensite to the enhanced strain-hardening rate is available. And there are few studies about the detailed deformation behavior of each constituent phase of TRIP steels.

Recent development of in-situ neutron diffraction techniques enables us to investigate the deformation and transformation behaviors of materials during deformation. There have been several reports about deformation behaviors of multi-phased materials studied by the in-situ neutron diffraction [19–21], in which the internal stress of each constituent phase was precisely measured from the diffraction profiles. Besides the internal stress, dislocation densities of each constituent phase which reflect the information of plastic deformation could also be estimated from the diffraction profiles [22]. Therefore, the purpose of this chapter is to clarify the mechanism of the enhanced strain hardening caused by deformation induced martensitic transformation and detailed deformation behavior of TRIP steel by utilizing in-situ neutron diffraction.

2.2 Material and experimental methods

A Fe-24Ni-0.3C (wt.%) alloy was used in this study and its chemical composition is listed in **Table 2.1.** The as-received material in the form of sheet with a thickness of 1 mm was fabricated by hot rolling and then cold rolling and austenitized at 900 °C for 3600 s.

Table 2.1 Chemical composition of Fe-24Ni-0.3C (wt%)

Ni	C	Si	Mn	S	P	O	N	Fe
24.09	**0.3**	0.01	0.07	<0.0005	<0.005	0.0008	0.0006	Bal.

Microstructure observations were performed by the use of a field emission-type scanning electron microscopy (FE-SEM) (JEOL, JSM-7100/7800F) equipped with backscattered electron (BSE) and electron backscattering diffraction (EBSD) detectors. Both SEM-BSE and SEM-EBSD was operated at 15 kV with a working distance of 15 mm. The obtained EBSD data was analyzed by the TSL OIM Analysis software (ver. 7) in which the data points having confidence index (CI) value lower than 0.1 were removed. The surface preparations for BSE and EBSD observation were firstly mechanically polished by 2400 grid grind paper then electropolished in an electrolyte (90 vol.% ethanol + 10 vol.% perchloric acid) at 0 °C for 2 min with a voltage of 20 V.

Tensile tests were carried out at room temperature at an initial strain rate of 8.3×10^{-4} s^{-1} on a universal tensile test machine (SHIMADSU, AG-100kN Xplus). The tensile test specimens having gauge dimensions of 6.0 mm × 2.5 mm × 1.0 mm were cut from the as-received material by a wire electrical discharge machine. The longitudinal direction of the tensile specimens was parallel to the rolling direction (RD) of the sheet. A digital image correlation (DIC) system (Vic-2D) was used in order to precisely measure the displacement of the gage part during the tensile test [23]. A digital image correlation (DIC) system (Vic-2D) was used. All of the tensile test specimens were initially sprayed with white and black inks to create a random speckle pattern that acts as markers for tracking displacements of each region. During the tensile deformation, the images of the tensile specimen surface with the speckle pattern were continuously captured by a CCD camera. From the recorded digital images, the DIC software computed the displacement that occurring on the specimen by tracking the speckle pattern in the images. Then, the tensile elongation was readily measured.

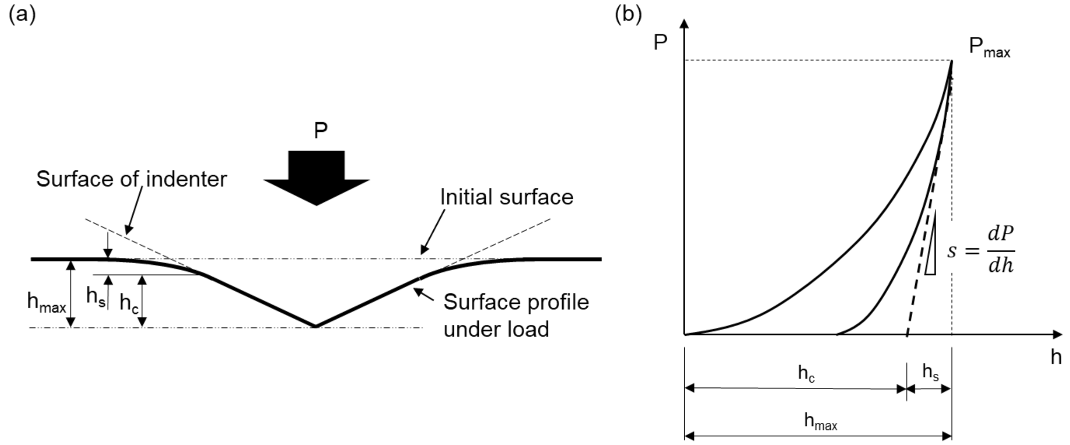

Figure 2.1 Schematic illustrations of **(a)** the nano-indentation test and **(b)** a load-displacement curve.

In order to measure the hardness of different phases in the specimen (i.e. austenite and martensite), nano-indentation tests were carried out using a Hysitron Tribolab nano-indentation system in the load control mode at a constant loading rate of 200 μN·s^{-1} to the maximum load of 1000 μN. The holding time at the maximum load was 5 s. A Berkovich type indenter with a centerline-to-face angle of 65.3º was used. **Figure. 2.1** shows schematic illustrations of (a) the nano indentation test and (b) a load-displacement curve. The nano-hardness can be evaluated by the following **Equation 2.1** [24].

$$H = \frac{P_{max}}{A_c} \qquad (2.1)$$

where H, P_{max} and A_C denote the hardness, the load at the maximum and the contact area shown in **Figure. 2.1 (a)**. The contact area (A_C) can be calculated by following two equations:

$$A_c = F(h_c) \qquad (2.2)$$

$$h_c = h_{max} - \epsilon \frac{P_{max}}{S} \qquad (2.3)$$

where h_C, ϵ and S are the contact depth, the geometric constant for the indenter and the slope at unloading shown in **Figure. 2.1 (b)**. When the contact depth (h_C) is determined by **Equation. 2.3**, contact area (A_C) can be valuated from the contact depth according to the geometry of the indenter (**Equation. 2.2**, which was calibrated using a quartz as a standard sample).

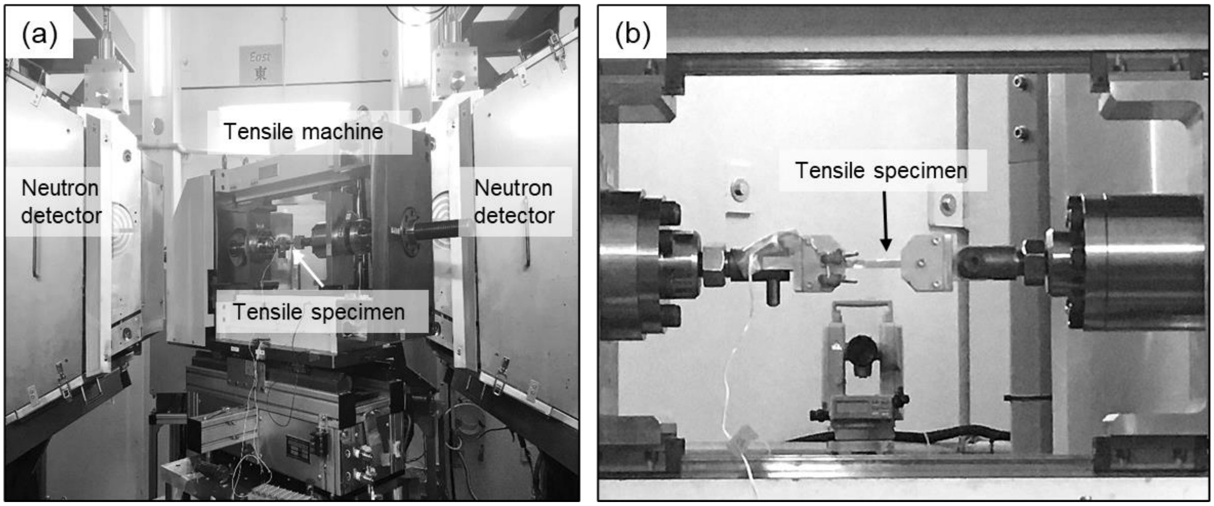

Figure 2.2 Photographs of the in-situ neutron diffraction equipment. **(a)** A front view; **(b)** a tensile test specimen and the tensile machine.

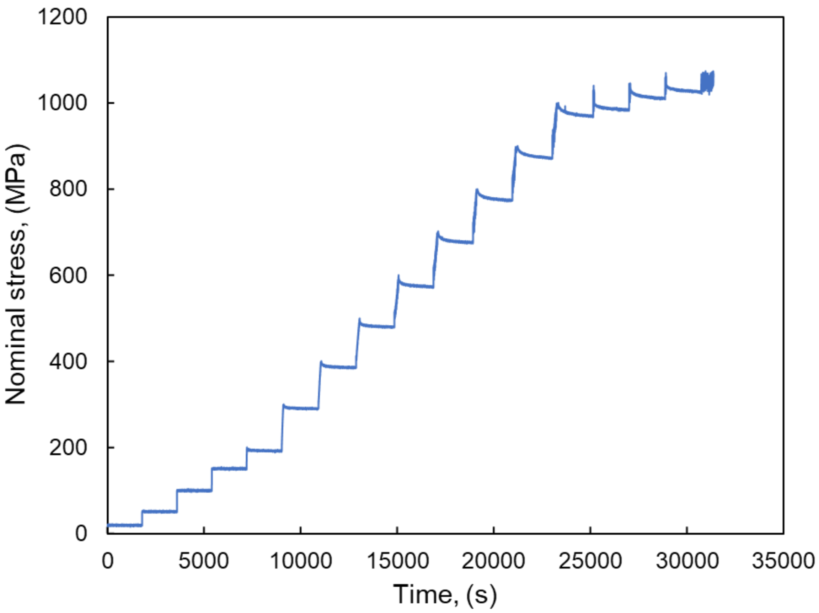

Figure 2.3 Change of applied stress to the specimen as a function of time.

Tensile tests with in-situ neutron diffraction were carried out by using an engineering materials diffractometer at the beam line 19 (TAKUMI) in J-PARC (Japan Proton Accelerator Research Complex). **Figure. 2.2** shows the images of the in-situ neutron diffraction equipment. A spallation neutron source was used in the in-situ neutron diffraction experiment, which has a continuous range of velocities and wavelengths of neutrons. By measuring the time of flight (TOF) of the detected neutrons, the wavelengths can be calculated, and diffraction profiles can be obtained [25,26]. The specimens having a gauge part 50 mm in length, 6 mm in width and 1 mm in thickness were tensile deformed at room temperature at an initial strain rate of 8.3×10^{-4} s^{-1} in a stepwise manner up to fracture, as shown in **Figure 2.3**. The crosshead was temporarily stopped for 10 min at each step to acquire enough intensities of the diffraction profiles. During the temporary stop of the crosshead, stress relaxation of specimen occurred but the stress quickly got stabilized after 1-2 minutes, and the diffraction profiles were obtained from after the stabilization of stress. The schematic illustration of the geometry of measurement in the in-situ neutron diffraction test is shown in **Figure. 2.4 (a)**. The angle between the tensile direction and the incident neutron beam was set at 45° and two neutron detectors (Axial detector and Transverse detector) were arranged 90° and – 90° positions to the incident neutron beam on the horizontal plane. The diffraction of the (hkl) planes that are perpendicular to the tensile direction can be recorded by the Axial detector and the diffraction of the planes parallel to the tensile direction can be recorded by the Transverse detector. An enlarged diffraction peaks of (111) plane of austenite obtained by the Axial detector are shown in **Figure. 2.4 (b)** as an example to represent the effect of stress on the diffraction peaks (peak shifts), which was carefully fitted by Voigt function. It is clearly seen that the (111) diffraction peak of austenite shifts to larger lattice spacing side with increasing the applied stress, which corresponds to the elastic deformation of the lattice in the tensile direction. The elastic strain of a specific lattice plane (ε_{hkl}) was determined by the deviation of lattice plane spacing (d_{hkl}) from the stress-free lattice plane spacing d_{hkl}^{0} by the use of **Equation. 2.4** [21].

$$\varepsilon_{hkl} = (d_{hkl} - d_{hkl}^{0})/d_{hkl}^{0} \qquad (2.4)$$

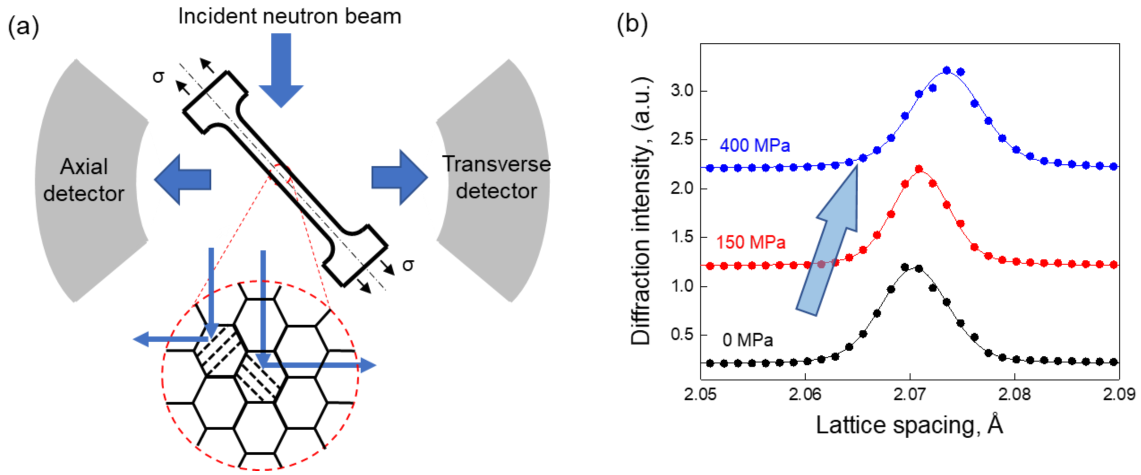

Figure 2.4 (a) Schematic illustration of the geometry of measurements in the in-situ neutron diffraction. **(b)** Example of an enlarged change in the reflection of (111) plane (peak shift) of austenite obtained by the axial detector. The diffraction peak was fitted by Voigt function.

The volume fraction of martensite was measured from the ratio of the integrated intensity of diffraction profiles corresponding to BCC lattice by the following equation [27]:

$$V_M = \frac{\frac{1}{n}\sum_{j=1}^{n}\frac{I_M^j}{R_M^j}}{\frac{1}{n}\sum_{j=1}^{n}\frac{I_M^j}{R_M^j}+\frac{1}{n}\sum_{j=1}^{n}\frac{I_A^j}{R_A^j}} \qquad (2.5)$$

where I_A and I_M are the integrated intensities of the diffraction peaks of austenite (FCC) and martensite (BCC), respectively; R_A and R_M are the ideal integrated intensities of austenite and martensite for the volume ratio of 1:1 without any texture, which were obtained from a Z-Rietveld software. In this study, the diffraction peaks of (111), (200), (220), (311) crystallographic planes of austenite and (110), (200), (211), (220) crystallographic planes of martensite were used to calculate the volume fraction of martensite.

The dislocation density in constituent phases was estimated by using modified Williamson-Hall (WH) method as the following equation 2.6 [28].

$$\Delta K = \alpha + \varphi K\sqrt{C} + OK^2C \qquad (2.6)$$

where $K = 1/\,d_{hkl}$ is the magnitude of reciprocal lattice vector of (hkl) plane; α is a parameter dependent on the crystalline size. C is the average contrast factor for correcting the elastic anisotropy in WH plots and it is expressed at the following equation:

$\mathrm{C} = C_{h00}(1 - qH)$ (2.7)

where C_{h00} denotes the contrast factor in the crystal plane {h00} and q indicate a constant depends on the component of screw dislocations S and H is an orientation parameter. They are expressed as follows:

$C_{h00} = (1 - S)C_{h00}^{E} + SC_{h00}^{S}$ (2.8)

$q = (1 - S)q^{E} + Sq^{S}$ (2.9)

$H = (h^2k^2 + k^2l^2 + l^2h^2)/(h^2 + k^2 + l^2)^2$ (2.10)

Superscript E and S indicates the value when the fraction of edge or screw dislocation is 100% respectively. For the austenite of Fe-24Ni-0.3C, $C_{h00}^{E} = 0.291$, $C_{h00}^{S} = 0.304$, $q^{E} = 1.62$ and $q^{S} = 2.40$, which was calculated according to the research of Ungar et. al[29]

It is confirmed by Ungar that the third term (OK^2C) on the right-hand side of **Equation 2.6** is negligibly small when compared with the value of other terms [30], thus the above equation could be simplified as follows:

$\varDelta K = \alpha + \varphi K\sqrt{C}$ (2.11)

The parameter φ involve the information of dislocation density (ρ) and it is expressed by the following equation:

$\varphi = Ab\sqrt{\pi\rho/2}$ (2.12)

where A is a parameter determined by the effective outer cutoff radius of dislocations; b is the magnitude of Burgers vector of dislocation density (b = 0.254 nm for austenite in Fe-24Ni-0.3C).

By combining **Equation 2.7** and **Equation 2.11**, the following equation could be obtained:

$(\Delta K - \alpha)^2/K^2 = \varphi^2 C_{h00}(1 - qH)$ (2.13)

It indicates that the right-hand side of above equation linearly depends on the orientation parameter H of each diffraction peak. Therefore, the value of parameter α is determined to yield the optimal linear fit in the $(\Delta K - \alpha)^2/K^2$ vs H plots, and the value of q is determined from the slope of the plots. Base on the determined value of q, value of S could be calculated by **Equation 2.9**, then C_{h00} and C could be easily calculated by **Equation 2.8** and **2.7**, respectively. Once the average contrast factor C of each diffraction peak is determined, the value of φ could be obtained from the slope of ΔK vs $K\sqrt{C}$ plots. Then, dislocation density could be estimated according to **Equation 2.12**. It has been reported by Takaki et.al that the parameter A in **Equation 2.12** is almost constant during plastic deformation [31]. In the present study, the parameter A is taken as 0.5 for estimating the dislocation density, which is measured in Fe-0.0056%C alloy [31].

Full width at half maximum (FWHM) of diffraction peaks measured form transverse detector were used in the modified WH method, since the number of diffraction peaks of austenite and martensite having measurable intensity was limited at later stage of deformation due to strong tensile texture of austenite and martensite. In the analysis, the measured FWHM of austenite and martensite was subtracted by the instrumental peak broadening which was determined by the diffraction profiles of a fully annealed austenitic steel and pure Fe.

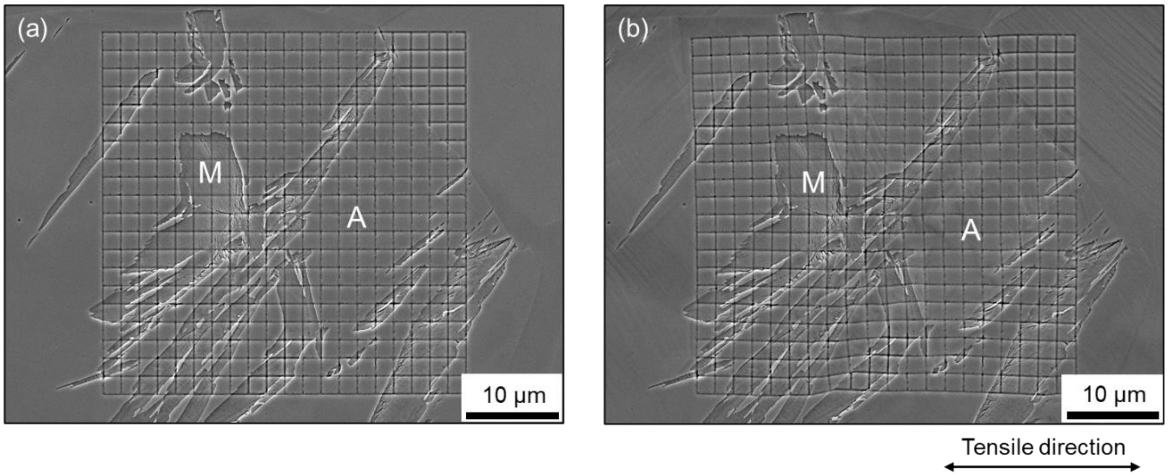

Figure 2.5 SEM images of an identical area in a tensile specimen with a mean grain size of 35 μm. (a) 20% pre-deformed, and (b) 4.5% tensile-deformed in addition to the pre-deformation.

In order to investigate partitioning of plastic strain between austenite and martensite during the tensile test, ex-situ micro-DIC experiment was performed. The tensile specimen was pre-deformed to a certain tensile strain in order to obtain a certain volume fraction of deformation induced martensite. Then, the pre-deformed specimen was electrolytic polished to reveal microstructures. Square-shaped grid was introduced on the surface of the polished specimens by focused ion beam (FIB) with Ga prior to further tensile deformation in order to improve precision of DIC calculation. Afterwards, the pre-deformed specimen was further tensile deformed to a given strain. SEM images before and after the tensile deformation of the specimens were analyzed by the DIC technique. **Figure. 2.5** (a) and (b) exhibits SEM images of a 21% pre-deformed specimen and the identical area after an incremental strain of 4.5%, respectively. Both microstructures and micro-grids were used to identify local areas in the specimen for tacking displacements of identical areas.

2.3 Microstructure and tensile behavior of Fe-24Ni-0.3C

Figure 2.6 (a) and **(b)** displays the BSE and EBSD image of the as-received Fe-24Ni-0.3C specimen, respectively. In the EBSD image, white color represents austenite with FCC structure and the green indicates martensite or ferrite with BCC structure. The low angle boundaries with misorientation between 2º and 15º are drawn in red lines, high-angle grain boundaries with misorientation larger than 15º are drawn in black lines, and annealing twin boundaries (TBs, Σ3) are drawn in blue lines. As can be seen in **Figure 2.6 (a)**, the specimen has a fully recrystallized microstructure composed of nearly equiaxed grains. Whole white color in the phase may of **Figure 2.6 (b)** indicates the as-received specimen is composed of fully austenitic structure. The average grain size of the specimen is about 35 μm, which was measured by interception method including TBs.

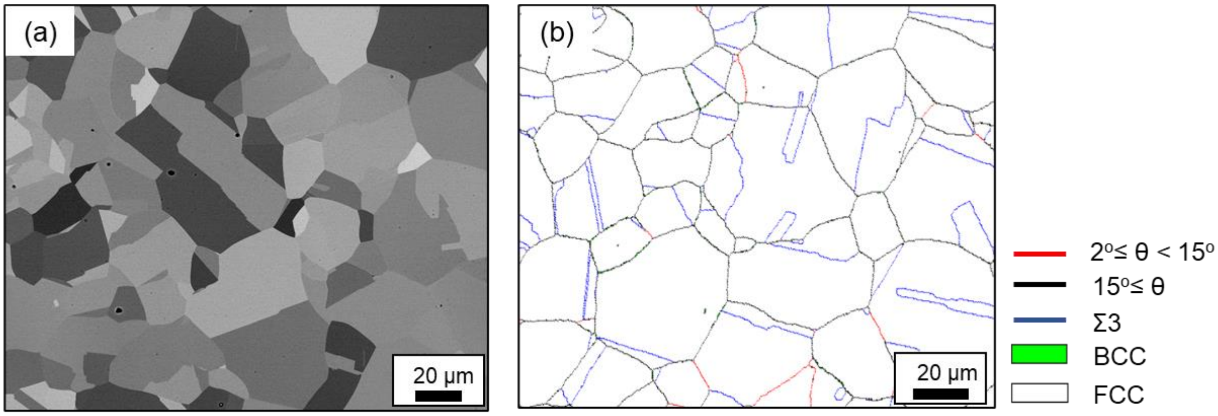

Figure 2.6 (a) BSE and **(b)** EBSD image of Fe-24Ni-0.3C specimen with a mean grain size of 35 μm.

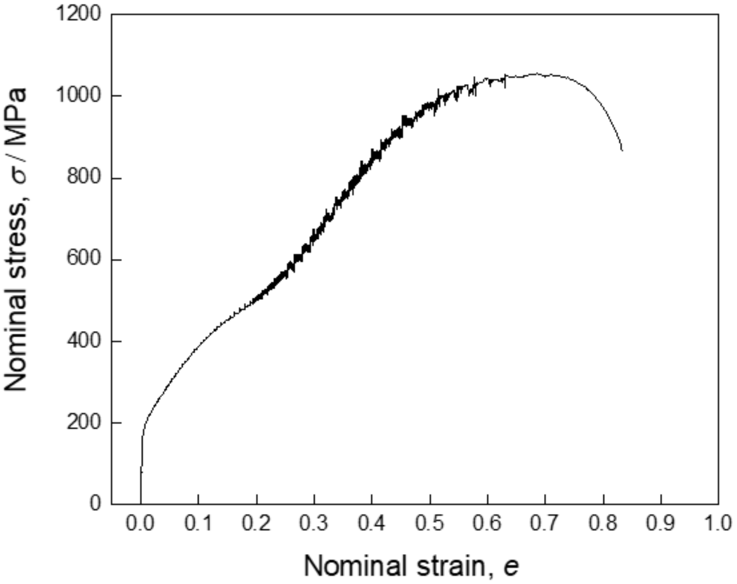

Figure 2.7 Nominal stress-strain curve of the specimen (d_{ave} = 35 μm) at room temperature.

Table 2.2 Mechanical properties of tensile deformation at room temperature for Fe-24Ni-0.3C

Yield strength, $\sigma_{0.2\%}$ / MPa	Ultimate tensile strength, σ_{UTS} / MPa	Uniform elongation	Total elongation
180	1050	0.7	0.86

Nominal stress-strain curve of tensile strain at room temperature for the specimen is shown in **Figure 2.7** and properties of the tensile deformation is listed in **Table 2.2**. It can be seen that 0.2% offset yield strength of the specimen is 180 MPa while the ultimate tensile strength is as high as 1050 MPa, indicating extremely large strain-hardening occurred during tensile deformation. Owing to the high strain-hardening capability, the specimen exhibited a very high uniform elongation about 0.7 which is much larger than that of conventional FCC metallic material, like Al [32]. In addition, serrated flow was observed on the tensile stress-strain curve which is a characteristic behavior of Fe-Ni-C alloy [33]. Although it is no fully clear in the present, it might be due to the dynamic strain aging effect and deformation induced martensitic transformation [34]. **Figure 2.8** shows the true stress-strain curve and strain hardening rate curve of the specimen calculated from the nominal stress-strain curve (**Figure 2.7**). Due to the serration of stress-strain curve, the strain hardening rate curve was obtained from a smoothing processed true stress-strain curve, indicated by dashed line in **Figure 2.8**. It can be seen that the strain hardening rate of the specimen during tensile deformation firstly decreased, then started to increase, and finally decreased again, in which a significant enhancement of strain hardening rate was observed. Such enhancement of strain hardening might be due to the formation of deformation induced martensite.

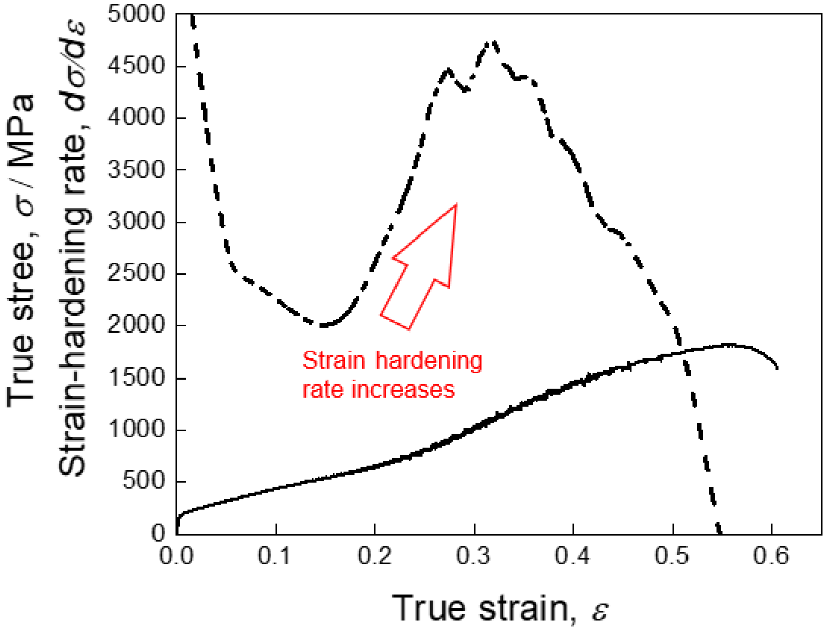

Figure 2.8 True stress-strain curve and strain hardening rate curve of the specimen (d_{ave} = 35 μm) at room temperature.

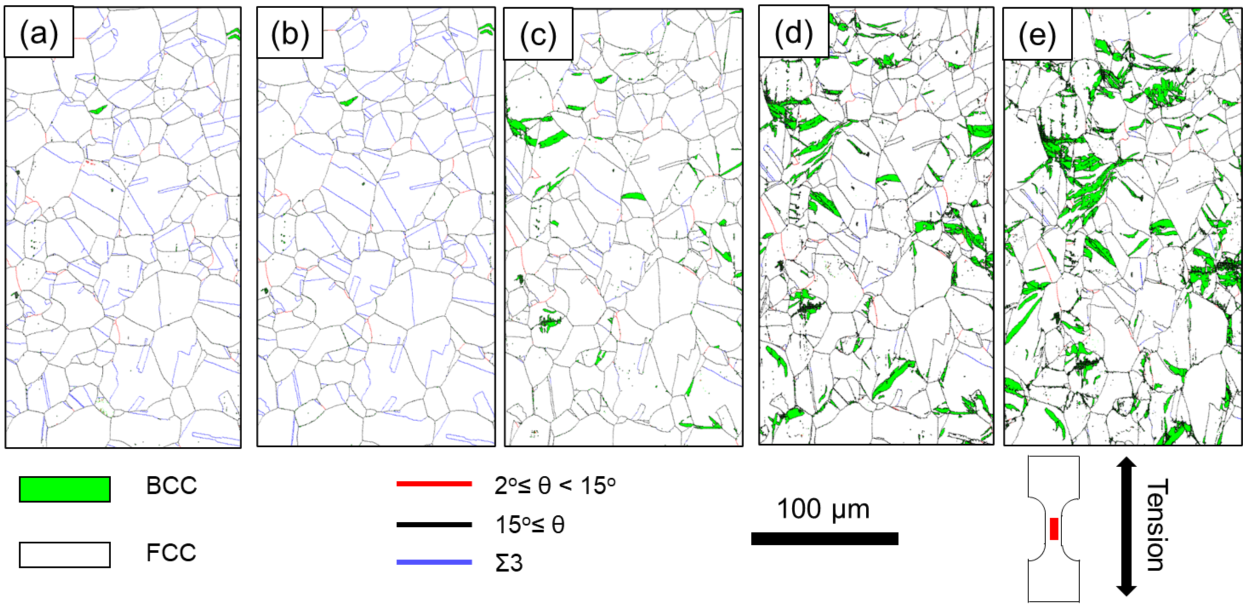

Figure 2.9 EBSD images of the specimen (d_{ave} = 35 μm) after tensile strain of (a) 0; (b) 0.01; (c) 0.11; (d) 0.15; (e) 0.2. A few of martensite plates observed in the undeformed specimen were introduced by the mechanical polishing.

In order to investigate the evolution of microstructure during the tensile deformation, identical area observation was performed by EBSD measurement on the normal directed surface of tensile specimen indicated by the red area as shown in **Figure 2.9**. **Figure 2.9 (a) - (e)** shows EBSD images of the microstructure of the identical area after tensile strain of 0, 0.01, 0.11, 0.15 and 0.2, respectively. It can be clearly seen that deformation induced martensite formed during the tensile deformation and the volume fraction of martensite increased with increasing the tensile strain. These result reveals that the deformation induced martensitic transformation started at tensile strain of 0.11. However, it should be noted that the formation of martensite is preferred at the surface of material because the restraint of matrix for the martensitic shear transformation at surface is weaker than that interior the material [35]. Therefore, the change in volume fraction of martensite as increasing the tensile strain measured at the surface could not represent the real kinetics of deformation induced martensitic transformation. To precisely measure the change of volume fraction of martensite of the entire specimen during tensile deformation, the microstructure on the transverse section of specimens at different stages were observed by optical microscopy. **Figure 2.10** shows the increasing in volume fraction of martensite as increasing the tensile strain at room temperature, and the strain hardening rate curve of the specimen is presented as well. Though comparing the changes of martensite volume fraction and strain hardening rate during deformation, it was found that the increase of the strain hardening rate of the specimens was strongly related to the formation of deformation induced martensite, since the true strains at which the deformation induced martensitic transformation started corresponded well with the true strains where the strain hardening rate started to increase significantly, indicated by a mark ‘M’. Therefore, it can be speculated that the enhancement of strain-hardening was attributed to the deformation induced martensitic transformation and the deformation behavior of the specimen is closely related to the martensitic transformation. In the following sections detailed studies of the mechanism of enhanced strain hardening and the deformation behavior of Fe-24Ni-0.3C will be introduced.

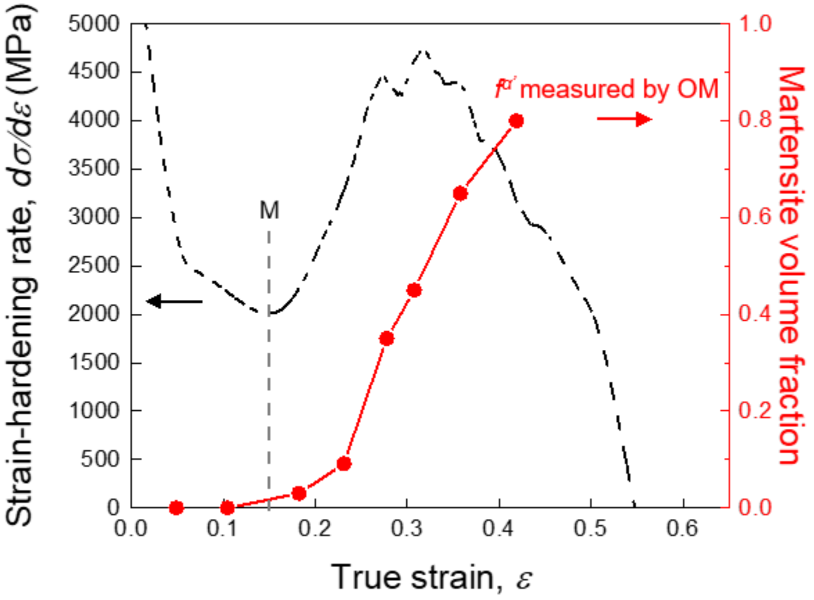

Figure 2.10 Change of volume fraction of martensite as a function of true strain and the strain hardening rate curve of the specimen at room temperature. M indicates the starting point of the martensitic transformation.

2.4 The validity of the simple rule of mixture on the strain hardening behavior of Fe-24Ni-0.3C.

In order to clarify the origin of the enhanced strain-hardening observed in **Figure 2.8**, changes in the nano-hardness of austenite and martensite in the specimen having the mean grain size of 35 µm was measured by nano-indentation tests at different stages of tensile deformation. **Figure 2.11** shows the changes of average nano-hardness of austenite and martensite as a function of the true strain in the tensile deformation. The results revealed that the nano-hardness of austenite gradually increased during the tensile deformation whereas that of martensite was almost constant.

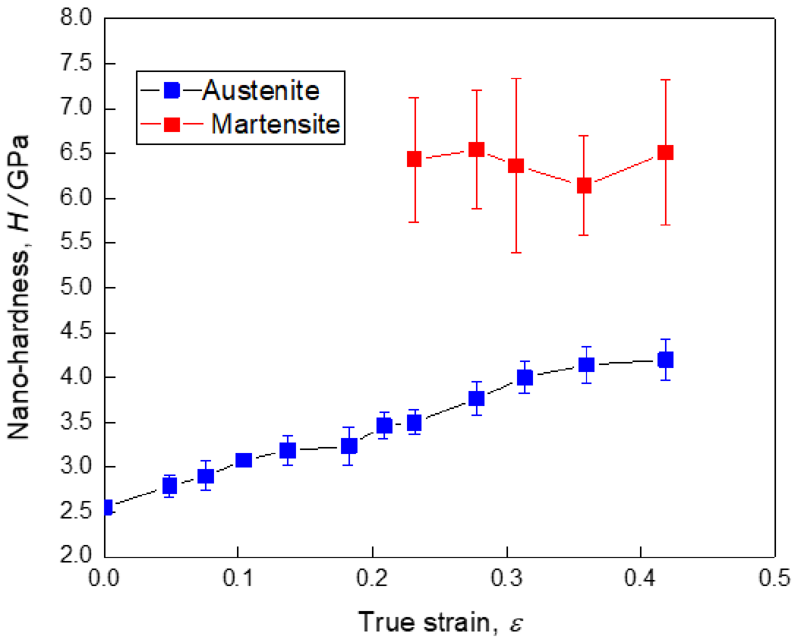

Figure 2.11 Changes in the nano-hardness of austenite and martensite in the specimen having a mean grain size of 35 µm, plotted as a function of the true strain in the tensile deformation.

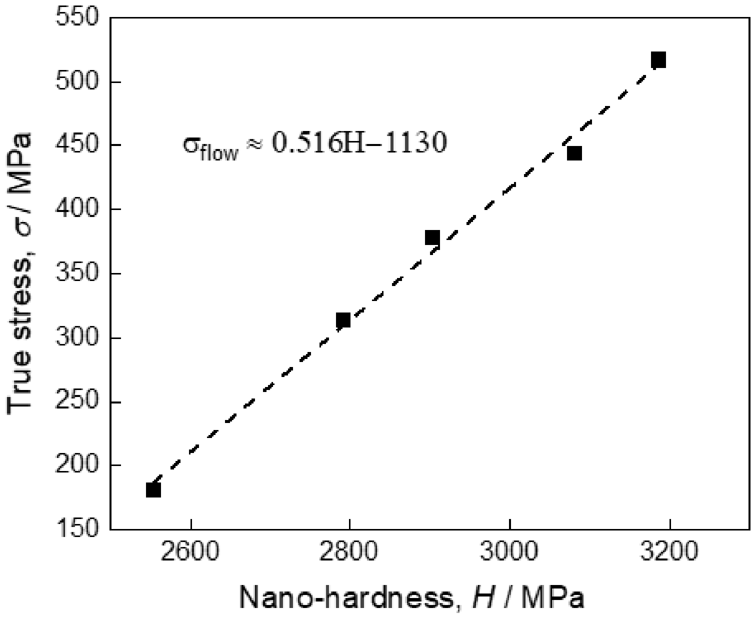

Figure 2.12 Linear relationship between the nano-hardness and the flow stress of austenite, according to **Equation 2.15**.

Generally, for a large indentation depth (larger than 2 μm), Tabor's relationship shown below can be assumed to correlate the nano-hardness with the flow stress [36]:

$$\sigma_{flow} = aH \qquad (2.14)$$

where σ_{flow} is the flow stress at a certain plastic strain; H is the nano-hardness and a is a proportional constant. However, for a small indentation depth, the Tabor's relationship needs to be modified in a following way [36]:

$$\sigma_{flow} = a'H + b \qquad (2.15)$$

where a' and b are constants depending on the imposed depth. In this study, the depth of indentation was about 0.1 µm which was a relatively small value for nano-hardness tests. Thus, before the onset of deformation induced martensitic transformation where the specimen was fully composed for austenite, a linear relation between the nano-hardness of austenite and its flow stress could be obtained according to

Equation 2.15. The obtained result is shown in **Figure 2.12**. It was assumed that the obtained linear relationship expressed in **Equation 2.15** could be applied to martensite as well. Consequently, the flow stress of austenite phase and martensite phase at different strains could be separately estimated from their nano-hardness values. **Figure 2.13** shows changes of the estimated flow stresses of two different phases (austenite and martensite) as a function of the true strain in the tensile deformation. It is seen that the flow stress of austenite significantly increased from 187 MPa (at ε = 0.002) to 1000 MPa (at ε = 0.42), implying that austenite was significantly strain hardened. On the other hand, the flow stress of martensite was much higher than that of austenite, but kept nearly constant value of about 2.1 GPa. The estimated flow stress of martensite was similar to the tensile strength of fully martensitic steels having 0.3 wt% carbon reported in previous researches [37].

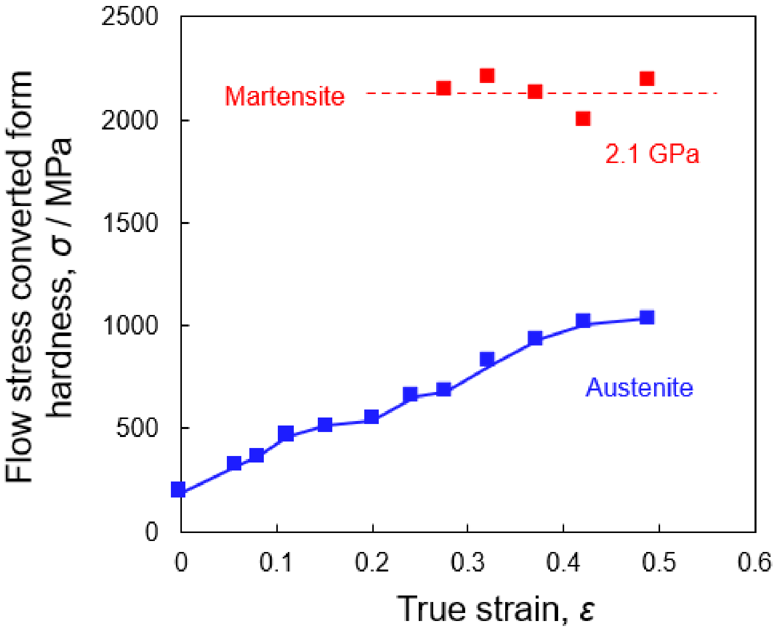

Figure 2.13 Flow stress of austenite and martensite phases in the specimen with the mean grain size of 35 μm, estimated from the measured nano-hardness.

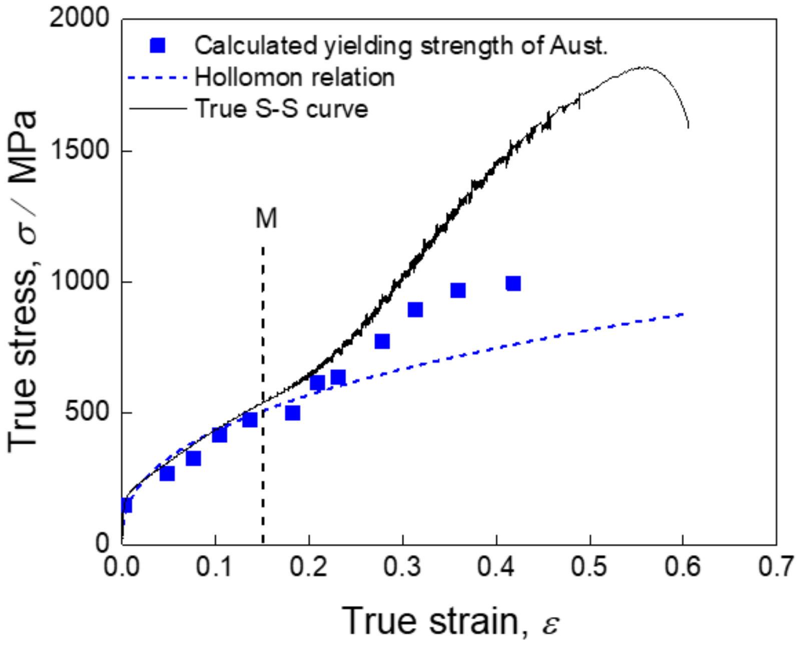

Figure 2.14 Flow stress of austenite converted from the nano-hardness (indicated by blue squares) and the true stress-strain curve of austenite estimated by Hollomon relation (indicated by a dashed line) and the experimentally obtained true stress-strain curve for the specimen having the mean grain size of 35 µm.

It is well known that true stress-strain curves for polycrystalline metals (without deformation induced martensitic transformation) can be empirically described by the Hollomon relation [38]:

$$\sigma_{flow} = K(\varepsilon)^n \qquad (2.16)$$

where σ_{flow} is the flows stress; ε is the true strain; K is a constant and n is a strain-hardening exponent. Therefore, the true stress-strain curve of the austenite in the present alloy can be obtained by fitting the true stress-strain curve at early stages of tensile deformation without an effect of deformation induced martensitic transformation, using the Hollomon equation. The obtained stress-strain curve was then extrapolated to the larger strains, as shown in **Figure 2.14.** In **Figure 2.14**, the flow stress of the austenite at different strains, that was converted from the nano-hardness (shown in **Figure 2.11**), are also presented. The graph showed that flow stress of austenite converted from the nano-hardness (blue squares in **Figure**

2.14) fits very well with the experimentally obtained true stress-strain curve and the Hollomon relation at early stages of tensile deformation. The experimentally obtained true stress-strain curve shows a positive deviation from the Hollomon relation when the tensile true strain is higher than 0.2, which corresponds to the initiation of deformation induced martensitic transformation. This means that the flow stress of the alloy increased due to the deformation induced martensitic transformation.

In addition, after the deformation induced martensitic transformation started, the flow stress of the austenite converted from the nano-hardness also deviated upward from the Hollomon relation (but lower than the true stress), implying that the flow stress of austenite was also increased due to the deformation induced martensitic transformation. It was reported in the previous studies that the deformation induced martensitic transformation can increase the accumulation of dislocations in austenite phase leading to the increase in the strength of austenite [16]. On the other hand, another possible explanation is that the plastic strain was concentrated in softer austenite phase during deformation, so that the substantial plastic strain austenite phase experienced was higher than the average true strain of the tensile specimen. However, the increase in the flow stress of austenite is relatively small, which is insufficient to explain the increment of the flow stress of the entire specimen. Thus, it is considered that the contribution from martensite to the enhanced strain-hardening is more important.

It has been often assumed that the strength of materials consisting of two or more phases having different strength follows the rule of mixture in which each constituent phase shares a part of the total flow stress, depending on its strength and volume fraction [12–14]. Therefore, it has been widely accepted that the total strength of TRIP steels increases with increasing the volume fraction of martensite due to its high strength, and the strain-hardening rate was proportional to the formation rate of martensite. To verify the contribution of martensite to the enhanced strain hardening, the total flow stress of the specimen was calculated using the rule of mixture. For the calculation, the flow stress of austenite and martensite converted from their nano-hardness was used. **Figure 2.15** shows the calculated total flow stress obtained by the rule of mixture (indicated by red circles), together with the experimentally obtained true stress-strain curve. Unexpectedly, the result revealed that the calculated flow stress became larger than the experimentally measured true stress after the deformation induced martensitic transformation started, implying that the simple rule of mixture could not work to express the total flow stress of the metastable austenitic steel.

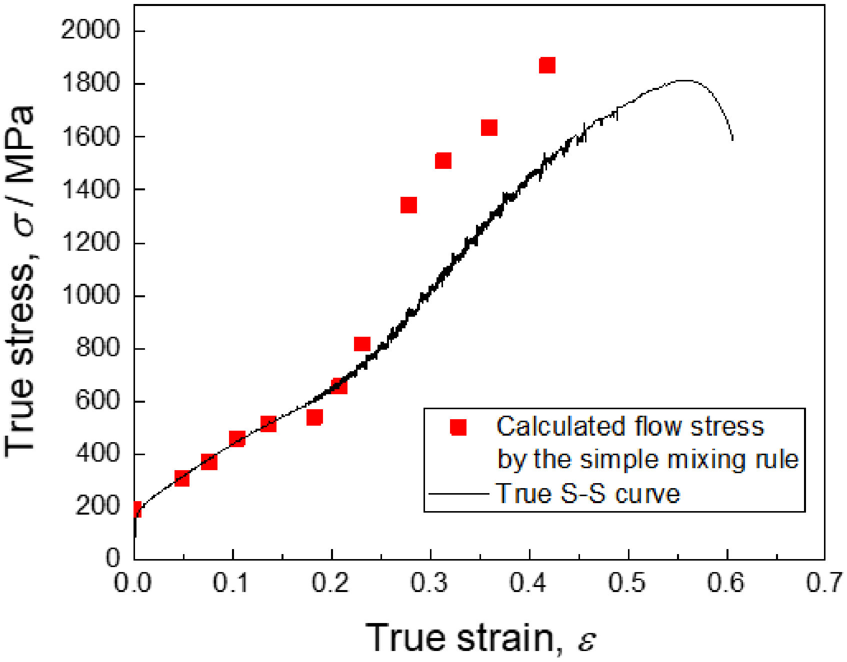

Figure 2.15 The total stress of 35 μm specimen calculated by the rule of mixture in which the strength and of austenite and martensite converted from their nano-hardness was used and the corresponding true stress-strain curve.

The inconsistency between the calculated flow stress and the experimentally obtained flow stress is possibly attributed to the interaction between two phases (austenite and martensite), which is neither considered in the simple rule of mixture nor reflected by the nano-hardness of each phase. The nano-indentation tests were performed within the austenite phase or martensite phase independently, so that, the measured nano-hardness corresponded to the flow stress of each phase when it is deformed independently. But in the actual specimen, two phases having different mechanical properties (strength, elastic constant) are not equally deformed. The two phases embedded in the material and connected at interphases have to accommodate to each other during plastic deformation to maintain the compatibility, resulting in a stress and strain partitioning between two phases [19–21]. Thus, the actual flow stress of austenite and martensite during plastic deformation cannot be determined by their nano-hardness. The stress partitioning behavior must be considered for discussing the enhanced strain hardening of the whole specimen. Then, the in-situ neutron experiments were carried out for evaluating the internal (partitioned) stress in austenite and martensite phase during deformation.

2.5 Stress partitioning behavior between austenite and martensite studied by in-situ neutron diffraction

In order to investigate the stress partitioning behavior between martensite and austenite during deformation, tensile tests at room temperature with in-situ neutron diffraction were performed at the beam line 19 (TAKUMI) in J-PARC. Neutron diffraction profiles of the specimen at different tensile strains recorded by the axial detector in **Figure 2.3 (a)** (corresponding to the diffraction from the lattice planes perpendicular to the tensile direction) are presented in **Figure 2.16**, in order to show changes of the diffraction profiles during the deformation. It can be clearly seen that $(110)_{\alpha'}$ and $(211)_{\alpha'}$ peaks of martensite phase appeared during the deformation and their intensity increased with increasing the tensile strain, indicating the developing of deformation induced martensitic transformation. In addition, strong textures of austenite and martensite could be observed in diffraction profiles of the tensile deformed specimen. In order to quantitatively determine the texture of deformed specimens, inverse pole figure (IPF) images of austenite and martensite in the specimen at different strain stages in the tensile direction are shown in **Figure 2.17**, which were obtained from the ratio of integrated intensities of diffraction peaks (shown in **Figure 2.16**) normalized to their crystal structure factors by using analysis software MAUD [39]. **Figure 2.17 (a)** shows the IPF image of austenite in the Fe-24Ni-0.3C specimen before tensile deformation, indicating that the undeformed specimen has relatively weak texture. As increasing the tensile strain to

0.17, <111>$_{\gamma}$ and <100>$_{\gamma}$ parallel to the tensile direction is strengthened in the tensile deformation as shown in Figure 2.17 (b), since it is known that FCC metals and alloys tensile-deformed are used to have <111>$_{\gamma}$ + <100>$_{\gamma}$ fiber texture [40]. However, as can be observed in **Figure 2.17 (c)** and **(d)**, with further increasing the tensile strain the <100>$_{\gamma}$ texture in tensile direction was gradually weakened probably due to the deformation induced martensitic transformation. As a result, austenite grains in the tensile deformed specimens had a strong <111>$_{\gamma}$ texture where <111>γ direction was parallel to the tensile direction. Meanwhile, **Figure 2.17 (e)** and **(d)** reveal that the deformation induced martensite also exhibited a strong texture. Most of deformation induced martensite grains had <110>$_{\alpha'}$ direction parallel to the tensile direction, which is also a typical fiber texture developing in BCC metals and alloys deformed in tension. Thus, in this study the lattice strains of (111)$_{\gamma}$ plane of austenite and (110)$_{\alpha'}$ plane of martensite was used to represent the elastic deformation of austenite and martensite in tensile direction, respectively.

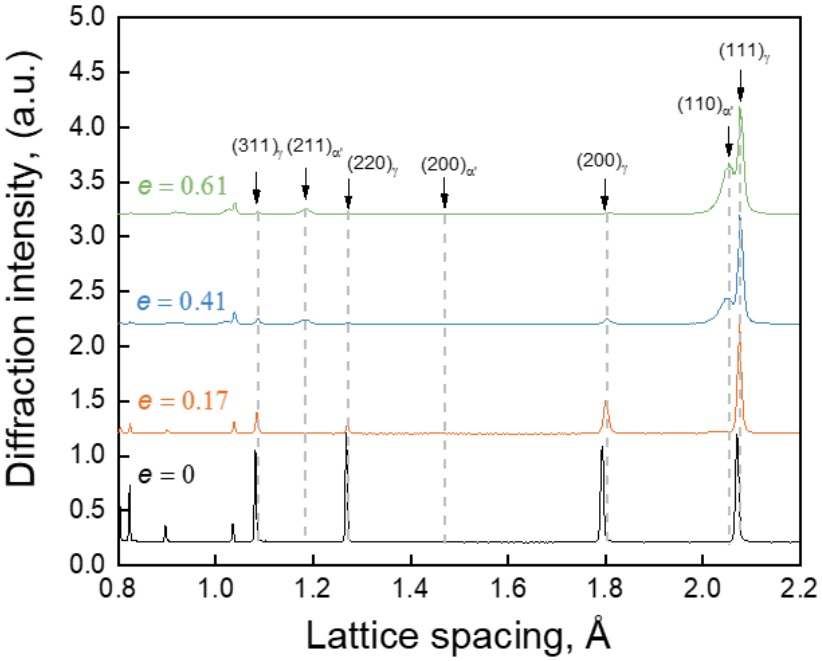

Figure 2.16 Typical diffraction profiles for the axial direction taken at different strain stages.

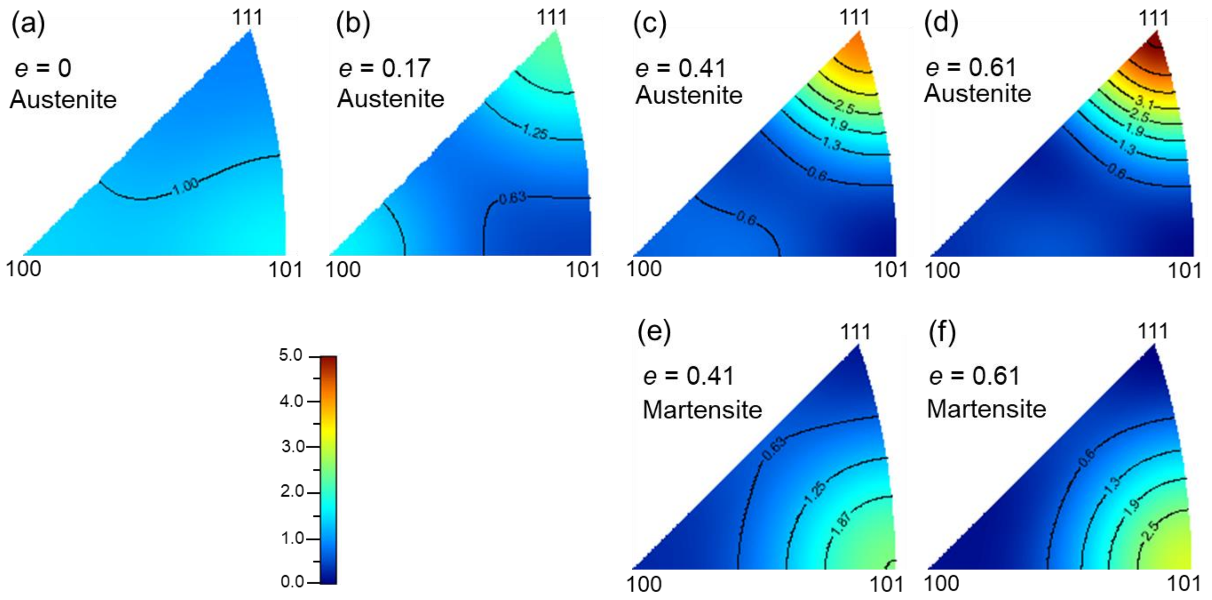

Figure 2.17 Inverse pole figure (IPF) images in the tensile direction. (a) is IPF image of austenite before deformation; (b)-(d) and (e)-(f) are IPF images of austenite and martensite at the different tensile strain, respectively. The IPF images were obtained from the diffraction profiles shown in **Figure 2.16**.

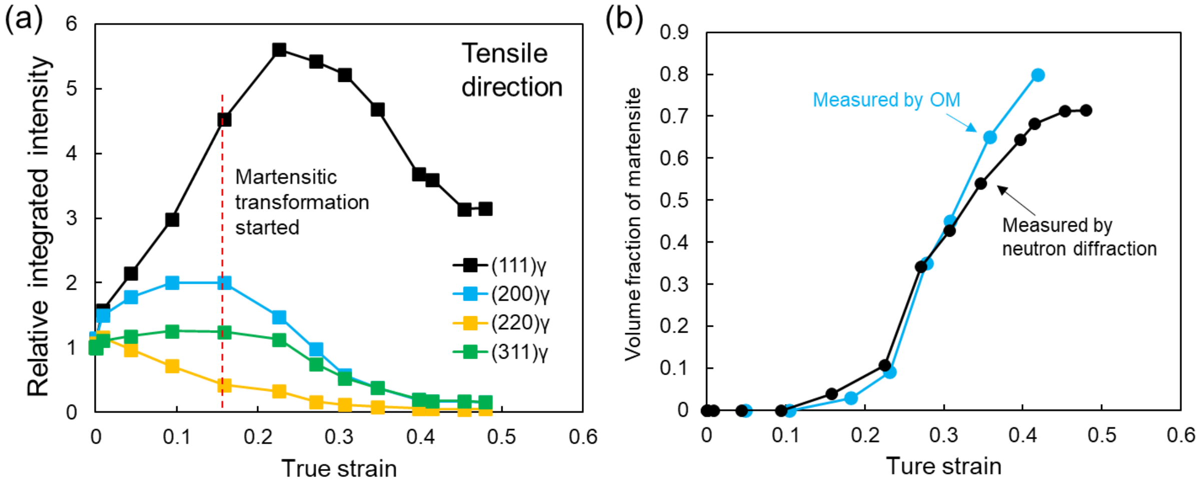

Figure 2.18 (a) Changes of relative integrated intensities of several diffraction peaks of austenite as a function of the tensile true strain; **(b)** Increasing in the volume fraction martensite with increasing the tensile true strain.

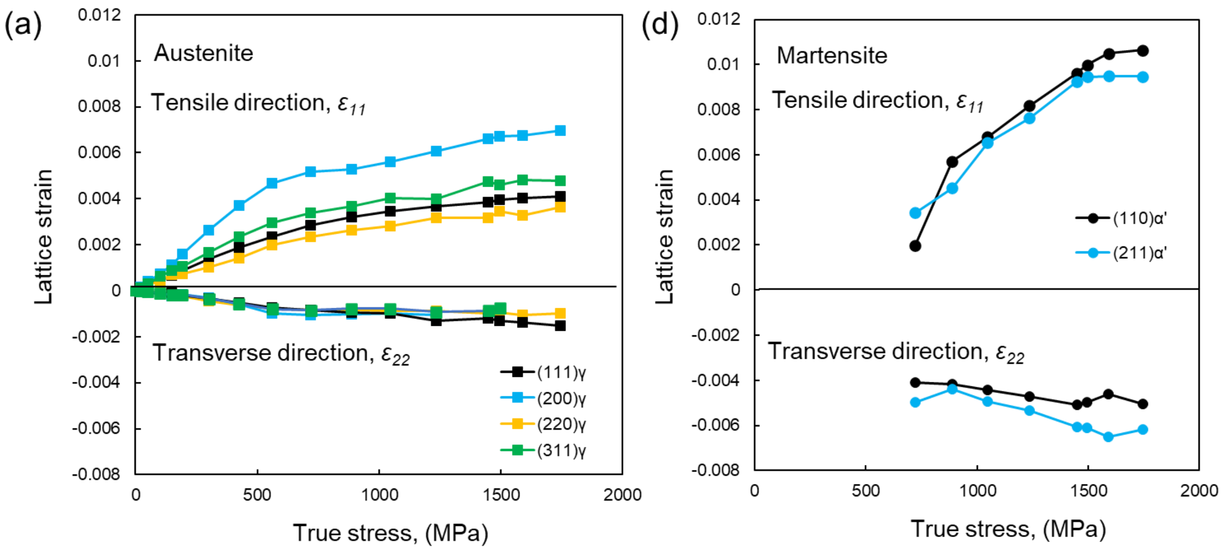

Figure 2.19 Measured lattice strains of **(a)** in austenite and **(b)** in martensite in the specimens with the mean grain size of 35 μm along the tensile direction (ε_{11}) and the transverse direction (ε_{22}), plotted as a function of the true stress applied to the tensile specimen.

Figure 2.18 (a) shows the changes on relative integrated intensities of diffraction peaks of austenite in tensile direction during the deformation, which was evaluated by normalizing the integrated intensities of diffraction peaks during deformation to those obtained before deformation. It can be observed that with increasing the true strain from 0 to 0.15 the integrated intensity of $(111)_\gamma$ and $(200)_\gamma$ in tensile direction increased, while the integrated intensity of $(311)_\gamma$ was almost unchanged and that of $(220)_\gamma$ was decreased, corresponding to the enhanced $<111>_\gamma$ + $<100>_\gamma$ texture of austenite in tensile direction. After the deformation induced martensitic transformation started, the integrated intensity of $(111)_\gamma$ firstly increased then decreased with increasing the strain, while the others monotonically decreased. The integrated intensity of $(111)_\gamma$ of austenite was much larger than that of other diffraction peaks. The result implied the evolution of texture of austenite in the tensile direction, which is in good agreement with the IPF images shown in **Figure 2.17**. According to the integrated intensities of diffraction peaks of austenite and martensite, the volume fraction of martensite was evaluated by **Equation 2.5**, as plotted in **Figure 2.18 (b)**

by black dots in which the volume fraction of martensite measured by optical microscopy is also plotted by blue dots. It can be seen that the volume fraction of martensite measured by neutron direction is consistent well with that measured by optical microscopy and hereafter only the volume fraction of martensite measured by neutron direction would be used.

The lattice strains were calculated from the shift of the peak position by the use of **Equation 2.4**. The lattice spacing of hkl planes in austenite obtained before deformation was used as the d_{hkl}^0 values for evaluating the lattice strains of austenite. However, the martensite did not exist before deformation, so that the d_{hkl}^0 values for martensite could not be determined from the in-situ neutron diffraction data. Therefore, the d_{hkl}^0 value of thermally induced martensite obtained by neutron diffraction was used as the d_{hkl}^0 value for deformation induced martensite. The thermally induced martensite was obtained by a subzero-treatment into liquid nitrogen (77 K) for 1800 s, using the as-received specimen. **Figure 2.19 (a)** and **(b)** shows the changes of the lattice strains of hkl planes of austenite and hkl planes of martensite, respectively, as a function of the true stress applied to the specimen. The lattice strain along tensile direction and transverse direction is expressed as ε_{11} and ε_{22}, respectively. In the tensile direction, the tensile strains of austenite and martensite were observed and increased with increasing the applied stress. On the contrary, compressive strains were observed in both austenite and martensite in the transvers direction, which was due to the Poisson effect. It reveals that along tensile direction tensile stress in the austenite and martensite increased while in transverse direction compressive stress increased with developing the deformation. In this study, only the lattice strain and internal stress in the tensile direction will be discussed. In **Figure 2.19 (b)**, one thing should be noted that at the strain where the martensitic transformation just initiated the lattice strains in martensite along tensile direction is relatively small and even much smaller than those of martensite along transverse direction. It is because martensitic transformation is a diffusionless (displasive) transformation accompanied with a dilatation strain and a shear strain parallel to the habit plane [41], and the transformation strain could introduce a compressive strain field due to a constraint by the matrix, and the compressive internal strain is speculated to cancel out a part of tensile strain in the tensile direction but enhance the compressive stress component in the transverse direction at the transformation region. Thus, in the tensile direction the initial lattice strains in martensite was smaller than those of austenite, but in the transverse direction the initial lattice strains of martensite was larger than those of austenite, as shown in **Figure 2.19**. With further progressing the deformation, the lattice strains of martensite gradually increased to quite high value.

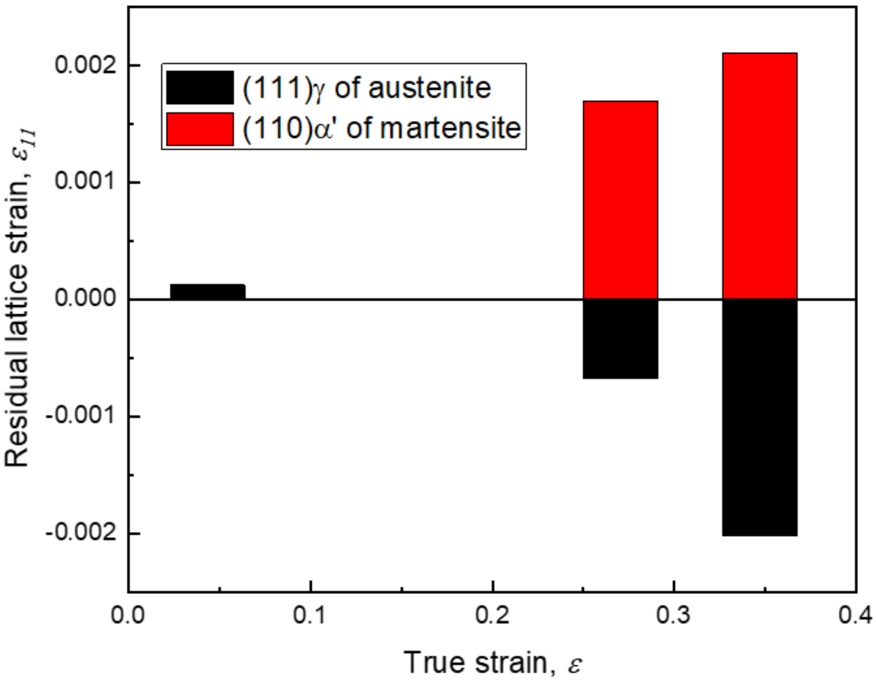

Figure 2.20 Residual lattice strain in <111> oriented austenite grains and <110> oriented martensite grains in the tensile direction, after the applied tensile stress was removed.

Figure 2.20 shows the residual lattice strains of $<111>_{\gamma}$ oriented austenite grains and $<110>_{\alpha'}$ oriented martensite grains after the applied tensile stress was removed at different strain stages. Before the martensite formed, a tensile residual lattice strain was observed in $<111>_{\gamma}$ oriented austenite grains which was introduced by the strain incompatibility between austenite grains with different orientations [42]. After the martensite formed, a tensile residual lattice strain was observed in martensite while a compressive lattice strain in austenite. Such residual lattice strains corresponded to the internal elastic stress within each phase generated from the (plastic) strain incompatibilities between austenite and martensite [43]. And the residual lattice strains in austenite and martensite increased with progressing the tensile deformation, indicating that the strain incompatibilities increased during deformation. These results revealed that extra tensile elastic strains were required in martensite to accommodate the incompatibility with austenite during deformation, leading to the rapid increase in the lattice strain of martensite observed in **Figure 2.19 (b)**. The rapid increase in the lattice strain of martensite indicated that the internal stress in martensite significantly increased during deformation and the increase in the internal stress of martensite could result in the increase in the strain-hardening rate of the entire specimens.

Table 2.3 Diffraction elastic constant of austenite and martensite

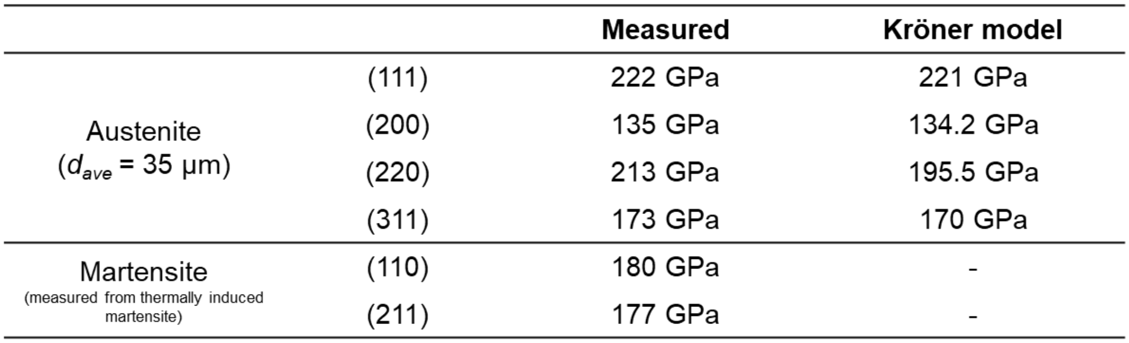

		Measured	**Kröner model**
Austenite (d_{ave} = 35 μm)	(111)	222 GPa	221 GPa
	(200)	135 GPa	134.2 GPa
	(220)	213 GPa	195.5 GPa
	(311)	173 GPa	170 GPa
Martensite (measured from thermally induced martensite)	(110)	180 GPa	-
	(211)	177 GPa	-

For estimating the internal stress within austenite and martensite, diffraction elastic constants E^{hkl} of austenite and martensite were measured from the slope of true stress vs lattice strain at elastic region, in which the diffraction elastic constants E^{hkl} of martensite were measured from thermally induced martensite. **Table 2.3** shows the measured diffraction elastic constants of austenite and martensite, and estimated E^{hkl} of austenite by Kröner model [44]. Elastic constants C_{11}=180 GPa, C_{12}=106 GPa, C_{44}=111GPa of Fe-23Ni-0.3C at room temperature was used for Kröner model [45]. It reveals that the measured diffraction elastic constants of austenite have good agreement with the value calculated by Kröner model. Then, the tensile stress σ_{11}^{hkl} borne by different oriented grains of austenite and martensite can be estimated by the following equation according to the Hook's rule;

$$\sigma_{11}^{hkl} = E^{hkl}\varepsilon_{11}^{hkl} \qquad (2.17)$$

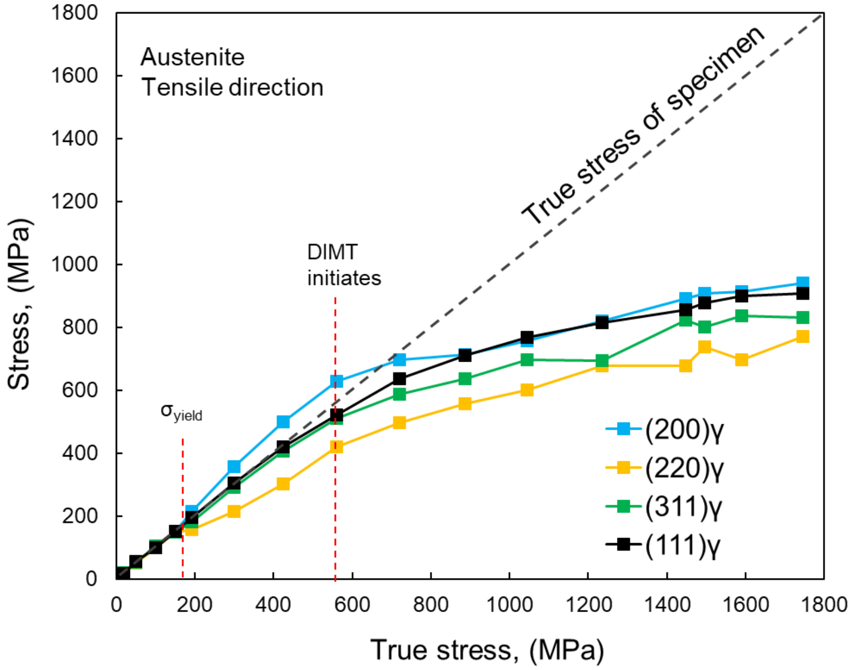

Figure 2.21 Changes of tensile stress in the different oriented austenite grains as a function of the applied true stress. The gray dashed line indicates the true stress applied in the specimen and the strain point of plastic yield and starting of the deformation induced martensitic transformation is marked by red dashed lines.

Figure 2.21 shows the evolution of tensile stress in the different oriented austenite grains with increasing the true stress applied to the specimen, in which the gray dashed line indicates the true stress applied in the specimen. Since the undeformed specimen was composed of 100% austenite, before the martensitic transformation started the deformation of specimen represents the deformation of single austenite phase. It can be seen that before plastic yielding of the specimen the tensile stress in the different oriented austenite grains was consistent well with the applied true stress, but started to deviate from the applied true stress after yielding. It is because that different oriented austenite grains have different capability for plastic deformation which results the plastic strain incompatibility between different oriented austenite grains leading to the stress partitioning between the different oriented austenite grains [42]. After yielding the <200>$_\gamma$ oriented austenite grains borne more tensile stress than other austenite grains shown in

Figure 2.20, indicating <200>$_\gamma$ oriented grains are plastically harder than others. On the other hand, <220>$_\gamma$ oriented austenite grains are plastically softer than others. However, the deviation of tensile stress in <111>$_\gamma$ and <311>$_\gamma$ oriented austenite grains from the true stress of specimen was very small, indicating that the stress in <111>$_\gamma$ and <311>$_\gamma$ oriented austenite grains is less affected by the intergranular interaction and is much closer to the stress applied on the austenite phase. After the deformation induced martensitic transformation started, the lattice strains of austenite obviously deviated to the lower side of the applied true stress with developing the deformation since the formed martensite took a charge of a part of the global flow stress.

The internal stress distributing between austenite and martensite hold the following the rule of mixture [20,21]:

$$\sigma_{\gamma,11}(1-f_{\alpha\prime})+\sigma_{\alpha',11}f_{\alpha\prime}=\sigma_{11}^{applied} \qquad (2.18)$$

where $\sigma_{\gamma,11}$ and $\sigma_{\alpha',11}$ are the average internal stress in austenite and martensite (hereafter termed as phase stress) and $\sigma_{11}^{applied}$ is the applied stress in tensile direction; $f_{\alpha\prime}$ is the volume fraction of martensite. In the case of polycrystalline materials having anisotropy, the phase stress σ_{11} of the constituent phase could be evaluated from the volumetrically weighted average of internal stress in different oriented grains [46] as the following equation:

$$\sigma_{11}=\sum_{hkl}f^{hkl}E^{hkl}\varepsilon_{11}^{hkl} \qquad (2.19)$$

where f^{hkl} is the volume fraction of <hkl> orientated grains in the constituent phase; E^{hkl} is the diffraction elastic constants in <hkl> direction and ε_{11}^{hkl} is the lattice strain of (hkl) plane in tensile direction. In the previous studies, the stresses in <311>$_\gamma$ oriented austenite grains and <211>$_{\alpha'}$ oriented martensite grains are usually selected to represent the phase stress of austenite phase and martensite phase, respectively [13]. However, considering that the deformed specimens had strong textures in which the most of austenite grains and martensite grains had <111>$_\gamma$ and <110>$_{\alpha'}$ direction parallel with the tensile direction (shown in **Figure**

2.17), the equation of phase stress of austenite and martensite was simplified as the following equation in the present study:

$$\sigma_{\gamma,11} = E_{\gamma}^{111}\varepsilon_{\gamma,11}^{111} \qquad (2.20)$$

$$\sigma_{\alpha',11} = E_{\alpha'}^{110}\varepsilon_{\alpha',11}^{110} \qquad (2.21)$$

where E_{γ}^{111} and $E_{\alpha'}^{110}$ is the diffraction elastic constants for <111>$_{\gamma}$ in austenite and <110 >$_{\alpha'}$ in martensite, respectively, as shown in **Table 2.3**.

Figure 2.22 shows the phase stresses of austenite ($\sigma_{\gamma,11}$) and martensite ($\sigma_{\alpha',11}$) in tensile direction. The Meanwhile, the estimated phase stresses were verified by the rule of mixture (**Equation 2.18**). The calculated total stresses are indicated by red triangles in the **Figure 2.22** in which the corresponding true stress-strain curves were also presented. Stress partitioning between austenite and martensite can be clearly observed in **Figure 2.22**. It can be seen that the phase stress of martensite dramatically increased after the martensitic transformation started with increasing the tensile true strain, and became much larger than that of austenite. More importantly, the calculated total stress using the phase stresses was in good agreement with the applied stress, which is significantly different from the total stress calculated from the nano-hardness (shown in **Figure 2.15**). This result demonstrated that the origin of contribution of martensite to strain-hardening is the phase stress (internal stress) of martensite which is generated due to the strain incompatibility, rather than the hardness of martensite.

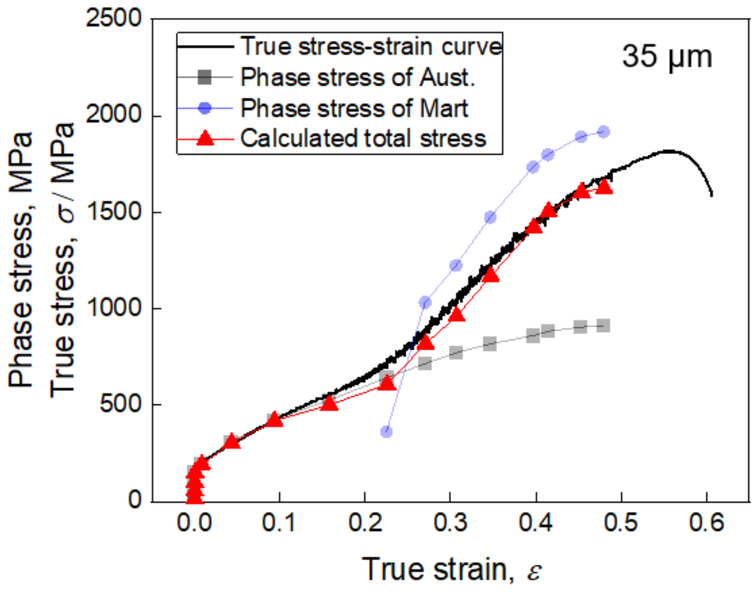

Figure 2.22 Changes of phase stress of austenite and martensite in the specimen as a function of true strain. The total stress was calculated by the rule of mixture, which is indicated by the red triangles.

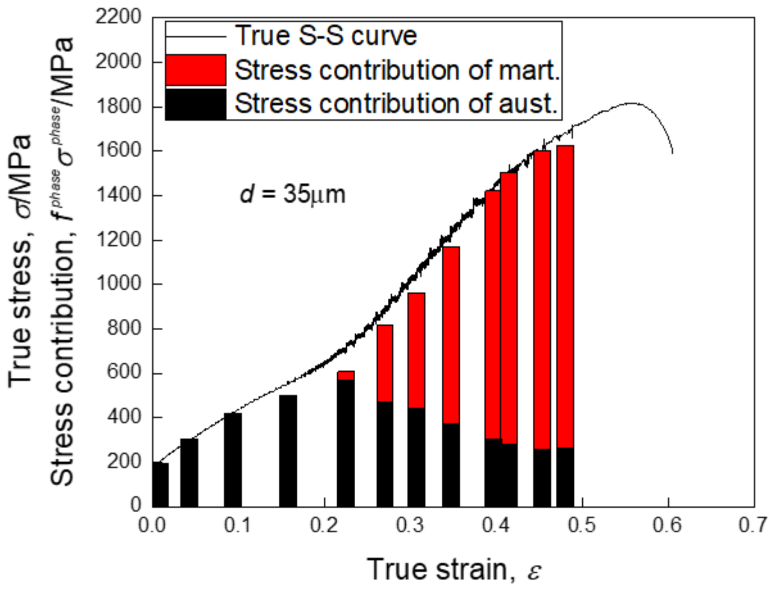

Figure 2.23 Changes of the tensile stress contributed from austenite and martensite with increasing the tensile true strain.

Stress contribution from austenite and martensite can be determined by multiplying their phase stress and volume fraction, as shown in **Figure 2.23** together with the true stress-strain curves. The summation of the stress contributed from austenite and martensite is equal to the applied stress as shown in **Figure 2.22.** After the deformation induced martensitic transformation started, with progressing the deformation the stress contributed by the martensite gradually increased while the stress contributed by the austenite decreased although the phase stress of austenite was increased. As the increase of the volume fraction of martensite, the macro loading gradually transferred from austenite to martensite. Therefore, the increase of strain-hardening rate caused by the TRIP effect mainly comes from the increase of stress contribution of martensite in which the increase of phase stress of martensite played an important role. These results revealed that the general understanding of the rule of mixture which excludes the interaction between different phases is unreasonable. And the enhancement of strain-hardening rate by deformation induced martensitic transformation was caused by not only the increase of the volume fraction of martensite but also by the increase of the phase stress in martensite.

2.6 Strain partitioning behavior between austenite and martensite

In the last section, a significant stress partitioning between austenite and martensite was observed during tensile deformation according to the result of in-situ neutron diffraction. It is considered that the phase stress of martensite dramatically increased during deformation due to the plastic strain incompatibility between austenite phase and martensite phase. However, the plastic strain partitioning between austenite and martensite is still unclear. Since the martensite dynamically forms during the deformation, it is difficult to directly measure the strain partitioning between austenite and martensite by conventional methods like micro-DIC measurement. Therefore, there are few reports about plastic strain partitioning between austenite and martensite during the deformation of TRIP steels. This section aims to investigate the plastic strain partitioning behavior according to the evolution of dislocation density in the austenite phase.

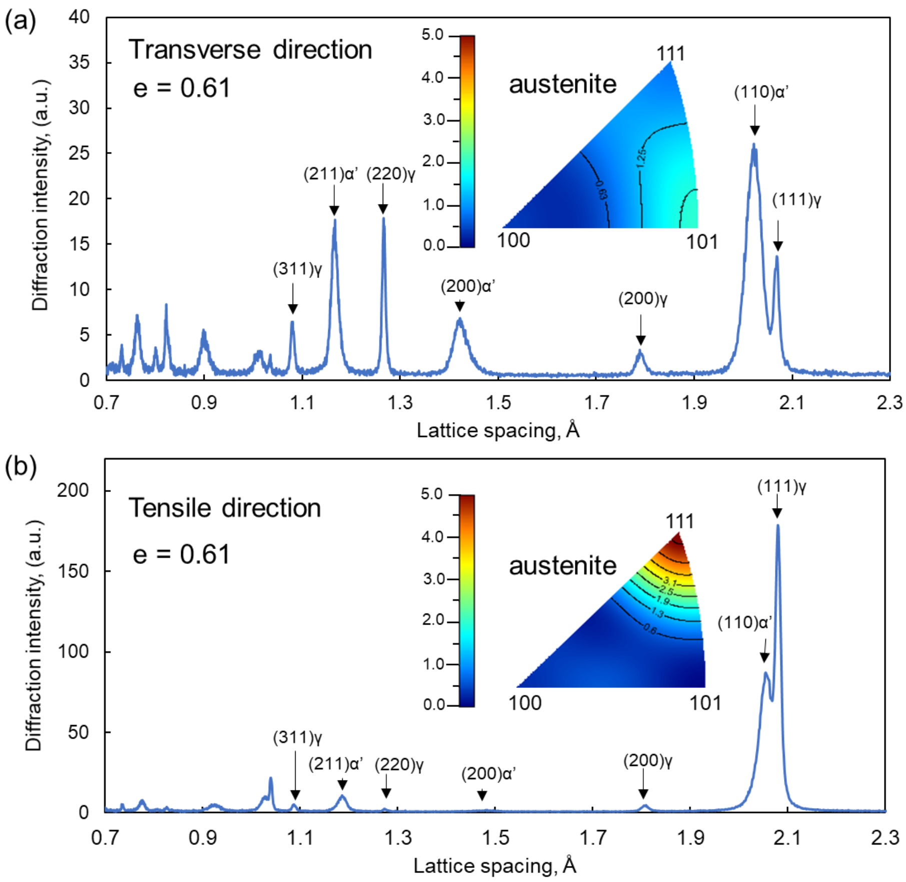

Figure 2.24 Diffraction profiles obtained from (a) transverse direction and (b) tensile direction, respectively, at tensile strain of 0.61. IPF images of austenite obtained from each diffraction profile is embedded in the corresponding figure.

Diffraction profiles obtained in the transverse direction were used for estimating dislocation density of austenite, instead of those obtained in the tensile direction. **Figure 2.24 (a)** and **(b)** show diffraction profiles obtained from transverse direction and tensile direction, respectively, at tensile strain of 0.61. IPF images of austenite obtained from each diffraction profile is embedded in the corresponding figure. It can be observed that in the transverse direction the texture of austenite in the deformed specimen is weaker than that in tensile direction. Thus, FWHM of diffraction peaks of austenite and martensite can be measured more accurately in the diffraction profiles obtained in transverse direction, so that the estimated dislocation density would be more reliable. **Figure 2.25 (a)** and **(b)** show the changes of FWHM of diffraction peaks of austenite and martensite measured from the transverse direction with increasing the true strain, in which the FWHM is expressed by the magnitude of reciprocal lattice vector (ΔK). In **Figure 2.25 (a)**, the peak widths of austenite significantly increased with increasing the true strain of specimen, implying that the dislocation density in austenite increased due to the plastic deformation. On the other hand, the peak widths of martensite were almost unchanged during the deformation, as shown in **Figure 2.25 (b)**. It is possibly because martensite naturally has high dislocation density and the plastic deformation in martensite is relatively small, as a result, the increase of dislocation density caused by the plastic deformation could not introduce obvious increase in the peak widths of martensite.

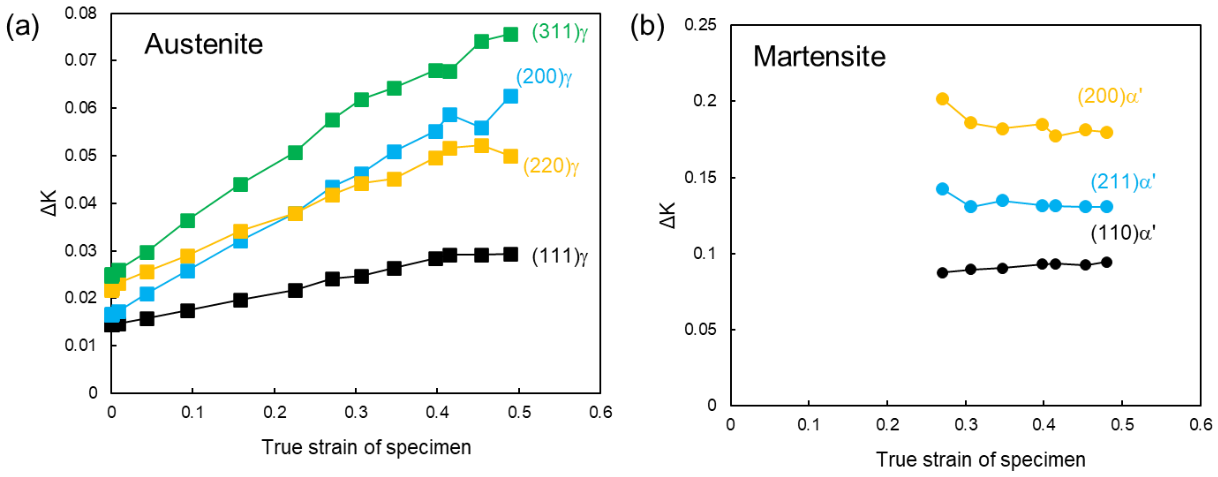

Figure 2.25 Changes of FWHM of diffraction peaks of **(a)** austenite and **(b)** martensite as a function of the true strain of specimen.

The dislocation density of austenite was estimated from the FWHM of diffraction peaks by using the modified Williamson-Hall method. **Figure 2.26** shows the evolution of the estimated dislocation density in the austenite with increasing the true strain of specimen. The dislocation density of undeformed specimen is about 1×10^{13} m^{-2}, which is a typical dislocation density for fully annealed material [47]. With increasing the tensile true strain of specimen, the dislocation density in the austenite monotonically increases. According to Kocks-Mecking-Estrin model [48], the increment of dislocation density as increasing the plastic strain is the linear superposition of contributing mechanisms: dislocation storage and annihilation due to cross slip and dynamic recovery, as expressed:

$$\frac{d\rho}{Md\varepsilon} = \frac{1}{bL} - K_2\rho \qquad (2.22)$$

where M is the Taylor factor (≈3), L is the average free path for dislocation movement and K2 is a material constant. The average free path L can be assumed to be proportional to $1/\sqrt{\rho}$. Therefore, **Equation 2.22** can also be written as:

$$\frac{d\rho}{Md\varepsilon} = K_1\sqrt{\rho} - K_2\rho \qquad (2.23)$$

where K_1 is a material constant. The first term in the right-hand side of **Equation 2.23** ($K_1\sqrt{\rho}$) is related to the dislocation storage, while the second term ($K_2\rho$) represents the annihilation of dislocations. The **Equation 2.23** on direct integration yields:

$$\sqrt{\rho} = \left(\sqrt{\rho_0} - \frac{K_1}{K_2}\right) exp(-MK_2\varepsilon/2) + \frac{K_1}{K_2} \qquad (2.24)$$

where ρ_0 is the initial dislocation density at $\varepsilon = 0$. **Equation 2.24** describes the dislocation density as a function of the plastic strain. Therefore, by fitting the data plots of dislocation density vs true strain at the early stage of deformation without deformation induced martensite (in **Figure 2.26**), the relationship between dislocation density and plastic strain for the austenite could be obtained. Then, the obtained relationship could be extrapolated to larger strain stage, as indicated by the dashed line in **Figure 2.26**. According to the measured dislocation density of austenite and the obtained relationship (**Equation 2.24**), the plastic strain of austenite could be easily estimated. **Figure 2.27** presents the estimated plastic strain of austenite (labeled as ε_γ) as a function of the true strain of specimen, in which the dashed line indicates the true strain of specimen. It can be seen that after the martensite formed true plastic strain of austenite gradually became larger than that of the specimen and the gap increased with increasing the tensile strain, which means more and more plastic strain concentrated on the austenite phase.

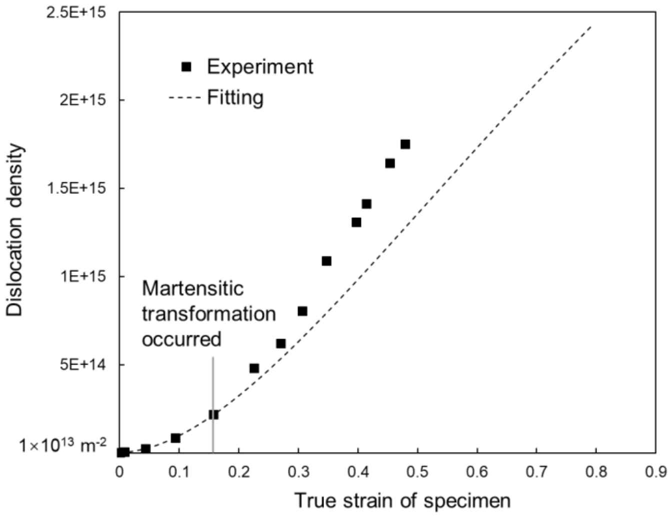

Figure 2.26 Increase in the dislocation density of austenite with increasing the true strain of specimen. The data plots of dislocation density vs true strain before the martensite formed were fitted by Kocks-Mecking-Estrin model and the obtained relationship is extrapolated to larger stage, representing the relationship between dislocation density and plastic strain for the austenite phase.

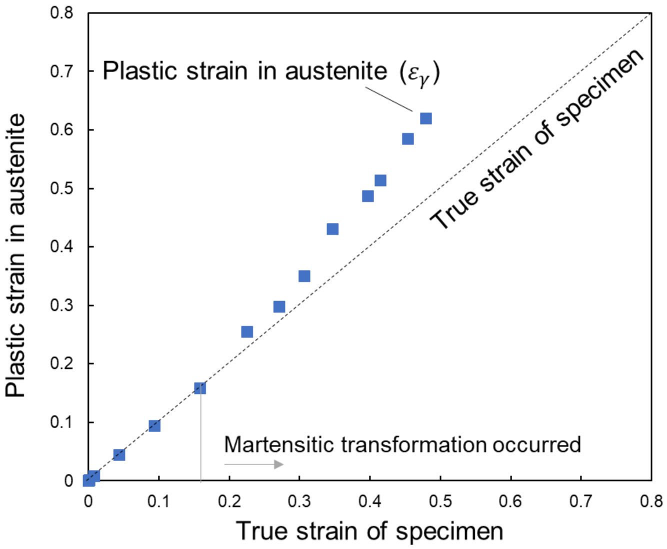

Figure 2.27 Estimated plastic strain of austenite according to its dislocation density, plotted as a function of the true strain of specimen.

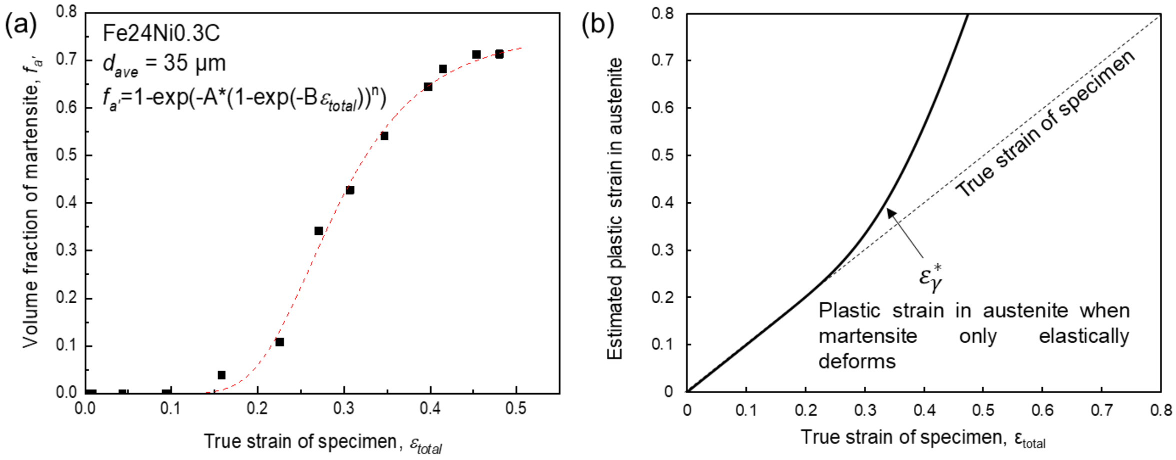

Figure 2.28 (a) Evolution of volume fraction of martensite with increasing the true strain of specimen fitted by the empirical equation proposed by Olson [52]; **(b)** Plastic strain of austenite when martensite only elastically deforms, indicated by the black curve.

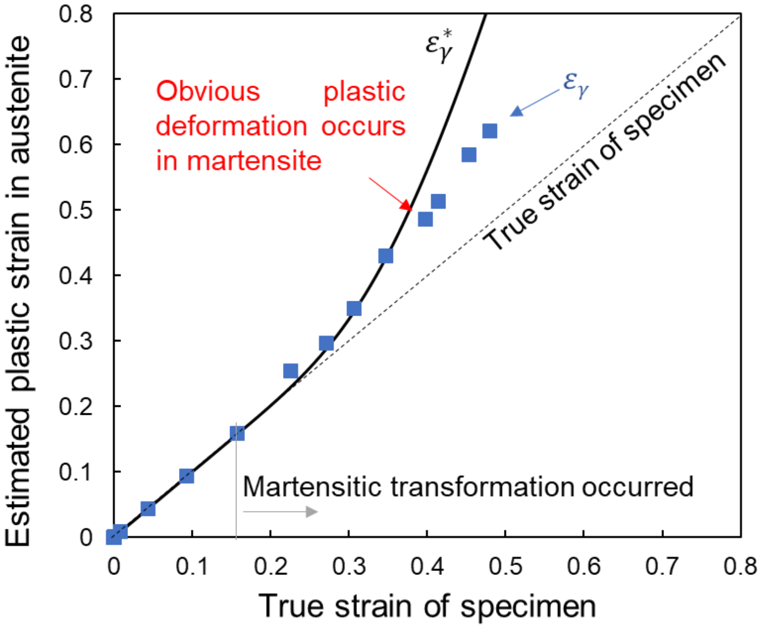

Figure 2.29 Comparison the estimated plastic strain of austenite according to its dislocation density (ε_γ) and the plastic strain of austenite estimated by assuming that martensite only elastically deforms (ε_γ^*).

Due to the dynamic formation of martensite during deformation, the plastic strain of martensite could not be directly estimated from the true strain of specimen and the plastic strain of austenite using the mixing rule. However, infinitesimal increment of plastic strain of specimen obeys the mixing rule, since the change of volume fraction of martensite in the infinitesimal increment of plastic strain could be negligible. Therefore, the increment of plastic strain of specimen is expressed as:

$$d\varepsilon_{total} = f_{\alpha\prime} d\varepsilon_{\alpha\prime} + (1 - f_{\alpha'}) d\varepsilon_{\gamma} + \varepsilon_{trans} df_{\alpha\prime} \qquad (2.25)$$

where ε_{total} represents the plastic strain of specimen, $\varepsilon_{\alpha\prime}$ and ε_{γ} represents the plastic strain of martensite and austenite, respectively. ε_{trans} represents the plastic strain contributed by the formation of martensite due to the displacive transformation. The maximum tensile elongation due to the displacive martensitic transformation is about 0.15 [49]. However, it is estimated by assuming that all austenite completely transforms to the most favored variant whose shear direction and habit plane normal lie in the same plane with the tensile axis. In the fact, the martensite variants would accommodate to each other to cancel the shear strains [50] and the transformation strain of martensite would also be accommodated by the plastic strain of matrix by forming geometrically necessary dislocations [51]. Therefore, the contribution of martensitic transformation to the tensile elongation is actually much smaller than 0.15. Based on this consideration, Equation 2.25 could be simplified as the following:

$$d\varepsilon_{total} = f_{\alpha\prime} d\varepsilon_{\alpha\prime} + (1 - f_{\alpha'}) d\varepsilon_{\gamma} \qquad (2.26)$$

If it is assumed that martensite only elastically deforms during the deformation of specimen, then, the increment of plastic strain of specimen could be expressed as:

$$d\varepsilon_{total} = (1 - f_{\alpha'}) d\varepsilon_{\gamma} \qquad (2.27)$$

The volume fraction of martensite could be express as a function of the true plastic strain of specimen by the following equation [52]:

$$f_{a\prime} = 1 - \exp(-A(1 - \exp(-B\varepsilon_{total}))^{n}) \qquad (2.28)$$

where *A*, *B* and *n* are material constants, which could be obtained by fitting the plots of martensite volume fraction vs true strain of specimen as shown ins **Figure 2.28 (a)**. Then, by substituting **Equation 2.28** into **Equation 2.27** and performing numerical integration, the evolution of plastic strain of austenite when martensite only elastically deforms could be obtained (labeled as ε_{γ}^{*}), as indicated by the black solid line in **Figure 2.28 (b)**. **Figure 2.29** summarizes the estimated plastic strain of austenite according to its dislocation density (ε_{γ}) and the plastic strain of austenite estimated by assuming that martensite only elastically deforms (ε_{γ}^{*}). Through the comparison of ε_{γ} and ε_{γ}^{*}, it can be found that at early stage of deformation ε_{γ} corresponded well with ε_{γ}^{*}, implying that at early stage of deformation the martensite was mostly elastically deformed. However, at later stage of deformation ($\varepsilon_{total} > 0.35$), the ε_{γ} started to deviate form ε_{γ}^{*} to lower side and it reveals that obvious plastic deformation occurred in martensite since the critical strain stage. Based on this speculation, the plastic strain of martensite ($\varepsilon_{\alpha'}$) could be roughly estimated by the following method:

When $\varepsilon_{total} < 0.35$, $\varepsilon_{\alpha'} \sim 0$

When $\varepsilon_{total} > 0.35$, $\Delta\varepsilon_{\alpha'} \sim \frac{\Delta\varepsilon_{total} - (1 - \overline{f_{\alpha'}})\Delta\varepsilon_{\gamma}}{f_{\alpha'}}$ (2.29)

where $\Delta\varepsilon_{\alpha'}$ and $\Delta\varepsilon_{\gamma}$ represent the increment of plastic strain of martensite and austenite during the increment of plastic strain specimen ($\Delta\varepsilon_{total}$) respectively; $\overline{f_{\alpha'}}$ is the average volume fraction of martensite when the plastic strain of specimen increases from ε_{total} to $\varepsilon_{total} + \Delta\varepsilon_{total}$. The deformation from the true strain of 0.35 to 0.48 was divided into four small deformation processes by four times interruption in the in-situ neutron diffraction, corresponding to the four data plots at the strain region $\varepsilon_{total} > 0.35$ in **Figure 2.29**. In each small deformation processes, the increment of plastic strain of martensite could be calculated by **Equation 2.29**. Then, by accumulating of the increment $\Delta\varepsilon_{\alpha'}$ during each small deformation process the overall plastic strain of martensite $\varepsilon_{\alpha'}$ could be obtained. **Figure 2.30** shows the estimated plastic strain of austenite and martensite as a function of the true strain of specimen. Obviously, most of plastic deformation was concentrated on the austenite phase during the deformation of specimen. Until the necking of specimen, only about 10% plastic strain occurred in the martensite phase.

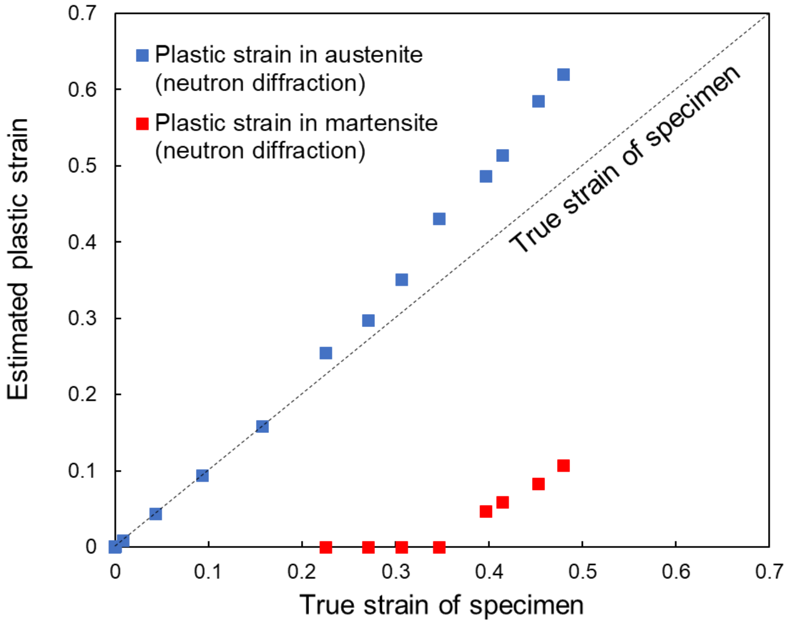

Figure 2.30 Evolution of plastic strain of austenite and martensite during the tensile deformation.

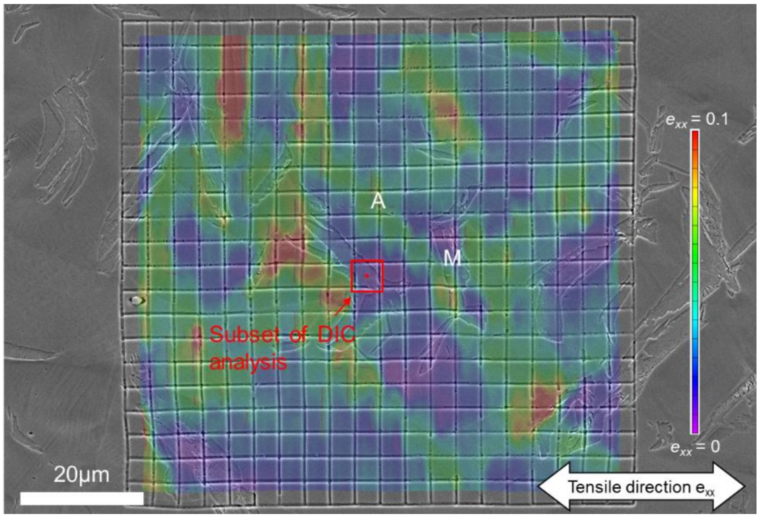

Figure 2.31 Color-coded map of strain distribution obtained by DIC analysis when the specimen was strained from 0.2 to 0.25. Average strain of analyzed area is about 0.038, average strain on austenite phase is about 0.041, and average strain on martensite is about 0.01.

For confirming the plastic strain of austenite and martensite estimated from the neutron diffraction, a step-by-step micro-DIC analysis was performed to measure the plastic strain partitioning between austenite and martensite. Since the martensite dynamically forms during the deformation, the surface relief caused by the formation of martensite would deteriorate the quality of the analysis of DIC and it is difficult to distinguish new formed martensite from austenite. Therefore, micro-DIC analysis could only be performed within a small strain, in which the effect of new formed martensite could be ignored. The deformation of specimen from nominal strain of 0.2 to 0.55 was divided into 7 parts, and in each part the increment of nominal strain is about 0.05. Micro-DIC analysis was performed in each part of deformation to measure the increment of plastic strain of austenite and martensite. **Figure 2.31** shows an example of micro-DIC analysis from the nominal strain of 0.2 to 0.25. The color bar of strain distribution map from blue to red indicated the tensile strain from 0 to 0.1. Martensite could be easily distinguished from austenite matrix according its lenticular morphology, such as the area in **Figure 2.31** marked by M (A indicates austenite). It can be seen that the plastic deformation mostly concentrated on the austenite phase. The increment of the total true strain is about 0.038 on the observed area, in which average plastic tensile strain in austenite is 0.041 and in martensite is about 0.01. The same analysis was also performed in other part of deformation. Then, the overall plastic strain of austenite and martensite is obtained by the accumulation of the increment of their plastic strain in each part of deformation. **Figure 2.32** shows accumulated plastic strain of austenite and martensite measured by the micro-DIC indicated by open circles as well as the estimated plastic strain of austenite and martensite by the neutron diffraction indicated by solid squares. The plastic strain of austenite and martensite estimated from neutron diffraction almost consistent with that measured by the micro-DIC, implying that the plastic strain of austenite and martensite estimated from neutron diffraction is reliable. However, it can be observed that the plastic strain of martensite measured by micro-DIC is slightly larger than that estimated from neutron diffraction. It might because the necessary size of subset for DIC analysis is larger than the thickness of martensite as shown in **Figure 2.31** by a red square, so that the strain of martensite actually includes some strain component of austenite. That is, the resolution of the micro DIC is not high enough to precisely measure the plastic strain within the martensite. As a result, the plastic strain of martensite was overestimated by micro DIC analysis, and the error of measurement was also accumulated in the step-by-step analysis. Therefore, the plastic strain of martensite estimated from the neutron diffraction is more reliable.

These results demonstrate that a significant plastic incompatibility between austenite and martensite exists during the deformation of the Fe-24Ni-0.3C. It can be considered that with increasing the plastic deformation of austenite the dislocations in the austenite would accumulate at the interphase boundaries between austenite and martensite due to the plastic incompatibility. As a result, a back-stress opposite to the slip direction of dislocation would arise at the interphase boundaries in the austenite side. Meanwhile, the internal stress (phase stress) of martensite would increase with increasing the degree of plastic incompatibility, as shown in **Figure 2.22**.

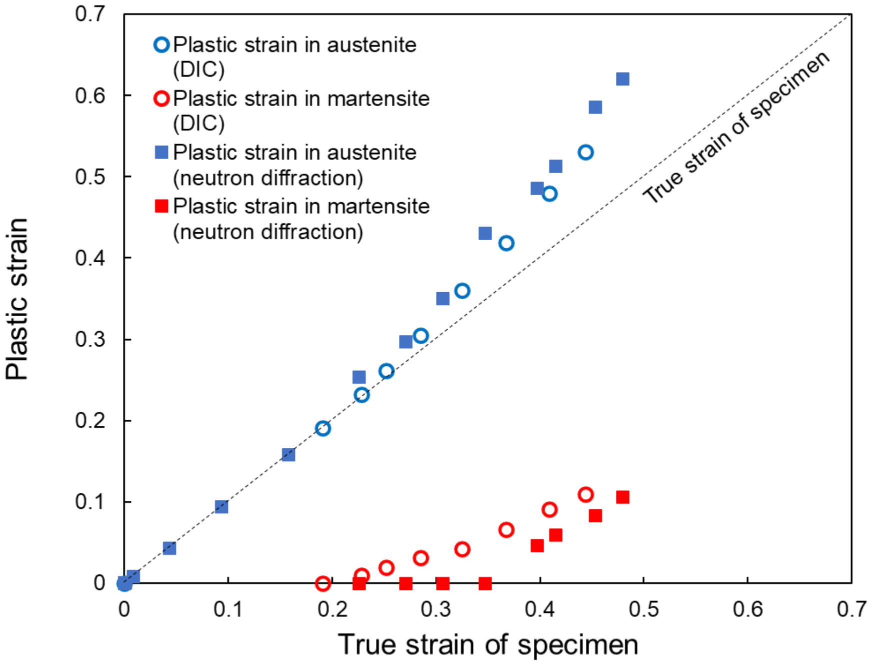

Figure 2.32 Evolution of plastic strain of austenite and martensite measured by step-by-step micro-DIC analysis (open circles) and in-situ neutron diffraction (solid square).

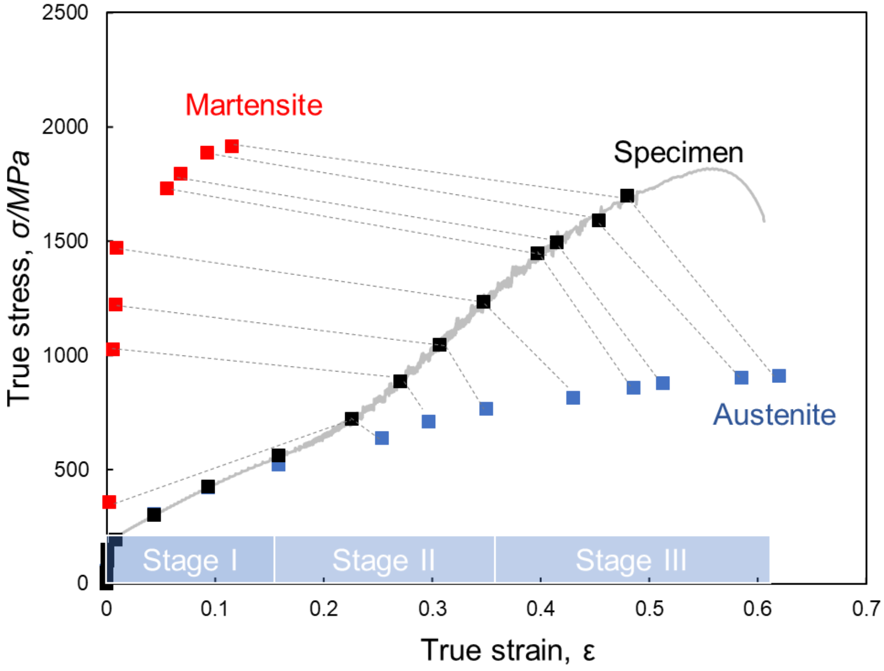

Figure 2.33 Stress-strain response of austenite and martensite during the tensile deformation of the specimen. The data plots at the same strain stage are linked by dashed lines.

2.7 Discussion

In the **Section 2.5**, the phase stress of austenite and martensite has been obtained from the peak shift of the diffraction profiles, as shown in **Figure 2.22**. In the **Section 2.6**, plastic strain of austenite and martensite has been estimated from evolution of dislocation density of austenite phase, as shown in **Figure 2.30**. Combining the phase stresses of austenite and martensite with their strains, the actual deformation behavior of austenite and martensite during the deformation of the specimen could be clarified. In **Figure 2.33**, the phase stresses of austenite and martensite are plotted against their own true strain (estimated plastic strain + lattice strain) by blue and red squares, respectively, and the gray curve is the true stress-strain curve of the specimen on which the measurement points for neutron diffraction are marked by black squares, and the data plots at the same strain stage are connected by dashed lines. According to this result, the deformation of the specimen could be divided into three stages, as shown in **Figure 2.33**. In stage I, the specimen is only composed of austenite phase and the deformation of specimen is the deformation of pure austenite phase. In stage II, deformation induced martensitic transformation occurs, however, the martensite is only elastically deformed and plastic deformation only occurs in the austenite phase. Therefore, for accommodating the plastic strain incompatibility between the two phases, elastic strain of martensite quickly increases leading to a high phase stress in martensite. In stage III, both martensite and austenite plastically deform.

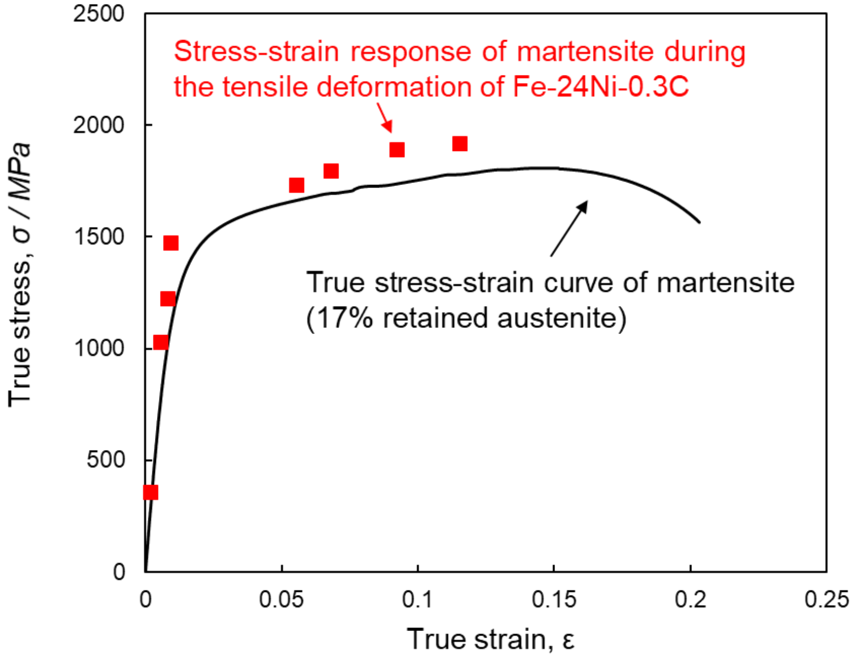

Figure 2.34 Comparison between the stress-strain response of martensite during the deformation of the specimen and true stress-strain curve of a subzero treated specimen having 83 vol% martensite.

It can be easily found out that the one of reasons for the high elongation of specimen is the high deformation capability of austenite. However, more important thing is that at deformation stage II and III the formation of martensite and the increase of the phase stress in martensite provides a high strain hardening rate to prevent the plastic instability of deformation, and ensures the uniform deformation of specimen. The stress-strain response of the deformation induced martensite plays an important role in the deformation of the specimen. However, is the stress-strain response of the deformation induced martensite during deformation of specimen similar to that of single-phase martensite? For confirming the stress-strain response of single-phase martensite, the undeformed Fe-24Ni-0.3C specimen was subzero treated at liquid He (about 2K). But due to the hydrostatic pressure caused by the displacive martensitic deformation, the stability of austenite is greatly enhanced as a result there is still about 17 vol% austenite retained even at 2 K (measured by EBSD observation). The true stress-strain curve of subzero treated specimen with 83 vol% martensite was used as a reference for the stress-strain response of single-phase martensite. **Figure 2.34** shows the true stress-strain of the subzero-treated specimen and the stress-strain response of martensite during the deformation of Fe-24Ni-0.3C specimen. It can be seen that the stress-strain response of the deformation induced martensite during the deformation is very close to the true stress-strain curve of the subzero-treated specimen. The obvious plastic deformation was observed in the deformation induced martensite when the phase stress becomes higher than about 1500 MPa, which corresponds to the yield stress of the subzero-treated specimen. And the flow stress and strain hardening of the deformation induced martensite is also close to that of the subzero-treated specimen. It reveals that the stress strain response of the deformation induced martensite during deformation of specimen is similar to that of single-phase martensite. However, the evolution of strain or phase stress of the deformation induced martensite is determined by the interaction between two phases for accommodating the strain incompatibility. Therefore, although the flow stress and strain hardening behavior of the specimen is not directly determined by the hardness or strength of martensite, the hardness or strength of martensite determines its yield point and the maximum phase stress.

The deformation of Fe-24Ni-0.3C is similar to the deformation of dual-phase steels. For dual-phase stress, the deformation is divided into three stages: (1) dual-phase elastic deformation; (2) the soft phase yields firstly while the hard phase still elastically deforms, termed as elasto-plastic region; (3) dual-phase plastic deformation. The stage II of deformation of Fe-24Ni-0.3C specimen is analogous to the elasto-plastic region where the austenite plastically deforms but the martensite only elastically deforms. However, the evolution of phase stress of martensite (hard phase) during the deformation of Fe-24Ni-0.3C is not identical with that in dual-phase steels. Usually, in dual-phase steels, the evolution of phase stress of the hard phase at elasto-plastic region with increasing the plastic strain of the material could be modeled by the Eshelby solution [53]. It is assumed that a hard phase grain is embedded in an infinite isotropy continuum, and the soft phase and hard phase has a same elastic constant. In the case that the hard phase is in a shape of sphere, the stress in the hard phase could be expressed as:

$$\sigma_{11}^{Hard} = \frac{E(7-5\nu)}{15(1-\nu^2)} \varepsilon_p^{Soft} \qquad (2.30)$$

where σ_{11}^{Hard} is the phase stress of hard phase in tensile direction; E and ν is the Yang's modular and the Poisson's ration of material; ε_p^{Soft} is the plastic strain of the soft phase. In the elasto-plastic region of the deformation of dual-phase steels, the phase stress of hard phase would quickly increase until its yield strength with increasing the strain, therefore, the elasto-plastic region is transient about 1-2% strain [54,55]. On the other hand, compared with that of dual-phase steels, the increasing rate of phase stress of the martensite is much slower and the duration of elasto-plastic region is much longer in the deformation of Fe-24Ni-0.3C specimen than that in dual-phase steels, which could not be described by the Eshelby solution. It can be seen in **Figure 2.33** that the elasto-plastic region in the deformation of Fe-24Ni-0.3C specimen is continuous from the true strain of 0.16 to 0.35. Such relatively slow increase of phase stress of martensite might be due to the dynamic formation of the deformation induced martensite during deformation, which is the significant difference between dual-phase steels and Fe-24Ni-0.3C. **Figure 2.35** shows the evolution of microstructure within one austenite grain from the nominal strain of 0.11 to 0.2, which are extracted from **Figure 2.9**. It can be observed that the volume fraction of martensite increases with increasing the strain by forming new martensite crystals. The new formed martensite prefers to locate near to the previous formed martensite and at the interphase boundaries between austenite and martensite where the localized stress is usually high during the deformation. And due to the martensitic shear deformation, formation of new martensite could release the localized stress at the transformed region. The phase stress of the old martensite would be released by the formation of adjacent new martensite repeatedly, as a result, the phase stress of martensite increase in a relatively slow rate at the elasto-plastic region. We think the relatively slow increase of phase stress of martensite is benefit for improving the elongation of Fe-24Ni-0.3C specimen. The gradually increased phase stress of martensite at the elasto-plastic region ensures that the formation of martensite can provide effective strain hardening rate within larger strain region.

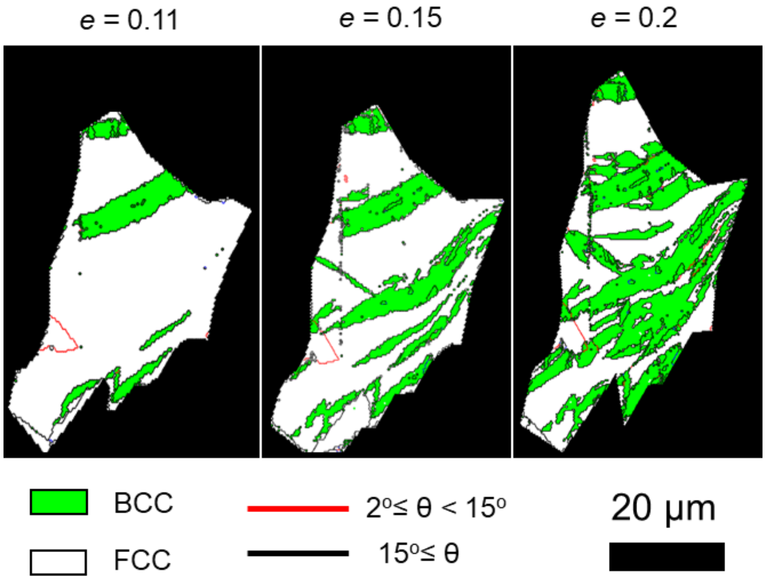

Figure 2.35 Evolution of microstructure within one austenite grain from the nominal strain of 0.11 to 0.2

2.8 Conclusion

In **Chapter 2**, the deformation mechanism of Fe-24Ni-0.3C alloy was systemically investigated by using tensile test, nano-indentation and in-situ neutron diffraction. The tensile test at room temperature reveals that the Fe-24Ni-0.3C specimen has both the high tensile strength and high uniform elongation which is mainly attributed its high strain hardening capability. Different from dislocation slip dominated materials whose strain hardening rate usually monotonically decreases with increasing the strain, the strain hardening rate of Fe-24Ni-0.3C specimen once significantly increased during the deformation. The enhancement of strain hardening rate effectively postponed the plastic instability and ensured the high uniform elongation of the specimen. The observation of deformed microstructure reveals that the starting of the enhancement of the strain hardening is accompanied with the initiation of the deformation induced martensitic transformation.

Generally, it has been widely accepted that the enhancement of strain hardening caused by the deformation induced martensitic transformation is due to the high strength of martensite and the increase of volume fraction of martensite as the deformation progresses, according to the simple rule of mixture. However, the results in **Section 2.4** reveal that the increase of the flow stress of the specimen could not be fully comprehended by the simple rule of mixture. The total flow stress calculated from the strength of austenite and martensite (estimated from nano-hardness) and their volume fraction was much larger than the true stress-strain curve of specimen. It is because the interaction between austenite and martensite is neither considered in the simple rule of mixture nor reflected by the nano-hardness of each phase. The nano-hardness only corresponds to the flow stress of each phase when it deforms independently. But in the actual specimen, two phases having different mechanical properties (strength, elastic constant) are not equally deformed. The two phases connected at phase boundary must accommodate to each other during plastic deformation to maintain the compatibility. Thus, the real internal stress on each phase should be determined by the interaction between the two phases.

To confirm this argument, tensile tests with in-situ neutron diffraction were performed to measure the phase stress (internal stress) of austenite and martensite during the deformation. The results of in-situ neutron diffraction in Section 2.5 reveal that the phase stress of martensite gradually increased from about 500 MPa to 2000 MPa during the tensile deformation. Beside the increase of martensite volume fraction, the increase of the phase stress of martensite also contributed to the enhancement of the strain hardening of the specimen. More importantly, the calculated total stress using the phase stress of austenite and martensite corresponded well with the true stress−strain curve. It reveals that the phase stresses of austenite and martensite determine the flow stress of the specimen much better than their strength estimated from the nano-hardness.

Plastic strain partitioning between austenite and martensite is also investigated by using the in-situ neutron diffraction as introduced in Section 2.6. It reveals that the most of plastic deformation was concentrated on the austenite phase and only 10% plastic strain was occurred on the martensite phase. According to the deformation state of austenite and martensite, the deformation of Fe-24Ni-0.3C specimen could be divided into three stages: (1) deformation of single-phase austenite; (2) elasto-plastic region: austenite plastically deforms while martensite only elastically deforms; (3) both austenite and martensite plastically deform. What's more, it is found that the stress-strain response of the deformation induced martensite during the tensile deformation of the specimen is quite similar with that of single-phase martensite, suggesting that the interaction between austenite and martensite only determines the deformation of the two phases, but not change the stress-strain response of each phase. Moreover, we speculate that dynamic formation of the martensite during deformation would also influence the evolution of the phase stress of martensite as well.

References

1. Tamura, I. Deformation-induced martensitic transformation and transformation-induced plasticity in steels. *Met. Sci.* **16**, 245–253 (1982).

2. Soleimani, M., Kalhor, A. & Mirzadeh, H. Transformation-induced plasticity (TRIP) in advanced steels: A review. *Mater. Sci. Eng. A* **795**, 140023 (2020).

3. Jacques, P. J. Transformation-induced plasticity for high strength formable steels. *Curr. Opin. Solid State Mater. Sci.* **8**, 259–265 (2004).

4. Liu, L., He, B. & Huang, M. The Role of Transformation-Induced Plasticity in the Development of Advanced High Strength Steels. *Adv. Eng. Mater.* **20**, (2018).

5. Bleck, W., Guo, X. & Ma, Y. The TRIP Effect and Its Application in Cold Formable Sheet Steels. *Steel Res. Int.* **88**, 35–45 (2017).

6. Byun, T. S., Hashimoto, N. & Farrell, K. Temperature dependence of strain hardening and plastic instability behaviors in austenitic stainless steels. *Acta Mater.* **52**, 3889–3899 (2004).

7. Tsuchida, N. *et al.* Effects of temperature and strain rate on trip effect in SUS301L metastable austenitic stainless steel. *ISIJ Int.* **53**, 1881–1887 (2013).

8. Järvenpää, A., Jaskari, M., Kisko, A. & Karjalainen, P. Processing and properties of reversion-treated austenitic stainless steels. *Metals (Basel).* **10**, (2020).

9. Gibbs, P. J. *et al.* Austenite stability effects on tensile behavior of manganese-enriched- austenite transformation-induced plasticity steel. *Metall. Mater. Trans. A Phys. Metall. Mater. Sci.* **42**, 3691–3702 (2011).

10. Tirumalasetty, G. K. *et al.* Deformation-induced austenite grain rotation and transformation in TRIP-assisted steel. *Acta Mater.* **60**, 1311–1321 (2012).

11. Wang, H. *et al.* Effect of martensitic phase transformation on the behavior of 304 austenitic stainless steel under tension. *Mater. Sci. Eng. A* **649**, 174–183 (2016).

12. Spencer, K., Embury, J. D., Conlon, K. T., Véron, M. & Bréchet, Y. Strengthening via the formation of strain-induced martensite in stainless steels. *Mater. Sci. Eng. A* **387**–**389**, 873–881 (2004).

13. Harjo, S., Tsuchida, N., Abe, J. & Gong, W. Martensite phase stress and the strengthening mechanism in TRIP steel by neutron diffraction. *Sci. Rep.* **7**, 2–4 (2017).

14. Shi, J. *et al.* Enhanced work-hardening behavior and mechanical properties in ultrafine-grained steels with large-fractioned metastable austenite. *Scr. Mater.* **63**, 815–818 (2010).

15. Guimarães, J. R. C. & De Angelis, R. J. Hardening by a deformation induced phase transformation. *Mater. Sci. Eng.* **15**, 291–294 (1974).

16. Narutani, T. Effect of Deformation-Induced Martensitic Transformation on the Plastic Behavior of Metastable Austenitic Stainless Steel. *Materials Transactions, JIM* vol. 30 33–45 (1989).

17. Li, Z., Pradeep, K. G., Deng, Y., Raabe, D. & Tasan, C. C. Metastable high-entropy dual-phase alloys overcome the strength-ductility trade-off. *Nature* **534**, 227–230 (2016).

18. Jacques, P., Furnémont, Q., Mertens, A. & Delannay, F. On the sources of work hardening in multiphase steels assisted by transformation-induced plasticity. *Philos. Mag. A Phys. Condens. Matter, Struct. Defects Mech. Prop.* **81**, 1789–1812 (2001).

19. Harjo, S. *et al.* In situ neutron diffraction study of alpha-gamma Fe-Cr-Ni alloys under tensile deformation. *Acta Materialia* vol. 49 2471–2479 (2001).

20. Tomota, Y., Lukáš, P., Neov, D., Harjo, S. & Abe, Y. R. In situ neutron diffraction during tensile deformation of a ferrite-cementite steel. *Acta Mater.* **51**, 805–817 (2003).

21. Tomota, Y. *et al.* Tensile behavior of TRIP-aided multi-phase steels studied by in situ neutron diffraction. *Acta Mater.* **52**, 5737–5745 (2004).

22. Harjo, S. *et al.* Work Hardening, Dislocation Structure, and Load Partitioning in Lath Martensite Determined by In Situ Neutron Diffraction Line Profile Analysis. *Metall. Mater. Trans. A Phys. Metall. Mater. Sci.* **48**, 4080–4092 (2017).

23. Pan, B., Qian, K., Xie, H. & Asundi, A. Two-dimensional digital image correlation for in-plane displacement and strain measurement: A review. *Meas. Sci. Technol.* **20**, (2009).

24. Oliver, W. C. An improved technique for determining hardness and elastic modulus using load and displacement sensing indentation experiments. *J. Mater. Res.* **7**, 1564–1583 (1992).

25. Michael, T. H. & Aaron, D. K. *Measurement of residual and applied stress using neutron diffraction*. *Measurement of Residual and Applied Stress Using Neutron Diffraction* (1991). doi:10.1007/978-94-011-2797-4_46.

26. Daymond, M. R., Bourke, M. A. M., Von Dreele, R. B., Clausen, B. & Lorentzen, T. Use of Rietveld refinement for elastic macrostrain determination and for evaluation of plastic strain history from diffraction spectra. *J. Appl. Phys.* **82**, 1554–1562 (1997).

27. De, A. K., Murdock, D. C., Mataya, M. C., Speer, J. G. & Matlock, D. K. Quantitative measurement of deformation-induced martensite in 304 stainless steel by X-ray diffraction. *Scr. Mater.* **50**, 1445–1449 (2004).

28. HajyAkbary, F., Sietsma, J., Böttger, A. J. & Santofimia, M. J. An improved X-ray diffraction analysis method to characterize dislocation density in lath martensitic structures. *Mater. Sci. Eng. A* **639**, 208–218 (2015).

29. Ungár, T., Dragomir, I., Révész, Á. & Borbély, A. The contrast factors of dislocations in cubic crystals: The dislocation model of strain anisotropy in practice. *J. Appl. Crystallogr.* **32**, 992–1002 (1999).

30. Takaki, S., Masumura, T. & Tsuchiyama, T. Proposal of simplified modified Williamson-Hall equation. *ISIJ Int.* **58**, 2354–2356 (2018).

31. Takaki, S., Masumura, T. & Tsuchiyama, T. Dislocation characterization by the direct-fitting/modified Williamson–Hall (DF/mWH) method in cold worked ferritic steel. *ISIJ Int.* **59**, 567–572 (2019).

32. Tsuji, N., Ito, Y., Saito, Y. & Minamino, Y. Strength and ductility of ultrafine grained aluminum and iron produced by ARB and annealing. *Scr. Mater.* **47**, 893–899 (2002).

33. Maxwell, P. C., Goldberg, A. & Shyne, J. C. INFLUENCE OF MARTENSITE FORMED DURING DEFORMATION ON THE MECHANICAL BEHAVIOR OF Fe-Ni-C ALLOYS. *Met. Trans* **5**, 1319–1324 (1974).

34. Rodriguez, P. Serrated Plastic Flow. *Bull. Mater. Sci.* **6**, 653–663 (1984).

35. Klostermann, J. A. & Burgers, W. G. Surface martensite in iron-nickel. *Acta Metall.* **12**, 355–360 (1964).

36. Rodríguez, R. & Gutierrez, I. Correlation between nanoindentation and tensile properties influence of the indentation size effect. *Mater. Sci. Eng. A* **361**, 377–384 (2003).

37. Magee, C. L. & Davies, R. G. The structure, deformation and strength of ferrous martensites. *Acta Metall.* **19**, 345–354 (1971).

38. Ludwigson, D. C. Modified stress-strain relation for FCC metals and alloys. *Metall. Trans.* **2**, 2825–2828 (1971).

39. Xie, Y., Lutterotti, L., Wenk, H. R. & Kovacs, F. Texture analysis of ancient coins with TOF neutron diffraction. *J. Mater. Sci.* **39**, 3329–3337 (2004).

40. Barbier, D., Gey, N., Allain, S., Bozzolo, N. & Humbert, M. Analysis of the tensile behavior of a TWIP steel based on the texture and microstructure evolutions. *Mater. Sci. Eng. A* **500**, 196–206 (2009).

41. Nishiyama, Z. *Martensitic Transformation*. (1972).

42. Hounkpati, V. *et al.* In situ neutron measurements and modelling of the intergranular strains in the near-β titanium alloy Ti-β21S. *Acta Mater.* **109**, 341–352 (2016).

43. Withers, P. J. & Bhadeshia, H. K. D. H. Residual stress. Part 2–Nature and origins. *Mater. Sci. Technol.* **17**, 366–375 (2001).

44. De Wit, R. Diffraction elastic constants of a cubic polycrystal. *J. Appl. Crystallogr.* **30**, 510–511 (1997).

45. Diesburg, D. E. The elastic constants of Fe-Ni-C alloys. (1971).

46. Fitzpatrick, M. E. & Alain, L. *Analysis of residual stress by diffraction using neutron and synchrotron radiation*. (2003).

47. Shintani, T. & Murata, Y. Evaluation of the dislocation density and dislocation character in cold rolled Type 304 steel determined by profile analysis of X-ray diffraction. *Acta Mater.* **59**, 4314–4322 (2011).

48. Hariharan, K. & Barlat, F. Modified Kocks–Mecking–Estrin Model to Account Nonlinear Strain Hardening. *Metall. Mater. Trans. A Phys. Metall. Mater. Sci.* **50**, 513–517 (2019).

49. Bhadeshia, H. K. D. H. TRIP-assisted steels? *ISIJ Int.* **42**, 1059–1060 (2002).

50. Hisaki, O., Oka, M. & Tamura, I. Couplings of Thin-plate Martensites in an Fe–Ni–C Alloy. *Trans. Japan Inst. Met.* **19**, 674–684 (1978).

51. Ramazani, A. *et al.* Quantification of the effect of transformation-induced geometrically necessary dislocations on the flow-curve modelling of dual-phase steels. *Int. J. Plast.* **43**, 128–152 (2013).

52. Olson, G. B. & Cohen, M. Kinetics of Strain Induced Martensitic Nucleation. *Metall. Trans. A* **6 A**, 791–795 (1975).

53. Eshelby, J. D. The determination of the elastic field of an ellipsoidal inclusion, and related problems. *Proc. R. Soc. London. Ser. A. Math. Phys. Sci.* **241**, 376–396 (1957).

54. Furnémont, Q., Lacroix, G., Godet, S., Conlon, K. T. & Jacques, P. J. Critical assessment of the micromechanical behaviour of dual phase and trip-assisted multiphase steels. *Can. Metall. Q.* **43**, 35–42 (2004).

55. Morooka, S., Umezawa, O., Harjo, S., Hasegawa, K. & Toji, Y. Quantitative analysis of tensile deformation behavior by in-situ neutron diffraction for ferrite-martensite type dual-phase steels. *Tetsu-To-Hagane/Journal Iron Steel Inst. Japan* **98**, 311–319 (2012).

Chapter 3 Effect of grain size on the deformation behavior of Fe-24Ni-0.3C

3.1 Introduction

As mentioned in **Chapter 1**, in metastable austenite, martensitic transformation could be initiated by applying stress or plastic deformation even above M_s temperature, which is termed as deformation induced martensitic transformation [1,2]. The formation of deformation induced martensite can enhance the strain hardening rate and lead to high strength and high ductility in the material. Therefore, the deformation behavior of materials having metastable austenite phase, such as austenitic steels [3,4] and TRIP aided steels [5,6], greatly depends on the stability of austenite phase, because the stability of austenite affects the deformation induced martensitic transformation and consequently changes the strain hardening capability of the material.

It is well known that grain size of austenite has a strong influence on the stability of austenite. Extensive studies reveal that with decreasing the grain size the stability of austenite would be enhanced [7,8]. Although it has not been fully understood in the present, the stabilization of austenite as grain refinement is possibly attributed to that the strengthening of austenite rises the resistance to martensitic transformation [9,10]. On the other hand, due the lack of acknowledgement about stress partitioning between austenite and martensite, usually the increase of strain hardening rate caused by the deformation induced martensitic transformation is only attributed to the increase of volume fraction of martensite having higher strength in the previous studies [11–13]. Therefore, when the grain size effect on the deformation behavior of austenitic steels and TRIP added steels is discussed, numerous researches usually focus solely on the grain size effect on the stability of austenite or the kinetics of the deformation induced martensitic transformation [14–16].

As demonstrated in Chapter 2, beside the kinetics of deformation induced martensitic transformation, the evolution of phase stress of martensite also plays an important role in the deformation of the Fe-24Ni-

0.3C alloy. The increase of phase stress of martensite has a significant contribution on the increase of strain hardening rate of the material. However, most of studies about the grain size effect on the TRIP effect ignored or have not considered the grain size effect on the evolution of phase stress or internal stress of two phases.

Therefore, this chapter aims to clarify the deformation behavior of Fe-24Ni-0.3C specimens with different grain sizes and to discuss the effect of grain size on the deformation behavior especially from the aspect of stress partitioning and strain partitioning between the two phases.

Table 3.1 Chemical composition of as-received bulky Fe-24Ni-0.3C alloy (wt.%)

Ni	**C**	Si	Mn	S	P	O	N	Fe
23.88	**0.29**	<0.02	0.05	<0.0005	<0.005	0.0018	0.0009	Bal.

3.2 Material and experimental methods

In order to manufacture specimens of Fe-24Ni-0.3C having different mean grain sizes, a bulky material of Fe-24Ni-0.3C was used in the current studies. A cast ingot of Fe-24Ni-0.3C alloy fabricated by vacuum melting was hot-forged at 1150 ^{o}C to a plate with a thickness of 20 mm. The chemical composition of the as-received bulky Fe-24Ni-0.3C alloy is shown in **Table 3.1**, which is slightly different from the material used in **Chapter 2** for the content of nickel and carbon. A block having dimension of 30 mm (length) × 20 mm (thickness) × 20 mm (width) was cut from the as-received plate by a wire electrical discharge machine, then austenitized at 700 ^{o}C for 10 min, which was used as the starting material. After austenitization, the starting material was composed of a fully austenitic structure that has equiaxed morphology with a coarse mean grain size around 40 μm, as shown in **Figure 3.1**. Low angle grain boundaries can be observed in some of the grains, which was possibly introduced during the hot forging processes.

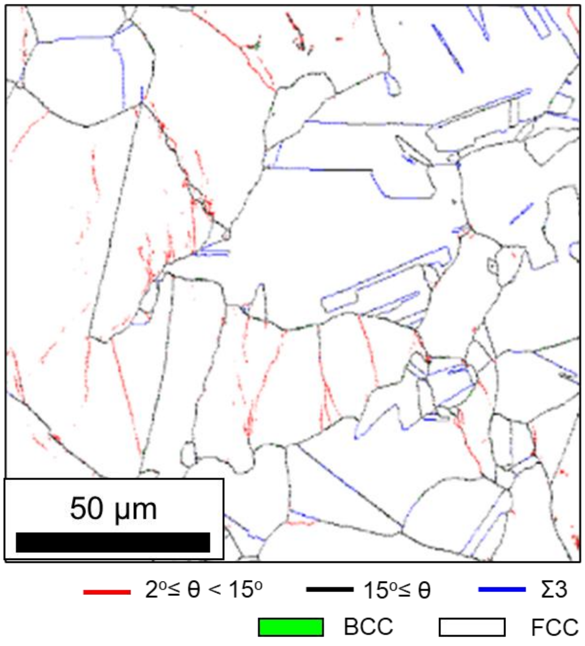

Figure 3.1 Microstructure of the as-received bulky Fe-24Ni-0.3C alloy.

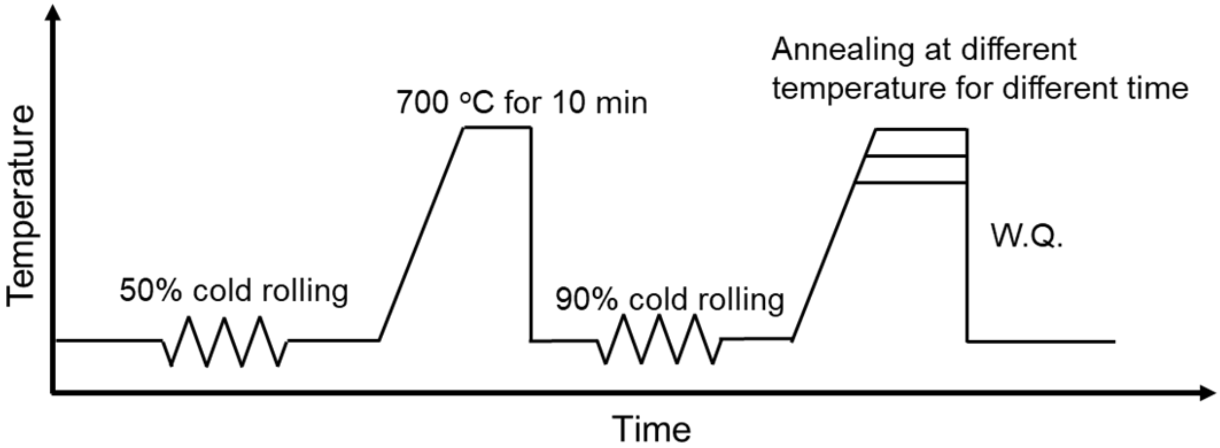

Figure 3.2 Schematic illustration of the fabrication process.

The fabrication process of the specimens is illustrated in **Figure 3.2**. The starting material was firstly cold rolled with a 50% reduction in the thickness to 10 mm. Then, the cold-rolled plate was annealed at 700 °C for 10 min to refine the microstructure and soften the material for further cold rolling. The annealed plate was further cold rolled to 1 mm with a 90% reduction in the thickness. Though annealing at different temperature for different time, specimens with various grain size was fabricated.

Microstructures of the fabricated specimens were observed by using field emission scanning electron microscopy (FE-SEM) equipped with backscattered electron (BSE) and electron backscattering diffraction (EBSD) detectors. Both SEM-BSE and SEM-EBSD was operated at 15 kV with a working distance of 15 mm. The obtained EBSD data was analyzed by the TSL OIM Analysis software (ver. 7) in which the data points having confidence index (CI) value lower than 0.1 were removed. The specimens for the microstructure observation were prepared by careful mechanical polishing to avoiding the formation of deformation induced martensite, followed by electropolishing in an electrolyte (90 vol.% ethanol + 10 vol.% perchloric acid) at 0 °C for 2 min with a voltage of 20 V.

The mechanical properties of the specimens were characterized by uniaxial tensile tests at room temperature. The tensile test specimens having gauge dimensions of 6.0 mm × 2.5 mm × 1.0 mm were cut from the cold-rolled plates by a wire electrical discharge machine. The longitudinal direction of the tensile specimens was parallel to the rolling direction (RD).   As same as Chapter 2, the elongation of tensile tests was precisely measured by using the digital correlation (DIC) method.

Tensile tests with in-situ neutron diffraction were carried out by using an engineering materials diffractometer at the beamline 19 (TAKUMI) in J-PARC (Japan Proton Accelerator Research Complex), aiming to investigate the phase composition and the stress and strain partitioning between austenite and martensite. The details of experiments and analyses have been introduced in **Chapter 2**.

3.3 Microstructure of Fe-24Ni-0.3C with various grain sizes

After the final cold rolling, the specimens were annealed at different temperatures for different time to adjust the grain size. **Figure 3.3 (a)** and **(b)** show BSE images of the specimen annealed at 650 °C for 30 s and 725 °C for 3600 s, respectively. For comparison, **Figure 3.3(c)** shows the microstructure of the specimen used in **Chapter 2** with a mean grain size of 35μm. As can be observed in **Figure 3.3 (a)** and

(b), the annealed specimens have fully recrystallized microstructures composed of mostly equiaxed grains, which is similar to the microstructure of the specimen used in **Chapter 2** (in **Figure 3.3(c)**). With decreasing the annealing temperature and annealing time, the grain size significantly decreased. After the heat treatment at 725 °C for 3600 s, the mean grain size of the specimen is about 4 μm, while 1.3 μm for the specimen annealed at 650 °C for 30 s. The mean grain sizes were measured by the linear intersection method in which twin grain boundaries were counted.

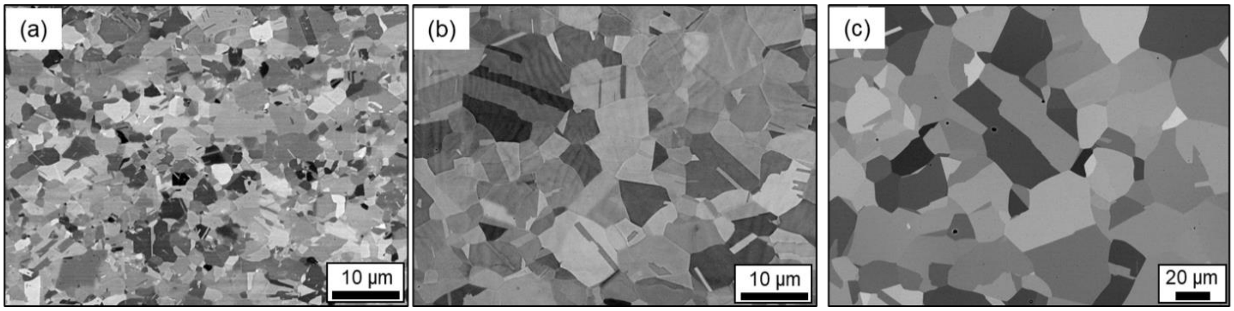

Figure 3.3 (a) and (b) BSE images of specimens annealed at 650 °C for 30 s and 725 °C for 3600 s after final cold rolling, respectively; (c) BSE image of the specimen with a mean grain size of 35 μm, which was used in the study of **Chapter 2**.

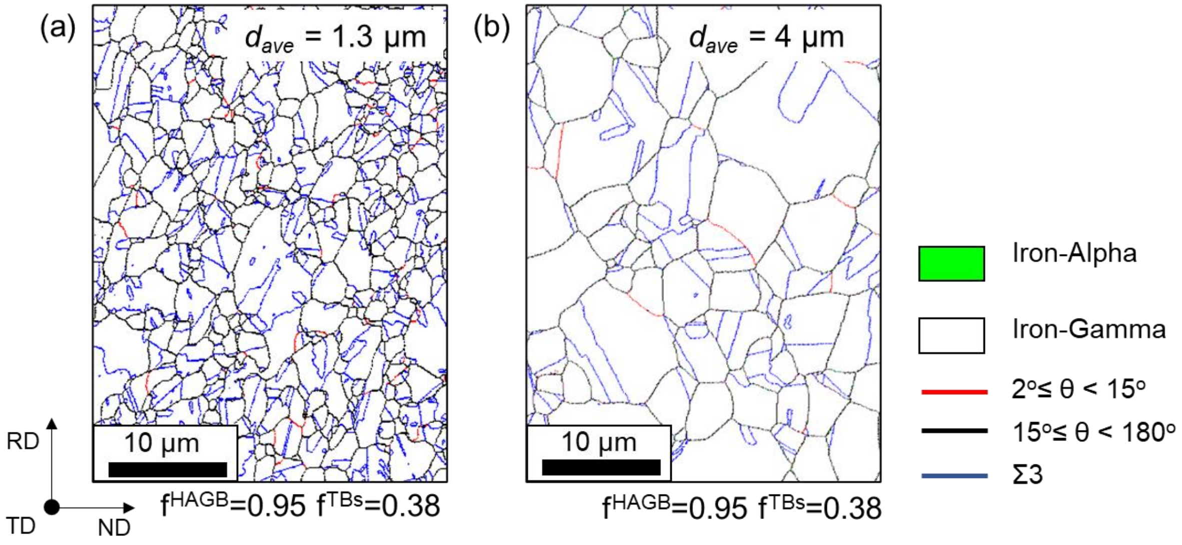

Figure 3.4 EBSD images of specimens annealed at **(a)** 650 °C for 30s and **(b)** 725 °C for 3600 s.

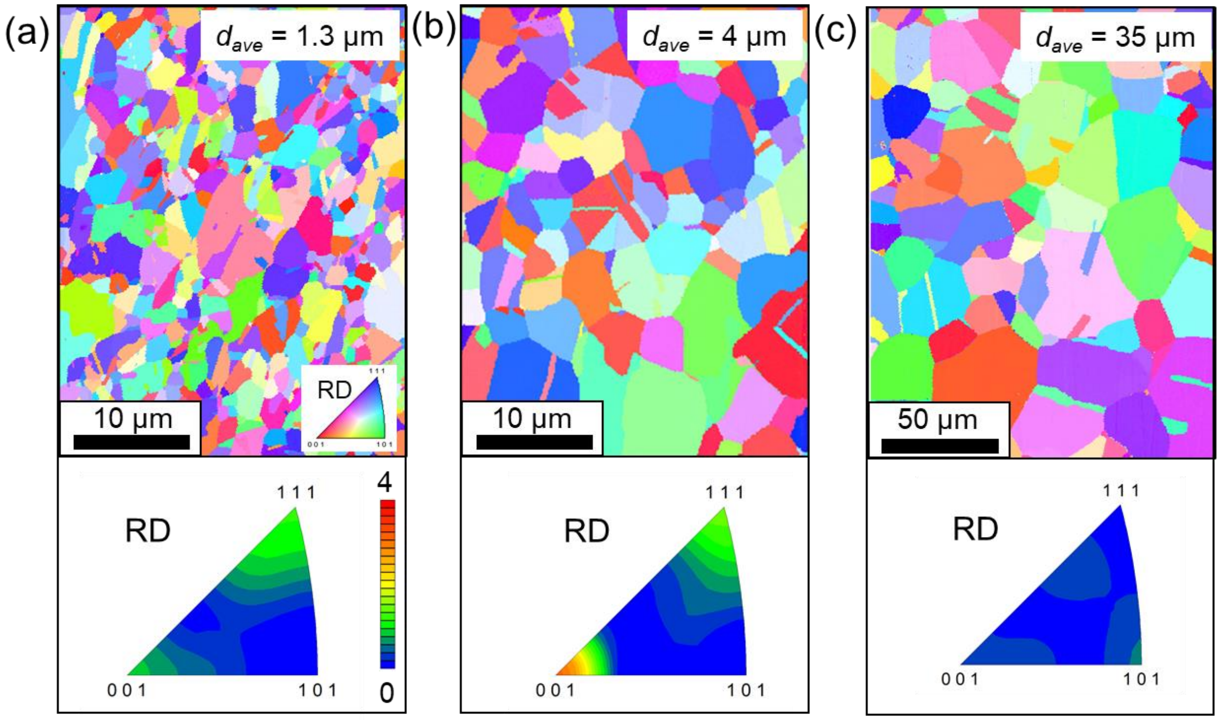

Figure 3.5 IPF image of RD and corresponding IPF of the specimens with mean grain sizes of **(a)**1.3 μm, **(b)** 4 μm and **(c)** 35 μm.

Figure 3.4 (a) and **(b)** show the EBSD phase and grain boundary maps of the specimens with mean grain sizes of 1.3 μm and 4 μm, respectively. In the EBSD image, the white background color represents austenite with FCC structure and the green indicates martensite or ferrite with BCC structure. The EBSD images indicate that the specimens annealed at 650 ^{o}C for 30 s and at 725 ^{o}C for 3600 s were fully composed of austenite phase. The low angle boundaries with misorientation between 2^{o} and 15^{o} are drawn in red lines, high-angle grain boundaries with misorientation larger than 15^{o} are drawn in black lines, and annealing twin boundaries are drawn in blue lines. It can be seen that both two specimens have a lot of annealing twin boundaries.

Figure 3.5 (a), **(b)** and **(c)** show inverse pole figure (IPF) images of RD and the corresponding IPF of the specimens with mean grain sizes of 1.3 μm and 4 μm and 35 μm, respectively. The specimens with mean grain sizes of 1.3 μm and 4 μm which were fabricated by cold rolling and subsequent annealing exhibited $\langle 111\rangle_{\gamma} + \langle 100\rangle_{\gamma}$ fiber texture in the RD, while the specimen with a mean grain size of 35 μm has relatively weak texture due to the high annealing temperature.

In conclusion, fully recrystallized austenitic Fe-24Ni-0.3C specimens with different grain sizes were fabricated by cold rolling and subsequent annealing. Hereafter, the specimen with the mean grain sizes of 1.3 μm, 4 μm, and 35 μm would be termed as ultrafine-grained (UFG) specimen, fine-grained (FG) specimen, and coarse-grained (CG) specimen, respectively.

3.4 Effect of grain size on the tensile behavior of Fe-24Ni-0.3C

The mechanical properties of the specimens were characterized by the uniaxial tensile tests at room temperature. **Figure 3.6** shows the nominal stress-strain curves of the specimens shown in **Figure. 3.3** with three different mean grain sizes. The embedded figure in **Figure 3.6** shows the details of the stress-strain curves at yield points. It can be seen that the yielding behavior of the specimens changed from continuous yielding to discontinuous yielding with a yield-drop when the grain size decreased from 4 μm to 1.3 μm. The similar transition of yielding behavior with grain refinement was also observed in other UFG materials, such as pure Al [17], Cu [18] and IF steel [17,19]. The yield-drop phenomenon in UFG materials is considered due to the lack of initial mobile dislocations and sudden multiplication of dislocations [19]. **Table 3.2** summarizes the mechanical properties of the specimens with various mean grain sizes obtained from the tensile tests. The 0.2 % offset proof stress was taken as the yield strength for the specimens exhibiting continuous yielding, while the upper yield stress was taken for that exhibiting yield-drop phenomenon. It can be seen from the stress-strain curves that with decreasing the grain size from 35 μm to 1.3 μm, the yield strength increased from 180 MPa to 415 MPa and the total elongation increased from 0.83 to 1.04, while the ultimate tensile strength slightly decreased from 1050 MPa to 960 MPa. The CG specimen exhibited the highest strain hardening and the highest tensile strength in the tensile deformation. However, the UFG specimen showed the largest uniform elongation. **Figure 3.7** shows the strength and ductility combination of the specimens with different grain sizes. The product of strength and elongation of the UFG specimen is higher than that of FG and CG specimen, indicating the UFG specimen has a better combination of strength and ductility.

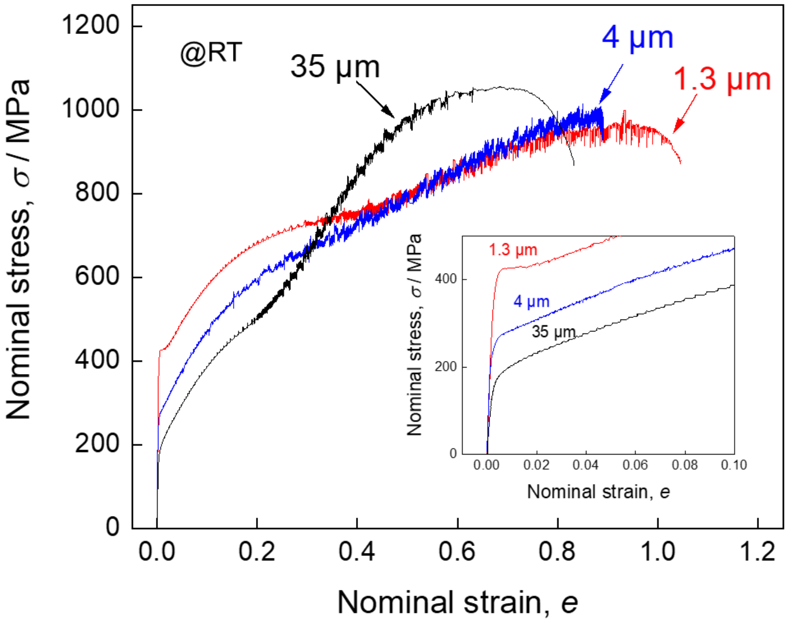

Figure 3.6 Nominal stress-strain curves of specimen with various grain size at room temperature. The details of the stress-strain curves at yield point are shown in the embedded figure.

Table 3.2 Yield strength, ultimate tensile strength, total elongation and uniform elongation at room temperature obtained from the nominal stress-strain curves of the specimens with three different average grain sizes of austenite.

Austenite grain size, d_{ave} / μm	**Yield strength, σ_y/MPa**	**Ultimate tensile strength, σ_{UTS}/MPa**	**Uniform elongation, e_u**	**Total elongation, e_t**
35	180	1050	0.7	0.83
4	257	1000	0.88	0.89
1.3	415	960	0.94	1.04

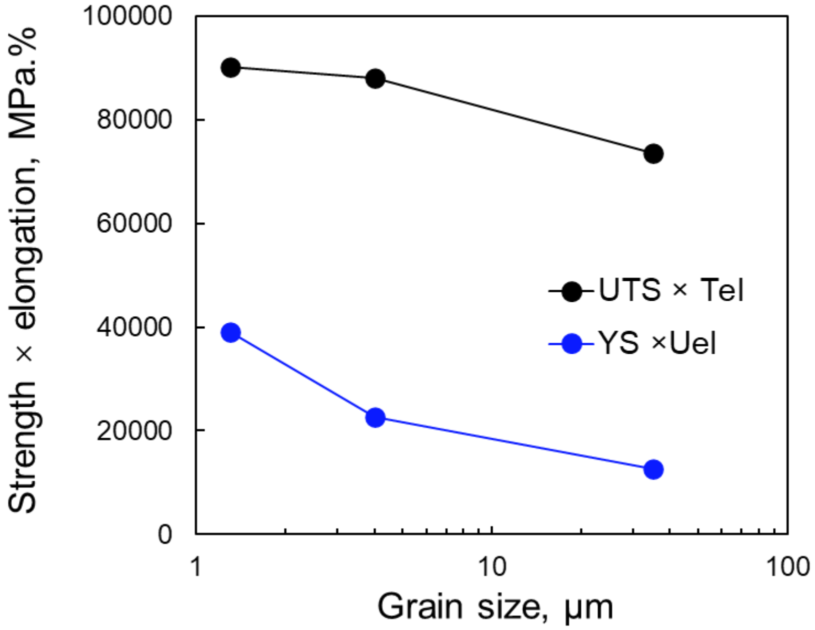

Figure 3.7 Yield strength-uniform elongation product (YS × Uel) and ultimate tensile strength-total elongation product (UTS × Tel) as a function of mean grain sizes of austenite.

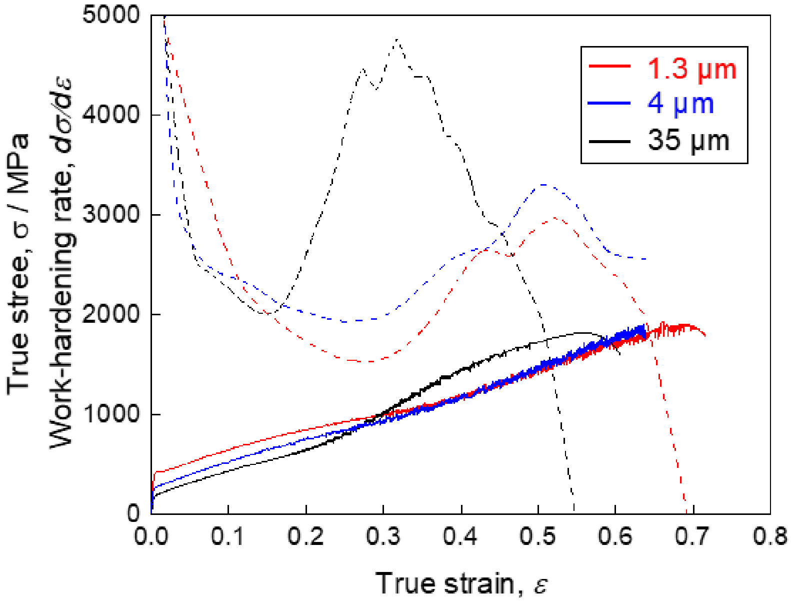

Figure 3.8 True stress-strain curves and strain hardening rate curve of specimen with various grain size at room temperature.

Figure 3.8 shows strain-hardening rate curves and corresponding true stress-strain curves of the specimens with three different mean grain sizes, plotted as a function of the true strain. For all the three specimens, the strain-hardening rate firstly decreased, then started to increase at different true strains depending on the grain size, and finally decreased again. With decreasing the grain size of austenite, the increment of the strain hardening rate decreased and the strain at where the strain hardening rate started to increase was postponed to t larger strain stage. As demonstrated in **Chapter 2**, the enhancement of strain hardening rate of Fe-24Ni-0.3C alloy during tensile deformation is due to the formation of deformation induced martensite. Therefore, the changes of volume fraction of the martensite in the UFG and FG specimens during deformation were measured by in-situ neutron diffraction. **Figure 3.9 (a)** and **(b)** show the changes of volume fraction of the martensite in the specimens with different mean grain size as a function of true strain and true stress, respectively. It can be seen that with decreasing the grain size of austenite the amount of martensite formed during the deformation decreased and the kinetics of deformation induced martensitic transformation significantly decreased. Meanwhile, the critical strain and stress for the initiation of the martensitic transformation increased. These results indicate that the deformation induced martensitic transformation was suppressed by grain refinement of austenite. The suppression of the martensitic transformation was known due to the increased stability of austenite against martensitic transformation by the grain refinement [7]. By comparing the strain hardening rate curves in **Figure 3.8** with the kinetics of the martensitic transformation shown in **Figure 3.9 (a)**, it can be easily found that the decrease of strain hardening as grain refinement is consistent with the decrease of the kinetics of the martensitic transformation. Postponed initiation of the deformation induced martensitic transformation as grain refinement resulted that the starting of enhancement of strain hardening delayed. Through comparison and analysis of the deformation behavior and kinetics of the martensitic transformation of the specimens with different mean grain size, it can be concluded that although high kinetics of the martensitic transformation could provide high strain hardening, however, if the kinetics of the martensitic transformation is too high, the TRIP effect would be consumed over a short strain region quickly, like the CG specimen. Only when the TRIP effect occurs at a relatively later stage of deformation (before necking) in a suitable transformation rate, like the UFG specimen, the TRIP effect could be fully utilized to improve the ductility of material.

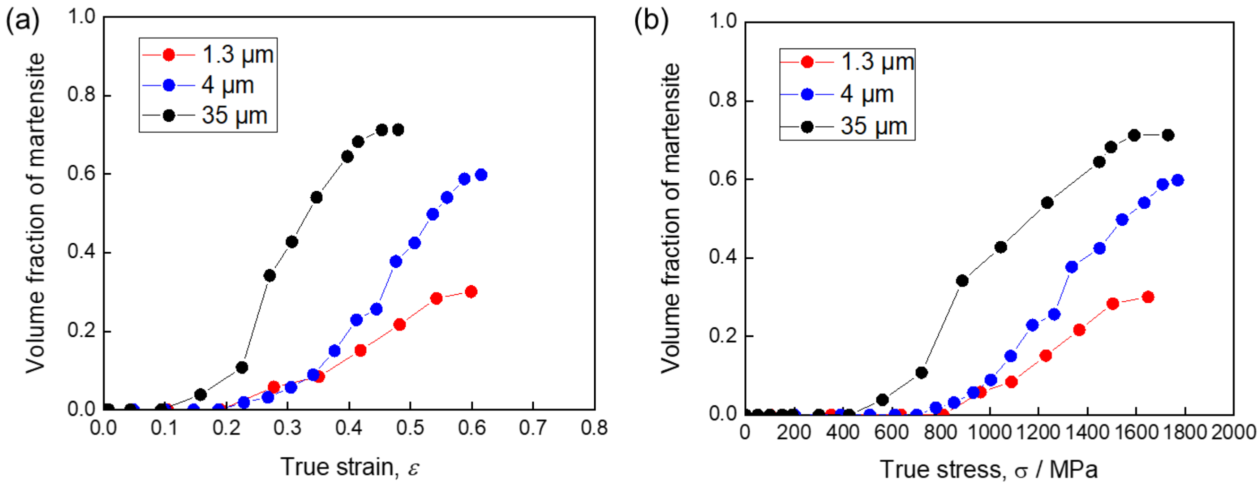

Figure 3.9 Changes of volume fraction of martensite during tensile deformation in the specimen with various grain sizes, **(a)** plotted at a function of true strain; **(b)** plotted as a function of true stress.

3.5 Effect of grain size on the stress partitioning behavior

It has been clarified in **Chapter 2** that the strain hardening behavior of Fe-24Ni-0.3C is not only determined by the kinetics of deformation induced martensitic transformation but also by the evolution of phase stress of martensite. In order to deepen our understanding about the effect of grain size on the deformation behavior of Fe-24Ni-0.3C, it is necessary to clarify the stress partitioning behavior between austenite and martensite in the specimens with various grain sizes. Therefore, tensile tests with in-situ neutron diffraction of the FG and UFG specimens were carried out at the beamline 19 (TAKUMI) in J-PARC and compared with the results of the CG specimen shown in **Chapter 2**.

Figure 3.10 (a) and **(b)** show changes of lattice strain of (hkl) planes of austenite and martensite in the UFG specimen, respectively, plotted as a function of the true stress applied to the specimen. Similarly, **Figure 3.11 (a**) and **(b)** show changes of lattice strain of (hkl) planes of austenite and martensite in the FG specimen, respectively. The lattice strain in the tensile direction is indicated as ε_{11}, while the lattice strain in the transverse direction is indicated as ε_{22}. As can be observed, for both FG and UFG specimens the tensile elastic strains of austenite and martensite were increased with increasing the applied true stress in the tensile direction, implying that the phase **s**tress in austenite and martensite increased during the tensile deformation. On the other hand, due to the Poisson effect, compressive strains were observed in austenite and martensite. However, since the deformation in the transverse direction is complicated and non-uniaxial, only the deformation and phase stress in the tensile direction would be discussed.

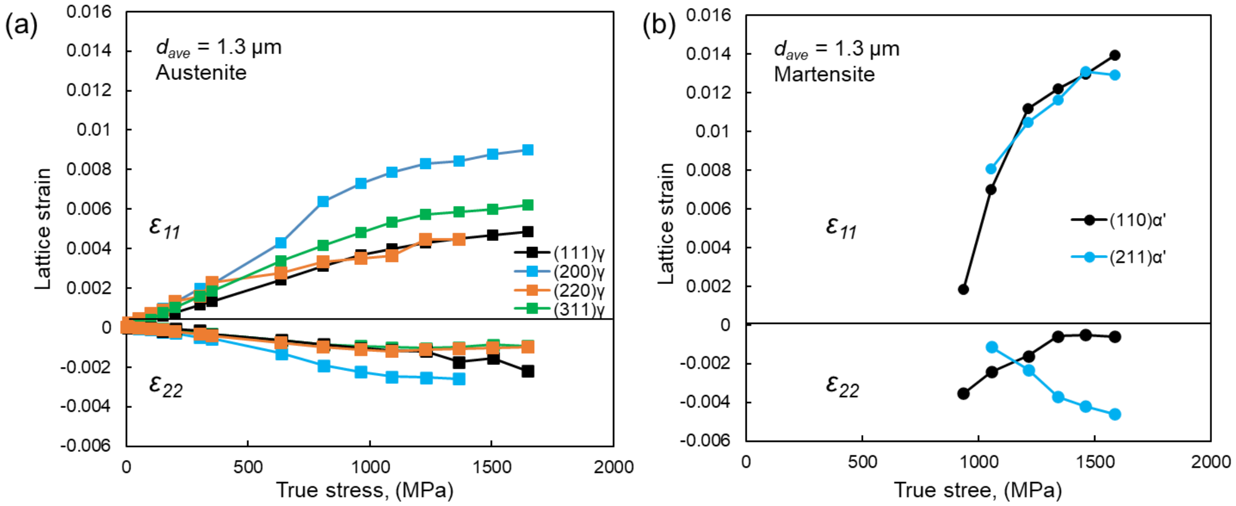

Figure 3.10 Measured lattice strains of **(a)** in austenite and **(b)** in martensite in the specimens with the mean mean grain size of 1.3 µm along the tensile direction (ε_{11}) and the transverse direction (ε_{22}), plotted as a function of the true stress applied to the tensile specimen.

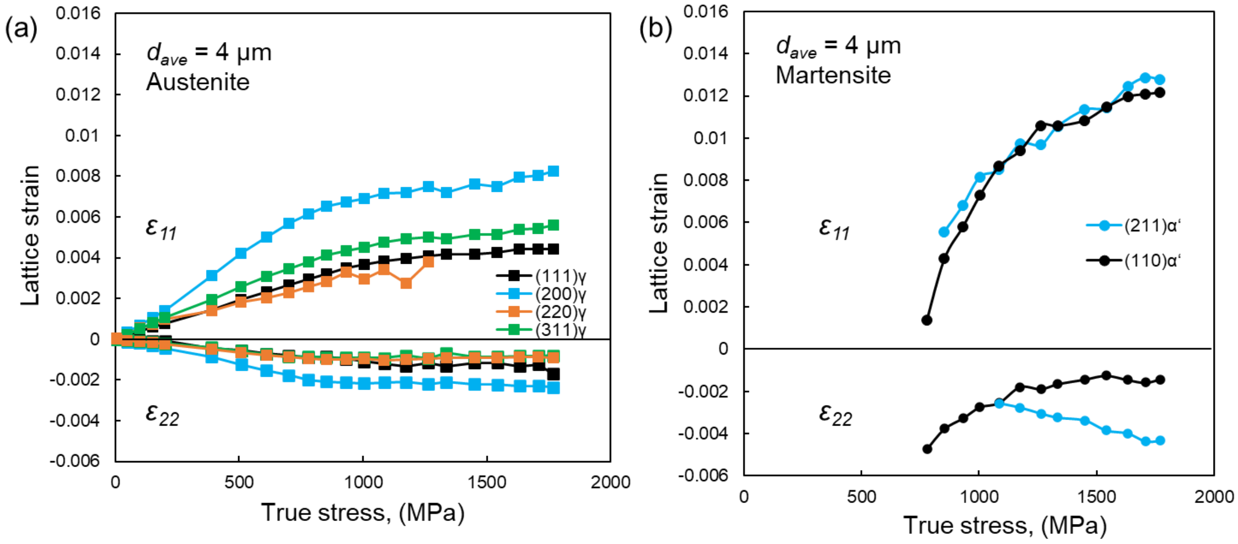

Figure 3.11 Measured lattice strains of **(a)** in austenite and **(b)** in martensite in the specimens with the mean grain size of 4 μm along the tensile direction (ε_{11}) and the transverse direction (ε_{22}), plotted as a function of the true stress applied to the tensile specimen.

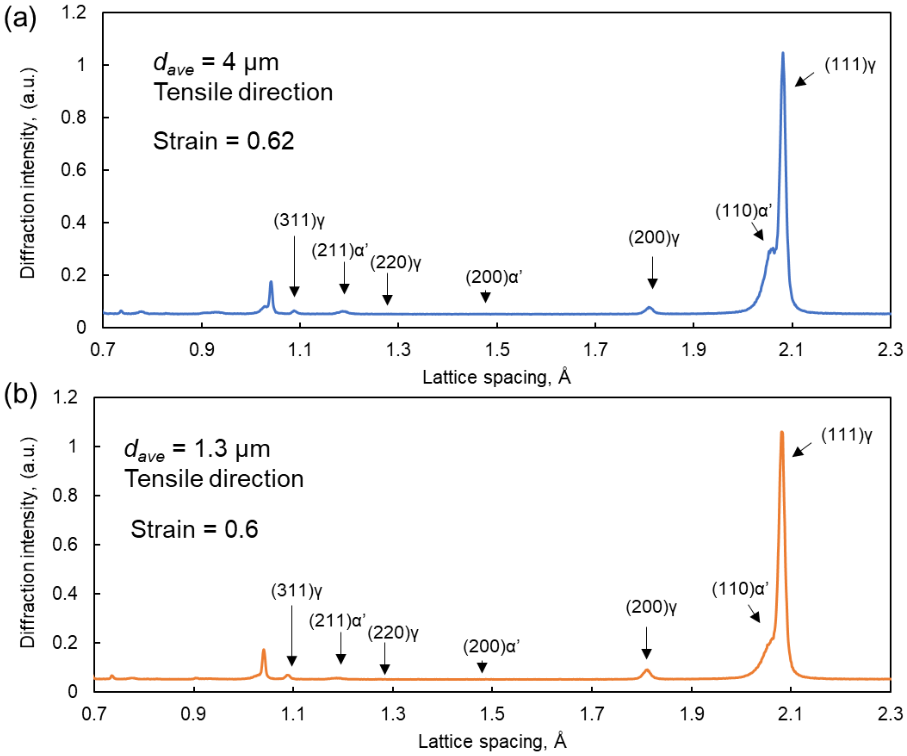

Figure 3.12 Diffraction profiles of tensile deformed FG and UFG specimen obtained by the axial detector.

Figure 3.12 shows the diffraction profiles of the deformed FG and UFG specimens obtained in the tensile direction. The deformed FG and UFG specimens show strong <111>$_\gamma$ texture for austenite and <110>$_{\alpha'}$ texture for martensite in tensile direction, as same as the CG specimen (**Figure 2.16**). Therefore, the lattice strain of (111)$_\gamma$ plan of austenite and (110)$_{\alpha'}$ plan of martensite could be used to represent the average elastic strain of austenite phase and martensite phase, respectively. **Figure 3.13** summarizes the changes of the lattice strain of (111)$_\gamma$ plan of austenite and (110)$_{\alpha'}$ plan of martensite in the specimens with the three different grain sizes as a function of the true stress. **Figure 3.13 (a)** shows the changes of the lattice strain of (111)$_\gamma$ plane of austenite in the specimens with three different mean grain sizes. For all the three specimens, the lattice strains of (111)$_\gamma$ plane in the tensile direction had an identical response proportional to the tensile stress in the elastic stage (before yielding), and the slope corresponded to the elastic modulus in <111>$_\gamma$ direction. After yielding (corresponding to true stresses of approximately 180 MPa, 257 MPa, and 415 MPa for the specimens with mean grain sizes of 35 μm, 4 μm, and 1 μm, respectively), the lattice strain of (111)$_\gamma$ in the tensile direction slightly deviated downward from the linearity due to the intergranular elastic strain that arises from the strain incompatibility between grains with different orientations [20,21]. However, the deviation was too small to be observed in **Figure 3.13 (a)**, which implies that the (111)$_\gamma$ is one of the planes in austenite less effected by the intergranular elastic strains. It is another reason why the lattice strain of (111)$_\gamma$ can be used to represent the entire elastic strain of austenite in the tensile direction. After the deformation induced martensitic transformation started, the lattice strain of (111)$_\gamma$ obviously deviated from the linearity downward with increasing the volume fraction of martensite since the martensite took a charge of a part of the global flow stress. **Figure 3.13 (b)** shows the changes of the lattice strain of (110)$_{\alpha'}$ plane of martensite in the specimens with three different mean grain size. As demonstrated in **Chapter 2**, since the displacive mechanism of martensitic transformation, the formation of martensite could release the tensile stress component in the tensile direction. Therefore, at the initial stage, the formed deformation induced martensite is mostly elastically deformed with relatively low internal stress. Due to the heterogeneity of the plastic deformation between austenite and martensite, the elastic lattice strain of the martensite quickly increased, for accommodating the strain incompatibility at the interphase boundaries, as shown in **Figure 3.13 (b)**. With decreasing the grain size of austenite, the lattice strain of martensite at the later stage of deformation significantly increased.

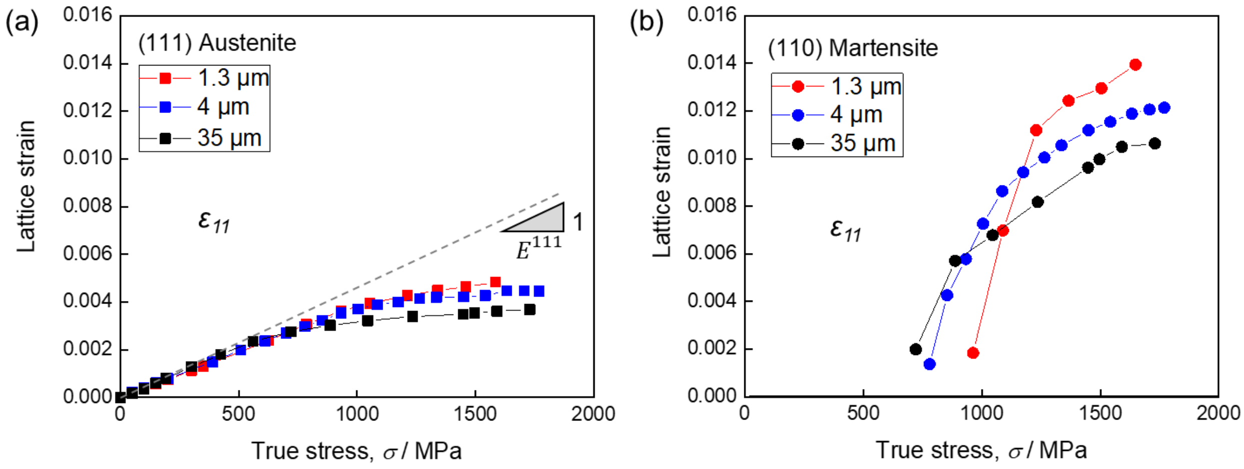

Figure 3.13 Measured lattice strains of **(a)** $(111)_\gamma$ plane in austenite and **(b)** $(110)_{\alpha'}$ plane in martensite in the specimens with three different mean grain sizes along the tensile direction (ε_{11}) and the transverse direction (ε_{22}), plotted as a function of the true stress applied to the tensile specimen. The dashed line in (a) indicates elastic constant in $<111>_\gamma$ direction for austenite.

After obtaining the changes of lattice strain of the FG and UFG specimens, the evolution of phase stress of austenite and martensite in the FG and UFG specimens during the deformation could be calculated according to **Equation 2.20** and **2.21** from their lattice strain of $(111)_\gamma$ plan of austenite and $(110)_{\alpha'}$ plan of martensite shown in **Figure 3.13**. **Figure 3.14 (a)** and **(b)** present the phase stresses of austenite and martensite in the FG and UFG specimens, respectively. Meanwhile, the estimated phase stresses were verified by the rule of mixture (**Equation 2.18**). The calculated total stresses are indicated by red triangles in **Figure 3.14** in which the corresponding true stress-strain curves were also presented. It can be observed that for both FG and UFG specimens the calculated total stress corresponded well with the true stress-strain curves, which demonstrated again that the flow stress of Fe-24Ni-0.3C is determined by the phase stress and volume fraction of austenite and the deformation induced martensite. The evolution of phase stresses of austenite and martensite with the true strain in the specimens with different mean grain sizes were compared in **Figure 3.15**. As shown in **Figure 3.15 (a)**, with decreasing the mean grain size, the phase stress of austenite at a given true strain increased due to the grain refinement strengthening [22], while the increasing rate of phase stress of austenite did not show obvious changes. On the other hand, the phase stresses of martensite in the specimens with different mean grain sizes are shown in **Figure 3.15 (b)**. It can be seen that the maximum phase stress that martensite could reach during the deformation increased with decreasing the grain size of austenite. In addition, when the grain size of austenite decreased from 35 μm to 4 μm, the evolution of the phase stress of martensite with the true strain was almost unchanged. However, when the grain size was further reduced to 1.3 μm, the increasing rate of phase stress of martensite with the true strain significantly increased. The high increasing rate and the high value of phase stress of the martensite in the UFG specimen may contribute to improving the strain hardening effect caused by the formation of deformation induced martensite.

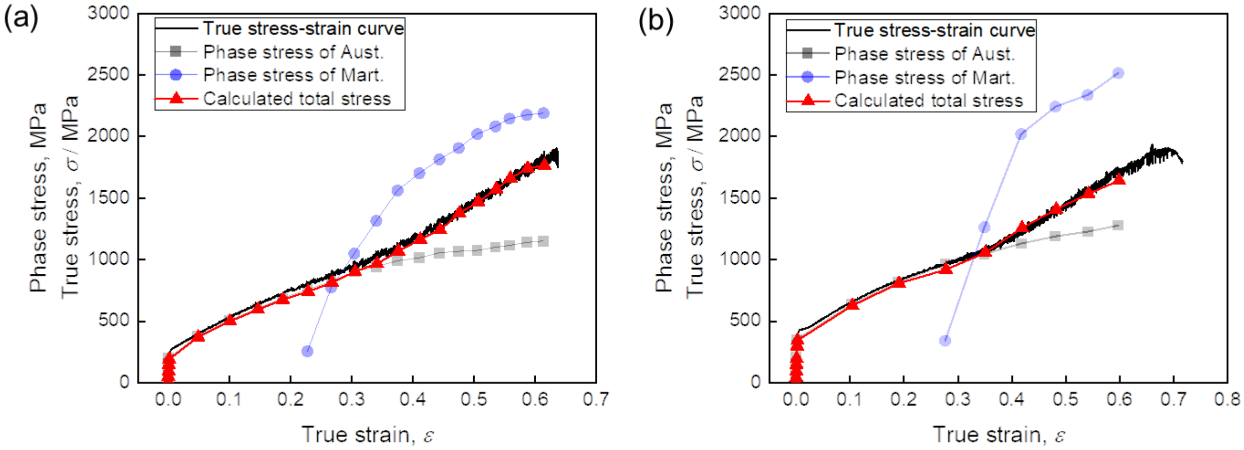

Figure 3.14 Changes of phase stress of austenite and martensite in the specimens with mean grain sizes of **(a)** 1.3 μm and **(b)** 4 μm as a function of true strain. The total stress was calculated by the rule of mixture, which is indicated by the red triangles.

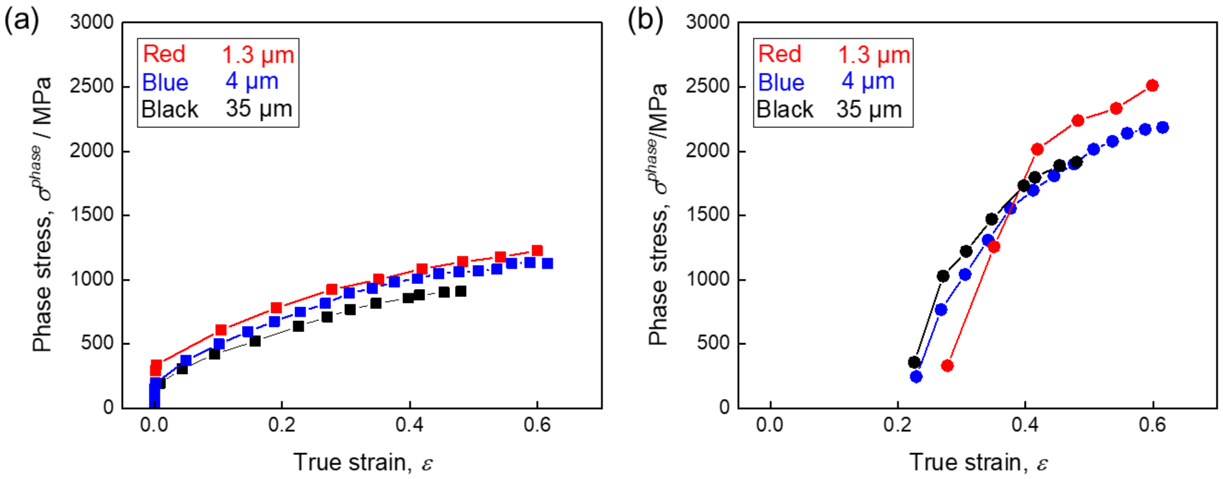

Figure 3.15 Changes of phase stress of **(a)** austenite and **(b)** martensite in the specimens with various grain sizes.

It has been proved in the CG, FG and UFG specimens that the flow stress of specimen obeys the mixing rule of phase stresses of austenite and martensite (**Equation 2.18**). **Equation 2.18** could be rearranged as follow:

$$\sigma_{11}^{applied} = \sigma_{\gamma,11} + f_{\alpha'}(\sigma_{\alpha',11} - \sigma_{\gamma,11}) \quad (3.1)$$

By taking the derivative of the above equation with respect to true strain of specimen, the following equation could be obtained:

$$\frac{d\sigma_{11}^{applied}}{d\varepsilon} = \frac{d\sigma_{\gamma}}{d\varepsilon} + f_{\alpha'}\frac{d(\sigma_{\alpha'} - \sigma_{\gamma})}{d\varepsilon} + (\sigma_{\alpha'} - \sigma_{\gamma})\frac{df_{\alpha'}}{d\varepsilon} \quad (3.2)$$

The lift side of the equation ($d\sigma_{11}^{applied}/d\varepsilon$) is the strain hardening rate of the specimen. On the right side of the equation, the first term ($d\sigma_{\gamma}/d\varepsilon$) is the increasing rate of phase stress of austenite with true strain. The stress partitioning between austenite and martensite could be quantified as the phase stress difference between the two phases ($\sigma_{\alpha'} - \sigma_{\gamma}$). So that, the second and third terms of the right side of Equation 3.2 are determined both by the stress partitioning and kinetics of deformation induced martensite.

The second term could be considered as a contribution of stress partitioning increment on the strain hardening rate. However, the contribution efficiency is determined by the volume fraction of martensite. Similarly, the third term can be considered as a contribution of the formation rate of martensite on the strain hardening rate whose efficiency is determined by the degree of stress partitioning. Therefore, there are three main determinants for the strain hardening rate of specimen: (1) increasing rate of phase stress of austenite; (2) kinetics of deformation induced martensitic transformation; (3) stress partitioning between austenite and martensite.

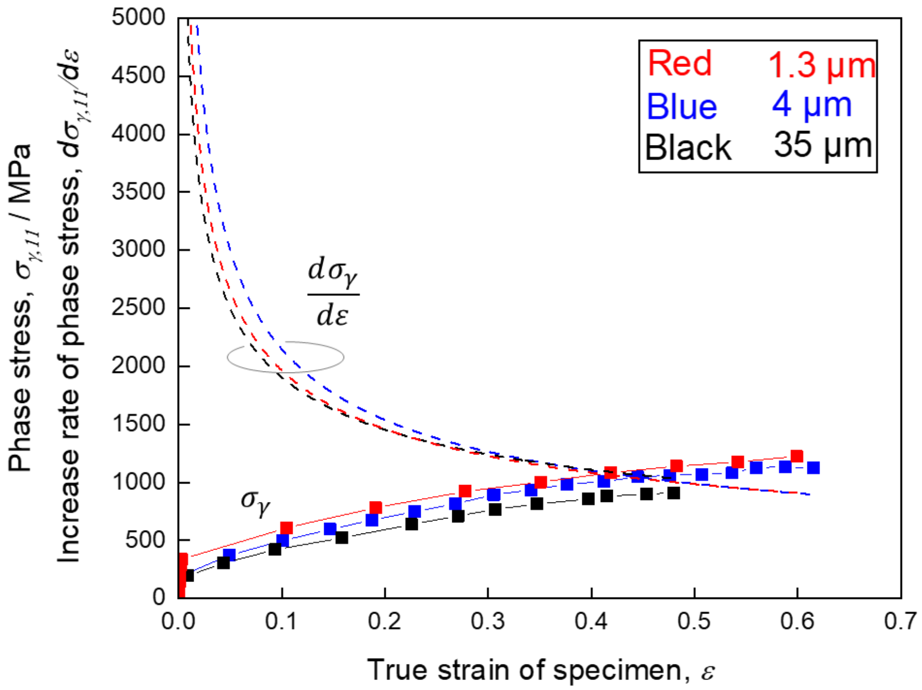

Figure 3.16 Increasing rate of phase stress of austenite in the specimens with various grain sizes, indicated by dashed lines. The plots of phase stress of austenite are fitted by Ludwik's equation (indicated by solid lines), and the increasing rate of phase stress of austenite is obtained from the derivation of the fitting curve.

Figure 3.16 shows the changes of phase stress of austenite in the specimens with different mean grain sizes as a function of true strain, plotted by squares, and the corresponding increasing rate of phase stress of austenite indicated by dashed lines. It should be noted that, due to the heterogeneous distribution of plastic strain between austenite and martensite and most of plastic strain is concentrated on austenite phase, the actual plastic strain of austenite is larger than that of specimen. Thus, the phase stress increasing rate of austenite is not the real strain hardening rate of austenite phase. For estimating the increasing rate of phase stress of austenite, the plots of phase stress of austenite were firstly fitted by Ludwik's equation [23]

$$\sigma_{flow} = \sigma_y + K\varepsilon^n$$

where σ_{flow} is the flow stress and here corresponds to the phase stress of austenite, σ_y is yield strength, K is a constant and n is the strain hardening exponent. The fitting curves are indicated by solid lines in **Figure 3.16**. The increasing rate of phase stress of austenite was obtained by taking the derivative of the fitting curves with respect to true strain. It can be seen that the increasing rate of phase stress of austenite monotonously decreased with increasing the true strain and the phase stress increasing rate curves of austenite are almost unchanged as grain refinement, which implies that the effect of grain size on the strain hardening behavior of specimen is not determined by the austenite phase.

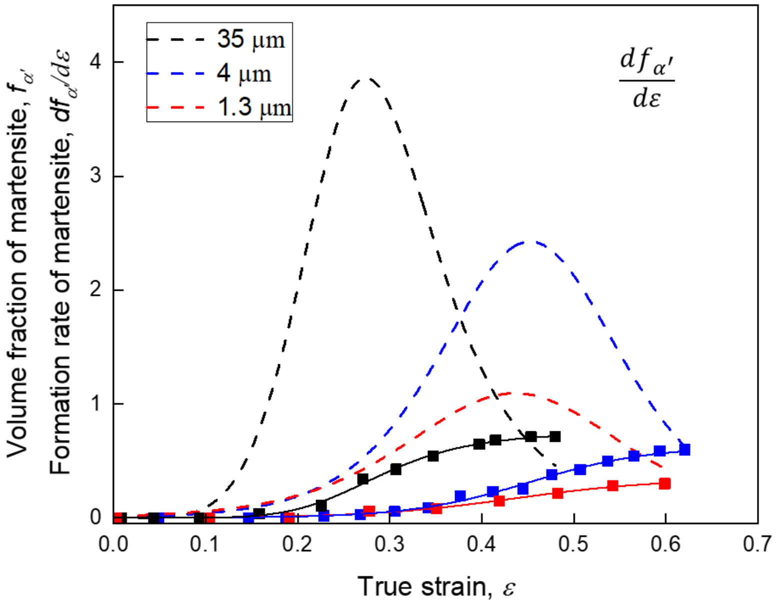

Figure 3.17 Formation rate of the deformation induced martensite in specimens with various grain sizes as a function of true strain, indicated by dashed lines. The plots of volume fraction of martensite are firstly fitted by **Equation 2.28**, then the formation rate of the martensite is obtained from the derivation of the fitting curve.

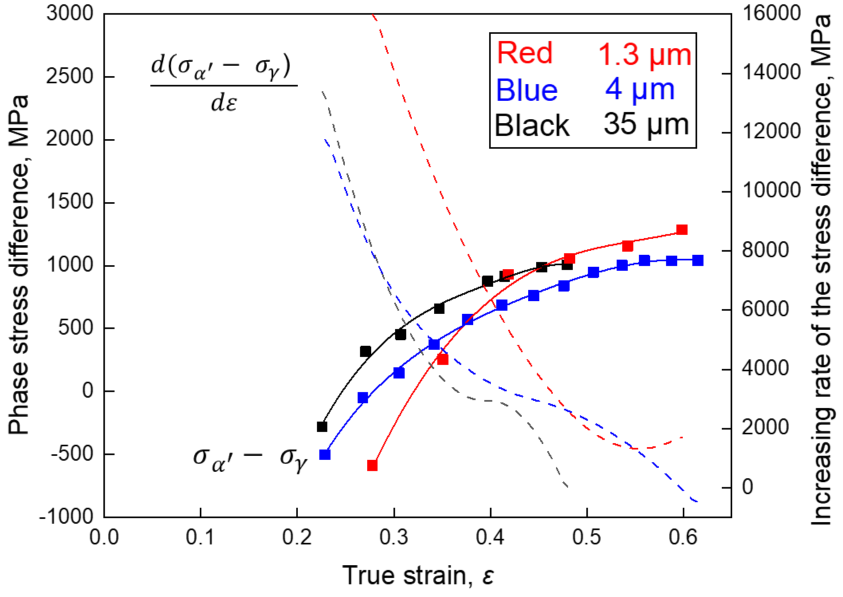

Figure 3.18 Evolution of stress partitioning $(\sigma_{\alpha'} - \sigma_{\gamma})$ between austenite and martensite in the specimens with different mean grain sizes during the deformation, which is expressed by a smooth curve using quadratic interpolation method. The increasing rates of stress partitioning are obtained by taking derivation of the interpolated curve, as indicated by dashed lines.

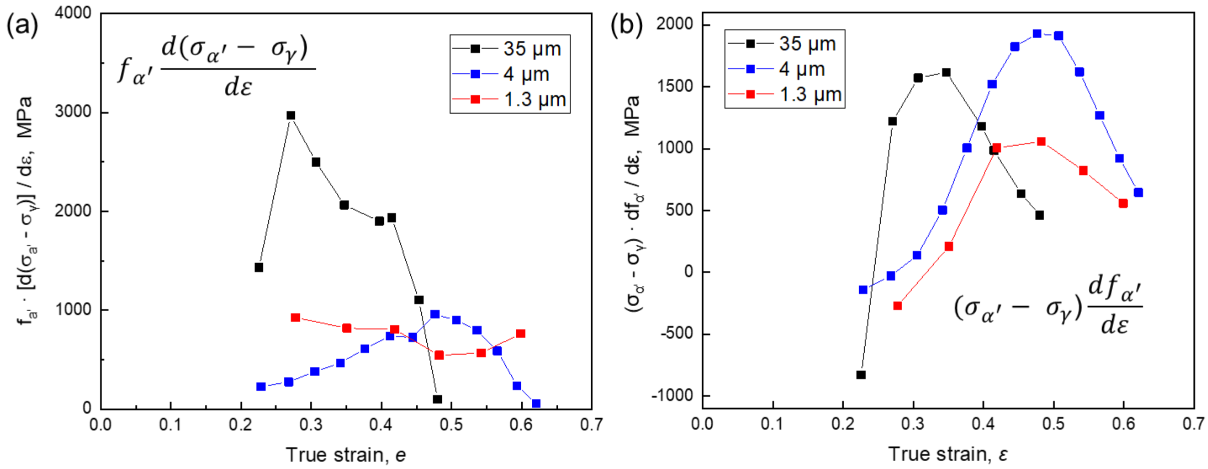

Figure 3.19 (a) Contribution of stress partitioning increasing and **(b)** Contribution of the martensite formation on the strain hardening rate of specimen.

In order to estimate the contribution of stress partitioning increment and the formation rate of martensite on the strain hardening rate, it is necessary to estimate the increasing rate of stress partitioning and martensite volume fraction firstly. **Figure 3.17** shows the volume fraction and the corresponding increasing rate of volume fraction of deformation induced martensite in the specimens with different grain sizes. The formation rate is the increasing rate of the volume fraction of martensite with the true strain instead of time. For estimating the volume fraction increasing rate of the martensite, the plots of martensite volume fraction vs true strain were firstly fitted by **Equation 2.28**, indicated by solid lines. The volume fraction increasing rate of martensite was obtained by taking the derivative of the fitting curves with respect to the true strain of specimen, indicated by dashed lines. It can be clearly seen that during the deformation the formation rate of deformation induced martensite firstly increased then decreased. In addition, the formation rate of deformation induced martensite significantly decreased with decreasing the grain size of austenite. **Figure 3.18** shows the stress partitioning between austenite and martensite ($\sigma_{\alpha'} - \sigma_{\gamma}$) and the corresponding increasing rate ($d(\sigma_{\alpha'} - \sigma_{\gamma})/d\varepsilon$) in the specimens with different grain sizes. Since there is no theoretical or empirical equation for expressing the evolution of stress partitioning between austenite and martensite during deformation, a quadratic interpolation method was used in the present study to describe the evolution of the stress partitioning as a function of true strain of specimen by a smooth curve indicated by solid lines in **Figure 3.18**. The increasing rate of stress partitioning is obtained by taking the derivative of the curves indicated by dashed lines. When the grain size decreased from 35 μm to 4 μm, the stress partitioning curve shifted to the right side due to the postponement of deformation induced martensitic transformation, nevertheless, the increasing rate of stress partitioning was almost unchanged. When the grain size was further reduced to 1.3 μm, the increasing rate of stress partitioning significantly increased, compared with the other two specimens.

Figure 3.19 (a) and **(b)** show the contribution of stress partitioning increment and the formation of martensite on the strain hardening rate for the specimens with different grain sizes respectively, which were calculated from the results shown in **Figure 3.17** and **Figure. 3.18**. **Figure 3.19 (a)** shows the contribution of stress partitioning increment on the strain hardening rate. By comparing the CG specimen with the FG specimen, it can be seen that for the similar stress partitioning increment larger amount of martensite provides larger strain hardening contribution. On the other hand, by comparing the UFG specimen with the FG specimen, when the volume fraction of the martensite in the FG and UFG specimen is almost same at the early stage of deformation (from true strain of 0.25 to 0.35), higher increasing rate of stress partitioning in the UFG specimen introduced larger contribution to the strain hardening. More importantly, as can be observed, at the later stage of deformation the strain hardening contribution caused by stress partitioning increment significantly decreased in the FG and CG specimens, while in the UFG specimen it kept at relatively high value. It is because, as shown in Figure 3.18, that at the latter stage of deformation the stress partitioning kept increasing in the UFG specimen and became larger than that of the FG and CG specimens, while in the CG and FG specimens the increase of the stress partitioning became very small. Since the increasing rate of phase stress of austenite was almost similar in the three specimens, the high increasing rate of stress partitioning in the UFG specimen is contributed to the high increasing rate of phase stress of martensite as shown in **Figure 3.15 (b)**.

Figure 3.19 (b) shows the contribution of the increasing of volume fraction of martensite on the strain hardening rate. Although the formation rate of martensite in the CG specimen is much higher than that in the other two specimens (in **Figure 3.17**), the contribution of the martensite volume fraction increasing on the strain hardening rate in the CG specimen did not exhibit a very large difference with that of the FG and UFG specimens. It is because that, due to its low stability of austenite, the peak formation rate of martensite in the CG specimen occurred at the early stage of deformation where the stress partitioning between the two phases was still low. However, for FG and UFG specimens, the martensitic transformation was suppressed due to the stabilization of austenite as grain refinement. Consequently, the peak formation rate of martensite was postponed to the later stage of deformation where the stress partitioning was relatively larger. As a result, the contribution of the martensite volume fraction increasing on the strain hardening rate in the FG specimen is even larger than that in the CG specimen while that in the UFG specimen is not smaller than that in the CG specimen very much.

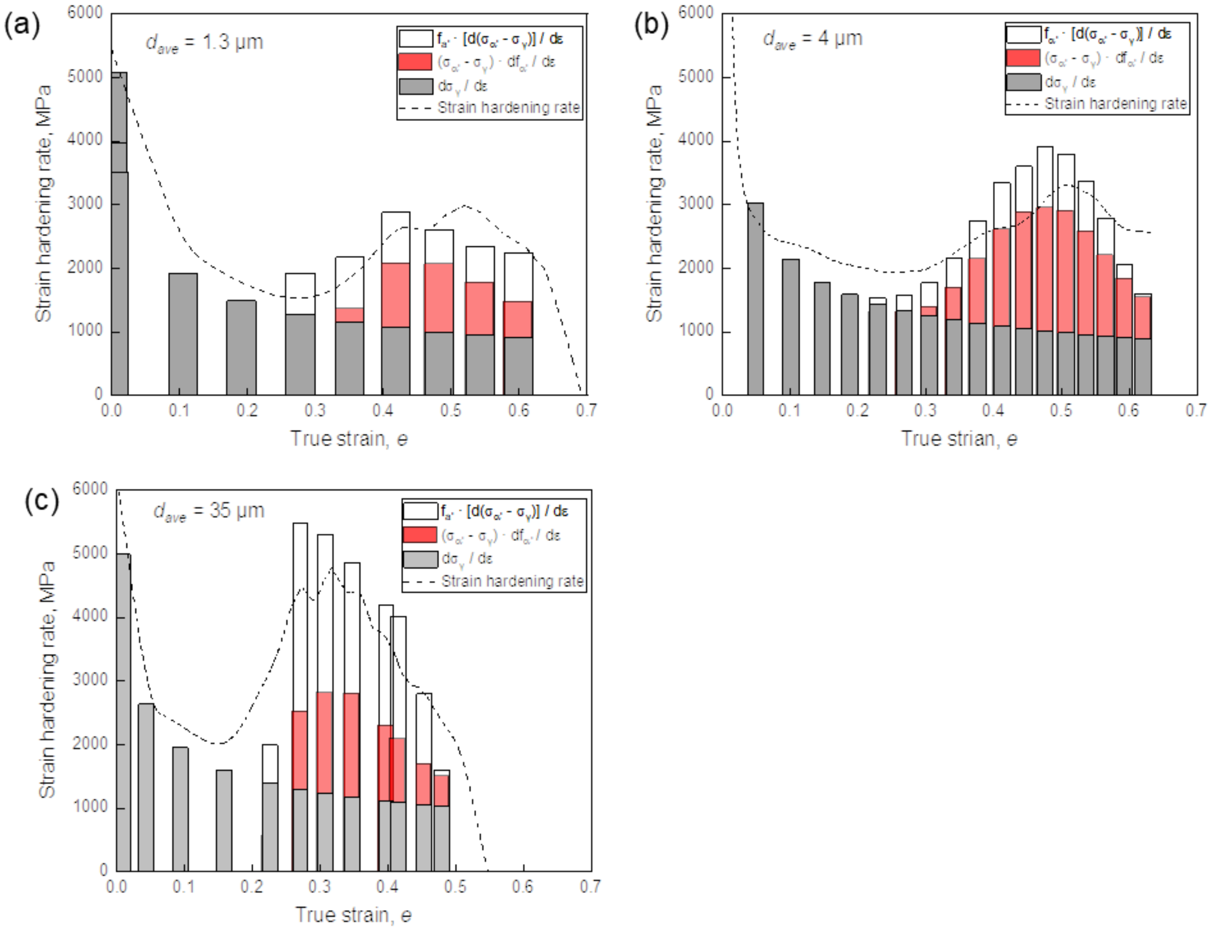

Figure 3.20 Accumulation of the contribution of austenite strain hardening, stress partitioning and martensite formation to the strain hardening of specimen in form of histograms. Dashed curves indicate the strain hardening rate curves of the specimens obtained from corresponding true stress-strain curves. **(a)-(c)** corresponds the specimen with mean grain sizes of 1.3 μm, 4 μm and 35 μm, respectively.

Figure 3.20 shows the accumulation of the contribution of austenite strain hardening, stress partitioning and martensite formation to the strain hardening of the specimen in form of histograms, in which gray parts indicate the strain hardening of austenite phase ($d\sigma_\gamma/d\varepsilon$) and red parts indicate the contribution of the formation of martensite ($(\sigma_{\alpha'} - \sigma_{\gamma})\frac{df_{\alpha'}}{d\varepsilon}$) and white parts indicate the contribution of the increase of stress partitioning ($f_{\alpha'}\frac{d(\sigma_{\alpha'} - \sigma_{\gamma})}{d\varepsilon}$) and the dashed curves indicate the strain hardening rate of specimens obtained from stress-strain curves. Although the accumulated strain hardening rate is a little deviated from the strain hardening rate curve, the changing trend of accumulated strain hardening rate is same as the strain hardening rate curve.

In conclusion, when the grain size decreased within the relatively coarse-grained region, the influence of grain refinement on the evolution of the phase stress in martensite was limited and the strain hardening behavior of the 24Ni-0.3C alloy was mainly determined by the increasing rate of the martensite volume fraction. On the other hand, when the grain size decreased to UFG scale, the phase stress in martensite significantly increased which introduced larger stress partitioning between the two phases and resulted in the increase of the entire strain-hardening rate. Therefore, as shown in Figure 3.8, although the formation rate of martensite in the UFG specimen was much lower than that in the FG specimen, the increment of strain-hardening rate in the UFG specimen was almost the same as that in the FG specimen due to the higher phase stress in martensite of the UFG specimen.

3.6 Effect of grain size on the strain partitioning behavior

It has been known that the stress partitioning between austenite and martensite is attributed to heterogeneous plastic deformation between the two phases. In order to understand the effect of grain size on the stress partitioning behavior, it is necessary to clarify the effect of grain size on the plastic partitioning behavior. As demonstrated in Chapter 2, the strain partitioning between austenite and martensite could be estimated according to the evolution of the dislocation density of austenite during the deformation.

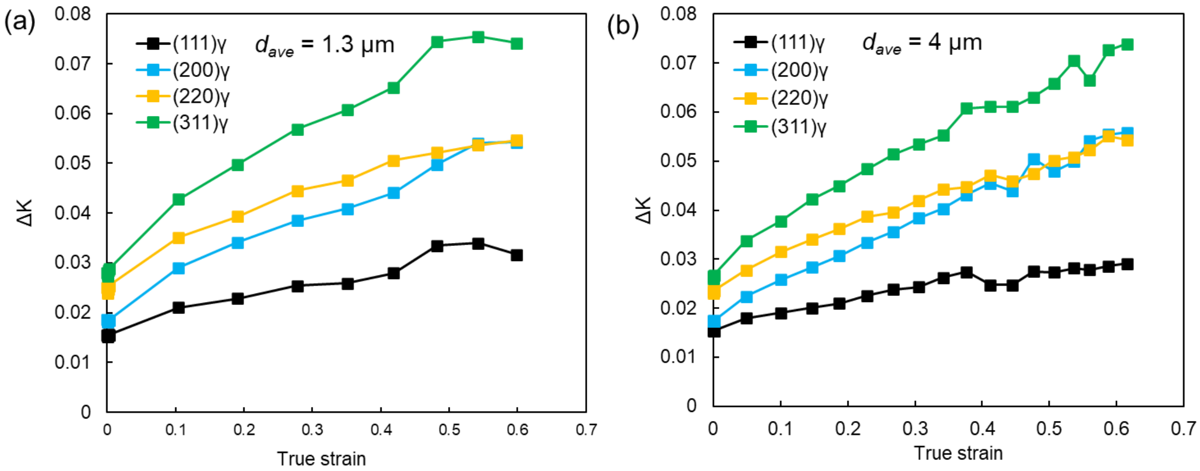

Figure 3.21 Changes of FWHM of diffraction peaks of austenite in the specimens with mean grain size of **(a)** 1.3 μm and **(b)** 4 μm, as a function of the true strain of specimen.

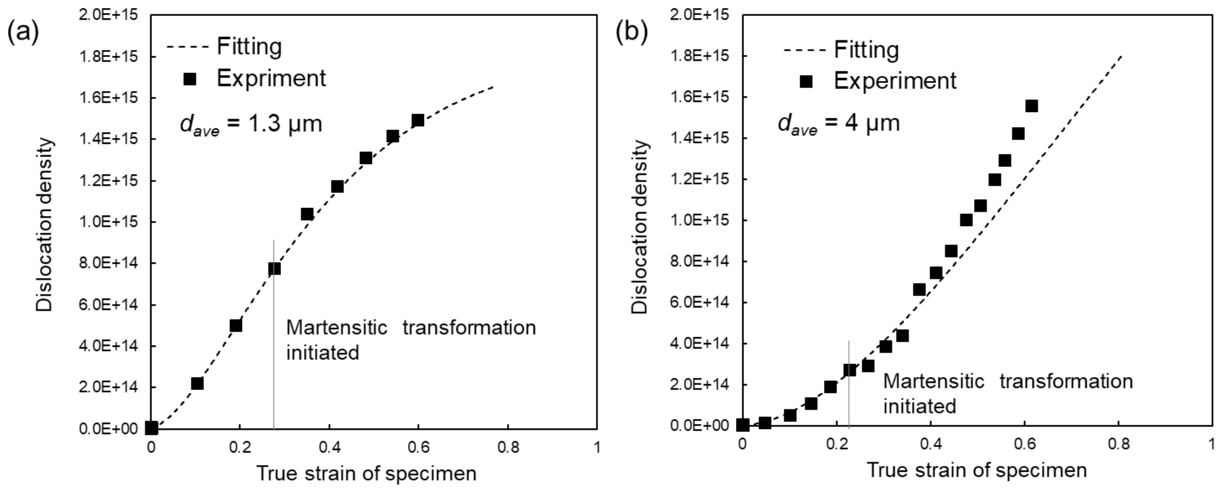

Figure 3.22 Increase of the dislocation density of austenite in the specimen with mean grain size of **(a)** 1.3 μm and **(b)** 4 μm with increasing the true strain of specimen. The data plots of dislocation density vs true strain before the martensite formed were fitted by Kocks-Mecking-Estrin model and the obtained relationship is extrapolated to larger stage, representing the relationship between dislocation density and plastic strain for the austenite phase.

Figure 3.21 (a) and **(b)** show changes of peak widths of (hkl) planes of austenite in the FG and the UFG specimens, respectively, as a function of true strain, which were measured in the diffraction profiles obtained in the transverse direction. It can be seen that peak width increased with increasing the true strain, indicating the increase of dislocation density in the austenite phase. By using the modified Williamson-Hall method [24], the dislocation density of austenite was estimated from the peak widths of (hkl) planes of austenite. **Figure 3.22 (a)** and (b) present the estimated dislocation density of austenite in the UFG and FG specimen, respectively, plotted as a function of the true strain of specimen. In **Figure 3.22**, the strain where the deformation induced martensitic transformation initiated is indicated by a vertical solid line. Before the initiation of the martensitic transformation, the specimens were fully composed of austenite phase. Therefore, the relationship between dislocation density and plastic strain of austenite could be obtained by fitting the plots of dislocation density vs true strain before the formation of the martensite using Kocks-Mecking-Estrin model [25] (**Equation 2.28**). Then, the obtained relationship was extrapolated to larger stage, which was indicated by dashed lines in **Figure 3.22**. It can be seen that before the formation of martensite the evolution of dislocation density of austenite corresponded well with the Kocks-Mecking-Estrin model for both the FG and the UFG specimens. After the formation of martensite, the dislocation density of austenite in the FG specimen (in **Figure 3.22 (b)**) started to deviate to the upper side of the dashed curve, which means that plastic strain started to concentrate on the austenite phase. However, for the UFG specimen (in **Figure 3.22 (a)**), even though the deformation induced martensite formed, the evolution of dislocation density of austenite did not obviously deviate from the dashed curve. It implies that the deformation in the UFG specimen is more homogeneous.

By using the relationship between the dislocation density and plastic strain of austenite, the plastic strain of austenite after the formation of martensite could be estimated according to the corresponding dislocation density. **Figure 3.23 (a)** and **(b)** show the estimated plastic strain of austenite in the UFG specimen and FG specimen, respectively, indicated by blue squares. In **Figure 3.23**, the dashed lines indicate the true strain of the specimen. In order to determine the strain where the martensite started to plastically deform, the plastic strain of austenite estimated by assuming that the martensite only elastically deforms during deformation (ε_γ^*) was calculated by **Equation 2.27** and **2.28,** as indicated by black solid curves in **Figure 3.23**. Therefore, the strain where the plastic strain of austenite starts to deviate from the ε_γ^* (solid curves) to the lower side is the strain where the martensite starts to plastically deform. The offset points are indicated by red arrows in **Figure 3.23**. It can be found that after the true strain of 0.43 obvious plastic deformation occurred in the martensite phase for the UFG specimen, while after the true strain of 0.53 obvious plastic deformation occurred in the martensite phase for the FG specimen. Although the initiation of the martensitic transformation in the UFG specimen is later than that in the FG specimen (**Figure 3.9 (a)**), the martensite in the UFG specimen plastically deformed at the earlier stage of deformation than that in the FG specimen.

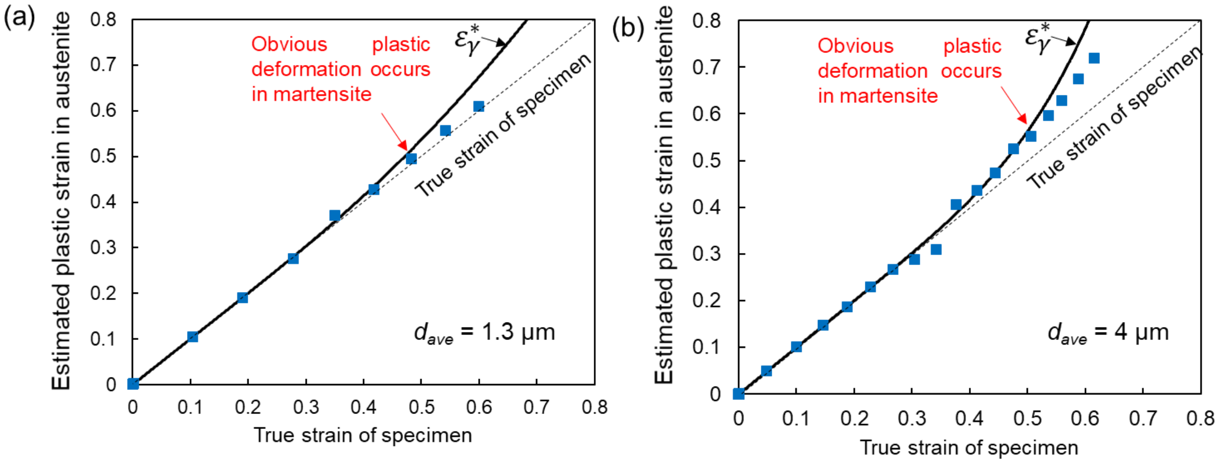

Figure 3.23 Evolution of plastic strain of austenite estimated from the dislocation density of austenite (indicated by blue squares). The plastic strain of austenite estimated by assuming that martensite only elastically deforms (ε_γ^*) is indicated by black solid lines. **(a)** corresponds to the 1.3 μm specimen; **(b)** corresponds to the 4 μm specimen.

After knowing the strain from where the martensite plastically deformed, the plastic strain of martensite could be calculated by accumulating the increment of its plastic strain in each step of deformation which could be calculated by **Equation 2.29**. **Figure 3.24** shows the plastic strain of austenite and martensite in the specimens with different mean grain sizes, plotted as a function of the true strain of specimen. It can be seen that with decreasing the grain size the deviation of plastic strain of austenite from the true strain of specimen (dashed line) becomes smaller, which means plastic deformation between austenite and martensite becomes more homogenous as grain refinement. On the other hand, the plastic strain of martensite in the UFG specimen was larger than that in the FG and CG specimens, while the difference of plastic strains in the FG and CG specimens is relatively small, which also proved that the plastic deformation in the UFG specimen is more homogeneous than that in the FG and CG specimens.

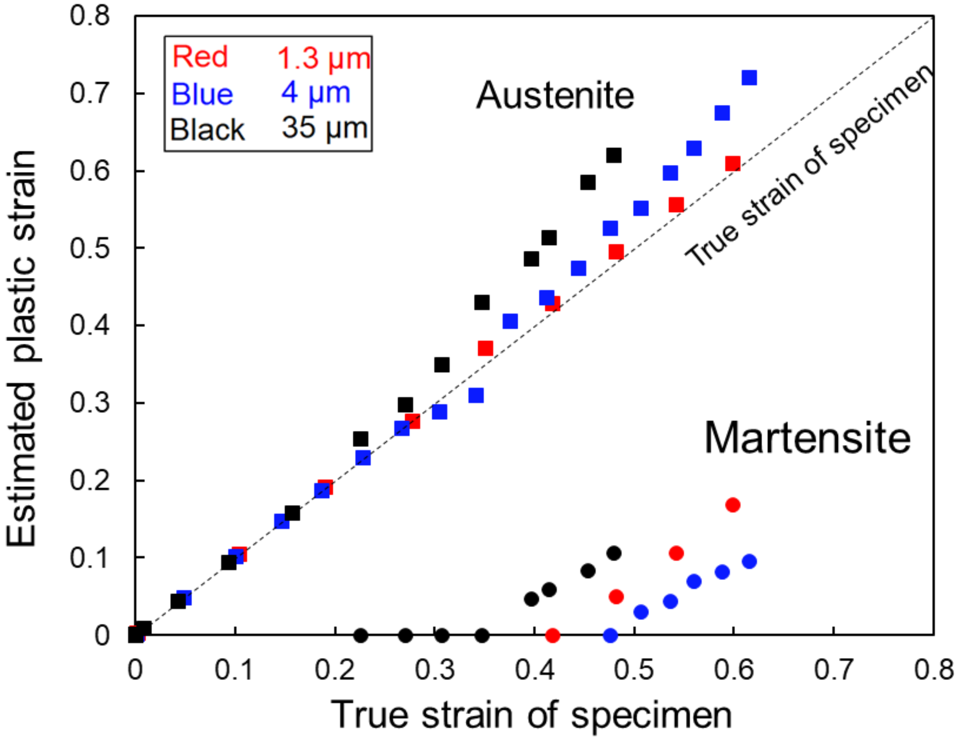

Figure 3.24 Evolution of plastic strain of austenite and martensite in the specimen with various grain sizes during the tensile deformation.

To confirm the effect of grain size on the deformation of the martensite, the deformations of martensite plates in the CG and UFG specimens were directly measured according to the change of their morphology. Firstly, the CG and UFG specimens were tensile deformed to strain of 25% and 48% respectively to introduce a certain amount of martensite. Then, the specimens were prepared by careful mechanical polish, followed by electropolishing. After electropolishing, martensite plates could be easily distinguished by its lenticular morphology [26]. For measuring the plastic strain in the martensite pate, square-shaped grids were introduced on the surface of the polished specimens by focused ion beam (FIB) prior to further tensile deformation. **Figure 3.25 (a)** and **Figure 3.26 (a)** show the microstructure of 25% pre-strained CG specimen and 48% pre-strain UFG specimen with square-shaped grids. Then, both the CG and UFG specimens were subjected to further 20% tensile deformation, whose microstructures are shown in **Figure 3.25 (b)** and **Figure 3.26 (b)** respectively. The plastic strain along the tensile direction of martensite could be directly measured from the change of the width of the grids, as exampled in **Figure 3.25** and **Figure 3.25**. It should be noted that since the martensite plates newly formed in the further 20% deformation could not be recognized the plastic strain was measured only in the previously formed martensite plates. The measured results are summarized as a strain histogram distribution, as shown in **Figure 3.27**. Black blocks correspond to the plastic strain of martensite in the CG specimen and the red blocks correspond to the UFG specimen. As can be seen in **Figure 3.27**, the plastic strain of martensite in the UFG specimen is larger than that in the CG specimen. In the 20% deformation, the average plastic strain of martensite in the CG specimen is about 8%, while the average plastic strain of martensite in the UFG specimen is about 12%. The result of the microstructure measurement confirmed that when the grain size decreased to UFG scale, the martensite would undergo more plastic strain for the same deformation of the specimen.

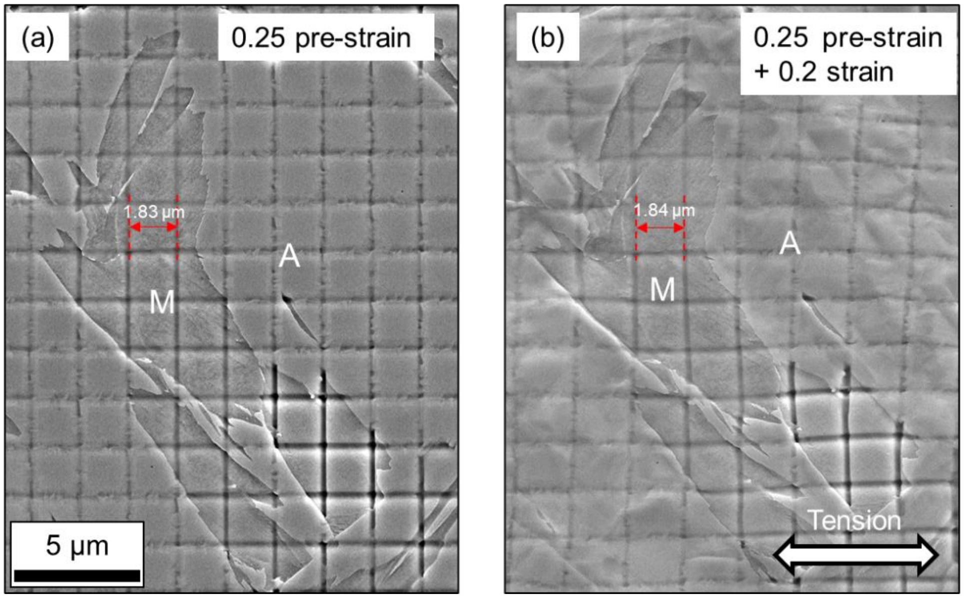

Figure 3.25 SEM images of the identical area in the CG specimen **(a)** after 0.25 pre-straining and **(b)** further 0.2 straining. Austenite and martensite is indicated by 'A' and 'M', respectively. The surface of specimen was carved with square-shaped grids by focused ion beam (FIB) after 0.25 pre-straining. Plastic strain along tensile direction in the martensite was measured according to the width changing of grids.

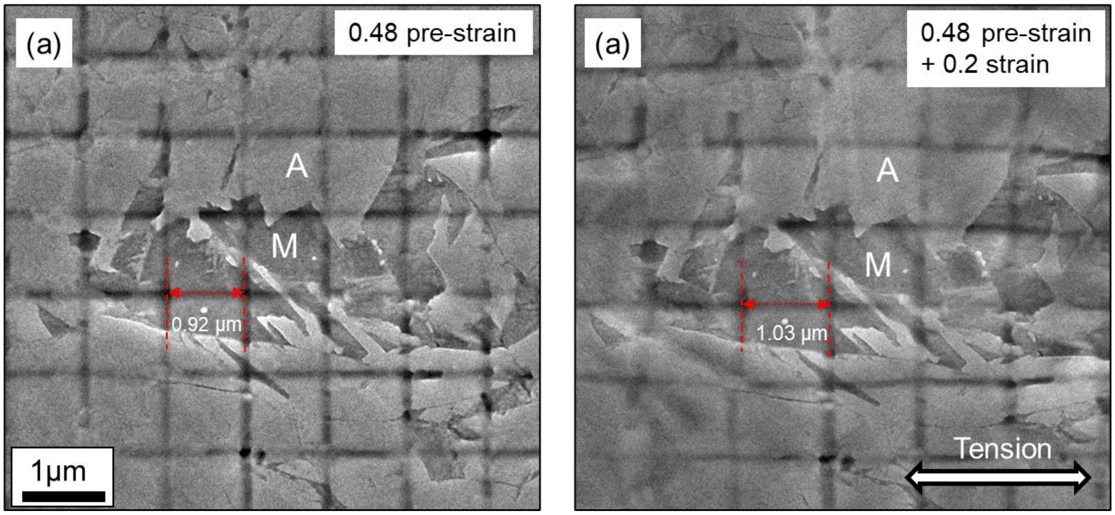

Figure 3.26 SEM images of the identical area in the UFG specimen **(a)** after 0.48 pre-straining and **(b)** further 0.2 straining. Austenite and martensite is indicated by 'A' and 'M', respectively. The surface of specimen was carved with square-shaped grids by focused ion beam (FIB) after 0.48 pre-straining. Plastic strain along tensile direction in the martensite was measured according to the width changing of grids.

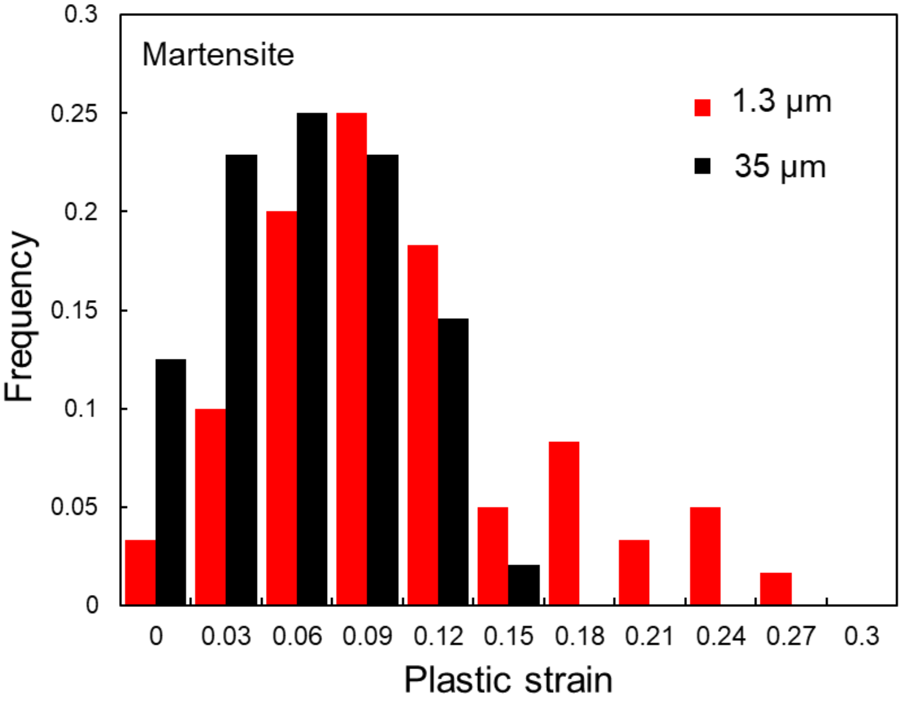

Figure 3.27 Distribution of plastic strain along tensile direction in the martensite phase of the CG and UFG specimens during 0.2 straining.

3.7 Discussion

It has been revealed in **Section 3.3.2** that the effects of grain size on the phase stress of martensite play an important role in the grain size effect on the deformation of Fe-24Ni-0.3C. In order to clarify the deformation behavior of martensite in the specimens with different mean grain size during deformation, the obtained phase stresses of austenite and martensite are plotted as a function of their corresponding true strain (estimated plastic strain + lattice strain) in **Figure 3.28**. **Figure 3.28 (a)-(c)** correspond to the CG, FG, and UFG specimens, respectively, in which the corresponding true stress-strain curves are also presented and the measurement points of neutron diffraction are indicated by black triangles. According to the deformation condition of austenite and martensite, the deformation of the Fe-24Ni-0.3C specimens could be divided into three stages, as indicated in the horizontal axes in **Figure 3.28**: (1) deformation of austenite single-phase; (2) the deformation induced martensite forms and only elastically deforms while austenite continuously plastically deforms (elastoplastic region); (3) both martensite and austenite plastically deform. The corresponding strain regions of the different specimens are listed in **Table 3.3**. The deformation behavior of martensite in the specimen naturally depends on its strength. In order to facilitate the comparison of deformation of martensite at stage III, the stress-strain response of martensite during the deformation of the specimens with different mean grain size is summarized in **Figure 3.29**. It can be observed that with decreasing the mean grain size of austenite the yield strength and flow stress of martensite significantly increased. It has been reported that the prior austenite grain size has a strong effect on the size of the quenched martensite, consequently affecting the strength of the martensite [27,28]. **Figure 3.30** shows the mean grain size of martensite crystals formed in the specimens with different austenite grain sizes, which was measured by EBSD observation. It can be seen that with decreasing the mean grain size of austenite the size of the martensite almost linearly decreased. Therefore, the increase of yield strength and flow stress of martensite might be attributed to the grain refinement of the martensite phase.

Table 3.3 True strain region of different strain stage in the specimens with different mean grain sizes

Grain size	Stage I	Stage II	Stage III
35 μm	0-0.17	0.17-0.35	0.35-0.6
4 μm	0-0.23	0.23-0.48	0.48-0.64
1.3 μm	0-0.27	0.27-0.42	0.42-0.71

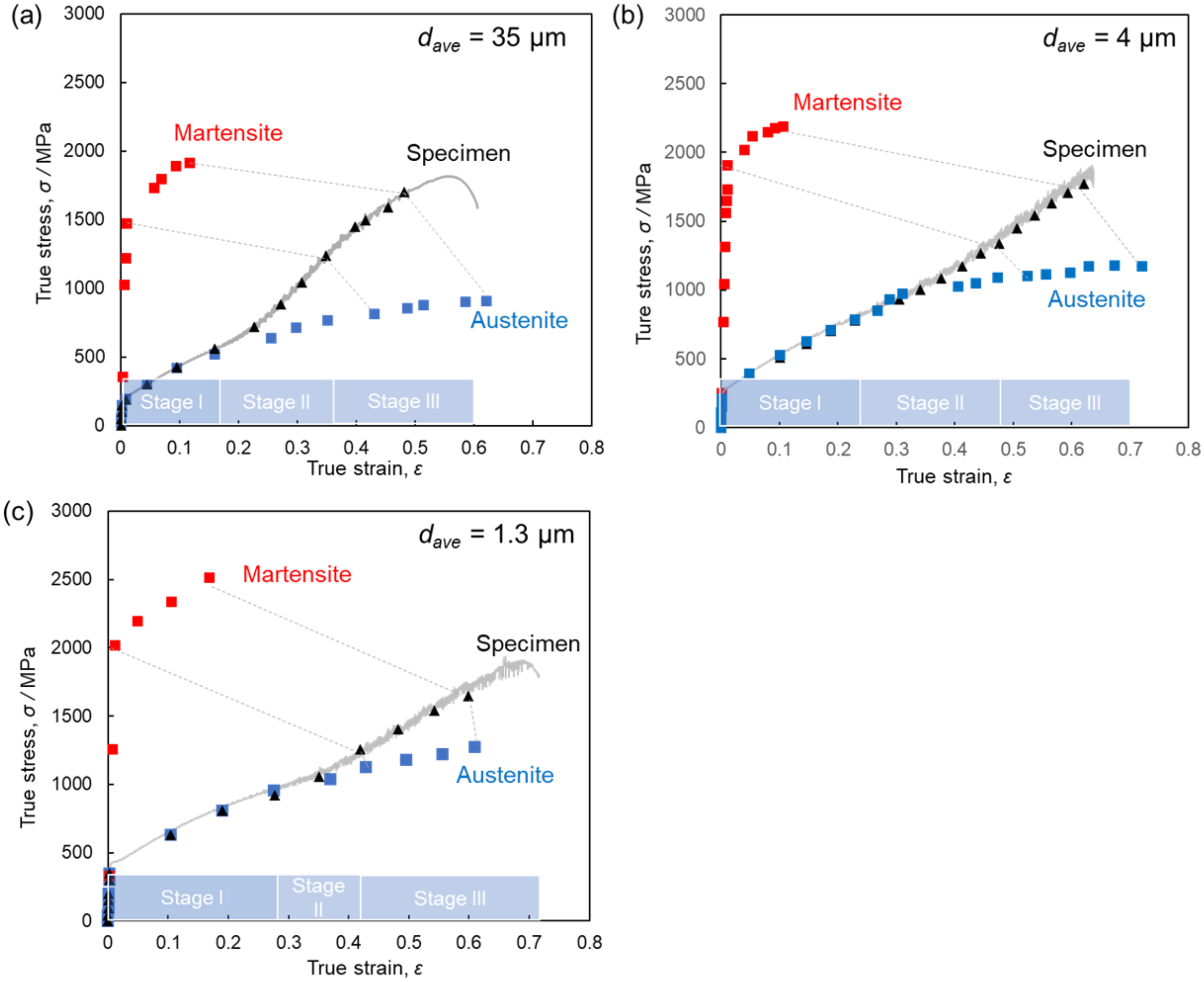

Figure 3.28 Stress-strain response of austenite phase and martensite phase during the deformation of the specimens with mean grain size of (a) 35 μm, (b) 4 μm and (c) 1.3 μm. The corresponding true stress-strain curves are also presented and the measurement points of neutron diffraction are indicated by black triangles. The deformation of the Fe-24Ni-0.3C specimens could be divided into three stages according to the deformation condition of austenite and martensite, as indicated above horizontal axis.

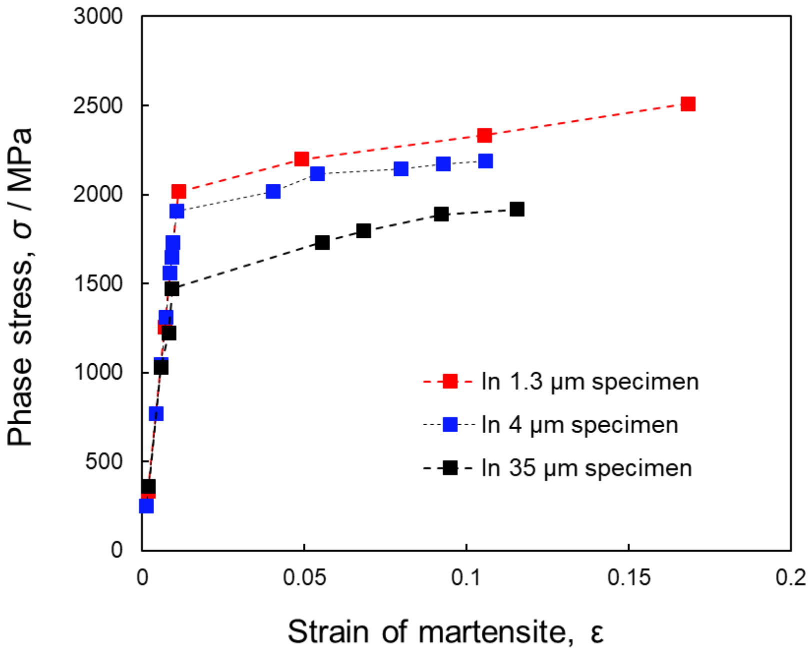

Figure 3.29 Stress-strain response of martensite during the deformation of the specimen with different mean grain sizes.

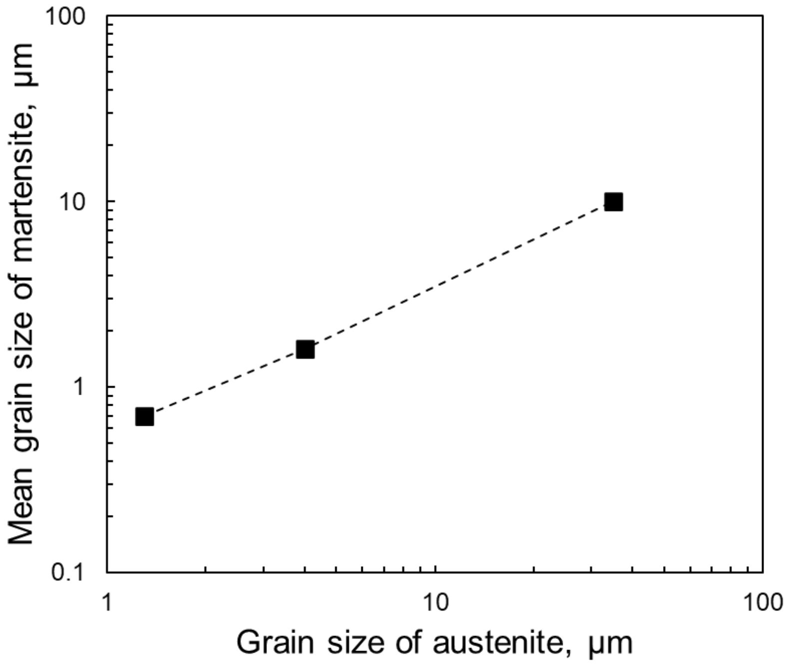

Figure 3.30 Change of mean grain size of martensite plate as a function of prior austenite grain size, measured by EBSD observation.

However, the evolution of the phase stress or the deformation of martensite depends on the interaction between the two phases caused by their plastic strain incompatibility. As shown in **Figure 3.15 (b)**, the difference in the evolution of phase stress of martensite is relatively small between the CG and FG specimens. Therefore, as the yield strength of martensite increased as the grain size reduced from the CG to the FG, correspondingly the elastoplastic region of the deformation of the FG specimen extended. For the FG specimen, the elastoplastic region is from true strain of 0.23 to 0.48, while from true strain of 0.17 to 0.35 for the CG specimen. The interesting thing is that when the grain size reduced to UFG scale, the evolution of phase stress of martensite significantly accelerated, as shown in **Figure 3.15 (b)**. As a result, the martensite in the UFG specimen soon yielded after formation. It has been reported, however in FCC single-phase metals, that the interactions between differently oriented grains caused by the intergranular incompatibilities increases as the size of the grain decrease [21,29,30]. It is possibility because that, for fine grain size, a higher density of geometrically necessary dislocations is required for accommodating the intergranular incompatibility which increases the intergranular stress [31]. Although it is not fully clarified, we can speculate that the grain size refinement could also reinforce the interaction between austenite and martensite caused by the phase-to-phase strain incompatibilities. On the other hand, as demonstrated in **Section 3.6**, the plastic deformation in the UFG specimen is more homogeneous than that in the FG and CG specimens, which implies that for the same deformation of the specimen the martensite in the UFG specimen is more plastic deformed. We think it is another evidence proving that the interaction between two phases caused by plastic strain incompatibility increased in the UFG microstructure.

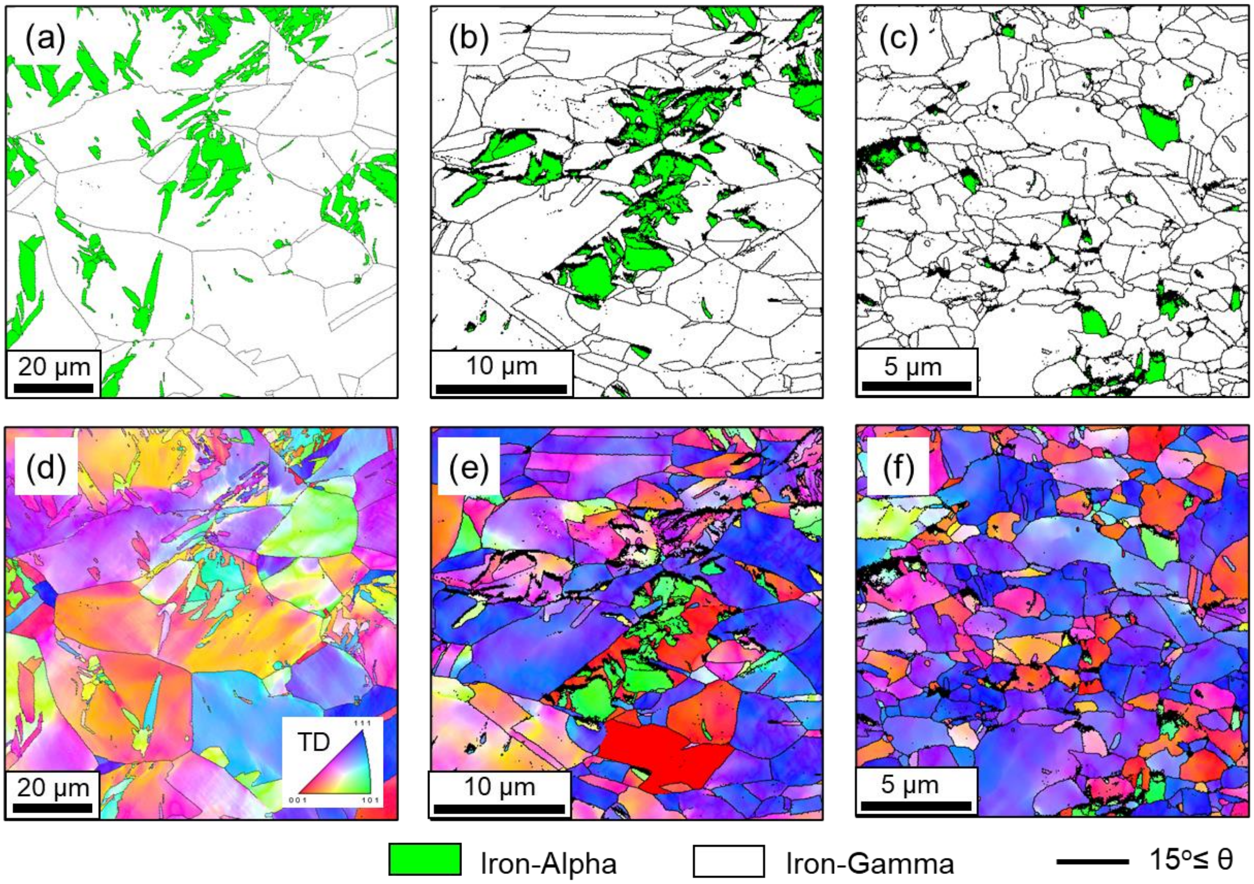

Figure 3.31 Microstructures of the specimens with different mean grain sizes at stage II of deformation. (a), (d) microstructure of the CG specimen at strain of 0.22; (b), (e) microstructure of the FG specimen at strain of 0.35; (c), (f) microstructure of the UFG specimen at strain of 0.35. Since data points whose CI value is lower than 0.1 have been removed, some area in the martensite having low CI value is black.

Besides the interaction between the two phases, as discussed in **Chapter 2**, the dynamic formation of martensite at the interphase boundaries would release the internal stress of previously formed martensite, consequently slowing the increasing rate of phase stress of martensite. Therefore, we think the high increasing rate of phase stress of martensite in the UFG specimen might be also related to its deformation microstructure. **Figure 3.31 (a)-(c)** shows the typical microstructure of the specimens with different grain sizes at stage II of deformation observed by EBSD measurement. The true strain of the CG specimen in **Figure 3.31 (a)** is 0.22, and the true strain of the FG specimen in **Figure 3.31 (b)** and the UFG specimen in **Figure 3.31 (c)** is 0.35. Both three specimens have about 10 vol.% deformation induced martensite. **Figure 3.31 (c)-(e)** is the IPF images corresponding to the microstructure shown in **(a)-(c)**. It can be found that in the CG and FG specimen the deformation induced martensitic transformation tends to form martensite variant clusters in which different martensite variants are adjacent to each other. It is mainly because the interphase boundaries usually have high internal stress which is in favor of the formation of martensite. However, in the UFG specimen, the deformation induced martensite exhibited more homogeneous and isolated distribution. The number of martensite variants within one austenite grain in the UFG specimen obviously smaller than that in the FG and CG specimen. It has been reported by Takaki et.al that in Fe-Ni-Cr alloy when the grain size of austenite is reduced to 0.8 μm the morphology of quenched martensite changes from stratified structure with multi variants to a simplified structure composed of a single variant [7,8]. The result shown in **Figure 3.31** implies that a similar varying tendency may also exist in the deformation induced martensitic transformation. We think that when the formation of martensite is in a form of relatively discrete distribution, the internal stress in previously formed martensite plates would be less released by the formation of new martensite plates, compared with the formation of martensite in a form of variants cluster. Therefore, the increase of phase stress of the martensite with discrete distribution in the UFG specimen is much faster.

It has been revealed at **Section 3.5** that at the later stage (corresponding to stage III) of deformation the larger increment of phase stress of martensite in the UFG specimen contributed to the increase of strain hardening for postponing the occurrence of plastic instability, even though the volume fraction of martensite in the UFG specimen was relatively low. As shown in **Figure 3.29**, the plastic flow of martensite corresponds to the deformation of martensite at stage III of deformation. It can be found that the strain hardening capability of martensite was almost unchanged as grain refinement. Therefore, we think that the larger increment of phase stress of the martensite in the UFG specimen at stage III of deformation was mainly attributed to its larger plastic strain.

In conclusion, when the grain size is reduced to UFG scale, the interaction between two phases caused by plastic strain incompatibility would significantly increase. As a result, the increasing rate of phase stress of martensite is increased and the plastic deformation between two phases becomes more homogeneous in the UFG specimen, which contributes to the increase of strain hardening rate of the specimen.

3.8 Conclusion

In Chapter 3, the deformation behavior of Fe-24Ni-0.3C specimens with mean grain sizes of 4 μm and 1.3 μm was studied by utilizing in-situ neutron diffraction and compared with the specimen with a mean grain size of 35 μm. The specimens with mean grain sizes of 35 μm, 4 μm and 1.3 μm represent CG, FG and UFG specimens, respectively. The tensile tests revealed that all three specimens had an enhanced strain hardening during the deformation which is accompanied by the formation of deformation induced martensite. With decreasing the mean grain size, the increment of strain hardening rate of the specimen caused by the martensitic transformation decreased. At the same time, the measurement of volume fraction of the martensite by in-situ neutron diffraction revealed that the grain refinement decelerated the formation of the martensite. The kinetic of deformation induced martensitic transformation has a strong influence on the strain hardening behavior of Fe-24Ni-0.3C alloy. However, we think that the grain size effect on the deformation behavior of Fe-24Ni-0.3C could not be fully interpreted only by the grain size dependence of the kinetics of the deformation induced martensitic transformation. Because the evolution of phase stress of martensite also has a significant contribution to the strain hardening of the specimen. Therefore, the present study also studied the effect of grain size on the deformation behavior of Fe-24Ni-0.3C alloy from the viewpoints of stress partitioning and strain partitioning between austenite phase and martensite phase. The main conclusions are summarized as follows:

(1) With decreasing the mean grain size of austenite, the mean grain size of martensite decreases as well. Consequently, the intrinsic strength of the martensite phase increases due to the grain refinement strengthening. However, since the strength of austenite increases at the same time, the effect of grain refinement on the maximum stress partitioning between austenite and martensite that can be reached during

deformation is limited. Only when the grain size decreased to the UFG scale, the stress partitioning between two phases had a considerable increase.

(2) When the grain size changed within the coarse-grained region the influence of the grain size on the evolution of phase stress in martensite was relatively small, thus the strain hardening behavior of the 24Ni-0.3C metastable austenitic steel having mean grain size at CG region was mainly determined by the increasing rate of the martensite volume fraction. However, when the grain size was decreased down to the UFG region, the evolution of phase stress of martensite significantly increased, which contributed to the increase of the strain hardening rate of the specimen.

(3) The strain partitioning between austenite and martensite in the specimens with different mean grain sizes revealed that the plastic deformation between austenite and martensite in the UFG specimen is more homogeneous than that in the FG and CG specimens. That is, for the same deformation of the specimen, the martensite in the UFG specimen underwent more plastic strain.

(4) In the elastoplastic region (stage II) of deformation, the increasing rate of phase stress of martensite in the UFG specimen was significantly larger than that in the FG and CG specimens. Thus, the martensite in the UFG specimen soon plastically yielded after formation. There are two possible reasons. On the one hand, the interaction between the two phases caused by the strain incompatibility strengthened in the UFG scale. On the other hand, since the number of martensite variants within one austenite grain decreased in the UFG specimen, for the martensite phase the stress release effect caused by the formation of new martensite crystals was weakened.

(5) In stage III of deformation, due to the martensite in the UFG specimen underwent more plastic strain, the increment of phase stress of martensite caused by its strain hardening in the UFG specimen was larger than the other two specimens. As a result, the increment of stress partitioning at stage III in the UFG specimen was increased which could contribute to maintain the strain hardening rate of the specimen at later stage of deformation.

In conclusion, the results in this chapter reveal that the interaction between austenite and martensite caused by the strain incompatibility in the UFG specimen might increase, which could accelerate the stress partitioning between the two phases and make the plastic deformation between the two phases more homogeneous. As a consequence, the increment of strain hardening by formation the same amount of martensite is higher in the UFG specimen.

Reference

1. Tamura, I. Deformation-induced martensitic transformation and transformation-induced plasticity in steels. *Met. Sci.* **16**, 245–253 (1982).
2. Maxwell, P. C., Goldberg, A. & Shyne, J. C. Stress-Assisted and strain-induced martensites in FE-NI-C alloys. *Metall. Trans.* **5**, 1305–1318 (1974).
3. Huang, G., Matlock, D. & Krauss, G. Martensite formation, strain rate sensitivity, and deformation behavior of type 304 stainless steel sheet. *Metall. Mater. Trans. A* **20**, 1239–1246 (1989).
4. Peterson, S. F., Mataya, M. C. & Matlock, D. K. The formability of austenitic stainless steels. *Jom* **49**, 54–58 (1997).
5. Kim, S. J., Lee, C. G., Lee, T. H. & Oh, C. S. Effect of Cu, Cr and Ni on mechanical properties of 0.15 wt.% C TRIP-aided cold rolled steels. *Scr. Mater.* **48**, 539–544 (2003).
6. Chiang, J., Lawrence, B., Boyd, J. D. & Pilkey, A. K. Effect of microstructure on retained austenite stability and work hardening of TRIP steels. *Mater. Sci. Eng. A* **528**, 4516–4521 (2011).
7. Takaki, S., Fukunaga, K., Syarif, J. & Tsuchiyama, T. Effect of Grain Refinement on Thermal Stability of Metastable Austenitic Steel. *Mater. Trans.* **45**, 2245–2251 (2004).
8. Matsuoka, Y., Iwasaki, T., Nakada, N., Tsuchiyama, T. & Takaki, S. Effect of grain size on thermal and mechanical stability of austenite in metastable austenitic stainless steel. *ISIJ Int.* **53**, 1224–1230 (2013).
9. Brofman, P. J. & Ansell, G. S. ON THE EFFECT OF FINE GRAIN SIZE ON THE Ms

TEMPERATURE IN Fe-27Ni-0. 025C ALLOYS. *Metall. Trans. A, Phys. Metall. Mater. Sci.* **14 A**, 1929–1931 (1983).

10. Nichol, T. J., Judd, G. & Ansell, G. S. The relationship between austenite strength and the transformation to martensite in Fe-10 pct Ni-0.6 pct C alloys. *Metall. Trans. A* **8**, 1877–1883 (1977).

11. Wang, H. *et al.* Effect of martensitic phase transformation on the behavior of 304 austenitic stainless steel under tension. *Mater. Sci. Eng. A* **649**, 174–183 (2016).

12. Tsuchida, N. *et al.* Effects of temperature and strain rate on trip effect in SUS301L metastable austenitic stainless steel. *ISIJ Int.* **53**, 1881–1887 (2013).

13. Järvenpää, A., Jaskari, M., Kisko, A. & Karjalainen, P. Processing and properties of reversion-treated austenitic stainless steels. *Metals (Basel).* **10**, (2020).

14. Naghizadeh, M. & Mirzadeh, H. Effects of Grain Size on Mechanical Properties and Work-Hardening Behavior of AISI 304 Austenitic Stainless Steel. *Steel Res. Int.* **90**, 1–9 (2019).

15. Jang, J. M., Kim, S. J., Kang, N. H., Cho, K. M. & Suh, D. W. Effects of annealing conditions on microstructure and mechanical properties of low carbon, manganese transformation-induced plasticity steel. *Met. Mater. Int.* **15**, 909–916 (2009).

16. Cai, M. H. *et al.* Dependence of deformation behavior on grain size and strain rate in an ultrahigh strength-ductile Mn-based TRIP alloy. *Mater. Sci. Eng. A* **653**, 35–42 (2016).

17. Tsuji, N., Ito, Y., Saito, Y. & Minamino, Y. Strength and ductility of ultrafine grained aluminum and iron produced by ARB and annealing. *Scr. Mater.* **47**, 893–899 (2002).

18. An, X. H. *et al.* Enhanced strength-ductility synergy in nanostructured Cu and Cu-Al alloys processed by high-pressure torsion and subsequent annealing. *Scr. Mater.* **66**, 227–230 (2012).

19. Gao, S., Chen, M., Joshi, M., Shibata, A. & Tsuji, N. Yielding behavior and its effect on uniform elongation in if steel with various grain sizes. *J. Mater. Sci.* **49**, 6536–6542 (2014).

20. Harjo, S., Abe, J., Aizawa, K., Gong, W. & Iwahashi, T. Deformation Behavior of An Austenitic Steel by Neutron Diffraction. **014017**, 1–6 (2014).

21. Feaugas, X. & Haddou, H. Grain-size effects on tensile behavior of nickel and AlSl 316L stainless steel. *Metall. Mater. Trans. A Phys. Metall. Mater. Sci.* **34 A**, 2329–2340 (2003).
22. Chokshi, A. H., Rosen, A., Karch, J. & Gleiter, H. On the validity of the Hall-Petch relastionship in nanocrystalline materials. *Scr. Metall.* **23**, 1679 (1989).
23. Ono, K. Strain-Hardening equations and uniform strain. *Metall. Trans.* **3**, 749–751 (1972).
24. Takaki, S., Masumura, T. & Tsuchiyama, T. Proposal of simplified modified Williamson-Hall equation. *ISIJ Int.* **58**, 2354–2356 (2018).
25. Hariharan, K. & Barlat, F. Modified Kocks–Mecking–Estrin Model to Account Nonlinear Strain Hardening. *Metall. Mater. Trans. A Phys. Metall. Mater. Sci.* **50**, 513–517 (2019).
26. Maki, T., Shimooka, S., Umemoto, M. & Tamura, I. The Morphology of Strain-Induced Martensite Martensite in Fe-Ni-C and Thermally Alloys. *Trans. Japan Inst. Met.* **13**, 400 (1972).
27. Morito, S., Yoshida, H., Maki, T. & Huang, X. Effect of block size on the strength of lath martensite in low carbon steels. *Mater. Sci. Eng. A* **438–440**, 237–240 (2006).
28. Morito, S., Saito, H., Maki, T. & Furuhara, T. Effect of PAGS on crystallography and morphology of lath martensite in low carbon steels. *ISIJ Int.* **45**, 91–94 (2004).
29. Feaugas, X. & Haddou, H. Effects of grain size on dislocation organization and internal stresses developed under tensile loading in fcc metals. *Philos. Mag.* **87**, 989–1018 (2007).
30. Haddou, H., Risbet, M., Marichal, G. & Feaugas, X. The effects of grain size on the cyclic deformation behaviour of polycrystalline nickel. *Mater. Sci. Eng. A* **379**, 102–111 (2004).
31. Meyersm, M. A. & Ashworth, E. A model for the effect of grain size on the yield stress of metals. *Philos. Mag. A Phys. Condens. Matter, Struct. Defects Mech. Prop.* **46**, 737–759 (1982).

Chapter 4. Influence factors for the kinetics of isothermal martensitic transformation in metastable austenite

4.1 Introduction

Numerous studies as well as our study have shown that the kinetics of deformation induced martensitic transformation plays an important role in the deformation of TRIP steels [1,2,3]. As demonstrated in Chapter 2 and Chapter 3, the increase of strain hardening rate of specimen caused by the TRIP effect greatly depends on the formation rate of martensite. For increasing the uniform deformation capability of material by TRIP effect, the formation of the martensite should be initiated at the later stage of deformation (just before the onset of necking) and at an appropriate transformation rate. An appropriate transformation rate of martensite is a rate that can keep the strain hardening just larger than the true stress to prevent the onset of plastic stability. An excessive transformation rate would deplete the TRIP effect over a short strain range and subsequently lead to the failure of the material, although it would cause a sharp strain hardening. However, a too low transformation rate of martensite could not provide enough strain hardening to prevent plastic instability. Therefore, in order to fully utilize the TRIP effect, it is necessary to deepen our understanding of the kinetics of martensitic transformation.

Figure 4.1 (a) shows a schematic for the changes of free energy of austenite and martensite as a function of temperature. As introduced in **Chapter 1**, it is generally believed that, when the chemical free energy difference between austenite and martensite reaches the critical value in cooling (at M_s temperature), the martensitic transformation will initiate spontaneously. The critical value of the chemical free energy difference at M_s temperature is regarded as the critical driving force for initiating the martensitic transformation. However, according to some simulation work [4,5], the free energy of the system (material) from FCC to BCC structure should firstly increase, then decrease after overcoming the energy barrier (that is, activation energy), as illustrated in **Figure 4.1 (b)**. In the general consideration for martensitic transformation, the critical driving force is just the free energy difference before and after the transformation at Ms temperature, while the energy barrier (activation energy) for nucleation has never been discussed in detail. However, the activation energy which determines the transformation rate of martensite has more practical significance. In most cases, the martensitic transformations in Fe-C alloys and Fe-Ni-C alloys have extremely high nucleation rate and growth rate [6–8]. Those martensitic transformations are only developed by decreasing temperature, and once the cooling is stopped the transformation would stop immediately. Those kinds of martensitic transformations are termed as athermal martensitic transformation. The characteristics of athermal martensitic transformation have been taken to imply that the nucleation processes take place without thermal activation [9], that is, the activation energy is zero. However, it is difficult to be convinced in physics that the nucleation process has no energy barrier. Maybe it is just because the energy barrier for athermal martensitic transformation is too low to be measured by current measurement techniques. On the other hand, some martensitic transformations in Fe-Ni-Mn alloys [10,11] and Fe-Ni-Cr alloys [12,13] have time-dependent nucleation, which is called isothermal martensitic transformation. The isothermal martensitic transformation occurs after a certain incubation time during isothermal holding and develops with increasing the holding time, which implies that the nucleation processes of the martensite need thermal activation and there is an energy barrier for the nucleation. According to the research performed by Kakeshita et.al [14], the kinetics of martensitic transformation in one material could be changed between athermal one and isothermal one by change the external conditions. It means that the two kinds of martensitic transformation might have the same nucleation mechanism. The difference between the athermal and isothermal martensitic transformation might be only the magnitude of the activation energy.

The martensitic transformation can be taken as a kind of plastic deformation mechanism for materials. The nucleation processes of martensite might be able to be understood in our ‘PLASTON’ concept [15]. When stress is applied to a material, a deformation mode needs to be activated, which leads to plastic deformation for relaxing the stress. At a region with high local stress or high energy (like grain boundary), a group of atoms would be activated thermally and mechanically, and form a defective zone. After overcoming the energy barrier, the propagation of the defective zone results in a plastic strain, which may leave a particular defect, such as a stacking fault, deformation twinning, or martensite. Such a localized defective zone of excited atomic structure at the plastic deformation front is termed as 'PLASTON'. Therefore, we think the nucleation of martensite is the process that a group of atoms with defective lattice overcomes the energy barrier with thermal activation. The transformation kinetics of martensite is determined by the magnitude of activation energy for its nucleation.

Since the nucleation rate of athermal martensitic transformation is too fast, the isothermal martensitic transformation is the only choice for studying the kinetics of martensitic transformation experimentally. In this study, we aim to investigate the effect of tensile stress, plastic strain and grain size on the kinetics of the isothermal martensitic transformation from the viewpoint of 'PLASTON'.

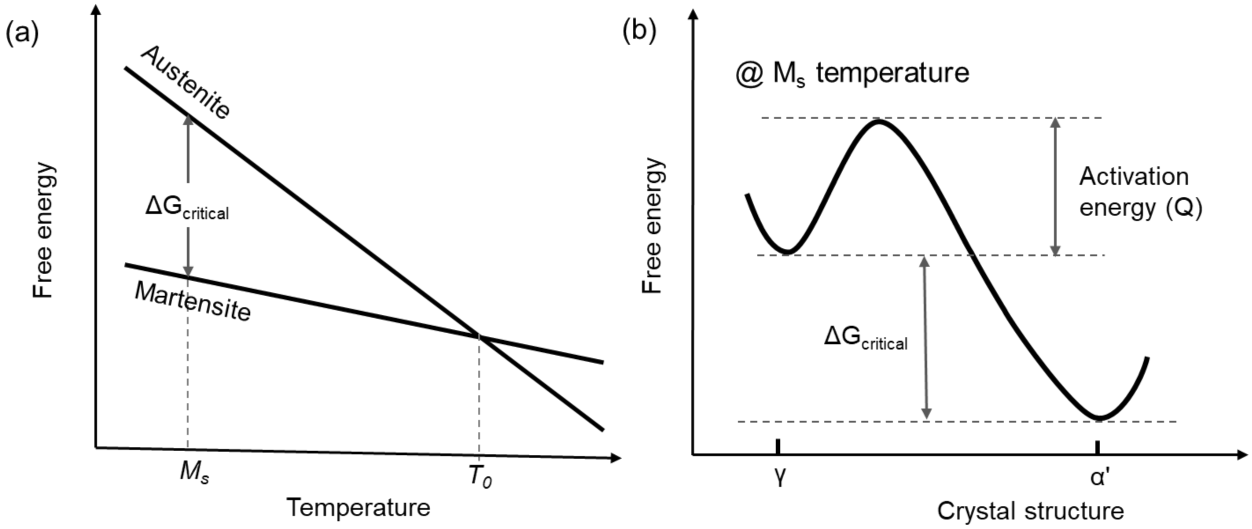

Figure 4.1 (a) Changes of free energy for austenite and martensite as function of temperature. The temperature where the chemical free energy of austenite and martensite equals to each other is indicated by T_0. M_s is the starting temperature for spontaneous martensitic transformation. **(b)** Illustration for the free energy change from austenite to martensite at M_s temperature.

4.2 Material and experimental methods

A Fe-23Ni-3.55Mn (wt.%) alloy was used in the present study and its chemical composition is shown in **Table 4.1**. The specimens were fabricated by cold rolling and subsequent annealing, as illustrated in **Figure 4.2**. Firstly, a block having dimensions of 30 mm (length) × 25 mm (width) × 20 mm (thickness) was cut from the as-received hot-rolled plate by a wire cutting machine. Then, the material was cold-rolled by 50% to reduce the thickness to 10 mm and homogenized at 1100 °C for 24 hours. The cold-rolling prior to homogenization could decrease the space between the segregation bands to promote the efficiency of homogenization. Afterward, the homogenized material was again cold-rolled by 90% to reduce the thickness to 1 mm and subsequently annealed at 800 °C for 1 hour.

Table 4.1 Chemical composition of Fe-23Ni-3.55Mn (wt.%) alloy.

Ni	**Mn**	Al	O	N	Fe
23.03	**3.55**	<0.001	0.004	0.001	Bal.

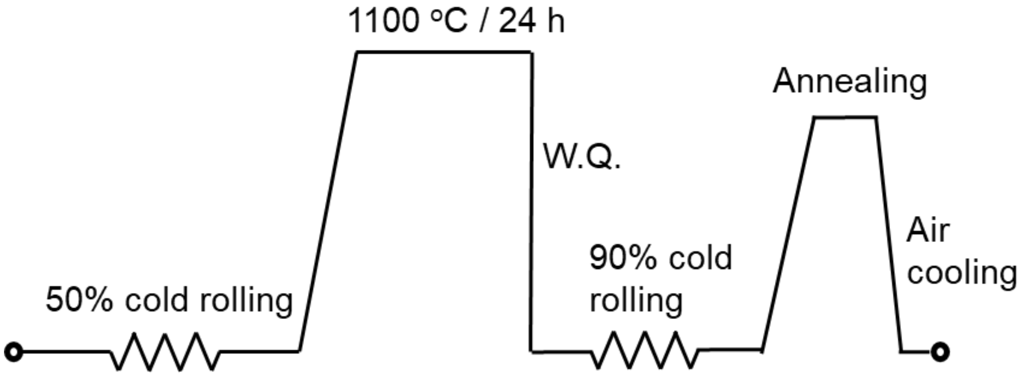

Figure 4.2 Schematic illustration of the fabrication process.

Transformation kinetics of isothermal martensitic transformation in the Fe-23Ni-3.55Mn specimen was investigated at several temperatures between -50 °C and -196 °C. Ethanol was used in the low temperature bath cooled by liquid nitrogen. The bath temperature was maintained within ± 1 °C. The specimens were isothermally held at the given temperatures for different periods of holding time from tens of seconds to 10,000 seconds. After the low temperature treatment, the specimens were quickly water quenched to room temperature. Microstructures of the fabricated specimens were observed by using field emission scanning electron microscopy (FE-SEM) equipped with backscattered electron (BSE) and electron backscattering diffraction (EBSD) detectors. Both SEM-BSE and SEM-EBSD was operated at 15 kV with a working distance of 15 mm. The obtained EBSD data was analyzed by the TSL OIM Analysis software (ver. 7) in which the data points having confidence index (CI) value lower than 0.1 were removed. The specimens for the microstructure observation were prepared by careful mechanical, followed by electropolishing in an electrolyte (90 vol.% ethanol + 10 vol.% perchloric acid) at room temperature for 2 min with a voltage of 20 V. The volume fraction of martensite was measured by metallographic observation using an optical microscope. In order to distinguish austenite and martensite in metallographic observation, the polished specimens were etched by a tint etchant (composed of 10 g $Na_2S_2O_5$ + 100 ml H_2O). For each specimen more than twenty microstructure images (490 μm × 490 μm) were taken to obtain the statistic average for the volume fraction of martensite. In order to investigate the effect of tensile stress on the transformation kinetics of isothermal martensite, a tensile test machine was combined with the low temperature bath through specially designed jigs, as illustrated in Figure 4.3. The specimen for the tensile test has dimensions of 10 mm (length) × 2.5 mm (width) × 1 mm (thickness) in the gauge part, and its length is parallel to the rolling direction. Since the elongation cannot be precisely measured when the specimen tensile deforms within the low temperature bath, the nominal strain is estimated form the displacement of cross-head in the present study.

rolling.

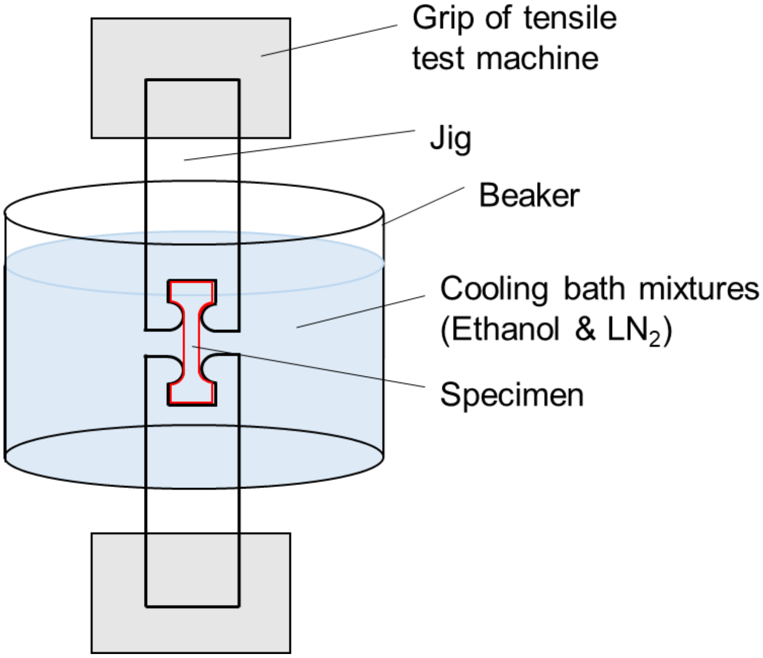

Figure 4.3 Illustration of low temperature tensile test.

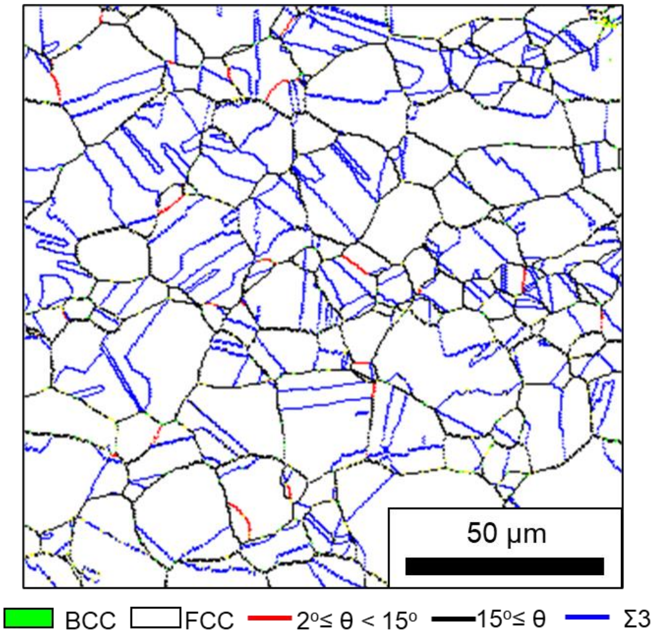

Figure 4.4 Phase and grain boundary map of the specimen annealed at 800 ^{o}C for 3600 s after the cold rolling.

4.3 Results & Discussion

4.3.1 Kinetics of the isothermal martensitic transformation and the estimation of activation energy

Figure 4.4 shows the microstructure of the annealed specimen observed by EBSD. It can be seen that the specimen has a fully austenitic structure composed of equiaxed austenite grains well defined by high-angle grain boundaries. The mean grain size of the specimen measured by the interception method was 7 μm including twin boundaries. After isothermal subzero treatment, part of austenite transforms to martensite. **Figure 4.5** shows an example of the microstructure after the isothermal martensitic transformation. By immersing the specimen into the tint etchant, martensite phase was darkly colored while austenite phase shows bright color. The metallograph reveals that the martensite formed in Fe-23Ni-3.55Mn is typical lath-type α' martensite in the form of single isolated laths or adjacent laths in a packet, which is usually observed in the Fe-Ni-Mn alloy [16]. According to the color difference between austenite and martensite, the volume fraction of martensite can be easily measured by using graphic software. **Figure 4.6** shows the isothermal martensitic transformation in the Fe-23Ni-3.55Mn specimen with a mean grain size of 7 μm at different temperatures, without external stress. It can be seen that the martensitic transformation in Fe-23Ni-3.55Mn alloy only exhibited isothermal kinetics, which initiated after a certain incubation period and developed with increasing the isothermal holding time. Actually, at each temperature, there is an apparent incubation period for the isothermal martensitic transformation in which no martensite forms. It has been clearly proved in the research of M. Cohen for a Fe-Ni-Mn alloy [10,11]. However, in the present study, since the change of the amount of martensite was not in-situ monitored during the isothermal holding, the time required to form 1 % martensite was taken as an alternate for incubation time. It can be observed that the transformation rate was a maximum and the incubation was a minimum at -110 ^{o}C in the present study. Both at higher and lower temperatures, the transformation rate decreased and the incubation period increased. **Figure 4.7** shows the temperature-time-transformation (TTT) curve for 1% transition, in which the curve between -110 ^{o}C and -196 ^{o}C is drawn by a dashed line due to lack of data.

It shows a C-shape with a nose temperature near -110 ^{o}C which is similar to the results in other isothermal martensitic transformations [11,17].

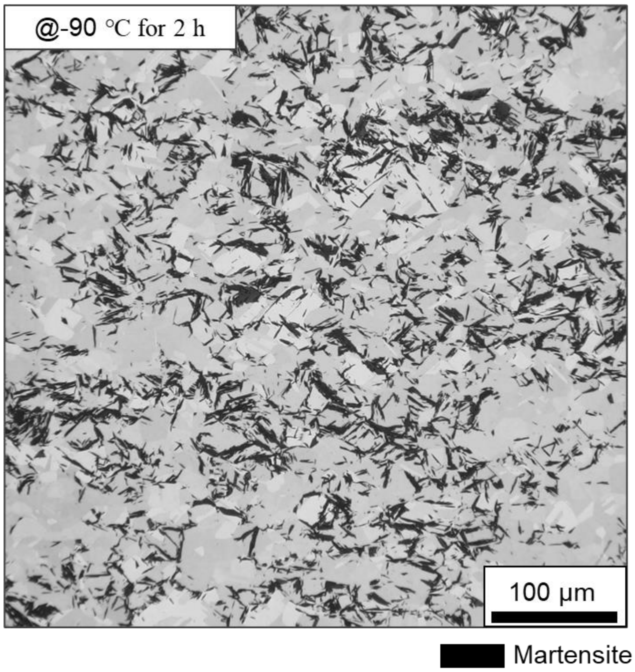

Figure 4.5 Optical metallograph of the specimen after isothermal subzero treatment at -90 ^{o}C for 2 hours. The specimen was etched by 9.1 wt.% $Na_2S_2O_5$ solution after electropolishing.

It is well known that the growth of the martensite crystal is very fast. Once the martensite nucleated, it would quickly grow up to the final shape and lose the mobility of grain boundary [18]. Therefore, the progress of martensitic transformation is mainly determined by the nucleation rate of martensite. On the other hand, the nucleation of martensite is a kind of heterogeneous nucleation [19]. Martensite tends to nucleate at defects like grain boundary, dislocations, or interphase boundaries. The overall kinetics of isothermal martensitic transformation can be expressed by a singly activated model which was proposed by M. Cohen et.al [20], in which it is assumed that the activation energies for all nucleation sites are uniform.

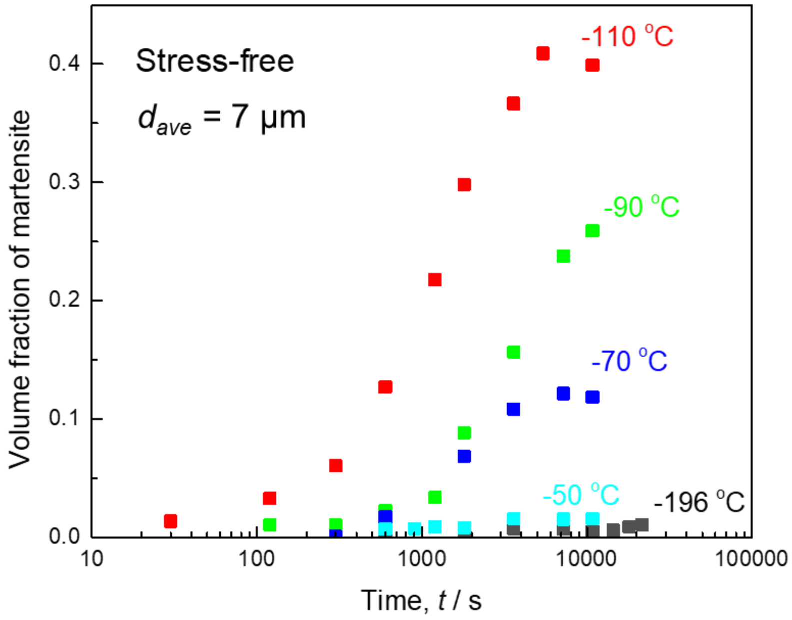

Figure 4.6 Isothermal martensitic transformation of the specimen at different temperatures.

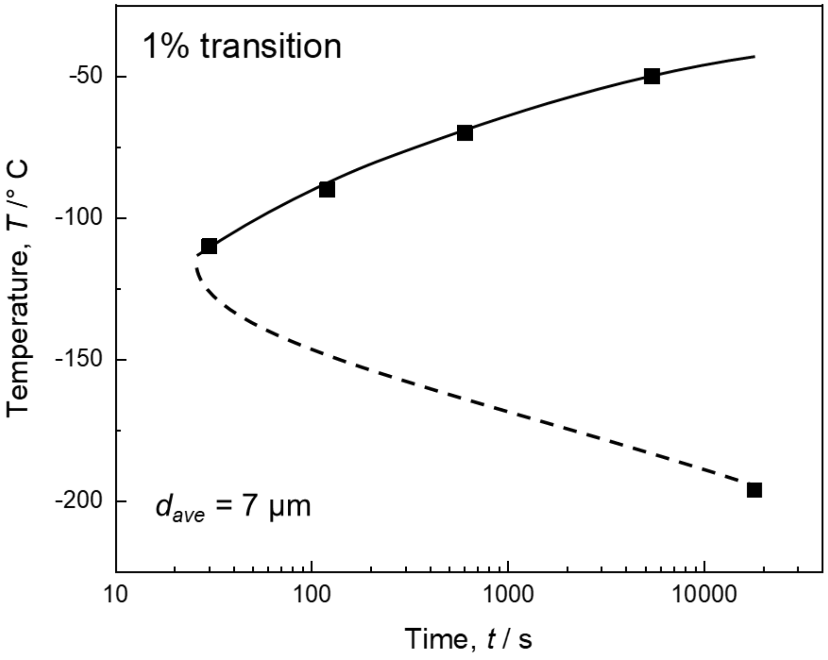

Figure 4.7 TTT diagram of the specimen with a mean grain size of 7 μm for 1 vol% transition

In the singly activated model, the nucleation rate ($\dot{N}$) of martensite at transformation time (t) is expressed by the following equation:

$$\dot{N} = n_t \nu \exp\left(\frac{-Q}{kT}\right) \qquad (4.1)$$

where n_t is the number of nucleation sites per unit volume at the transformation time (t); ν is nucleation attempt frequency; Q is activation free energy for nucleation; k is the Boltzmann's constant; T is temperature. The exact nucleation attempt frequency depends on the nucleation processes of martensite. In some previous studies, it was taken as the lattice vibration frequency (10^{13} s^{-1}) [11,17], while some researchers use the dislocation vibration frequency (10^{11} s^{-1}) since the nucleation of martensite might involve the motion of dislocations [21,22]. We think the nucleation of martensite must need to be realized by the collaborative displacement of a group of atoms. Therefore, the latter might be closer to the real situation. The nucleation attempt frequency is taken to be 10^{11} s^{-1} in the present study.

According to the quantitative metallography measurement, the nucleation rate of martensite could be presented by two measured value: f, the volume fraction of martensite; N_v, the number of martensite plates per unit volume of alloy, as following:

$$\dot{N} = \frac{1}{1-f}\frac{dN_v}{dt} \qquad (4.2)$$

where t is the transformation time. f and N_v has an interconnecting relationship, $f = \bar{V}N_v$. $\bar{V}$ is the mean volume of one martensite plate, which could be calculated by the following equation [23]:

$$\bar{V} = \frac{\pi^2 f}{8\bar{E}N_A} \qquad (4.3)$$

where $\bar{E}$ is the mean reciprocal of the plate lengths as intersected by a random section; N_A is the number of martensite per unit area. **Figure 4.8 (a)** shows the mean length of one martensite plate at different transformation progress at -110 °C, which was measured by EBSE observation. It can be seen that the mean length of one martensite plate was almost unchanged in the progress of the martensitic transformation. And the mean length of one martensite plate was also almost unchanged as the transformation temperature was changed as shown in **Figure 4.8 (b)**. It reveals that the size of the martensite plate is insensitive to the transformation progress and transformation temperature. Therefore, $\bar{V}$ was taken as a constant to be 4 × 10-^{17} m^3 in the present study.

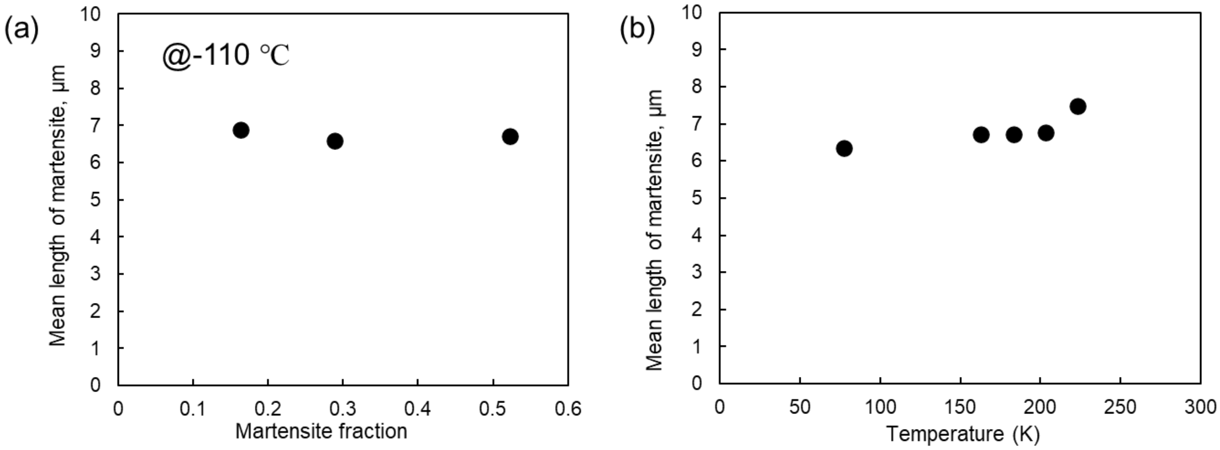

Figure 4.8 Changes of mean length of martensite plates as a function of **(a)** the volume fraction of martensite and **(b)** temperate.

Then, **Equation 4.2** could be rewritten as: $\dot{N} = \frac{1}{1-f}\frac{1}{\bar{V}}\frac{df}{dt}$ (4.4)

On the other hand, due to the autocatalysis effect of the martensitic transformation, the number of nucleation sites at the transformation time t (n_t) is expressed as:

$n_t = n_i + pf - N_V$ (4.5)

where n_i is the initial number of nucleation site per unit volume; p is the number of nucleation site generated per unit volume of martensite formed, which represents the autocatalysis effect.

If it is assumed that there is one most potent nucleation site per grain of austenite, n_i can be taken as the number of austenite grain per unit volume. For the specimen with a mean grain size of 7 µm, n_i is about 3 × 10^{15} m^{-3}.

By substituting **Equation 4.4** and **4.5** into **4.1** and reorganizing, the following equation could be obtained:

$$\frac{df}{dt} = [n_i + f\left(p - {}^{1}/_{\bar{V}}\right)](1-f)\nu\exp(\tfrac{-Q}{kT})\bar{V} \quad (4.6)$$

Then, we can perform integration of **Equation 4.6** to obtained the volume fraction of martensite as a function of time, as following:

$$f(t) = \frac{e^{\left[\left(p-{}^{1}/_{\bar{V}}+n_i\right)\nu\exp\left(\frac{-Q}{kT}\right)\bar{V}\right]t} - 1}{e^{\left[\left(p-{}^{1}/_{\bar{V}}+n_i\right)\nu\exp\left(\frac{-Q}{kT}\right)\bar{V}\right]t} - (p-{}^{1}/_{\bar{V}})/n_i} \qquad (4.7)$$

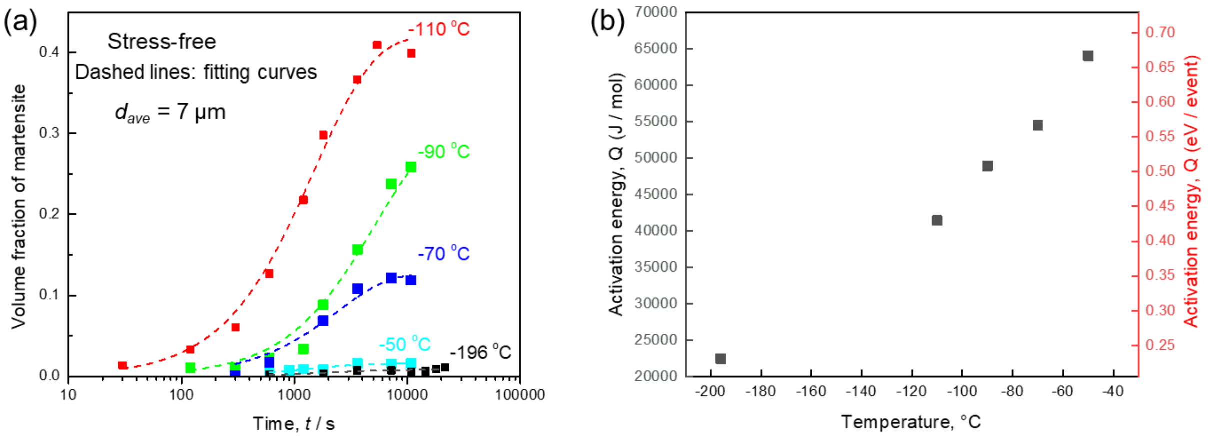

Figure 4.9 (a) Plots of martensite volume fraction vs time are fitted by the singly activated kinetical modal, indicated by dashed line; **(b)** Activation energy estimated from the results of fitting, plotted as a function of temperature.

By curve fitting to experimental $f - \mathrm{t}$ plots (in **Figure 4.6**) using **Equation 4.7**, the activation free energy, Q, could be evaluated. **Figure 4.9 (a)** shows the result of curve-fitting and the values of the activation free energy, Q, obtained from the fitting is plotted as a function of temperature in **Figure 4.9 (b)**. As can be observed in **Figure 4.9 (a)**, the kinetics of the isothermal martensitic transformation in Fe-23Ni-3.55Mn at different temperatures had a good agreement with the singly activated model. With decreasing the temperature, the activation energy for isothermal martensite transformation in Fe-23Ni-3.55Mn monotonically decreased. The activation energies obtained in the present study are compared in **Table 4.2** with previously reported research [20] in which the volume fraction of martensite was in-situ measured according to the change of the electrical resistance of the specimen. Although the chemical composition of the material is slightly different, the agreement is quite good at close temperature. It reveals that the activation energy obtained by fitting relatively fewer data plots obtained microstructure observation in the present study is also reliable.

Table 4.2 Activation energy for isothermal martensitic transformation in Fe-23Ni-3.55Mn estimated in the present study and Fe-24Ni-3Mn in the reference [20]

Fe-23Ni-3.55Mn (**present study**)		Fe-24Ni-3Mn [20]	
Temperature (°C)	Activation energy (J/mol)	Temperature (°C)	Activation energy (J/mol)
-50	6.4×10^4	-90	5.1×10^4
-70	5.6×10^4	-105	4.8×10^4
-90	5.0×10^4	-115	4.4×10^4
-110	4.2×10^4	-196	2.4×10^4
-196	2.3×10^4		

4.3.2 Effect of tensile stress on the kinetics of the isothermal martensitic transformation

In the present study, the effect of tensile stress on the kinetics of isothermal martensitic transformation in the Fe-23Ni-3.55Mn specimen was investigated at -50 ºC, -90 ºC and -196 ºC. **Figure 4.10** shows the nominal stress-strain curves of the specimen at the corresponding temperatures, and the inside table shows the yield strength of the specimen at each temperature. In order to prevent the disturbance of plastic deformation, the given tensile loads were smaller than its yield strength at the transformation temperature. **Figure 4.11 (a)-(c)** show isothermal martensitic transformation in the Fe-23Ni-3.55Mn specimen with different tensile loads at -50 ºC, -90 ºC and -196 ºC respectively. It can be seen that at each temperature the kinetics of the isothermal martensitic transformation was significantly increased by applying tensile stress. In addition, with increasing the tensile stress the final percent conversion of the martensite increased, which implies that more nucleation sites were activated by higher tensile stress.

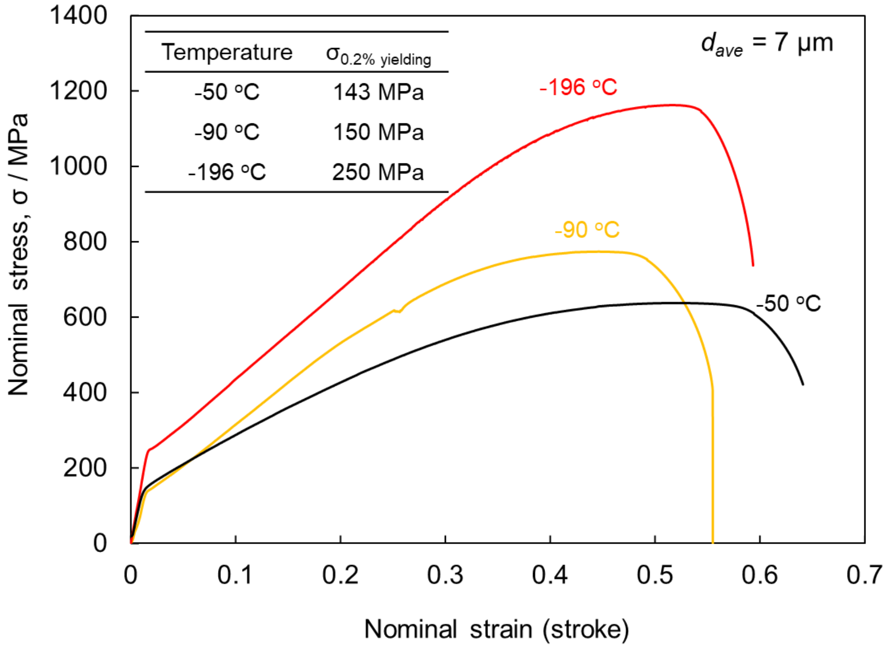

Figure 4.10 Nominal stress-strain curves of the specimen at different temperature.

By fitting plots of martensite volume fraction vs time in **Figure 4.11** (indicated by dashed curves) with **Equation 4.7**, the activation energy for the isothermal martensitic transformation under different tensile stresses was obtained. **Figure 4.12** shows the changes of the activation energy as a function of tensile stress. It reveals that the activation energy for the martensitic transformation approximately linearly decreased with increasing tensile stress. In the conventional opinion about the deformation induced martensitic transformation, above Ms temperature (below T_0) the martensitic transformation could be initiated when the external stress or deformation can provide the extra driving force to compensate the energy gape between the chemical driving force and the critical driving force for martensitic transformation, as illustrated in **Figure 4.13 (a)**. However, the results in our research reveal that the conventional consideration for deformation induced martensitic transformation might be incorrect. Although the mechanical deformation might increase the free energy difference between austenite and martensite, whether the transformation can be observed or not is determined by the magnitude of the activation energy. The effect of stress on the isothermal martensitic transformation at -196 ^{o}C provides a good example, in **Figure 4.11 (c)**. Obviously, the chemical free energy difference between austenite and martensite was larger than the crucial driving force at -196 ^{o}C. However, in the case without tensile stress, the kinetics of the isothermal martensitic transformation was extremely low, having an incubation time (of 1% transition) larger than 10000 s. By applying 200 MPa tensile stress, the kinetics of the isothermal martensitic transformation was greatly enhanced and its incubation time decreased down to 60 s. Whether the martensitic transformation can be observed or not after isothermal holding at -196 ^{o}C for 60 s is determined by its activation energy. Therefore, we think that the initiation of martensitic transformation by applying external stress might be due to the decrease of the activation energy, as illustrated in **Figure 4.13 (b)**.

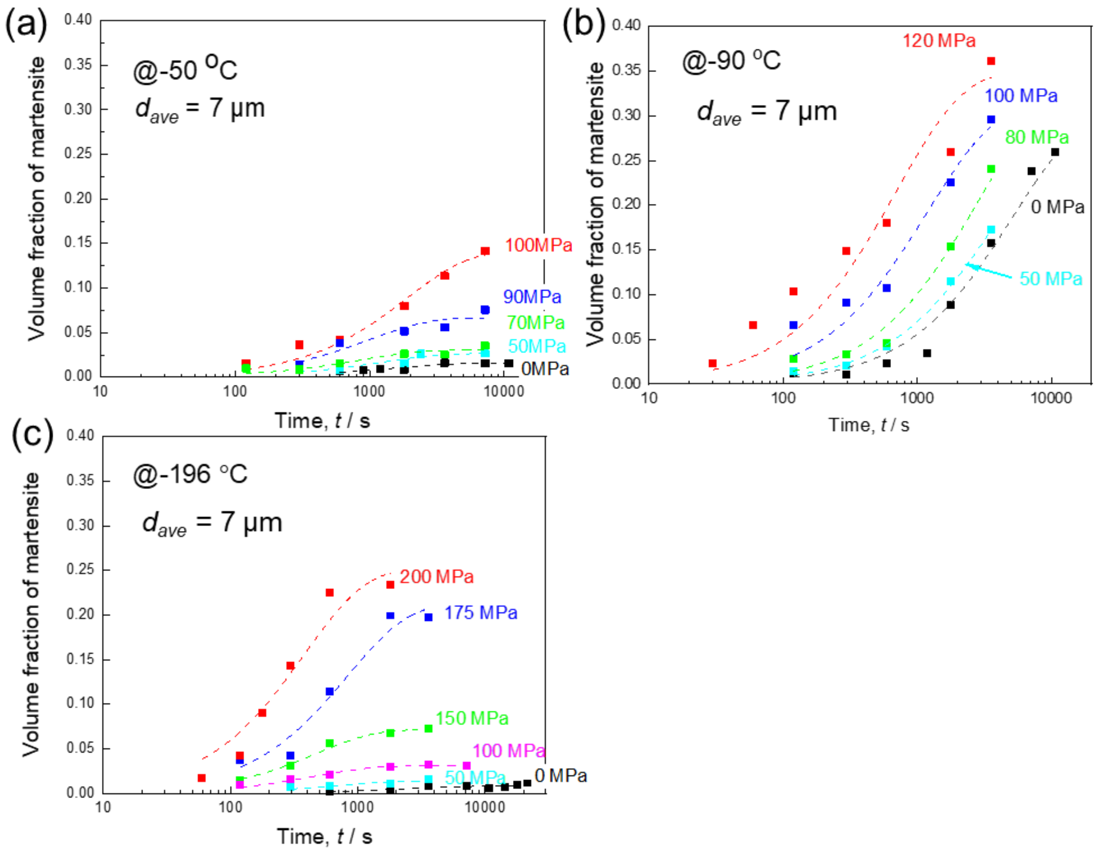

Figure 4.11 Isothermal martensitic transformation of the specimen with different tensile load at different temperatures: **(a)** at -50 ^{o}C; **(b)** at -90 ^{o}C; **(c)** at -196 ^{o}C. The dashed lines indicate the result of curve-fitting.

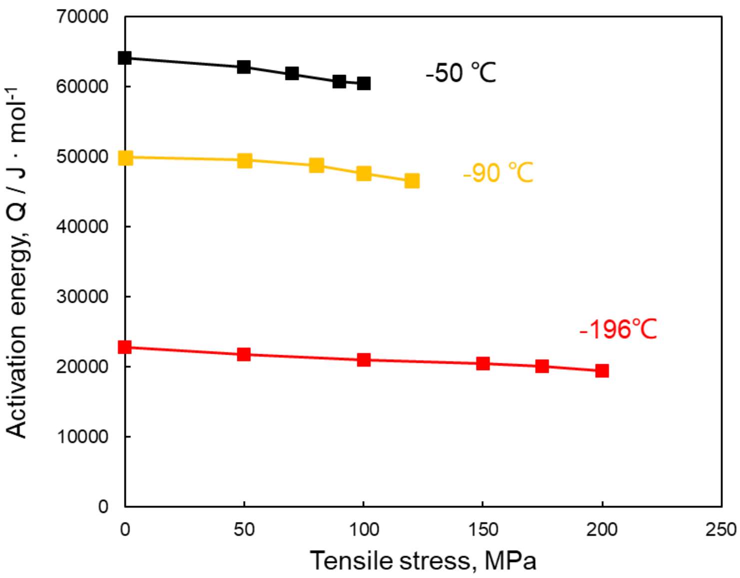

Figure 4.12 Changes of activation energy for the isothermal martensitic transformation as a function of tensile stress at different temperature.

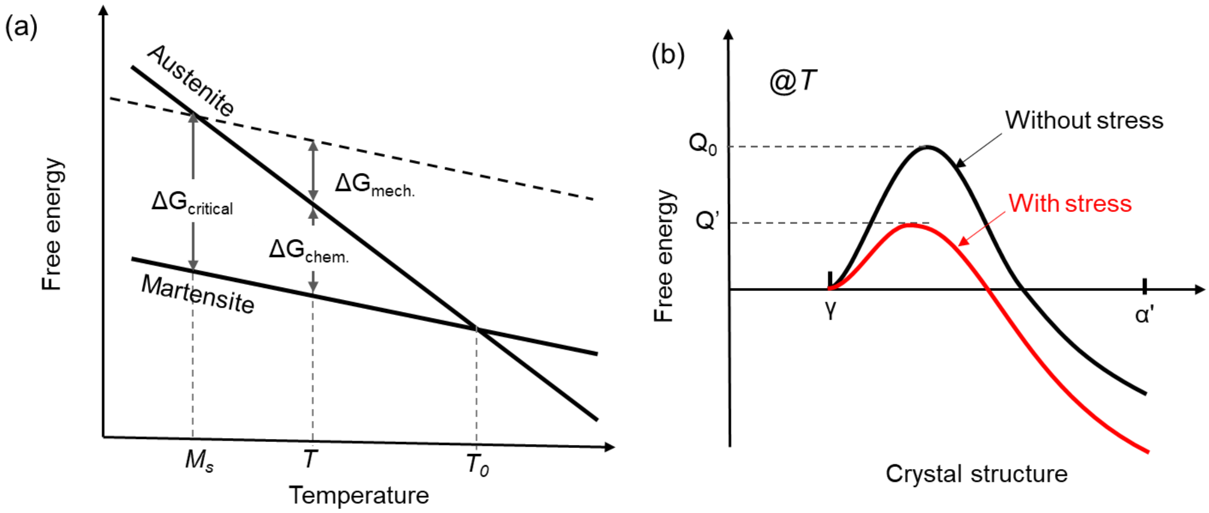

Figure 4.13 (a) Illustration for the effect of mechanical deformation on the martensitic transformation. Above M_s temperature (below T_0) the martensitic transformation could be initiated when the external stress or deformation can provide the extra driving force to compensate the energy gape between the chemical driving force and the critical driving force for martensitic transformation. **(b)** Illustration for the free energy change from austenite to martensite in a case without stress (black) and with stress (red).

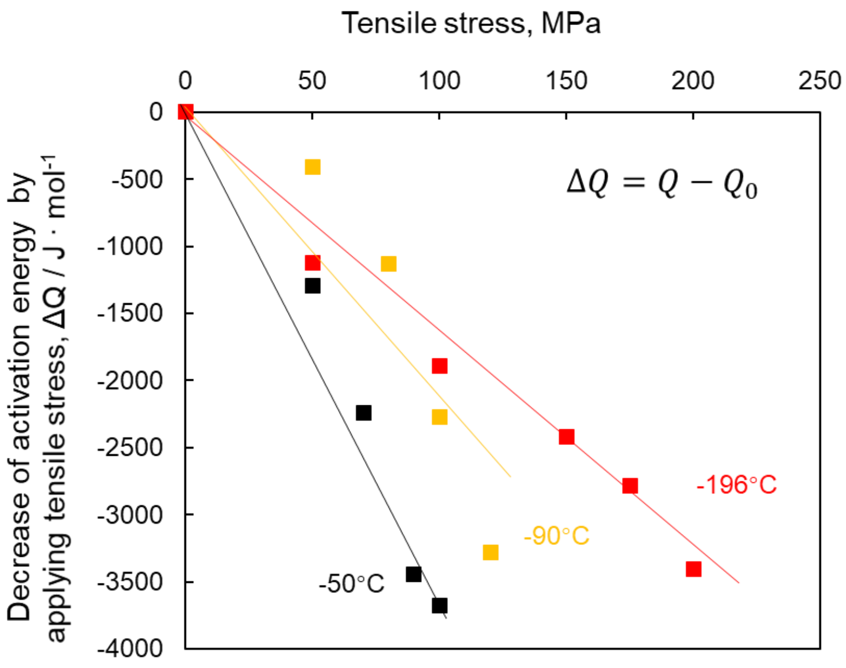

Figure 4.14 Decrement of the activation energy caused by applying tensile stress at different temperature. Q_0 is the activation energy at stress-free condition.

In order to compare the effect of tensile stress on the activation energy at different temperatures, we can plot the decrement of the activation energy (ΔQ) as a function of tensile stress, as shown in **Figure 4.14**. The result reveals that the decrement of the activation energy almost linearly depends on the tensile stress and the slop significantly decreased with decreasing the temperature. According to the thermodynamic principle, the minus of partial derivative of free energy with respect to stress is the activation volume. Therefore, the activation energy for the isothermal martensitic transformation can be expressed as a linear function of applied tensile stress at a certain temperature, as follows:

$$Q = Q_0 - V^*\sigma \quad (4.8)$$

where V^* is the apparent activation volume for the nucleation of the martensite. The apparent activation volumes at different temperatures are plotted in **Figure 4.15**. The physical meaning of the apparent activation volume depends on the detail of the nucleation process. In the nucleation model proposed by G.

B. Olson and M. Cohen [24–26], the nucleation of martensite starts from faulting on planes of closet packing. It is speculated that the martensite embryos are pre-existing, which are formed by faulting process and bounded by arrays of partial dislocations. They suggested that a martensite embryo must grow to some size in the fault morphology before changing to a macroscopic plate. Isothermal growth of these faults constitutes the rate-limiting step in isothermal martensitic transformation. Therefore, they think the apparent activation energy and activation volume for the isothermal martensitic nucleation are consistent with those for the movement of partial dislocation. However, our PLASTON concept provides a different opinion on the nucleation of martensite. As proposed in the **Introduction**, we think the embryo of martensite might be a group of atoms with distorted lattice configuration, i.e. the local defective regions at the grain boundaries. The nucleation of martensite is the process that those atoms overcome the activation energy to form BCC configuration with the help of thermal fluctuation or localized stress. Therefore, the apparent activation volume obtained in the present study might have a different meaning from that suggested by Olson et.al. For helping us to understand the nucleation of martensite from the viewpoint of PLASTON, a molecular dynamics (MD) simulation was performed by our collaborators, Prof. Ogata and Doc. Du, at Osaka University.

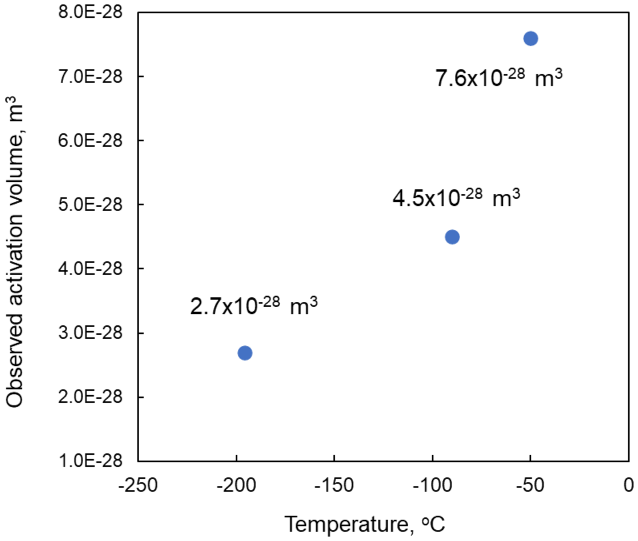

Figure 4.15 Apparent activation volume for the nucleation of martensite estimated from the slop of the plots in **Figure 4.14**.

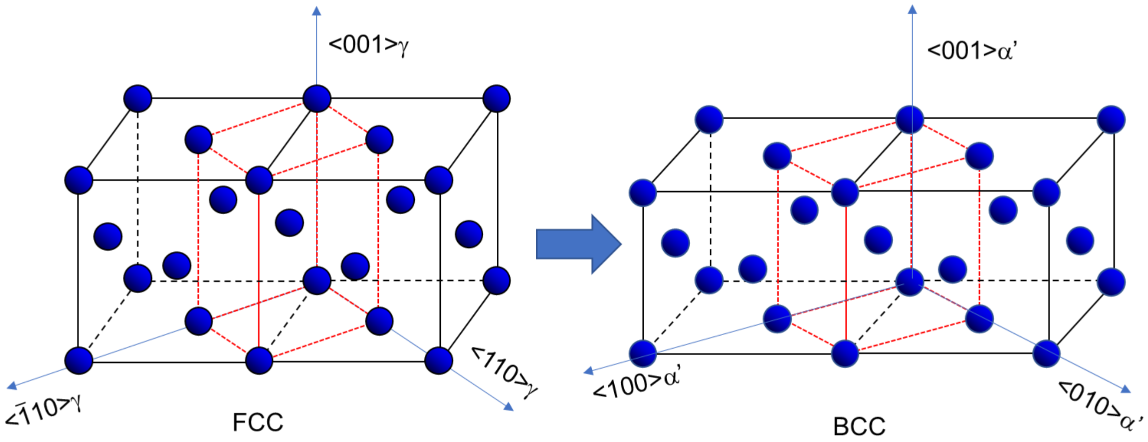

Figure 4.16 Bain distortion for FCC to BCC martensitic transformation.

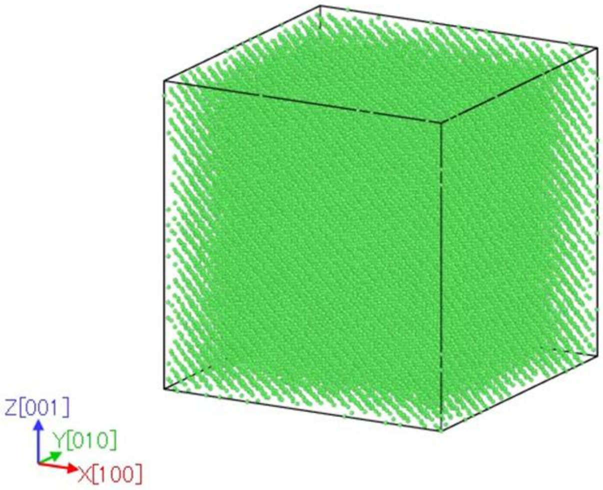

Figure 4.17 Image of the simulation box for the Fe-23Ni single crystal.

The MD simulation was performed in a single crystal of Fe - 23 at% Ni (24 wt%) binary alloy including 32000 atoms. The change of the potential energy when the single crystal transforms from FCC structure to BCC structure though the Bain path was calculated by the embedded-atom method [27]. **Figure 4.16** shows the Bain distortion in which a BCC lattice can be generated from an FCC lattice by compression along one principal axis (like [001]γ), and simultaneous uniform expansion along the other two axes perpendicular to it [18]. According to the first law of thermodynamics, the change in the internal energy for a closed system equals the amount of thermodynamic work done by its surroundings when no heat exchange occurs. Therefore, the activation energy should equal the required work done by the surrounding to the single crystal for overcoming the energy barrier in an adiabatic condition. **Figure 4.17** shows the simulation box of the Fe - 23 at% Ni single crystal with FCC lattice, whose x, y, z axes are parallel to $<100>_\gamma$, $<010>_\gamma$, $<001>_\gamma$ of austenite, respectively. Let us keep the x and y direction of the box at the stress-free condition and compress the box along the z axis, so that, the FCC lattice transforms to BCC lattice along the Bain path. **Figure 4.18 (a)** shows a schematic illustration for the energy change when the simulation box transforms from FCC lattice to BCC lattice along Bain path by compression along the z axis and **(b)** shows the corresponding change of applied stress along the z axis. In **Figure 4.18**, point A indicates the initial state of the simulation box (FCC lattice), and point B is at the top of the energy barrier. Thus, the integral of stress from A to B is the activation energy for transformation, which equals the shaded area indicated in **Figure 4.18 (b)**, and the distance AB (D_{AB}) is the activation distance for the nucleation of martensite at the stress-free condition. **Figure 4.19** shows the change of calculated stress when the simulation box is compressed from point A to point B along the z axis at different temperatures. It can be seen that the area between the curve and horizontal axis, that is, activation energy, decreases with decreasing the temperature. **Figure 4.20** shows the activation energies calculated by the MD simulation at different temperatures without external stress. Although the chemical composition of the material in the MD simulation is different from what we used in the experiment, the variation tendency of the activation energy with temperature is very similar to each other (comparing **Figure 4.9 (b)** with **Figure 4.20**), which implies that the activation energy does greatly depend on the temperature.

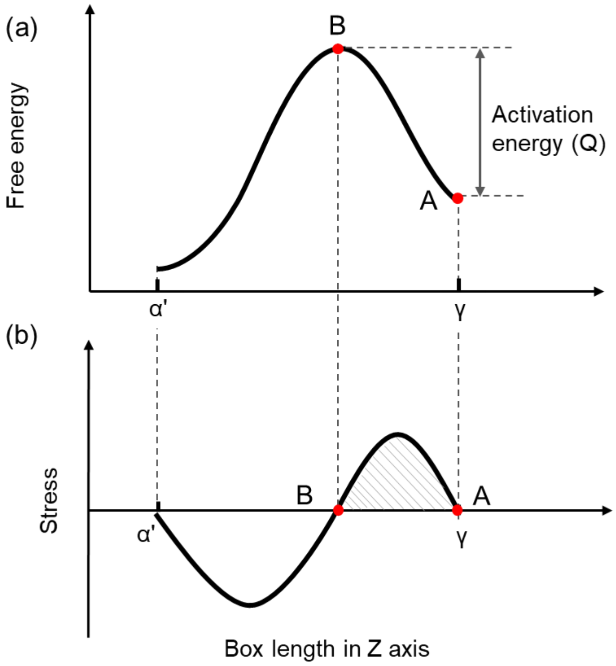

Figure 4.18 (a) Illustration for free energy change when the simulation box is compressed along Z axis; **(b)** Corresponding change of stress along Z axis. Point A indicates the initial state of the simulation box (FCC lattice), and point B is at the top of the energy barrier.

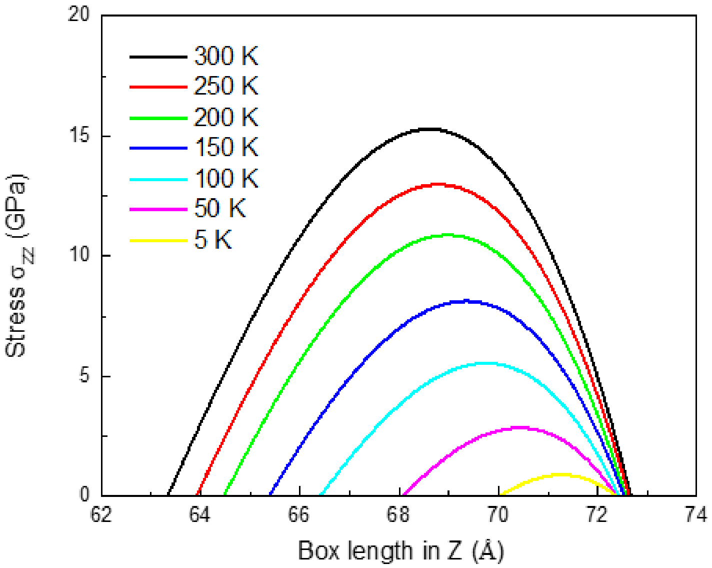

Figure 4.19 Change of calculated stress when the simulation box is compressed from the point A to the point B along Z axis at different temperatures.

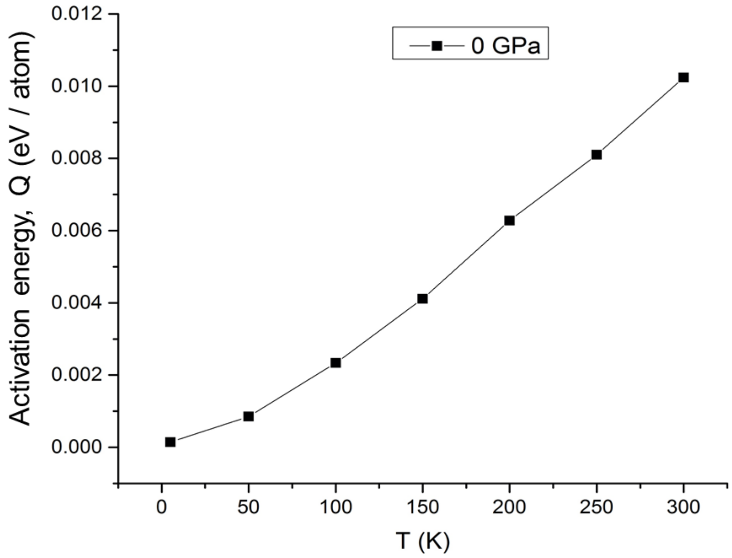

Figure 4.20 Activation energies calculated by the MD simulation at different temperatures without external stress.

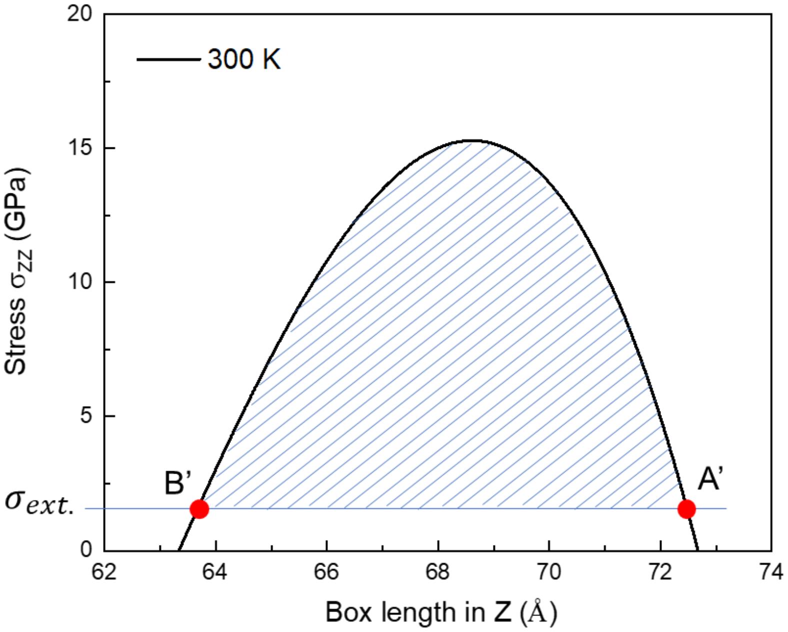

Figure 4.21 Effect of external stress on the activation process for the martensitic transformation.

If we apply extra external compressive stress ($\sigma_{ext.}$) on the simulation box along the z axis, the energy of the initial simulation box would rise to point A' and correspondingly the top of the energy barrier would down to point B', as illustrated in **Figure 4.21**. Clearly, the activation energy is decreased by applying external stress. If it is assumed that the activation distance $D_{A'B'}$ approximates to D_{AB} when external stress is relatively small and the change of length in the x axis (l_x) and the y axis (l_y) of the simulation box during the thermal activation process could be ignored, the activation energy could be expressed by a function of external stress as:

$$Q = Q_0 - D_{AB} l_x l_y \sigma_{ext.} \qquad (4.9)$$

Here, $D_{AB} l_x l_y = V'$ is the activation volume for the martensitic transformation in the MD simulation. It implies that the activation volume for the nucleation of martensite is determined by the activation distance and the size of the embryo. As can be observed in **Figure 4.19**, the activation distance D_{AB} decreases with decreasing the temperature. Consequently, the activation volume for the martensitic transformation in the MD simulation decreases with decreasing temperature, as shown in **Figure 4.22**. The similar variation tendency of the activation volume for the martensitic nucleation with temperature which was observed (in **Figure 4.15)** in our experimental results might be also due to a similar reason if the nucleation mechanism of martensite is based on the 'PLANSON' concept. Again, in our PLASON viewpoint, martensite nucleates from a group of atoms activated by high localized stress or thermal fluctuation. In this case, the result of MD simulation reveals that the activation volume of martensitic nucleation is determined by its embryo size and activation distance. If the critical size for the nucleation of martensite is insensitive to temperature, the decrease of the apparent activation volume with decreasing temperature (in **Figure 4.15)** is due to the decrease of the activation distance. However, in the real situation, the size of the nucleation embryo might also change with temperature. But it still needs further studies to clarify.

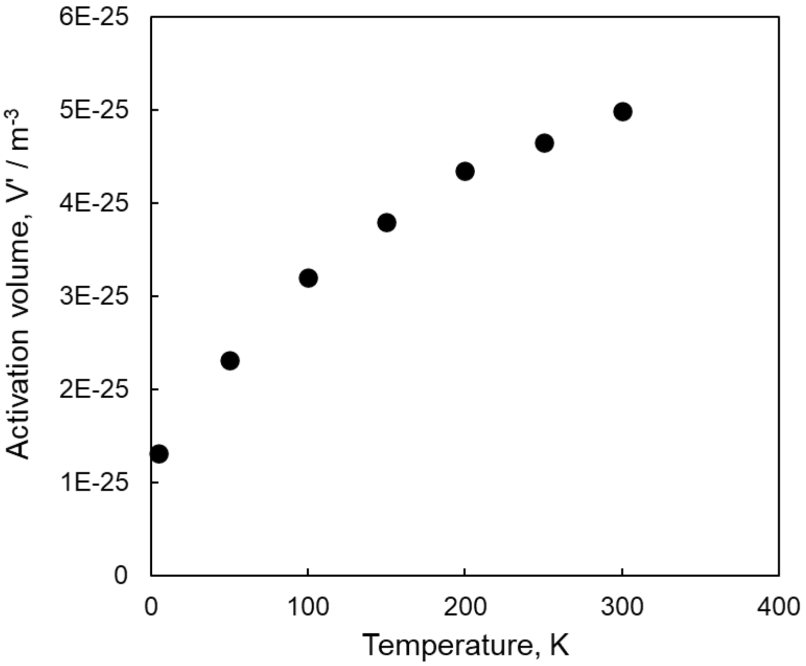

Figure 4.22 Activation volume for the martensitic transformation in the MD simulation at different temperature.

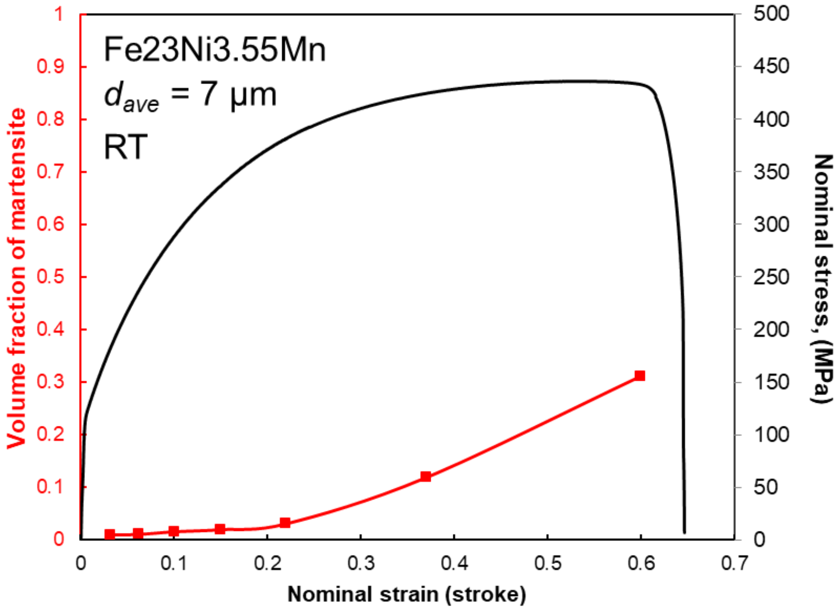

Figure 4.23 Nominal stress-strain curve and the change of volume fraction of martensite during the deformation.

4.3.3 Effect of plastic strain on the kinetics of the isothermal martensitic transformation

In the Fe-23Ni-3.55Mn specimen with a mean grain size of 35 μm, the isothermal martensitic transformation was not observed at room temperature even after several months. However, as shown in **Figure 4.23**, the martensitic transformation was initiated by tensile deformation at room temperature. However, it still unclear that stress or plastic strain which one determines the kinetics of deformation induced martensitic transformation.

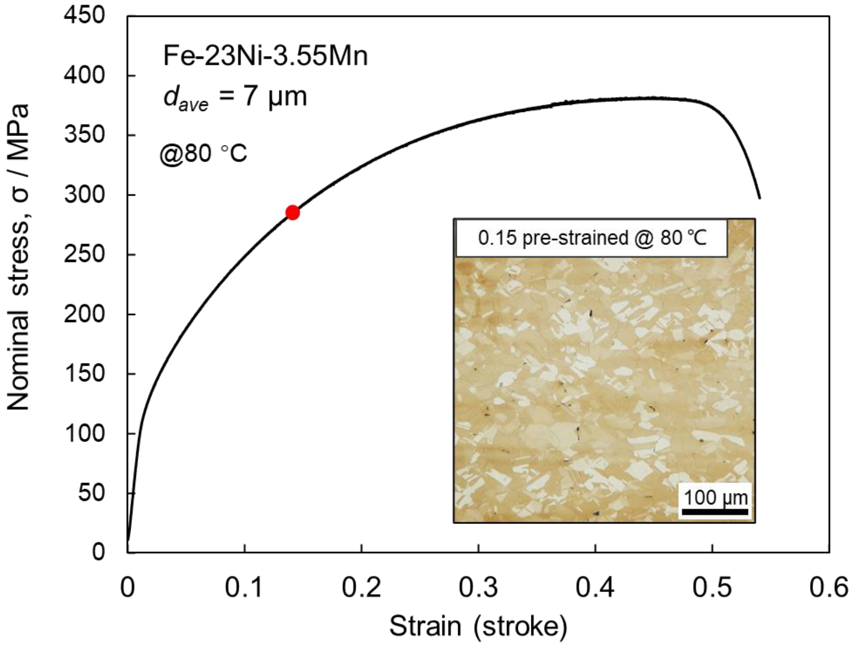

Figure 4.24 Stress-strain curve of the specimen at 80 °C. The embedded OM image is the microstructure at strain of 0.15.

In order to study the effect of plastic strain on the kinetics of the isothermal martensitic transformation, the specimen was deformed to several strains from 0.05 to 0.15 at 80 °C prior the isothermal subzero-treatment. Deformation at 80 °C aims to prevent the formation of martensite during the deformation. **Figure 4.24** shows the nominal stress-strain curve of the specimen at 80 °C. The microstructure after straining to 0.15 at 80 °C is below the stress-strain curve which reveals that there is almost no martensite formed up to 0.15 strain. The pre-strained specimens were isothermally transformed at -50 °C and -110 °C.

Figure 4.25 shows the isothermal martensitic transformation in the 0.1 pre-strained specimens at -50 ^{o}C and -110 ^{o}C, respectively, compared with that in the undeformed one. Clearly, the isothermal martensitic transformation was suppressed by 0.1 pre-strain. On the other hand, the effect of different prior plastic strains on the isothermal martensitic transformation was studied at -110 ^{o}C as shown in **Figure 4.26**. The result reveals that the kinetics of the isothermal martensitic transformation decreased with increasing plastic strain. Although it has been reported in several alloys that the stability of austenite will be decreased by slight plastic strain due the increase of nucleation sites [28,29], we have not observed the enhancing effect of plastic strain on the isothermal martensitic transformation in the present study.

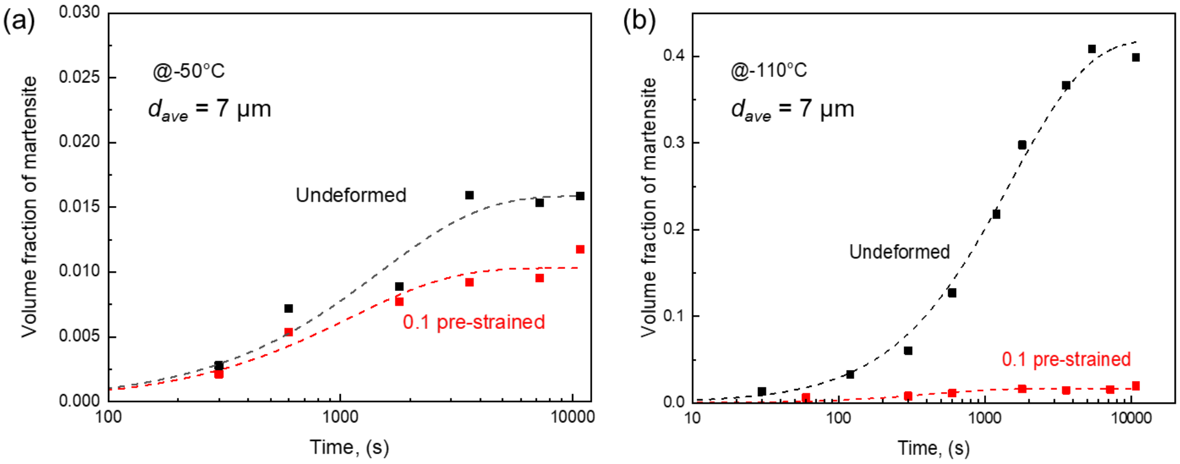

Figure 4.25 Isothermal martensitic transformation of the undeformed specimen and the 0.1 pre-strained specimen at **(a)** -50 ^{o}C and **(b)** -110 ^{o}C. The dashed lines indicate the result of curve-fitting.

It is widely accepted that plastic deformation introduces new nucleation sites by forming new defects in the material [30]. However, it is difficult to quantitatively evaluate the number of newly formed nucleation sites for the martensitic transformation. Therefore, for estimating the effect of prior plastic strain on the activation energy for the isothermal martensitic transformation, the same number of nucleation sites as the undeformed ones was used for the 0.1 pre-strained specimens. After 0.1 pre-straining, the activation energy for the isothermal martensitic transformation at -50 ^{o}C increased from 6.42×10^4 J/mol to 6.44×10^4

J/mol, while at -110 °C it increased from 4.23×10^4 J/mol to 4.54×10^4 J/mol. It reveals that the suppressive effect of plastic strain on the isothermal transformation is stronger at low temperature.

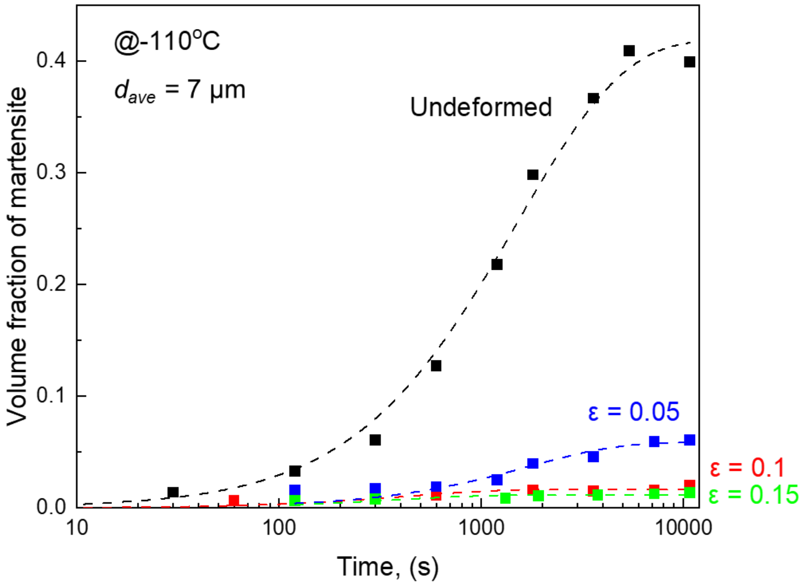

Figure 4.26 Effect of pre-strain on isothermal martensitic transformation of the specimen at -110 °C. Dashed lines are fitting curves. The dashed lines indicate the result of curve-fitting.

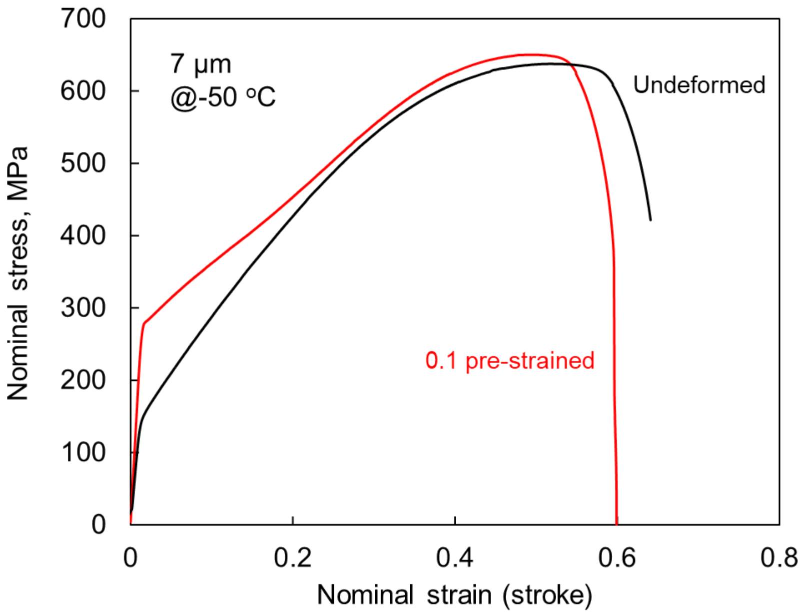

Figure 4.27 Stress-strain curves of the undeformed specimen and 0.1 pre-strained specimen at -50 °C.

In order to clarify that stress or strain who dominates the kinetics of the martensitic transformation during deformation, the effect of tensile stress on the isothermal martensitic transformation in the 0.1 pre-strained specimen was investigated at -50 °C. After the 0.1 pre-straining, the yield strength increased from 143 MPa to 270 MPa due to the strain hardening, as shown in **Figure 4.27**. Therefore, higher tensile stress could be applied to the pre-strained specimen during the isothermal transformation. **Figure 4.28** shows the isothermal martensitic transformation under different conditions. The green and blue data plots indicate the isothermal martensitic transformation in the 0.1 pre-strained specimens under 100 MPa and 200 tensile stress, respectively. It is clear that, although the kinetics of the transformation was suppressed by prior plastic strain (red plots), by applying tensile stress the kinetics of the transformation in the pre-strained specimen could be significantly enhanced. However, for the same tensile loading of 100 MPa, the kinetics of the transformation in the undeformed specimen is much larger than that in the pre-strained specimen.

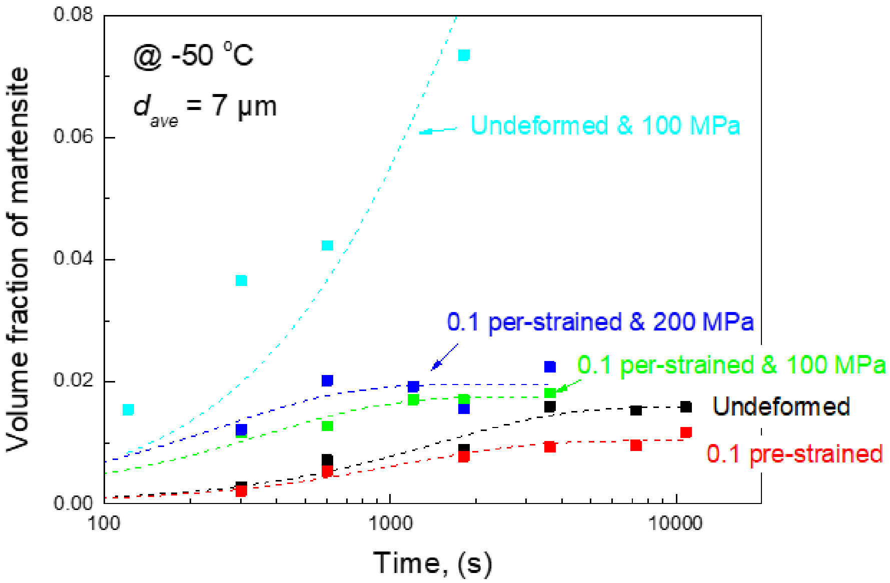

Figure 4.28 Effect of tensile stress on isothermal martensitic transformation of 0.1 pre-strained specimen and undeformed specimen at -50 °C. The dashed lines indicate the result of curve-fitting.

This result reveals that during deformation the enhancing effect of tensile stress is stronger than the suppressive effect of plastic strain, that is, the formation of deformation induced martensite is mainly attributed to the increment of stress caused by strain hardening. The histogram in **Figure 4.29** summarizes the activation energy for the isothermal martensitic transformation at different conditions. The activation energy for the transformation was increased by plastic deformation but decreased by tensile stress. Therefore, during plastic deformation, the kinetics of deformation induced martensitic transformation might be determined by the net effect of plastic strain and tensile stress.

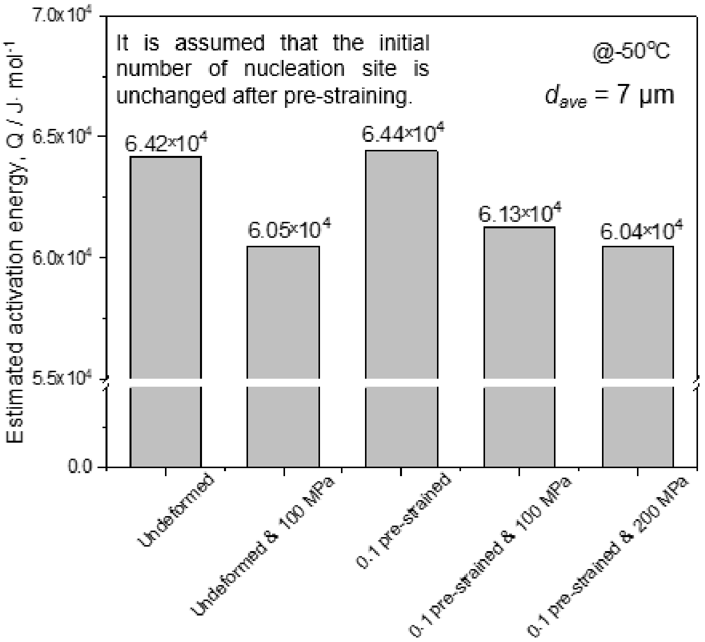

Figure 4.29 Activation energy for the isothermal martensitic transformation of the specimen at different conditions.

4.3.4 Effect of grain size on the kinetics of the isothermal martensitic transformation

In order to study the effect of grain size on the isothermal martensitic transformation in Fe-23Ni-3.55Mn alloy, specimens with different mean grain sizes were fabricated by changing the annealing temperature. **Figure 4.30 (a)-(c)** shows the microstructure of specimens annealed at 800 °C, 900 °C and 940 °C for 1 hour, respectively. After annealing, both the three specimens are fully composed of austenite phase. With increasing the annealing temperature, the mean grain size significantly increased. The mean grain sizes for the specimens annealed at 800 °C, 900 °C and 940 °C for 1 hour are 7 μm, 14 μm and 25 μm, respectively, which were measured by the interception method including twin boundaries.

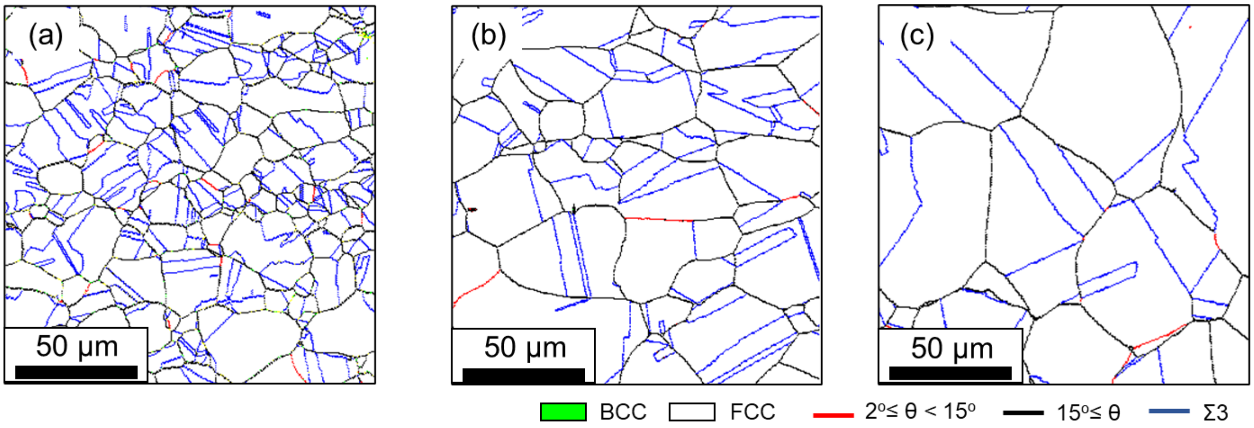

Figure 4.30 Phase and grain boundary maps of specimens after cold rolling and subsequent annealed at different temperature **(a)** 800 °C, **(b)** 900 °C and **(c)** 940 °C for 1 hour.

Figure 4.31 (a)-(c) shows the isothermal martensitic transformation at different temperatures in the specimens having different mean grain sizes. The martensitic transformation in all of the three specimens only exhibited isothermal kinetic behavior. For the sake of comparison, the isothermal martensitic transformations at the same temperature are reassembled in one figure, as shown in **Figure 4.32**. Clearly, with decreasing the grain size the kinetics of the isothermal martensitic transformation decreased. **Figure 4.33** shows the 1% transition TTT curves of the specimens with different mean grain size. The C-shape curve shifted to the right side as grain refinement indicating the increase of stability of austenite.

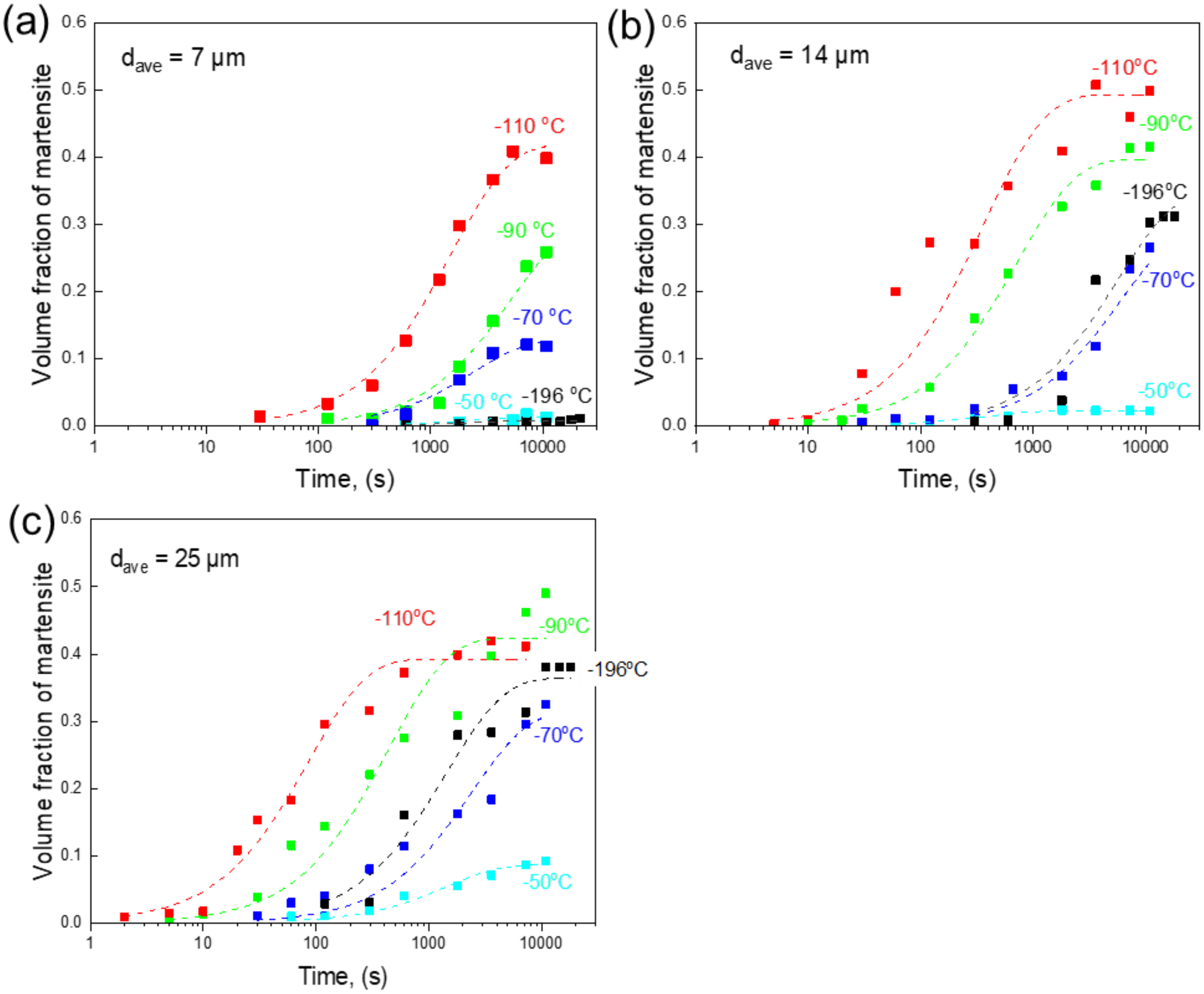

Figure 4.31 Isothermal martensitic transformation of the specimen different mean grain sizes of **(a)** 7 µm, **(b)** 14 µm and **(c)** 25 µm at different temperature. The dashed lines indicate the result of curve-fitting.

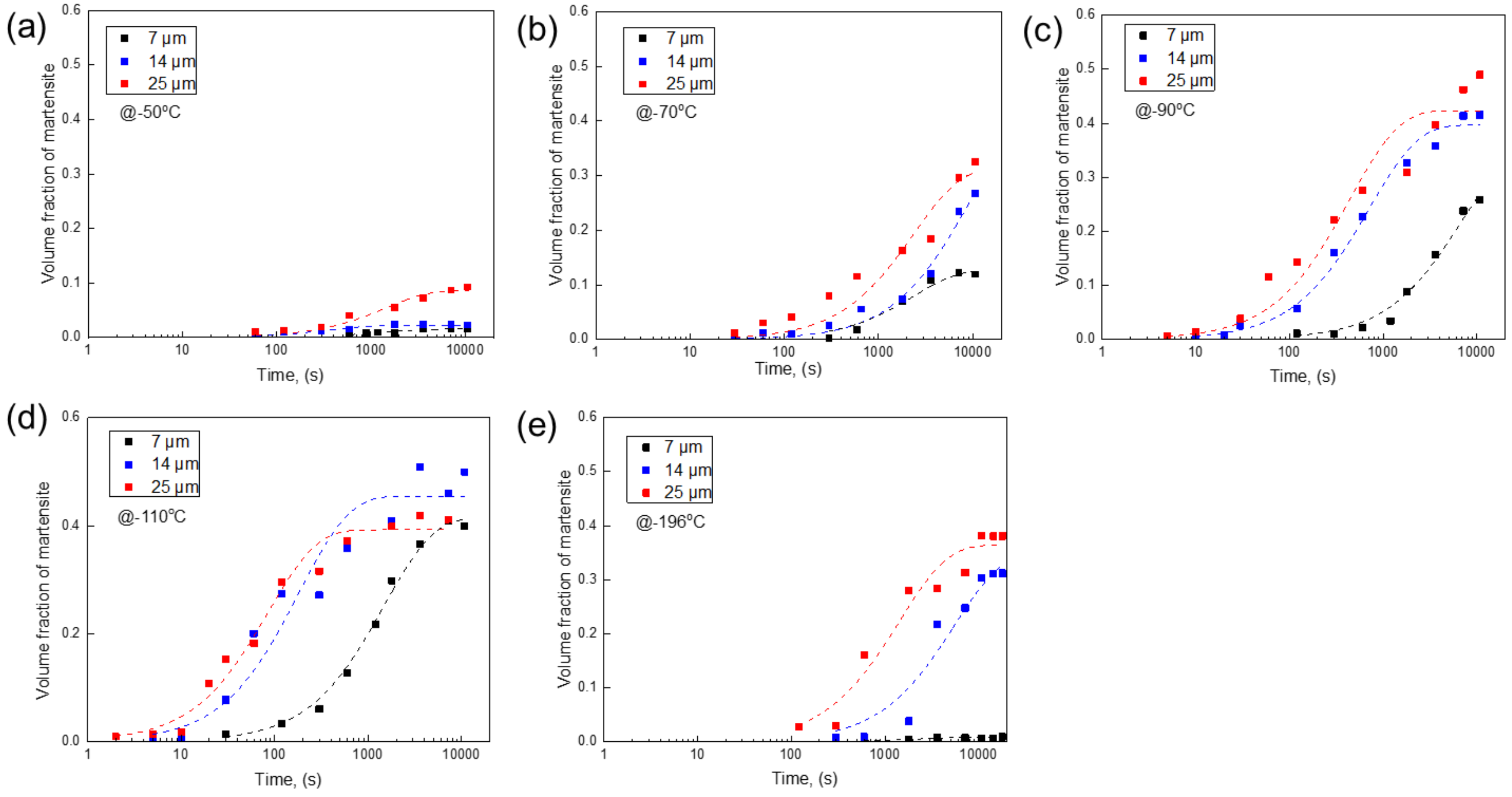

Figure 4.32 Comparison of isothermal martensitic transformation of the specimens with different mean grain sizes at different temperature. **(a)** -50 °C; **(b)** -70 °C; **(c)** -90 °C; **(d)** -110 °C; **(e)** -196 °C. The dashed lines indicate the result of curve-fitting.

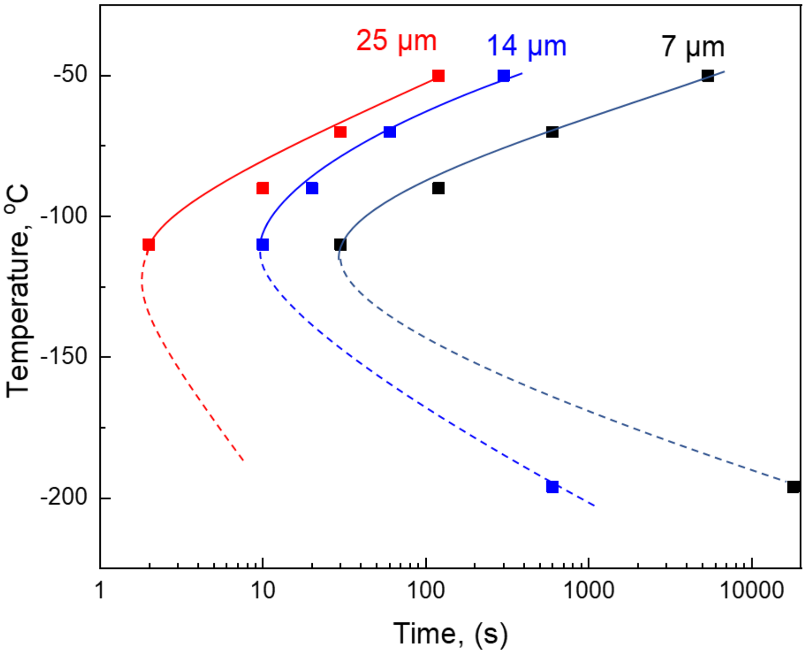

Figure 4.33 TTT diagram of the specimens with different mean grain sizes for 1 vol% transition.

In order to evaluate the activation energy for the isothermal martensitic transformation by curve-fitting the plots of martensite volume fraction vs time with **Equation 4.7**, two parameters need to be determined prior to the curve-fitting: the initial number of nucleation sites per unit volume and the mean volume of one martensite plate. As mentioned above, the initial number of nucleation sites per unit volume approximates the number of austenite grains per unit volume for the simple assumption that there is one most potent nucleation site per grain of austenite. Thus, the initial number of nucleation site per unit volume for the 7 μm specimen is about 3×10^{15} m^{-3}, for the 14 μm specimen is about 4×10^{14} m^{-3}, and for the 25 μm specimen is about 6×10^{13} m^{-3}. The mean volume of one martensite plate was estimated according to the microstructure observation by using **Equation 4.3**. **Figure 4.34** shows the changes of estimated mean volume of one martensite plate in the specimens with different mean grain sizes as a function of martensite volume fraction. It reveals that the mean volume of a single martensite plate was almost unchanged during the progress of the transformation. And the mean volume of single martensite plate in the 14 μm and 25 μm specimen was almost the same, for 2×10^{-16} m^3, while for the 7 μm is 4×10^{-17} m^3.

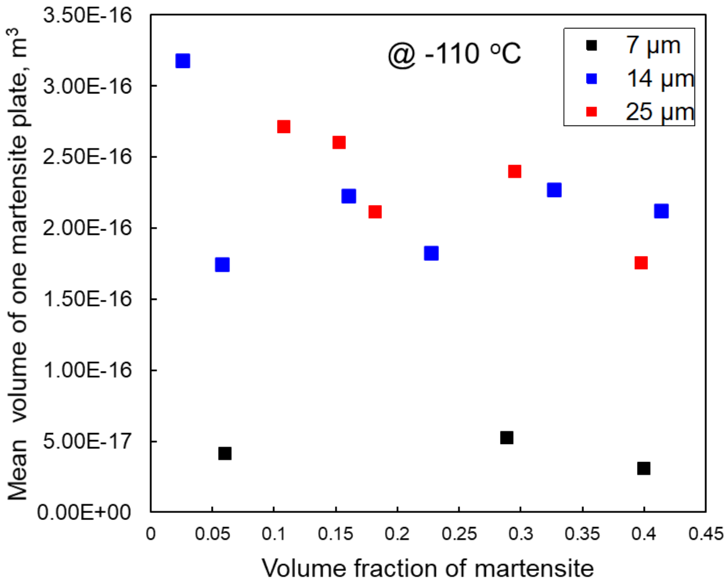

Figure 4.34 Changes of mean volume of martensite plates as a function of the volume fraction of martensite in the specimens with different mean grain sizes.

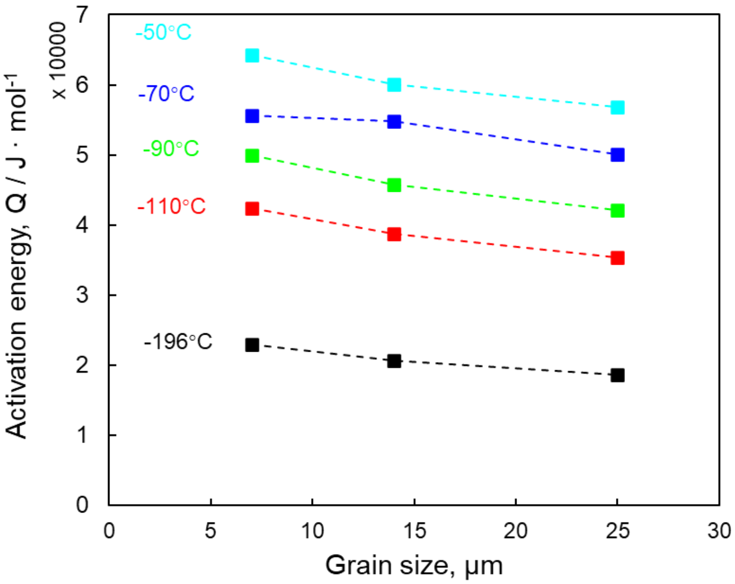

Figure 4.35 Changes of activation energy for the isothermal martensitic transformation in the specimens with different mean grain sizes.

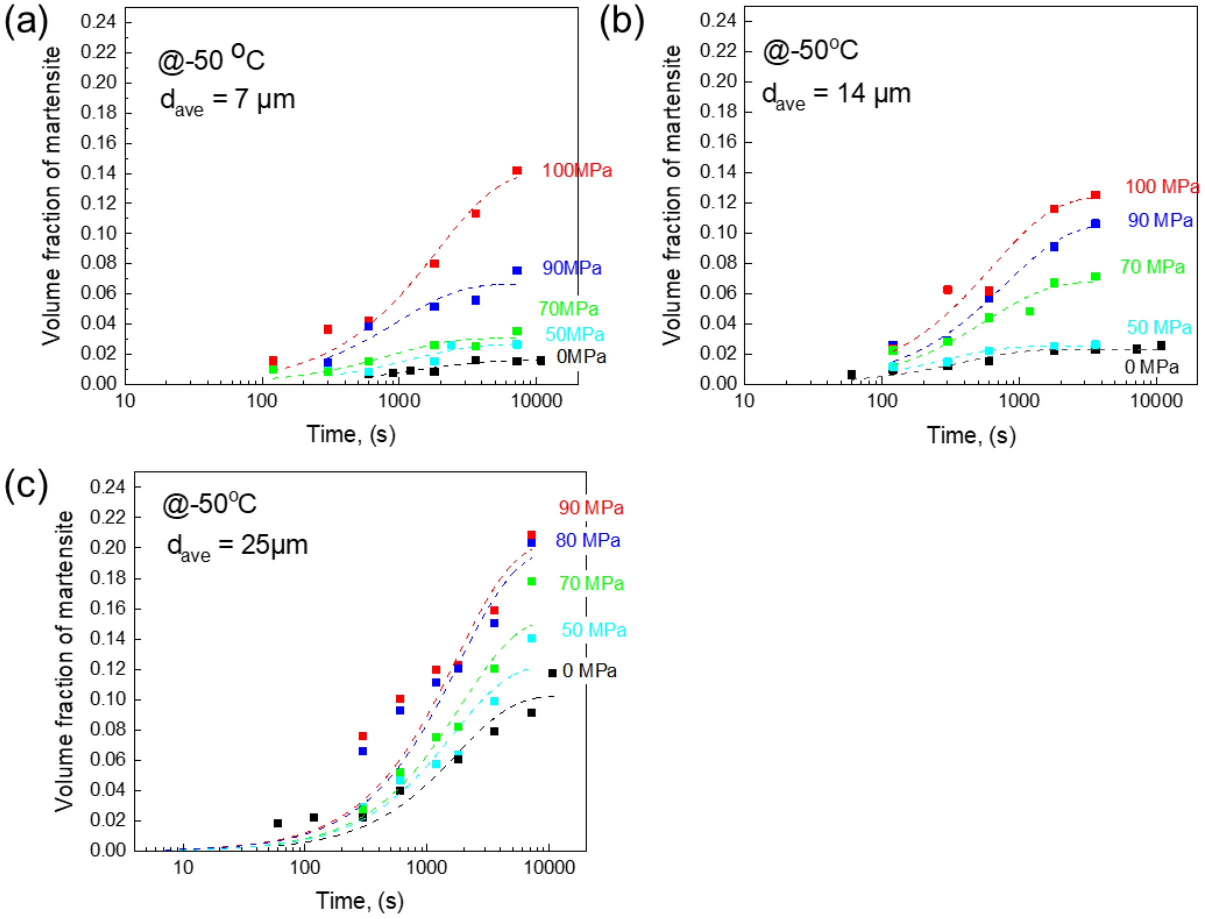

Figure 4.36 Effect of tensile stress on the isothermal martensitic transformation in the specimens having mean grain sizes of **(a)** 7 μm, **(b)** 14 μm and **(c)** 25 μm at -50 °C. The applied tensile stresses in each specimen during the isothermal martensitic transformation are smaller than their yield strength. The dashed lines indicate the result of curve-fitting.

Figure 4.35 shows the estimated activation energy for the isothermal martensitic transformation at different temperatures, plotted as a function of grain size. It can be clearly seen that the activation energy increased as the mean grain size decreased at a certain temperature. It is possibly because that, as the yield strength of austenite matrix increased due to grain refinement, the restriction from the matrix for the martensitic nucleation increased. As a result, the energy barrier for nucleation of martensite increases as grain refinement.

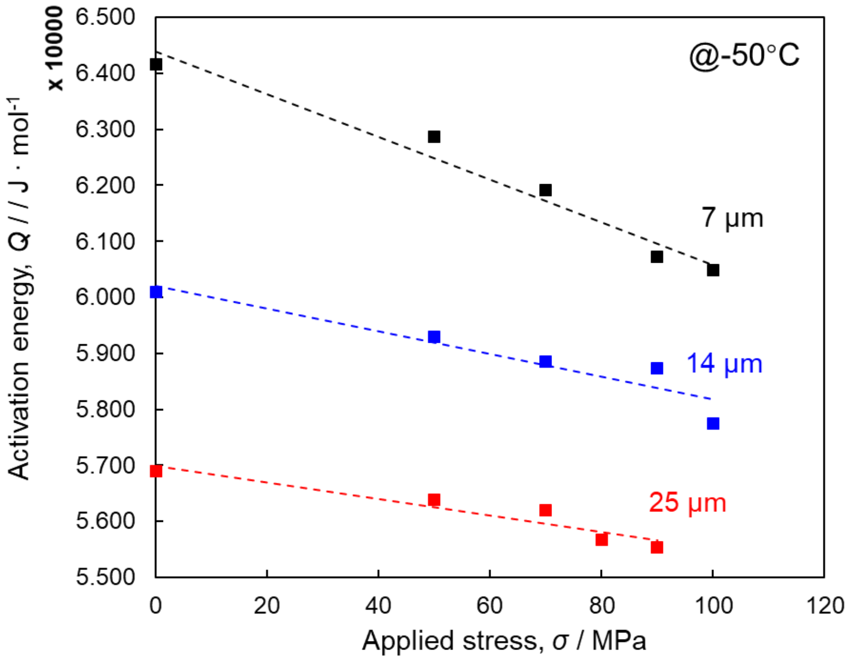

Figure 4.37 Changes of activation energy for the isothermal martensitic transformation in the specimens with different mean grain sizes as a function of tensile stress.

The effect of stress on the isothermal martensitic transformation in the specimens having different mean grain sizes was investigated at -50 ^{o}C, as shown in **Figure 4.36**. It can be seen again that the kinetics of the isothermal martensitic transformation was greatly enhanced by applying tensile stress. **Figure 4.37** shows the changes of activation energy for the isothermal martensitic transformation in the specimens with different mean grain sizes as a function of tensile stress, which was estimated by curve-fitting of the plots in **Figure 4.36**. This result proved once again that the activation energy for the martensitic transformation has a linear relationship with applied tensile stress which could be expressed by **Equation 4.8**. The equations of the best-fitting straight lines are as follows:

For the 7 μm specimen: $Q = 64382 - 37.98 \times \sigma \ (J \cdot mol^{-1})$;

For the 14 μm specimen: $Q = 60197 - 20.19 \times \sigma \ (J \cdot mol^{-1})$;

For the 25 μm specimen: $Q = 58994 - 14.74 \times \sigma \ (J \cdot mol^{-1})$;

Clearly, the slope of the fitting curve, that is, the apparent activation volume was increased with decreasing the mean grain size of austenite. It implies that the enhancing effect of tensile stress on the kinetics of the isothermal martensitic transformation seems to be enhanced when the mean grain size is reduced.

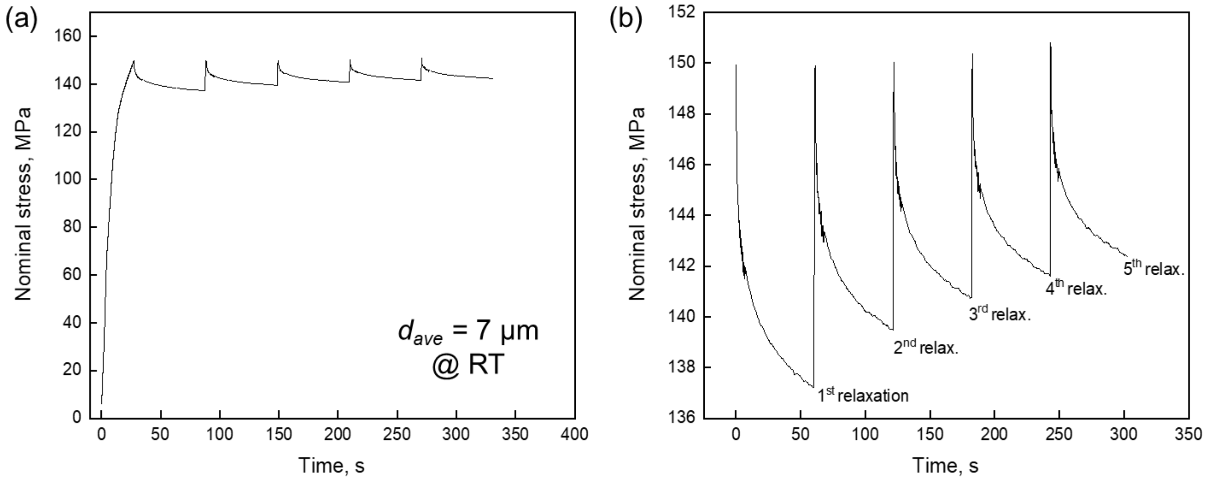

Figure 4.38 (a) Stress-relaxation experiment for the specimen with a mean grain size of 7 μm. **(b)** the corresponding stress-relaxation series, the starting time of the first relaxation is set as 0 s.

As stated in **Section 4.3.2**, G. B. Olson et.al suggested the apparent activation volume for the isothermal martensitic transformation is the activation volume for the partial dislocation motion involved in the nucleation of martensite. If their suggestion is correct, the activation volume for dislocation motion should increase as grain refinement in Fe-23Ni-3.55Mn specimens. In order to clarify the effect of grain size on the activation volume for the dislocation motion in Fe-23Ni-3.55Mn alloy, stress-relaxation experiments were performed on the specimens with different mean grain sizes. The stress-relaxation experiments were carried out at room temperature, because at low temperature the formation of martensite would disturb the measurement. The specimen was initially tensile strained to 150 MPa just after yielding in a strain rate of 8.3×10^{-4} s^{-1}. Then the cross-head was stopped and the stress was recorded with time. After the first relaxation over an interval of 60 s, the specimen was reloaded to the same stress level as the beginning of the previous cycle for the next relaxation. In order to obtained reproducible results, the stress relaxations of each specimen were performed five times and the average values of obtained results were used. **Figure 4.38 (a)** gives an example for the stress-relaxation experiment for the specimen with a mean grain size of 7 μm in which the nominal stress is plotted with time, and **(b)** the corresponding stress-relaxation series. The physical activation volume V^d for dislocation motion can be determined by the following equation:

$$V^d = -k_A T \frac{ln(\dot{\varepsilon_{\iota 2}}/\dot{\varepsilon_{f1}})}{\Delta\sigma^*} = -k_A T \frac{ln(\dot{\sigma_{\iota 2}}/\dot{\sigma_{f1}})}{\Delta\sigma^*} \quad (4.10)$$

where $\dot{\varepsilon_{\iota 2}}$ and $\dot{\varepsilon_{f1}}$ are the plastic strain rate at the onset of relaxation 2 and at the end of relaxation 1, respectively; k_A is a material constant; $\Delta\sigma^*$ is the stress drop of the first relaxation. The derivation process could be found in reference [31,32]. Since plastic strain ($\varepsilon_{plastic}$) and elastic strain ($\varepsilon_{elastic}$) has a relationship during the stress relaxation: $\varepsilon_{plastic} = -\varepsilon_{elastic}$, the plastic strain rate in the above equation could be replaced by the change rate of tensile stress. $\dot{\sigma_{\iota 2}}$ and $\dot{\sigma_{f1}}$ are the change rate of stress at the onset of relaxation 2 and at the end of relaxation 1, respectively. For obtaining the change rate of stress during the stress relaxation, the stress-relaxation curve was fitted by the following equation [31]:

$$\Delta\sigma = -\frac{k_A T}{V_a}\ln(1 + \frac{t}{C_r}) \quad (4.10)$$

where $\Delta\sigma$ is the stress drop at time t; V_a: is the apparent activation volume for dislocation motion; C_r is the relaxation time constant. **Figure 4.39** shows the fitting curve (solid curve) of the first relaxation shown in **Figure 4.38 (b)**. Then, the change rates of stress during the stress-relaxation were obtained by taking the derivation of the fitting curve.

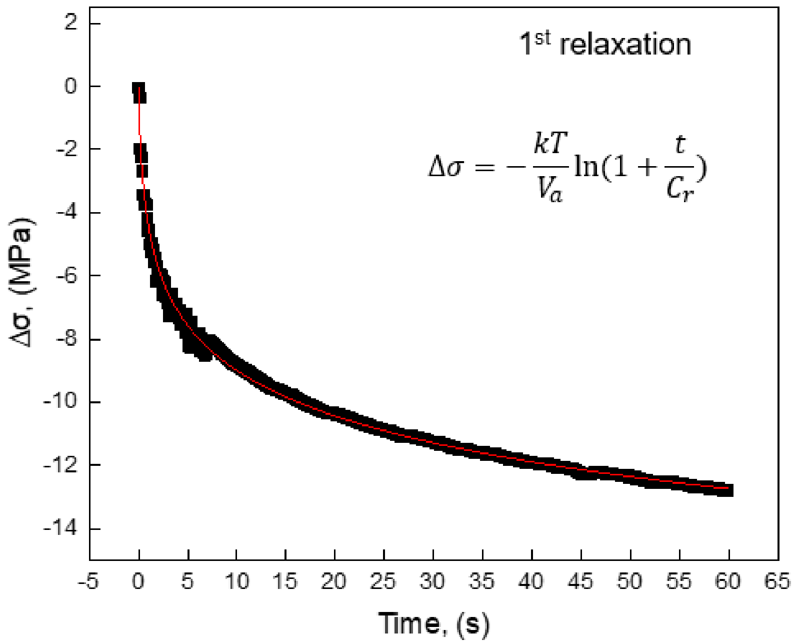

Figure 4.39 Fitting curve (solid red curve) of the first relaxation shown in **Figure 4.38 (b)**.

The physical activation volume estimated by **Equation 4.10** belongs to perfect dislocation (b = a_{fcc}<110>/2 ~ 0.253nm). However, in the nucleation model of G. B. Olson et.al [26], the rate limiting step of nucleation of martensite is the motion of the partial dislocation with a Burgers vector of a_{fcc}<112>/18. If we assume that the activation area for the thermal activation of the partial dislocation is the same as that for the perfect dislocation. The physical activation volume for the partial dislocation can be converted from that of perfect dislocation according to the magnitude ratio of their Burgers vectors. **Figure 4.40** shows the physical activation volume for the partial dislocation motion at room temperature and the apparent activation volume for the nucleation of martensite at -50 ^{o}C. Although the measurement temperature for these two physical quantities is different, the variation tendencies as grain refinement can still be compared. It can be seen that the physical activation volume for the partial dislocation was almost unchanged was grain refinement. However, the apparent activation volume for the martensitic nucleation had a significant increment when the grain size was reduced from 25 μm to 7 μm, which is not consistent with the former. It is revealed sidewise that the nucleation model proposed by G.B. Olson et.al might have limitations for explaining the grain size dependence of the kinetics of the isothermal martensitic transformation. Especially, the experimental fact that the stress fact on the kinetics of the isothermal martensitic transformation is enhanced by grain refinement could not be well explained by their nucleation model.

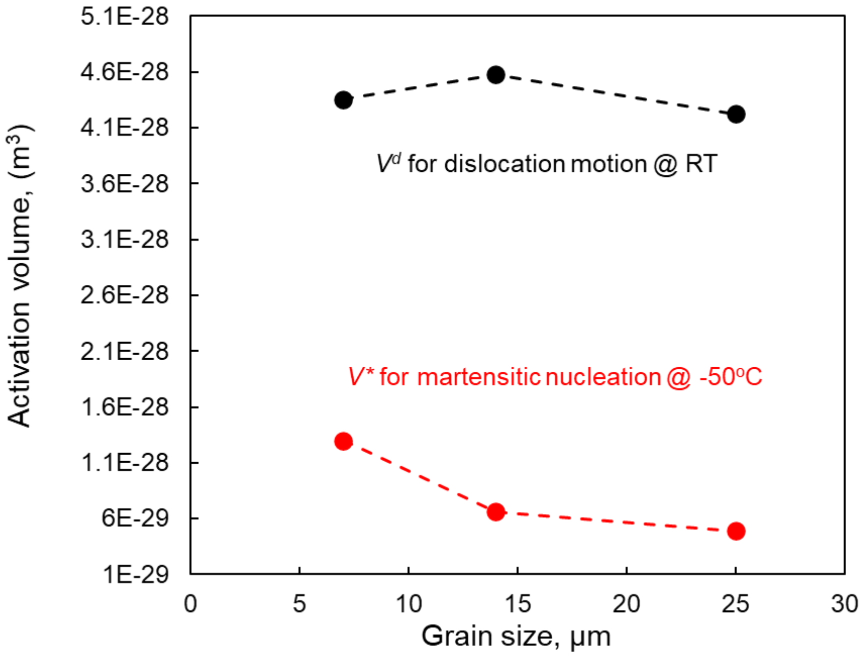

Figure 4.40 Estimated physical activation volume for the partial dislocation motion at room temperature and the apparent activation volume for the nucleation of martensite at -50 °C.

In our PLASTON concept, the regions with high localized stress are in favor of the nucleation of martensite. It has been reported that grain refinement could increase the intergranular interaction caused by grain-to-grain plastic strain incompatibility [33–35]. However, in the elastic region, there are few researches about the effect of grain refinement on the grain-to-grain interaction. Due to the anisotropy of elastic constants of austenite, the strain compatibility should exist at the grain boundaries between differently oriented grains and at the triple junctions between grains even at the elastic deformation region. We think that the area of the grain boundaries and the number of the triple junctions would increase as grain refinement, which might result in the increase of the probability of region with localized high internal stress, that is, the distribution of stress might become more heterogeneous. Therefore, for the same external stress, in the fine-grained material, there might be more ‘PLASTON’ activated by the localized high stress which shows the enhanced stress effect on the kinetics of the isothermal martensitic transformation.

4.4 Conclusion

In this Chapter, we studied the effect of tensile stress, prior plastic deformation and grain size on the kinetics of isothermal martensitic transformation in Fe-23Ni-3.55Mn (wt.%) from the viewpoint of ‘PLASTON’. The main conclusions are summarized as follows:

(1). The martensitic transformation in Fe-23Ni-3.55Mn alloy only shows isothermal transformation kinetics. The TTT curve for the isothermal martensitic transformation shows the typical C-shape, with the nose temperature near to -110 ^{o}C.

(2). The overall isothermal martensitic transformation in Fe-23Ni-3.55Mn alloy can be well described by the singly activated model in which the effect of autocatalytic effect is included and it is assumed that the activation energy for all nucleation sites are uniform.

(3). The activation energy for the martensitic nucleation is decreased by applying tensile stress. As a consequence, the kinetics of the isothermal martensitic transformation could be enhanced by increasing the tensile stress. The effect of stress on the isothermal martensitic transformation becomes weaker when the transformation temperature decreases. It is because that the activation volume decreases as the temperature is decreased. In the viewpoint of ‘PLASTON’, we think the activation volume for the martensitic nucleation is determined by the activation distance and the size of the nucleation embryo. According to the result of MD simulation, the decrease of activation volume as the temperature decreases might be attributed to the decreased in the activation distance.

(4). The isothermal thermal martensitic transformation is inhibited by prior plastic deformation at 80^{o}C. The inhibiting effect of prior plastic deformation increases with increasing the deformation. The initiation of deformation induced martensitic transformation during the deformation is attributed to the increase the stress. And the kinetics of the deformation induced martensitic transformation during deformation might be the net effect of stress and plastic deformation.

(5). Grain refinement increases the activation energy for the isothermal martensitic transformation. The accelerating effect of stress on the martensitic transformation becomes stronger as grain refinement. We speculate that the grain refinement might increase the probability of the formation of the region with high local stress since the area of grain boundaries and the number of triple junctions increases.

Reference

1. Byun, T. S., Hashimoto, N. & Farrell, K. Temperature dependence of strain hardening and plastic instability behaviors in austenitic stainless steels. *Acta Mater.* **52**, 3889–3899 (2004).

2. Gibbs, P. J. *et al.* Austenite stability effects on tensile behavior of manganese-enriched- austenite transformation-induced plasticity steel. *Metall. Mater. Trans. A Phys. Metall. Mater. Sci.* **42**, 3691–3702 (2011).

3. Tsuchida, N. & Tomota, Y. A Micromechanic Modeling for Transformation Induced Plasticity in Steels. *Mater. Sci. Eng. A* **285**, 346–352 (2000).

4. Grujicic, M. & Dang, P. Computer simulation of martensitic transformation in Fe-Ni face-centered cubic alloys. *Mater. Sci. Eng. A* **201**, 194–204 (1995).

5. Sandoval, L., Urbassek, H. M. & Entel, P. The Bain versus Nishiyama-Wassermann path in the martensitic transformation of Fe. *New J. Phys.* **11**, (2009).

6. Guimarães, J. R. C. & Rios, P. R. Fundamental aspects of the martensite transformation curve in Fe-Ni-X and Fe-C alloys. *J. Mater. Res. Technol.* **7**, 499–507 (2018).

7. Ansell, G. S., Donachie, S. J. & Messler, R. W. The effect of quench rate on the martensitic transformation in Fe-C alloys. *Metall. Trans.* **2**, 2443–2449 (1971).

8. Pradhan, R. & Ansell, G. S. Kinetics of the martensite transformation in athermal Fe-C-Ni-Cr alloys. *Metall. Trans. A* **9**, 793–801 (1978).

9. Entwisle, A. R. Kinetics of Martensite Formation in Steel. *Metall. Trans.* **2**, 2395- (1971).

10. Machlin, E. S. & Cohen, M. Isothermal Mode of the Martensitic Transformation. 489–500 (1952).

11. SHIH, C. H., AVERBACH, B. L. & COHEN, M. Some characteristics of the isothermal martensitic transformation. *Trans. AIME* **203**, 183–185 (1955).

12. Kakeshita, T. *et al.* Effects of magnetic field on athermal and isothermal martensitic transformations in Fe-Ni-Cr alloys. *Materials Transactions Jim* vol. 40 100–106 (1999).

13. Kakeshita T, Sato Y, Saburi T, et al. Effects of Static Magnetic Field and Hydrostatic Presure on the Isothermal Martensitic Transformation in an Fe-Ni-Cr Alloy. *Mater. Trans. JIM* vol. 40 107–111 (1999).

14. Kakeshita, T., Kuroiwa, K., Shimizu, K. & Al, E. Effect of magnetic fields on athermal and isothermal martensitic transformation in Fe-Mn-Ni alloys. *Mater. Trans.* **34**, 415–422 (1993).

15. Tsuji, N. *et al.* Strategy for managing both high strength and large ductility in structural materials–sequential nucleation of different deformation modes based on a concept of plaston. *Scr. Mater.* **181**, 35–42 (2020).

16. Wakasa, K. & Wayman, C. M. The morphology and crystallography of Ferrous lath martensite. Studies of Fe-20%Ni-5%Mn-III. Surface relief, the shape strain and related features. *Acta Metall.* **29**, 1013–1028 (1981).

17. Ghosh, G. & Raghavan, V. The kinetics of isothermal martensitic transformation in an Fe-23.2wt.%Ni-2.8wt.%Mn alloy. *Mater. Sci. Eng.* **80**, 65–74 (1986).

18. Nishiyama, Z. *Martensitic Transformation*. (1972).

19. Cech, R. E. & Turnbull, D. Heterogeneous Nucleation Of the Martensite Transformation. *J. Met.* **8**, 124–132 (1956).

20. Pati, S. R. & Cohen, M. Kinetics of isothermal martensitic transformations in an iron-nickel-manganese alloy. *Acta Metall.* **19**, 1327–1332 (1971).

21. Lin, M., Olson, G. B. & Cohen, M. Distributed-activation kinetics of heterogeneous martensitic nucleation. *Metall. Trans. A* **23**, 2987–2998 (1992).

22. Magee, C. L. The kinetics of martensite formation in small particles. *Metall. Trans.* **2**, 2419–2430 (1971).

23. Fullman, R. L. Measurement of Particle Sizes in Opaque Bodies. *Jom* **5**, 447–452 (1953).

24. Olson, G. B. & Cohen, M. A General Mechanism of Martensitic Nucleation: Part I Concepts and the FCC → HCP Transformation. *Metall. Trans. A* **7**, 1897–1904 (1976).

25. Olson, G. B. & Cohen, M. A general mechanism of martensitic nucleation: Part II. FCC→BCC and other martensitic transformations. *Metallurgical Transactions A* vol. 7 1905–1914 (1976).

26. Olson, G. B. & Cohen, M. A General Mechanism of Martensitic Nucleation： Part III. Kinetics of Martensitic Nucleation. *Metall. Trans. A* **7**, 1897–1904 (1976).

27. Meyer, R. & Entel, P. Martensite-austenite transition and phonon dispersion curves of Fe1-xNix studied by molecular-dynamics simulations. *Phys. Rev. B* **57**, 5140–5147 (1998).

28. Hosoi, Y. & KAWAKAMI, Y. Effect of Plastic Deformation and Stress on Martensite Transformation in Fe-Ni Alloy. *Tetsu-to-Hagane* **49**, 1780–1787 (1963).

29. Tsuzaki, K., Fukasaku, S. ichi, Tomota, Y. & Maki, T. Effect of prior deformation of austenite on the γ → ε martensitic transformation in Fe-Mn alloys. *Materials Transactions, JIM* vol. 32 222–228 (1991).

30. Olson, G. B. & Cohen, M. Kinetics of Nucleation Strain-Induced Martensitic. *Metall. Trans. A* **6**, 791 (1975).

31. Lu, L. *et al.* Stress relaxation and the structure size-dependence of plastic deformation in nanotwinned copper. *Acta Mater.* **57**, 5165–5173 (2009).

32. Wang, Y. M., Hamza, A. V. & Ma, E. Activation volume and density of mobile dislocations in plastically deforming nanocrystalline Ni. *Appl. Phys. Lett.* **86**, 1–3 (2005).

33. Feaugas, X. & Haddou, H. Effects of grain size on dislocation organization and internal stresses developed under tensile loading in fcc metals. *Philos. Mag.* **87**, 989–1018 (2007).

34. Haddou, H., Risbet, M., Marichal, G. & Feaugas, X. The effects of grain size on the cyclic deformation behaviour of polycrystalline nickel. *Mater. Sci. Eng. A* **379**, 102–111 (2004).

35. Rolim Lopes, L. C. & Charlier, J. Effect of grain size and intergranular stresses on the cyclic behaviour of a ferritic steel. *Mater. Sci. Eng. A* **169**, 67–77 (1993).

Chapter 5 Summary and conclusions

In this thesis, the deformation behavior of Fe-24Ni-0.3C (wt.%) which was accompanied by the formation of the deformation induced martensite was studied by utilizing the nano-indentation and in-situ neutron diffraction. It is found that the conventional simple rule of mixture could not fully explain the strain hardening behavior of the specimen. We suggested that the strain hardening behavior of the specimen is determined by the changes of the phase stress in austenite and martensite and the change of volume fraction of martensite. The increase of the phase stress of the martensite plays an important role in the regeneration of strain hardening of the specimen. In addition, by analyzing the strain partitioning behavior between the two phases, the details of the deformation of the austenite and the martensite were clarified. On this basis, the effect of grain size on the deformation behavior of Fe-24Ni-0.3C was investigated. The results reveal that in the UFG specimen the stress partitioning between the austenite and the martensite was accelerated and enhanced due to the reinforced interaction between the two phases, which increased the strain hardening efficiency of the martensite formation. In addition, the activation of the martensitic transformation by deformation was discussed based on the concept of "PLASTON". For studying the kinetics of the martensitic transformation, a Fe-23Ni-3.55Mn (wt.%) which shows isothermal martensitic transformation was used in this study. The effect of tensile stress, plastic strain, and grain size on the kinetics of the isothermal martensitic transformation was quantitatively studied.

The results obtained in this thesis are summarized as follows.

Chapter 1 reviewed the background of the present research. Progresses in studies on advanced high strength steel (AHSS) were introduced firstly. As one of the promising strategies for managing both high strength and large ductility, the feasibility of combining ultrafine-grained structure and the TRIP effect is demonstrated. Then, the purposes of the present thesis were proposed

In **Chapter 2**, the deformation mechanism of Fe-24Ni-0.3C alloy having a mean grain size of 35 μm was systemically investigated by using tensile test, nano-indentation and in-situ neutron diffraction. The tensile test at room temperature reveals that the Fe-24Ni-0.3C specimen has both high tensile strength and high uniform elongation which is mainly attributed to its high strain hardening capability. Different from dislocation slip dominated materials whose strain hardening rate usually monotonically decreases with increasing the strain, the strain hardening rate of Fe-24Ni-0.3C specimen once significantly increased during the deformation. The enhancement of strain hardening rate effectively postponed the plastic instability and ensured the high uniform elongation of the specimen. The observation of deformed microstructure reveals that the starting of the enhancement of the strain hardening is accompanied by the initiation of the deformation induced martensitic transformation.

Generally, it has been widely accepted that the enhancement of strain hardening caused by the deformation induced martensitic transformation is due to the high strength of martensite and the increase of volume fraction of martensite as the deformation progresses, according to the simple rule of mixture. However, the results in this chapter reveal that the increase of the flow stress of the specimen could not be fully comprehended by the simple rule of mixture. The total flow stress calculated from the strength of austenite and martensite (estimated from nano-hardness) and their volume fraction was much larger than the true stress-strain curve of the specimen. It is because the interaction between austenite and martensite is neither considered in the simple rule of mixture nor reflected by the nano-hardness of each phase. The nano-hardness only corresponds to the flow stress of each phase when it deforms independently. But in the actual specimen, two phases having different mechanical properties (strength, elastic constant) are not equally deformed. The two phases connected at phase boundary have to accommodate each other during plastic deformation to maintain compatibility. Thus, the real internal stress on each phase should be determined by the interaction between the two phases.

To confirm this argument, tensile tests with in-situ neutron diffraction were performed to measure the phase stress (internal stress) of austenite and martensite during the deformation. The results of in-situ neutron diffraction reveal that the phase stress of martensite gradually increased from about 500 MPa to 2000 MPa during the tensile deformation. Besides the increase of martensite volume fraction, the increase of the phase stress of martensite also contributed to the enhancement of the strain hardening of the specimen. More importantly, the calculated total stress using the phase stress of austenite and martensite corresponded well with the true stress−strain curve. It reveals that the phase stresses of austenite and martensite determine the flow stress of the specimen much better than their strength estimated from the nano-hardness. In addition, plastic strain partitioning between austenite and martensite is also investigated by using the in-situ neutron diffraction as introduced in Section 2.6. It reveals that the most of plastic deformation was concentrated on the austenite phase and only 10% plastic strain occurred on the martensite phase. According to the deformation state of austenite and martensite, the deformation of Fe-24Ni-0.3C specimen could be divided into three stages: (1) Stage I: deformation of single-phase austenite; (2) Stage II: elasto-plastic region: austenite plastically deforms while martensite only elastically deforms; (3) Stage III: both austenite and martensite plastically deform. What's more, it is found that the stress-strain response of the deformation induced martensite during the tensile deformation of the specimen is quite similar to that of single-phase martensite, suggesting that the interaction between austenite and martensite only determines the deformation of the two phases, but not change the stress-strain response of each phase. Moreover, we speculate that the dynamic formation of the martensite during deformation would influence the evolution of the phase stress of martensite as well.

In **Chapter 3**, the deformation behavior of Fe-24Ni-0.3C specimens with mean grain sizes of 4 μm and 1.3 μm was studied by utilizing in-situ neutron diffraction and compared with the specimen with a mean grain size of 35 μm. The specimens with mean grain sizes of 35 μm, 4 μm and 1.3 μm represent CG, FG and UFG specimens, respectively. The tensile tests revealed that all three specimens had an enhanced strain hardening during the deformation which is accompanied by the formation of deformation induced martensite. With decreasing the mean grain size, the increment of strain hardening rate of the specimen caused by the martensitic transformation decreased. At the same time, the measurement of volume fraction of the martensite by in-situ neutron diffraction revealed that the grain refinement decelerated the formation of the martensite. The kinetic of deformation induced martensitic transformation has a strong influence on the strain hardening behavior of Fe-24Ni-0.3C alloy.

On the other hand, the effect of grain size on the stress partitioning behavior between austenite and martensite was studied by tensile tests with in-situ neutron diffraction. The result reveals that, when the grain size changed within the coarse-grained region, the influence of the grain size on the stress partitioning behavior between austenite and martensite was relatively small. Thus, when the mean grain size is changed within the CG region the strain hardening behavior of the 24Ni-0.3C metastable austenitic steel was mainly determined by the increasing rate of the martensite volume fraction. However, when the grain size was decreased down to the UFG region, the evolution of the phase stress of martensite and the stress partitioning significantly accelerated and enhanced, which contributed to the strain hardening of the specimen. Therefore, although the formation rate of martensite in the UFG specimen was much lower than that in the FG specimen, the increment of strain-hardening rate in the UFG specimen was almost the same as that in the FG specimen due to the higher phase stress in martensite of the UFG specimen.

The evolution of plastic strain in the austenite phase and the martensite phase was estimated from the change of the dislocation density of the austenite. The stress-strain responses of martensite during the deformation in the specimens with various grain sizes were obtained by plotting the phase stresses of the martensite as a function of the estimated true strains of the martensite. The result reveals that the phase stress of the martensite increased with decreasing the grain size is because of the increase in the intrinsic strength of the martensite phase by the grain refinement. However, the higher increasing rate of phase stress of the martensite during the deformation of the UFG specimen at stage II of the deformation might because of the increase in the interaction between the two phases caused by the strain incompatibility. The stronger interaction between the two phases in the UFG specimen makes the martensite soon plastically deformed after its formation and have more plastic strain than that in the FG and the CG specimen. Therefore, the plastic deformation in the UFG specimen is more homogeneous. For the same reason, the martensite in the UFG specimen was more strain-hardened at stage III of deformation, which made the increment of the phase stress of the martensite was larger in the UFG specimen than that in the FG and CG specimens at stage III of deformation. In conclusion, the results in this chapter reveal that the interaction between austenite and martensite caused by the strain incompatibility in the UFG specimen might increase, which could accelerate the stress partitioning between the two phases and make the plastic deformation between the two phases more homogeneous. As a consequence, the increment of strain hardening by the formation of the same amount of martensite is higher in the UFG specimen.

In **Chapter 4**, the effect of tensile stress, prior plastic deformation and grain size on the kinetics of the isothermal martensitic transformation in Fe-23Ni-3.55Mn (wt.%) was quantitatively studied and discussed from the viewpoint of "PLASTON". The overall isothermal martensitic transformation in Fe-23Ni-3.55Mn can be well described by the singly activated model in which the effect of autocatalytic effect is included and it is assumed that the activation energies for all nucleation site are uniform.

The effect of tensile stress and prior plastic deformation on the kinetics of the isothermal martensitic transformation was studied by using a specimen with a mean grain size of 7 μm. The results reveal that the activation energy for the martensitic nucleation is decreased by applying tensile stress. As a consequence, the kinetics of the isothermal martensitic transformation could be enhanced by increasing the tensile stress. In addition, the effect of stress on the isothermal martensitic transformation becomes weaker when the transformation temperature decreases. It is because that the activation volume decreases as the temperature is decreased. In the viewpoint of 'PLASTON', we think the activation volume for the martensitic nucleation is determined by the activation distance and the size of the nucleation embryo. According to the result of the MD simulation, the decrease of activation volume as the temperature decreases might be attributed to the decreased in the activation distance. On the other hand, the isothermal thermal martensitic transformation is inhibited by prior plastic deformation at 80 ^{o}C. The inhibiting effect of prior plastic deformation increases with increasing the deformation. Therefore, the initiation of deformation induced martensitic transformation during the deformation is attributed to the increase the stress. And the kinetics of the deformation induced martensitic transformation during deformation might be the net effect of stress and plastic deformation.

When the grain size of austenite was reduced from 25 μm to 7 μm, the kinetics of the isothermal martensitic transformation in Fe-23Ni-3.55Mn was suppressed and the activation energy was increased. It might because the increase in the strength of the matrix as grain refinement enhanced the difficulty for the martensitic nucleation. However, the accelerating effect of stress on the martensitic transformation becomes stronger as grain refinement. We speculate that it might be attributed to that the grain refinement might increase the probability of the formation of the region with high local stress since the area of grain boundaries and the number of triple junctions increases.

In **Chapter 5**, all the obtained results in **Chapter 2 - 4** have been summarized.

This thesis clarified the deformation behavior of the metastable austenitic Fe-24Ni-0.3C steel accompanying the deformation induced martensitic transformation and its grain size dependency. The author believes that these results would be fundamentally helpful to develop advanced UFG TRIP steels with both high strength and large ductility. The kinetics of the deformation induced martensitic transformation was only preliminarily studied in this thesis. Although there are still many problems remained, the author thinks that the results obtained in this thesis could build a basic understanding of the activation of the martensitic transformation from the viewpoint of “PLASTON”.

Acknowledgements

Upon the completion of this thesis, I am grateful to those who have offered me encouragement and support during the course of my study.

First and foremost, my deepest gratitude goes to my supervisor, Professor Nobuhiro Tsuji of Kyoto University, for his constant encouragement and guidance. He has offered me valuable suggestions in the academic studies. Without his patient instruction, insightful criticism and expert guidance, this thesis could not have reached its present form.

Second, I also would like to thank Associate Professor Akinobu Shibata and Associate Professor Yu Bai of Kyoto University for having helpful discussion with me and providing me a lot of suggestions during my PhD study.

I also want to express my sincere thanks to Associate Professor. Si Gao who directly helped me in my studies and taught me a lot of experimental techniques all the time since the beginning of my research study.

I am also deeply grateful to Dr. Wu Gong in the Japan Proton Accelerator Research Complex who helped me greatly in the experiments of in-situ neutron diffraction and the data analysis.

I also want to thank Professor Shigenobu Ogata and Associate Professor Junping Du in the Department of Mechanical Science and Bioengineering, Osaka University, for helping us in the molecular dynamic simulation.

Special thanks to Ms. Akiko Koike and Ms. Aika Kaise and Ms. Chiaki Ii for their excellent secretarial work and daily helps all the time. Meanwhile, the equal gratitude is offered to all my laboratory members for the valuable discussion and the unforgettable time.

In addition, I would like to express sincere thanks to China Scholarship Council (CSC), P.R. China for supporting me to do PhD study in Japan. The supports are gratefully appreciated.

Last but not least, I should finally like to express my gratitude to my beloved family who have always been helping me out of difficulties and supporting without a word of complaint. I also owe my sincere gratitude to my friends and my fellow students who gave me their help and time in listening to me and helping me work out my problems during the difficult course of the thesis.

List of achievements

Journal papers

1) Gao S, Bai Y, Zheng R, **Mao W**, et al. Mechanism of huge Lüders-type deformation in ultrafine grained austenitic stainless steel. Scripta Materialia, 2019, 159: 28-32,

2) Tsuji N, Ogata S, Inui H, Tanaka I, Gao S, **Mao W**, et al. Strategy for managing both high strength and large ductility in structural materials–sequential nucleation of different deformation modes based on a concept of plaston. Scripta Materialia, 2020, 181: 35-42.

Conference papers

1) **Mao W**, Gao S, Bai Y, Shibata A, and Tsuji N, Proceedings of The Ninth Pacific Rim International Conference on Advanced Materials and Processing. The Japan Institute of Metals and Materials, 2016, pp: 663-665.

2) **Mao W**, Gao S, Gong W, et al. Proceedings of the International Conference on Martensitic Transformations: Chicago. Springer, Cham, 2018: 95-98.

International conference

1) **W. Mao**, S. Gao, Y. Bai, A. Shibata and N. Tsuji. The Ninth Pacific Rim International Conference on Advanced Materials and Processing (PRICM9), August 5th, 2016. Kyoto, Japan. Poster presentation.

2) **W. Mao**, S. Gao, Y. Bai, A. Shibata and N. Tsuji. International Conference on Martensitic Transformations (ICOMAT2017), July 10th, 2017. Chicago, America. Poster presentation.

3) **W. Mao**, S. Gao, Y. Bai, A. Shibata and N. Tsuji. The 15th International Conference on Advanced Materials (IUMRS-ICAM 2017), August 30th, 2017. Kyoto, Japan. Oral presentation.

4) **W. Mao**, S. Gao, W. Gong, Y. Bai, M. Park. A. Shibata and N. Tsuji. 18th international conference on the strength of materials (ICSMA18), July 15th, 2018. Ohio, American. Oral presentation.

5) **W. Mao**, S. Gao, W. Gong, Y. Bai, M. Park. A. Shibata and N. Tsuji. Gordon research conferences (GRC), June 24th, 2019, Hongkong, China. Poster presentation.

6) **W. Mao**, S. Gao, Y. Bai, M. Park. A. Shibata and N. Tsuji. PRICM10, August 19th, 2019. Xi'an, China. Oral presentation.

7) **W. Mao**, S. Gao, Y. Bai, M. Park. A. Shibata and N. Tsuji. Materials Science & Technology (MS&T), September 29th, 2019, Portland, America, Oral presentation.

Conference in Japan

1) **W. Mao**, S. Gao, W. Gong, Y. Bai, M. Park. A. Shibata and N. Tsuji. The Japan Institute of Metals and Materials, Annual Spring Meeting 2017, March, 2017, Tokyo, Oral presentation.

2) **W. Mao**, S. Gao, W. Gong, Y. Bai, M. Park. A. Shibata and N. Tsuji. The Japan Institute of Metals and Materials, Annual Autumn Meeting 2017, September, 2017, Hokkaido, Oral presentation.

3) **W. Mao**, S. Gao, Y. Bai, M. Park. A. Shibata and N. Tsuji. The Japan Institute of Metals and Materials, Annual Autumn Meeting 2018, September, 2018, Sendai, Poster presentation.

4) **W. Mao**, S. Gao, Y. Bai, M. Park. A. Shibata and N. Tsuji. The Japan Institute of Metals and Materials, Annual Spring Meeting 2019, March, 2019, Tokyo, Poster presentation.

5) **W. Mao**, S. Gao, Y. Bai, M. Park. A. Shibata and N. Tsuji. The Japan Institute of Metals and Materials, Annual Autumn Meeting 2019, September, 2019, Okayama, Oral presentation.

6) **W. Mao**, S. Gao, Y. Bai, M. Park. A. Shibata and N. Tsuji. The Japan Institute of Metals and Materials, Annual Spring Meeting 2020, March, 2020, Tokyo, Poster presentation.